AGH

AGH University of Krakow

FIELD OF SCIENCE : NATURAL SCIENCES

SCIENTIFIC DISCIPLINE : PHYSICAL SCIENCES

DOCTORAL DISSERTATION

Study of the hottest droplet of fluid through correlations and fluctuations of collective variables

Author : Rupam Samanta

Supervisor: Prof. dr. hab. Piotr Bożek

AGH University of Krakow
Faculty of Physics and Applied Computer Science

Kraków, 2024

I would like to dedicate this thesis to my beloved parents and my brother Dr. Chandan Samanta.

Declaration

Declaration of the Author of this dissertation:

Aware of legal responsibility for making untrue statements I hereby declare that I have written this dissertation myself and all the contents of the dissertation have been obtained by legal means.

....
Date, Author's signature

Declaration of the thesis Supervisor:

This dissertation is ready to be reviewed.

....
Date, Supervisor's signature

Acknowledgements

This thesis required a lots of guidance and assistance from many individuals, without whom its completion would not have been possible. I feel privileged to have received such supports throughout my journey and must express my sincere gratitude to all who helped me.

First and foremost, I would like to express my deepest and heartiest gratitude to my PhD supervisor, Prof. dr. hab. Piotr Bożek. His immense support, insightful guidance, and constant encouragement have been instrumental in the completion of this thesis. Prof. Bożek's expertise and dedication to my research have been invaluable. From writing research paper to the preparation of grant application, I am profoundly grateful for his mentorship throughout my doctoral journey.

Secondly, I am immensely thankful to Prof. Jean-Yves Ollitrault, at the Institute of Theoretical Physics, Saclay, France for hosting me for a six-month research internship and providing me proper guidance and mentorship. The research carried out during the internship constitute a part of this thesis. I am deeply grateful to the hospitality of IPhT during my stay. The experience gained at IPhT and the long-term collaboration with Prof. Ollitrault have significantly enriched my research.

I extend my sincere thanks to my research collaborators, Prof. Matthew Luzum, Prof. Jiangyong Jia, Somadutta Bhatta and Joao Paulo Picchetti. Their collaboration on the papers during my PhD has been crucial to my academic development. I also thank Tribhuban Parida for helpful discussions while writing the thesis, which helped me to learn many things in the particular field.

My heartfelt appreciation goes to the AGH University of Krakow, particularly the Faculty of Physics and Applied Computer Science (WFiIS), for providing an excellent academic platform and a suitable research infrastructure. I am grateful to my departmental colleagues for their useful inputs and for fostering a friendly and stimulating atmosphere that has greatly supported my research endeavors.

I would also like to acknowledge the incredible support from my family and friends. Their encouragement and understanding have been a constant source of strength throughout this journey. I am especially thankful to my parents, my brother Dr. Chandan Samanta whose constant belief in me has been a cornerstone of my achievements.

Finally, I gratefully acknowledge the financial support from the NCN Preludium Bis grant: 2019/35/O/ST2/00357, for funding my PhD research, and the NAWA grant: PPN/STA/2021/1/00040/U/00001, which supported my six-month research internship at IPhT, Saclay. These grants have been essential in facilitating my research, academic travel and overall growth.

Thank you all for your invaluable contributions and support !

Abstract

Collisions of two heavy nuclei at relativistic speeds at the Relativistic Heavy Ion collider (RHIC) at BNL and the Large Hadron Collider (LHC) at CERN, create a state of matter which has a temperature 10^5 times that of Sun's core, a size of the order of nuclear radius (femtometer) and which behaves like a perfect fluid with minimal viscosity. This matter under extreme condition, is a medium where the quarks and gluons, normally existing as bound states in hadrons, travel freely with color degrees of freedom, with their interactions governed by Quantum Chromodynamics (QCD). This hot, dense, fluid-like droplet of deconfined state of quarks and gluons is known as the Quark Gluon Plasma (QGP). The QGP medium, surviving for a very short time (10^{-22} s) with its evolution dynamics described by the relativistic viscous hydrodynamics, creates thousands of particles hitting the detectors at the end. One of the most remarkable features is the collective flow of these particles, serving as a key phenomenon for probing the QGP medium in high energy nuclear collisions. The most peculiar and intriguing characteristics of the collective anisotropic flow, quantified in terms of flow harmonics, is the importance of event-by-event fluctuations, stemming mostly from event-by-event fluctuations in the initial state. In this thesis, we focus on fluctuations and correlations between the collective observables such as mean transverse momentum per particle ($[p_T]$) and harmonic flow coefficients (v_n) etc. Specifically, we show that the fluctuations of harmonic flow can be probed by the factorization-breaking coefficients between flow vectors in different p_T-bins. Experimental difficulty can be reduced by taking one of the flow vectors momentum averaged. Fluctuations cause a decorrelation between the flow vectors, which can be attributed to equal contributions from the flow magnitude and flow angle decorrelation. We study fluctuations of mean transverse momentum per particle ($[p_T]$) in ultra-central collisions and show that our model can explain the steep fall of its variance observed by the ATLAS collaboration. We also present robust predictions for the skewness and kurtosis, and highlight the role of impact parameter fluctuations in ultracentral collisions. We study the Pearson correlation coefficients between $[p_T]$ and v_n^2, which can map the initial state correlations between the shape and size of the fireball. We show that higher order normalized and symmteric cumulants between these observables can be constructed, which put useful additional constraints on the initial state properties. Furthermore, we study the momentum dependent Pearson correlation between $[p_T]$ and the transverse momentum dependent flow. It shows sensitivity to the Gaussian width of the nucleon at the initial state. Finally, we show that such correlations and fluctuations of collective observables can be used to study nuclear deformation and put robust constraints on their deformation parameters through high energy nuclear collisions. The research presented in this thesis has significantly contributed to the advancement of the field leaving ample opportunities for further developments in future, which remain beyond its current scope.

Streszczenie

Zderzenia dwóch ciężkich jąder atomowych przy prędkościach relatywistycznych w Relatywistycznym Zderzaczu Ciężkich Jonów (RHIC) w BNL oraz Wielkim Zderzaczu Hadronów (LHC) w CERN, tworzą stan materii o temperaturze 10^5 razy wyższej niż temperatura jądra Słońca, rozmiarach rzędu promienia jądra atomowego (femtometr) i zachowujący się jak doskonała ciecz o minimalnej lepkości. Ta materia w ekstremalnych warunkach jest układem, w którym kwarki i gluony, normalnie występujące jako stany związane w hadronach, stają się swobodne z barwnymi stopniami swobody, a ich interakcje są regulowane przez Chromodynamikę Kwantową. Ta gorąca, gęsta, przypominająca ciecz kropla stanu kwarków i gluonóz uwolnionym ładunkiem kolorowym w jest znana jako Plazma Kwarkowo-Gluonowa (QGP). Materia QGP, istniejąca przez bardzo krótki czas (10^{-22} s) z dynamiką ewolucji opisaną przez relatywistyczną hydrodynamikę lepką, tworzy tysiące cząstek mierzonych w końcu w detektorach. Jedną z najbardziej niezwykłych charaterystyk tego układu jest zbiorowy przepływ tych cząstek, służący jako kluczowe zjawisko do badania QGP w wysokoenergetycznych zderzeniach jądrowych. Najbardziej specyficzną i intrygującą cechą zbiorowego anizotropowego przepływu, określanego w kategoriach współczynników harmonicznych przepływu, jest znaczenie fluktuacji od zderzenia do zderzenia, głównie wynikających z fluktuacji stanu początkowego. W tej pracy koncentrujemy się na fluktuacjach i korelacjach między kolektywnymi obserwablami takimi jak średni poprzeczny pęd na cząstkę ($[p_T]$) i współczynniki harmoniczne przepływu (v_n) itd. W szczególności pokazujemy, że fluktuacje współczynników harmonicznych można badać za pomocą współczynników łamania faktoryzacji między wektorami przepływu w różnych przedziałach p_T. Trudności eksperymentalne można zmniejszyć, biorąc jeden z wektorów przepływu jako średnio pędowy. Fluktuacje powodują dekorelację między wektorami przepływu, co można przypisać równym wkładom od dekorelacji wielkości przepływu i kąta przepływu. Badamy fluktuacje średniego poprzecznego pędu na cząstkę ($[p_T]$) w ultra-centralnych zderzeniach i pokazujemy, że nasz model może wyjaśnić strome zmniejszenie wariancji zw danych ATLAS. Przedstawiamy również prognozy dla skośności i kurtozy oraz podkreślamy rolę fluktuacji parametru zderzenia w ultra-centralnych zderzeniach. Badamy współczynniki korelacji Pearsona między $[p_T]$ a v_n^2, które mogą odwzorowywać korelacje stanu początkowego między kształtem a rozmiarem gorącej kropli. Pokazujemy, że można skonstruować wyższe rzędy normalizowanych i symetrycznych kumulantów między tymi obserwablami, które wnoszą dodatkowe użyteczne ograniczenia dotyczące właściwości stanu początkowego. Ponadto badamy zależną od pędu korelację Pearsona między $[p_T]$ a poprzecznie zależnym od pędu przepływem. Wykazuje ona wrażliwość na szerokość fluktuacji w stanie początkowym. Na koniec pokazujemy, że takie korelacje i fluktuacje kolektywnych obserwabli mogą być używane do badania deformacji jądrowych i otrzymania ograniczeń na parametry deformacji poprzez wysokoenergetyczne zderzenia jądrowe. Badania przedstawione w tej pracy w znaczący sposób przyczyniły się do rozwoju tej dziedziny, pozostawiając wiele możliwości na dalsze prace w przyszłości, które wykraczają poza jej obecny zakres.

Table of contents

List of figures

List of tables

Notations

- We use natural units : $\hbar = c = k_B = 1$.
- Metric : $g^{\mu\nu} = diag(1,-1,-1,-1)$.
- Position four vector : $x^\mu = (t,x,y,z)$.
- Fluid velocity : $u^\mu = (1,\vec{v})$.
- The projector : $\Delta^{\mu\nu} = g^{\mu\nu} - u^\mu u^\nu$.
- Rank 4 tensor : $\Delta^{\mu\nu}_{\alpha\beta} = \frac{1}{2}(\Delta^\mu_\alpha\Delta^\nu_\beta + \Delta^\mu_\beta\Delta^\nu_\alpha - \frac{2}{3}\Delta^{\mu\nu}\Delta^{\alpha\beta})$.
- The angular brackets and the parenthesis used :

$$X^{\langle\mu\rangle} = \Delta^\mu_\nu X^\nu, \qquad Y^{\langle\mu\nu\rangle} = \Delta^{\mu\nu}_{\alpha\beta}Y^{\alpha\beta} \quad \text{and} \quad Z^{(\mu\nu)} = \frac{1}{2}(Z^{\mu\nu} + Z^{\nu\mu}) .$$

Transverse Momentum

- General notation for transverse momentum : p_T .
- Mean transverse momentum per particle in an event : $[p_T]$.
- Average transverse momentum (averaged over events) : $\langle p_T\rangle$ or $\overline{p_T} \equiv \langle [p_T]\rangle$.
- We use $\delta p_T = p_T - \langle p_T\rangle$ or $p_T - \overline{p_T}$.
- Other notations used for transverse momentum to avoid confusions whenever necessary : p (Factorization-breaking coefficients) or q (momentum dependent Pearson correlation coefficients) .

Harmonic flow

- Harmonic flow vector in an event : $V_n = v_n e^{in\Psi_n}$. where, flow magnitude : $v_n = V_n V_n^\star$ and flow angle : Ψ_n.
- v_n denotes the integrated flow in an event .

- Two-particle cumulant for flow harmonic, which is an event averaged quantity : $v_n\{2\} = \sqrt{\langle V_n V_n^\star \rangle}$, the integrated flow averaged over events .
- Transverse momentum dependent or differential harmonic flow in an event : $V_n(p_T)$, other notations : $V_n(p)$ or $V_n(q)$, with $V_n(p) = v_n(p) e^{in\Psi_n(p)}$.
- Event averaged p_T-differential flow :

$$v_n\{2\}(p) = \frac{\langle V_n V_n^*(p) \rangle}{\sqrt{\langle V_n V_n^* \rangle}} \quad \text{and} \quad v_n[2](p) = \sqrt{\langle V_n(p) V_n^*(p) \rangle} = \sqrt{\langle v_n(p)^2 \rangle} \ .$$

Chapter 1

Introduction

The field of high-energy physics which can be broadly classified into nuclear and particle physics, deals with understanding the fundamental forces of nature governing the interactions between its microscopic constituents. The physics of the interaction between fundamental particles that are found in nature is largely governed by the *Standard Model* (SM) of particle physics[1] [1, 2] and accessed by colliding particles using high energy accelerators [3].

Initial years of nuclear physics focused on the properties and interactions of atomic nuclei at low energies. However, with the advancement of accelerator and collider technology, it became possible to explore nuclear collisions at much higher energies. In these colliders, by colliding two heavy nuclei such as gold (Au) or lead (Pb) at a speed very close to the speed of light c, it is possible to create a state of matter which existed just microseconds after the Big Bang [4]. This is known as *ultrarelativistic heavy-ion collision* which lies at the frontier of high-energy physics facilitating the study of fundamental properties of matter under extreme conditions [5–8]. The study of high-energy nuclear collisions is important for advancing our understandings of *Quantum Chromodynamics* (QCD), the theory governing the strong interaction [9, 10], one of the four fundamental forces in nature.

The state of matter created in ultrarelativistic heavy-ion collision is an extremely hot, dense, tiny medium of quarks and gluons, the fundamental constituents of hadrons, known as the *Quark-Gluon-Plasma* (QGP), which behaves like an almost perfect fluid. This QGP medium survives for a very short time (few fm/c) and what is ultimately seen in the detectors of such heavy-ion experiments, is a large number of hadrons produced in the collisions. A single head-on collision of Pb+Pb at 5.02 TeV centre of mass energy, creates around ~ 35000 hadrons which are mostly pions[2]. The study of the properties and the dynamics of the QGP medium accessed through those detected particles can unravel many interesting aspects of the matter under exotic

---

[1] The Standard Model does not describe the gravitational force which is one of the four fundamental forces in nature.

[2] If we consider only the identified charged hadrons, a large fraction of them are pions (~ 80%) while the rest are kaons (~ 17%) and protons (~ 3%) contributing to significantly smaller fractions.

conditions. The field of high-energy heavy-ion physics has evolved considerably over the past three decades answering some of the most fundamental questions of physics.

1.1 The Quark-Gluon-Plasma : hottest fluid ever known

The Quark-Gluon-Plasma created at the collision of two heavy nuclei moving at relativistic speed has an effective temperature of 212 MeV ($\equiv 10^{12}$K) [11], a size in the scale of femtometer (nuclear radius) and it is a nearly perfect fluid with a small viscosity [12]. The core of the Sun has a temperature 10^7 K, the QGP medium's temperature is another five orders of magnitude larger than that. Therefore, the QGP medium turns out to be the hottest, most dense and tiniest droplet of fluid that is ever known to the mankind and which can be crated at the laboratory [13]. Normally the quarks and gluons are never seen as free particles, rather they are always found as bound states such as proton, neutron or hadrons in general. The interaction between the quarks and gluons is governed by QCD involving their *color charges* . The quarks and gluons, called *partons* in general, individually carry color charges (or color quantum number) but the observed hadrons which are bound states of them are color neutral. This is known as *color confinement*.

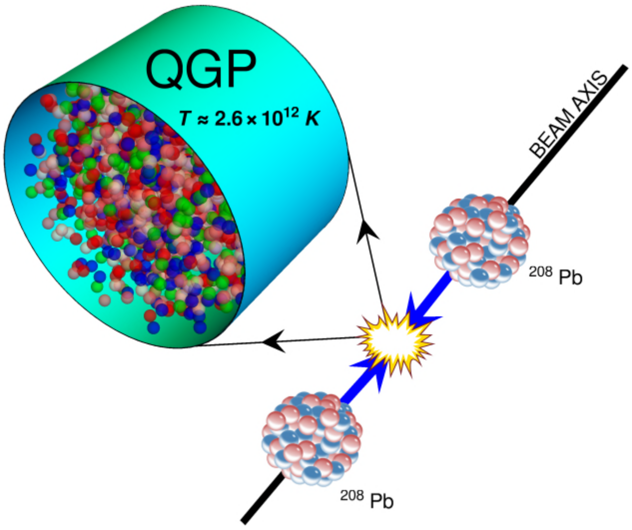

Fig. 1.1 Pictorial representation of Pb+Pb collision at the LHC and formation of the deconfined state of the Quark Gluon Plasma (QGP) medium, the hottest fluid (T~ 10^{12} K) that can be created in a laboratory. Figure taken from [11].

However, in QCD theory the interaction strength between the quarks and gluons is stronger at larger distance and become weaker or asymptotically zero at very short distance, a phenomena known as *the asymptotic freedom* [14, 15]. In ultrarelativistic heavy-ion collision, which occur at very high energy, these quarks and gluons become deconfined creating a quasi-free state : the Quark-Gluon-Plasma, making the color degrees of freedom deconfined. Thus the study of this little droplet of fluid would be very interesting, and could deepen our understanding of the strong nuclear force, QCD and basic building blocks of nature.

1.2 Experiments in heavy-ion collision

Almost fifty years ago, the first relativistic heavy-ion collision experiments were performed at the Bevatron in Berkeley at energies ~ 1-2 GeV. Since then heavier ions were collided at higher energies at facilities such as the Alternating Gradient Synchrotron (AGS) at the Brookhaven National Laboratory (BNL) and the Super Proton Synchrotron (SPS) at CERN providing early evidence of QGP formation.

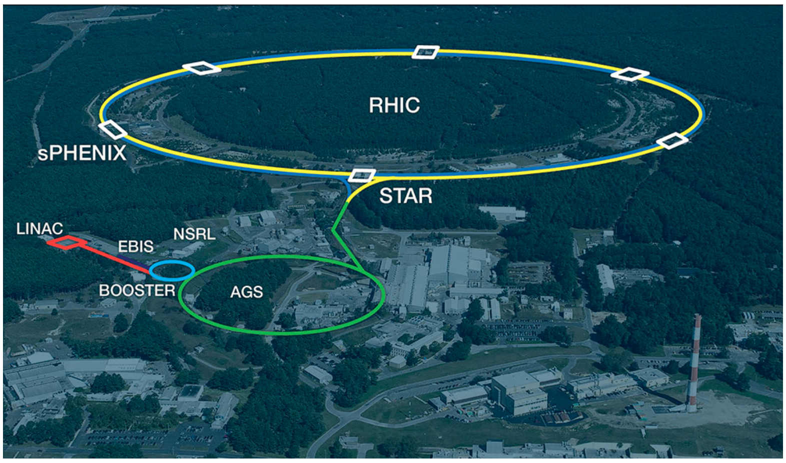

Fig. 1.2 The aerial view of the Relativistic Heavy Ion Collider (RHIC), located at the Brookhaven National Laboratory (BNL) in the United States, with its key experimental collaborations (e.g. STAR). Source : BNL .

However, with the rapid progress in accelerator and collider technology, soon there were dedicated heavy-ion colliders such as the Relativistic Heavy Ion Collider (RHIC) (Fig. 1.2) at BNL which started colliding heavy-ions since 2000 and the Large Hadron Collider (LHC) at CERN colliding heavy-ions and hadrons since 2010. At RHIC, located at BNL in the United States, gold (Au) ions are collided at up to 200 GeV center of mass energy per nucleon pair creating the QGP medium [13]. On the other hand heavy-ion collision entered its first TeV collision energy scale at the LHC (Fig. 1.3), located at CERN near France-Switzerland border, where two lead (Pb) ions are collided at a center of mass energy 2.76 TeV or 5.02 TeV, reinforcing the extreme conditions necessary for the QGP formation [16].

These collider facilities utilize sophisticated detectors to capture and analyze the plethora of particles produced in each collision. In particular, the key detectors or experimental collaborations at RHIC are STAR, PHENIX and very recently sPHENIX. At the LHC, dedicated measurements on heavy-ion collision are performed by the ALICE collaboration in addition to the ATLAS and CMS collaborations. These detectors use modern technology and intricate

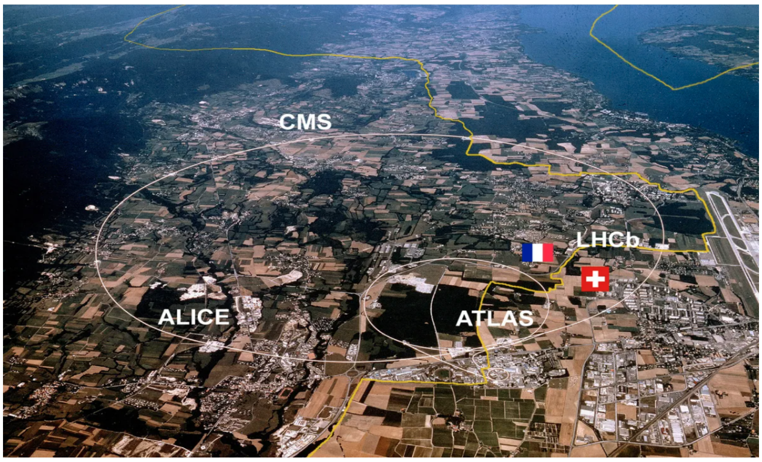

Fig. 1.3 The aerial view of the Large Hadron Collider (LHC), located at CERN near the France-Switzerland border, along with its key experimental collaborations: ALICE, ATLAS CMS and LHCb. Source : CERN .

methods to track thousands of particles created in a collision providing detailed information about their momenta, energies and interaction patterns.

1.3 Evolution of the QGP : different stages of HI collision

The QGP medium created in a heavy-ion collision lasts for a very short time ~ 10 fm/c. However, within such a short time the QGP fireball evolves and leaves some of its most exclusive signatures on the dynamics of the final state particles. The QGP medium has a very small[3] viscosity, making it the most perfect fluid and its evolution can be effectively described by relativistic viscous hydrodynamics, where the macroscopic physics can be applied at the femtoscale [17–26].

Specifically, an event of a heavy-ion collision, from the time of collision until the detection of particles, passes through a number of successive stages [25, 27, 28]. At the time of the collision, the colliding nuclei deposit energy or entropy at the overlap region, which serves as the *initial state* or initial condition of the collision. Then there exist a very short *pre-equilibrium phase* before the created fireball achieves *local thermal equilibrium* . After that, the thermalized QGP medium undergoes a relativistic viscous hydrodynamic evolution, where it *collectively expands* until it cools down to a certain temperature (T_c), where phase-transition occurs and the quarks and gluons again confine into hadroinc bound states. This is called the *QCD phase transition* [29–34] where a *smooth cross-over transition* from the QGP phase to Hadron Resonance Gas (HRG) phase occurs. Then the hadrons undergo elastic and in elastic collisions until a certain state is reached when such processes cease to occur, called the *freezeout*. After freezeout the hadrons stream towards the detectors.

---

[3] The shear viscosity to entropy ratio $\eta/s \sim 0.1$

It should be noted that relativistic hydrodynamics is one of the theoretical approaches to study the QGP medium. The properties and dynamics of the fireball created in heavy-ion collision can be studied in the light of other theoretical frameworks [35] such as relativistic kinetic theory approach or a transport model with string melting [36, 37]. All these theories can reasonably describe the properties of the final state particles across different momentum range. However, in this thesis we will be limited to the soft processes at low *transverse momentum*, where relativistic hydrodynamical picture is more applicable. High transverse momentum particles are useful for studying the *jet physics*[38, 39].

1.4 Collective flow and fluctuations

One of the most interesting and unique features of ultrarelativistic heavy-ion collisions is the *collective flow* of the final state particles [40–56]. This collective dynamics originate as an effect of the initial state of the collision and of the collective expansion of the fireball. The most notable is the *anisotropic flow* [40, 57–60] which originates due to the spatial anisotropy of the density distribution at the initial state of the collision. This spatial azimuthal anistoropy of the entropy or energy density distribution, through the evolution and collective expansion, translates into the azimuthal anisotropy of the momentum distribution of final state particles. This azimuthal anisotropy can be understood through different order of flow harmonics (v_n) such as the *elliptic flow*, *triangular flow* etc [61–64, 54].

The anisotropic flow depends on the *centrality* of the collision, defined by the transverse distance between the centers of colliding nuclei or the impact parameter (b) of the collision [66, 67] and determined in experiments through charged particle multiplicity N_{ch} or other centrality estimators [68–73]. As b become smaller, the collision is more central. The experimental evidence of the anispotropic flow, which caries an evidence of the formation of the tiny droplet of fluid, can be understood from the ridge like structure of the particle-pair distribution $d^2N^{pair}/d\eta d\phi$ on the (η,ϕ) plane, as measured by the CMS collaboration and shown in Fig. 1.4, where ϕ is the azimuthal angle on the transverse plane and η is the *pseudorapidity* of the particles. Moreover, the collective nature of the particle spectra can be realized through the *mean transverse momentum per particle*, which can be calculated from the transverse momentum (p_T) distribution of the particles in each event. These mean transverse momentum and harmonic flow coefficients constitute the basic collective observables in a heavy-ion collision event. Collective flow can be used to constrain the medium properties of the QGP such as the effective temperature, the viscosity and to gain broad insights of the dynamics of its evolution.

Another most peculiar characteristics of heavy-ion collisions are *event-by-event* fluctuations of collective flow [74–87], which originate due to event-by-event fluctuations of the initial state [88, 48, 89–94] as well as from dynamical fluctuations during evolution. These fluctuations lead to many interesting effects which could be studied by constructing suitable observables

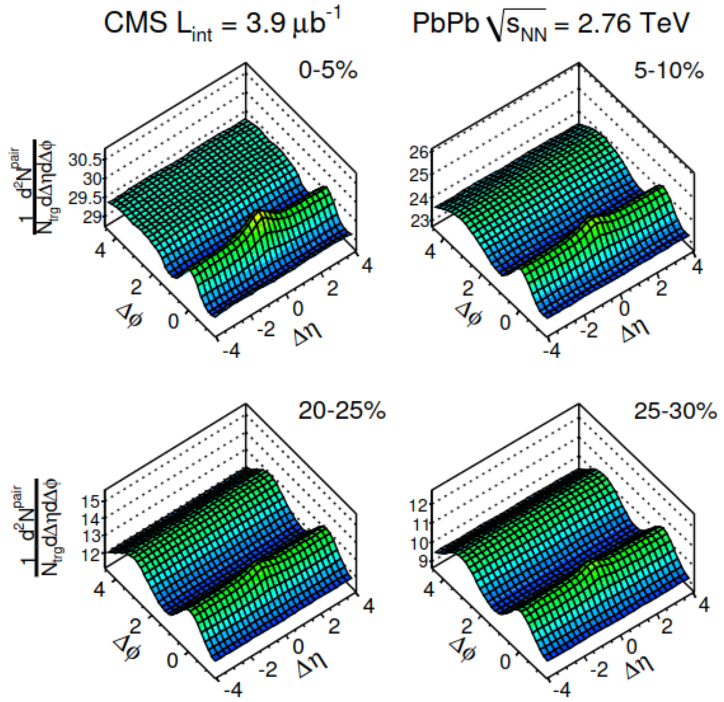

Fig. 1.4 Collective flow in ultrarelativistic heavy-ion collision seen from the *ridge*-like structures of the pair distribution of particles on the (η, ϕ) plane for different collision centrality as measured by the CMS collaboration. Figure taken from [65].

and can carry observable signature of fundamental properties of the QGP medium such as *thermalization* at the initial stage.

Additionally, one can construct correlation coefficients between the collective observables which contain important information and can be used to probe the initial state of collision providing useful constraints on the parameters [95–102]. Moreover, such correlation coefficients can be used to study nuclear structure and deformation in high energy nuclear collisions by colliding nuclei with different shapes and sizes (e.g. U+U, Xe+Xe, Ru+Ru and Zr+Zr etc.) [103–123, 101, 102, 124]. Such studies impose robust constraints on nuclear deformation parameters.

The main goal of this thesis is to look into different aspects of these event-by-event fluctuations of harmonic flow and mean transverse momentum, to study the correlations between the collective observables, proposing new constructions that can be measured in experiments and can potentially impose new robust constraints on the initial state, and to study nuclear structure (deformation) through similar observables by colliding deformed nuclei. Such studies will be helpful to broaden our knowledge about the initial state, dynamics and properties of the QGP medium and unravel nuclear structure at the ultrarelativistic energy scale.

1.5 Outline of the thesis

This thesis represents the culmination of the research conducted during my PhD study. In particular, the thesis is based on the following publications :

- Piotr Bozek, Rupam Samanta, '*Higher order cumulants of transverse momentum and harmonic flow in relativistic heavy ion collisions*', PRC 104 (2021) 1, 014905. arXiv: 2103.15338 [nucl-th].
- Piotr Bozek, Rupam Samanta, '*Factorization breaking for higher moments of harmonic flow*', PRC 105 (2022) 3, 034904. arXiv: 2109.07781 [nucl-th].
- Rupam Samanta, Piotr Bozek, '*Momentum-dependent flow correlations in deformed nuclei at collision energies available at the BNL Relativistic Heavy Ion Collider*', PRC 107 (2023) 3, 054916. arXiv: 2301.10659 [nucl-th].
- Rupam Samanta, Joao Paulo Picchetti, Matthew Luzum, Jean-Yves Ollitrault, '*Thermalization at the femtoscale seen in high-energy Pb+Pb collisions*', PRC 108 (2023) 2, 024908. arXiv: 2306.09294 [nucl-th].
- Rupam Samanta, Somadutta Bhatta, Jiangyong Jia, Matthew Luzum, Jean-Yves Ollitrault, '*Thermalization at the femtoscale seen in high-energy Pb+Pb collisions*', PRC 109 (2024) 5, L051902. arXiv: 2303.15323 [nucl-th].
- Rupam Samanta, Pitor Bozek, '*Momentum dependent measures of correlations between mean transverse momentum and harmonic flow in heavy ion collisions* ', Phys.Rev.C 109 (2024) 6, 064910. arXiv: 2308.11565 [nucl-th].

The thesis aims to provide an overview of the ultrarelativistic heavy-ion collision and the physics of the Quark-Gluon-Plasma with a special focus on the collective dynamics of the final state particles realized through correlations and fluctuations of the collective observables. The thesis is structured as follows :

- In Chapter-2, we provide an introductory overview of ultrarelativistic heavy-ion collision including its basic elements such as kinematics, collision geometry, collision centrality etc. We discuss Glauber modelling of nucleus-nucleus collision and its Monte-Carlo implementation. Next we briefly discuss the theory of relativistic ideal and viscous hydrodynamics which form the fundamental basis for the evolution of the QGP medium. We also briefly discuss Quantum Chromodynamics (QCD), the theory of strong interactions and how deconfinement occurs at the QGP state. Finally, we provide thorough discussions on the different stages of hydrodynamic framework of heavy-ion collisions, providing the details of the simulation set-up used in our analyses. Chapter-2 presents a short review on ultrarelativistic heavy-ion collision, based on published literature.

- In Chapter-3, we discuss the most distinctive feature of the heavy-ion collision, the collective flow and its basic phenomenological properties. We provide an overview of the anisotropic flow, its origin, the theoretical and experimental methods of flow analysis. Next we discuss the most peculiar characteristics of the collective flow: its event-by-event fluctuations. We show how event-by-event fluctuations of harmonic flow can be probed by constructing factorization-breaking coefficients in different transverse momentum bins. We discuss how the experimental limitation due to low statistics can be removed while measuring such observables. We extend the study to momentum dependent mixed-flow correlations as a probe of non-linearity present in the system. Chapter-3 is partly a brief review on collective flow based on published literature and partly presents original results published in [125].

- In Chapter-4, we discuss the transverse momentum fluctuations in ultracentral Pb+Pb collisions. In the first part, we show how the sudden fall of the variance in ATLAS data can be explained by a simple model of correlated Gaussian distribution between multiplicity and mean transverse momentum per particle. We show separately different contributions to the variance in our model and highlight the remarkable effect of impact parameter fluctuations. We perform a model fit to the ATLAS data and based on our fit results we provide crucial physical argument that could be responsible behind such phenomena. We point out important features of the ATLAS measurements in terms of the effect of p_T-cut and different centrality estimator. In the second part, we study the non-Gaussian characteristics of $[p_T]$-fluctuation, namely the skewness and kurtosis. Based on a similar model, we present predictions for ultracentral behavior of those cumulants and compare with the existing experimental data. Unless otherwise stated, Chapter-4 presents results published in [126] and [127].

- In Chapter-5, we discuss the correlation between mean transverse momentum $[p_T]$ and harmonic flow square v_n^2. We study the Pearson correlation coefficient $\rho([p_T], v_n^2)$ which can be used to probe correlation present in the initial state. We also present linear predictor to map the final state to the initial state of the collision. We propose new higher order normalized and scaled symmetric cumulants which could potentially put useful additional constraints and measure genuine higher order correlations. In the second part of the chapter, we study correlation coefficient between $[p_T]$ and momentum dependent harmonic flow which is independent of the specific p_T-cut and could be sensitive to particular properties of the initial state such as nucleon width w. We also propose experimentally feasible alternate definitions and direct measure of such correlations through normalized covariance. Unless otherwise specified, Chapter-5 presents results published in [128] and [129].

- In Chapter-6, we discuss how nuclear deformation can be accessed through high energy nuclear collision experiments. In particular we show how the deformation parameter β of ^{238}U nucleus can be constrained by studying similar correlations (e.g. $\rho([p_T], v_n^2)$ and symmetric cumulants) and the factorization-breaking coefficients probing fluctuations in central U+U collisions. Unless otherwise stated, Chapter-6 presents results published in [128] and [130].

- In Chapter-7, we summarize our main findings and draw conclusions based on our study. We briefly discuss scopes for further developments on the topics that we studied. We also present our plans with prospective research projects that we would be interested to pursue in future.

Chapter 2

Ultrarelativistic heavy-ion collision

In ultrarelativistic heavy-ion collision experiments performed at the LHC and RHIC, two heavy nuclei collide at a speed close to the speed of light, producing the hot dense QGP matter at the point of collision. This QGP fireball expands and cools down in a very short time before producing thousands of particles, a fraction of which are detected at the detector [6–8]. Therefore, in order to understand the properties and the evolution dynamics of the QGP medium, it is indispensable to discuss the kinematics of the collision, its different stages starting from the time of first hard collisions to the detection of the particles and the underlying theoretical frameworks that can be used to model the collision dynamics. In this chapter, we discuss these components of ultrarelativistic heavy-ion collisions with appropriate details wherever necessary. For the theoretical framework, we restrict ourselves to relativistic hydrodynamics [17–26] with brief discussions on QCD and the deconfinement. Towards the end of this chapter, we briefly describe the simulation set-up used in our analysis for producing the results presented in the subsequent chapters.

2.1 Kinematics and invariants

The properties and dynamics of heavy-ion collisions are studied through experimental measurements of physical observables, which broadly depend on the kinematics of the measurements. Fig. 2.1 shows the geometry of the heavy-ion collision experiments. Two heavy nuclei (Pb in this case) move at a relativistic speed along the z-axis and collide at z=0. After each collision a large number of particles are produced, denoted by the black arrows, and hit the detector's wall. The plane (x, y), transverse to the direction of the two nuclei (beam axis), is called the *transverse plane*. In the laboratory frame, each particle carries momentum, and in the experiments particles are detected and identified by their momentum coordinates.

In a Cartesian frame, the momentum space coordinates of a particle are denoted by the four vector, $p^\mu = \{p^0, p^i\} = \{E, p_x, p_y, p_z\}$. The four-momentum p^μ is often represented in the context of collider experiments as, $p^\mu = \{E, \vec{\boldsymbol{p}}_T, p_z\}$, where $\vec{\boldsymbol{p}}_T$ is called the *transverse momentum* of the particle and is defined as

$$\vec{p_T} = \{p_x, p_y\} \qquad \text{where} \qquad p_T = \sqrt{p_x^2 + p_y^2}\,. \tag{2.1}$$

The vector $\vec{p_T}$ lies in the plane (x,y). In a collision event, particles are emitted in random directions on the transverse plane. The momentum conservation requires that the total transverse momentum $\sum \vec{p_T} = 0$ in each event. More completely, one can write the four momentum p^μ in terms of spherical coordinates as, $p^\mu = \{E, psin\theta\cos\phi, p\sin\theta\sin\phi, p\cos\theta\}$ where ϕ is the azimuthal angle on the transverse plane with respect to the x axis and the angle θ is the polar angle on the (y,z) plane with respect to the z axis (Fig. 2.1).

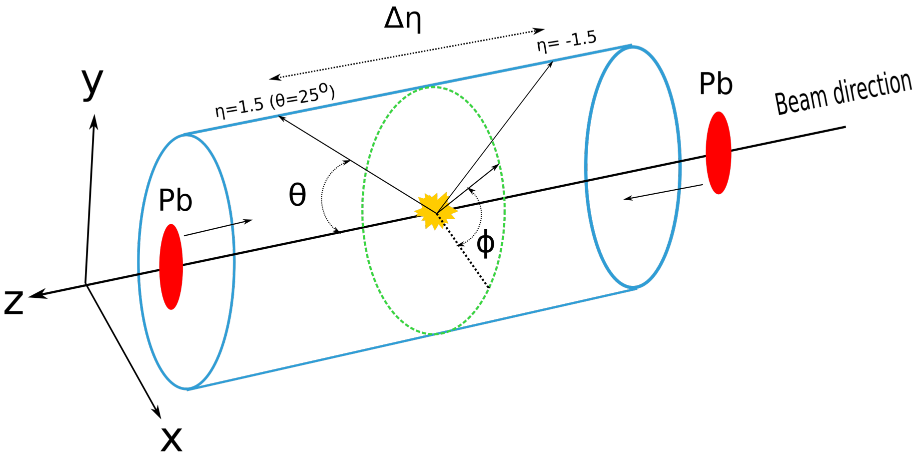

Fig. 2.1 Schematic representation of the geometry of ultrarelativistic heavy-ion collision (Pb+Pb) experiments. The collision axis is along the z-axis, and the detectors with a cylindrical form around this axis cover the full solid angle. The azimuthal angle ϕ is the angle on the transverse plane (x,y) perpendicular to the beam axis. The polar angle θ is associated with the pseudorapidity η, accounting for the longitudinal boost along the z-axis. The figure is motivated from [131].

As the two nuclei move with an ultrarelativistic speed, in laboratory frame they appear like flat pancakes [58], when viewed vertically from x-axis. This occurs because the nuclei are Lorentz-contracted due to the boost along z-axis. In general, the Lorentz transformation between the laboratory frame and the rest frame of the nuclei is given by,

$$X'^\mu = \Lambda^\mu_\nu \, X_\nu \,, \tag{2.2}$$

where $X'^\mu = \{t, x, y, z\} = \{t, \vec{x_T}, z\}$ is the position four vector, where $x_T = \sqrt{x^2 + y^2}$ is the transverse distance on (x,y) plane. For Lorentz boost along the z-axis,

$$\Lambda^{\mu}_{\nu} = \begin{pmatrix} \gamma & 0 & 0 & -\beta\gamma \\ 0 & 1 & 0 & 0 \\ 0 & 0 & 1 & 0 \\ -\beta\gamma & 0 & 0 & \gamma \end{pmatrix}, \tag{2.3}$$

where $\gamma = \sqrt{1-\beta^2}$ is the Lorentz factor and $\beta = v$ is the velocity of the nuclei. [Note: We use natural units, $\hbar = c = k_B = 1$ and metric $g^{\mu\nu} = diag(1,-1,-1,-1)$]. Fig. 2.2 shows the space-time picture of a collision event in (t,z) plane. The vertical and horizontal lines denote time and beam axis respectively. The lower part and the upper part of z-axis represent the scenarios before and after the collision respectively. The two nuclei collide at $t = z = 0$. As this is a relativistic collision, it is more appropriate to use *proper time coordinates* (*Milne coordinates*) defined as ,

$$\begin{aligned} \text{proper time, } \tau &= \sqrt{t^2 - z^2} \\ \text{and space-time rapidity, } \eta_s &= \frac{1}{2}\ln\frac{t+z}{t-z}. \end{aligned} \tag{2.4}$$

The two diagonal lines defined as $t = \pm z$ define the *light-cone*; along these lines $t^2 - z^2 = 0 (\tau = 0)$.

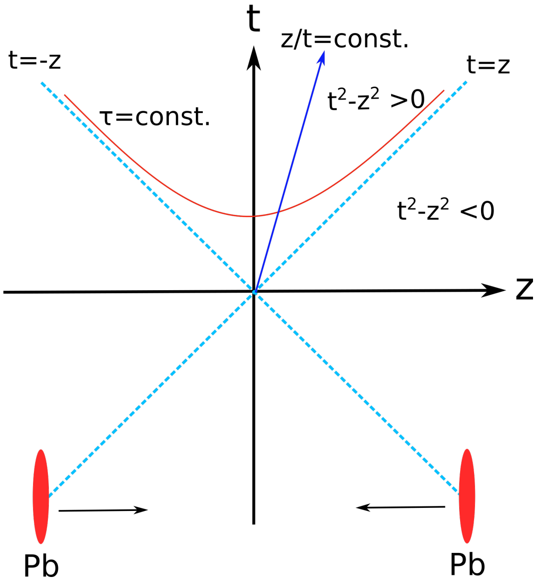

Fig. 2.2 Space-time representation of the collision in (t,z) plane. The vertical axis represents time and the horizontal axis denotes the beam direction. The lower and upper part of the plot represent before and after the collision respectively. The collision occurs at t=z=0. The diagonal lines t= ± z form the light cone. The region on the plot with $t^2 - z^2 > 0$ is called time-like region and $t^2 - z^2 < 0$ is called space-like region. Particle production occurs within the time-like region only. The figure is adapted from [20]

The region within the light-cone with $t^2 - z^2 > 0$ $(\tau > 0)$ is called *time-like* region and region outside with $t^2 - z^2 < 0$ $(\tau < 0)$ is called *space-like* region. The space-time rapidity η_s which spans from $-\infty$ to $+\infty$ is properly defined only in the time-like region and the particle production occurs on the upper-half part within this region.

Next we introduce two important variables in heavy-ion collision, namely *rapidity* and *pseudorapidity*. The rapidity of a particle is defined as ,

$$y = \frac{1}{2}\ln\frac{E+p_z}{E-p_z} , \tag{2.5}$$

which is expressed in terms of longitudinal velocity of the particle, $\beta_z = p_z/E$ as,

$$y = \frac{1}{2}\ln\frac{1+p_z/E}{1-p_z/E} = \tanh^{-1}\left(\frac{p_z}{E}\right) = \tanh^{-1}(\beta_z) . \tag{2.6}$$

An advantage of using rapidity over longitudinal velocity is that rapidity is additive under longitudinal boosts, therefore it provides a measure of Lorentz boost along z-axis. Rapidity can be understood as the relativistic analog of non-relativistic ($\beta_z << 1$) velocity. From Eq. (2.6),

$$y = \frac{1}{2}\ln\frac{1+\beta_z}{1-\beta_z} = \frac{1}{2}[\ln(1+\beta_z) - \ln(1-\beta_z)] \simeq \beta_z \equiv v_z . \tag{2.7}$$

Similar to transverse momentum, one can also define the *transverse mass* of a particle,

$$m_T^2 = m^2 + p_T^2 = E^2 - p_z^2 , \tag{2.8}$$

which is invariant under the Lorentz boost along the z direction. E and p_z can be expressed in terms of rapidity and transverse mass,

$$E = m_T \cosh y \quad \text{and} \quad p_z = m_T \sinh y . \tag{2.9}$$

Therefore, the four momentum of a particle can be written as, $p^\mu = \{m_T \cosh y, p_x, p_y, m_T \sinh y\}$. On the other hand pseudorapidity accounts for the polar angle θ of the particle and is defined as,

$$\eta = -\ln\tan(\theta/2) , \tag{2.10}$$

which is also expressed as ,

$$\eta = \frac{1}{2}\ln\frac{|\boldsymbol{p}| + p_z}{|\boldsymbol{p}| - p_z} = \tanh^{-1}\left(\frac{p_z}{|\boldsymbol{p}|}\right) . \tag{2.11}$$

At ultrarelativistic energy, $p \gg m$ and the rapidity,

$$y = \frac{1}{2}\ln\frac{\sqrt{p^2+m^2}+p_z}{\sqrt{p^2+m^2}-p_z} \simeq \frac{1}{2}\ln\frac{p+p\cos\theta}{p-p\cos\theta} = -\ln\tan\theta/2 = \eta . \tag{2.12}$$

Therefore, for very high energy ultrarelativistic particles, rapidity is equal to pseudorapidity. Pseudorapidity is more conveniently used by experimentalists as it can be used for the unidentified particles (charged particles) because η does not depend on the mass of the particles whereas y does.

The momentum distribution of particles is expressed in terms of particle spectrum,

$$E\frac{d^3N}{d^3p} = E\frac{d^3N}{dp_z d^2p_T} = \frac{d^3N}{dy d^2p_T} , \tag{2.13}$$

which is Lorentz invariant because the element d^3p/E (or dp_z/E) is Lorentz invariant. The transformation between rapidity and pseudorapidity distribution is given by,

$$\frac{d^3N}{d\eta d^2p_T} = \sqrt{1 - \frac{m^2}{m_T^2 \cosh^2 y}} \frac{d^3N}{dy d^2p_T} . \tag{2.14}$$

2.2 Collision geometry

In a heavy-ion collision, the geometry of the overlap region is important to determine the volume of the QGP medium and its evolution time. In particular, the initial state of the collision depends on the collision geometry, which in turn affect the final state observables. The main features of the collision geometry are described by the following quantities :

2.2.1 Nuclear density distribution

First, we need to know the density distribution of each of the colliding nuclei. One considers two kinds of density distribution: nuclear charge density distribution and nuclear matter (mass) density distribution. The charge density distribution is related to the distribution of protons, which is obtained from the electron scattering experiments. The matter density distribution considers both neutrons and protons. It is usually a good assumption that the nuclear matter distribution is proportional to the charge distribution [132] . The nuclear density distribution $\rho(r)$ at a distance r from the center, is often represented by a three parameter Fermi-distribution function [133, 134]:

$$\rho(r) = \rho_0 \frac{1 + w(\frac{r}{R})^2}{1 + \exp(\frac{r-R}{a})} , \tag{2.15}$$

which is known as *Woods-Saxon parametrization* of the nuclear density distribution. ρ_0 is the nucleon density, R is the nuclear radius, a is the *skin-depth* or nuclear diffusivity and the term with w is a correction for small nuclei. The overall normalization factor ρ_0 can be obtained from

$$\int d^3r \, \rho(r) = A , \tag{2.16}$$

where A is the total number of nucleons. The values of the other parameters for few nuclei are listed in Table 2.1. Fig. 2.3 shows the Woods-Saxon nuclear density distribution for different nuclei.

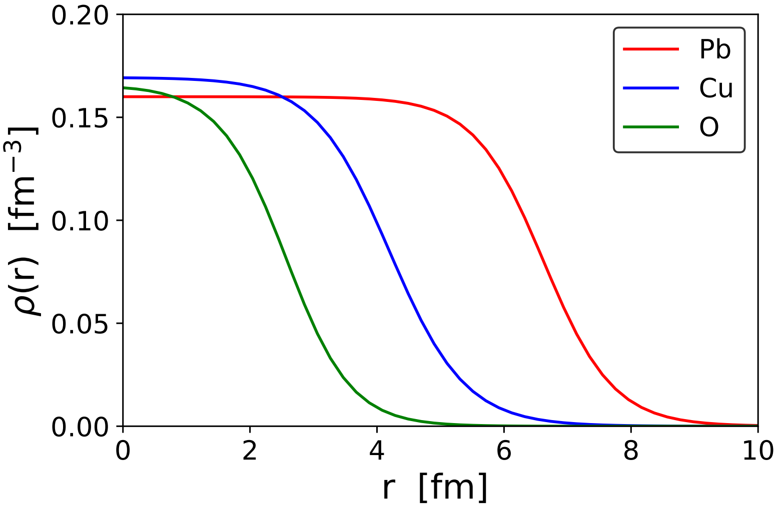

Fig. 2.3 Woods-Saxon density distribution for lead (red) , copper (blue) and oxygen (green) nucleus.

Nucleus	R (fm)	a (fm)	w
^{197}Au	6.38	0.535	0
^{208}Pb	6.624	0.549	0
^{16}O	2.608	0.513	-0.051
^{63}Cu	4.2	0.596	0

Table 2.1 Values of Woods-Saxon parameters for nuclear density distribution for different nuclei [133, 134]

2.2.2 Impact parameter

In an untrarelativistic nucleus-nucleus collision, impact parameter, b is a crucial quantity and it is defined as the spatial distance between the centers of the two nuclei at the time of collision ($t = 0$). The transverse shape and the size of the QGP medium is largely determined by the collision impact parameter. Impact paremeter is a semi-classical quantity and cannot be measured experimentally. In a collision experiment, the direction of the impact parameter is random. However, for theoretical calculation $\vec{\mathbf{b}}$ (which is a two dimensional vector) is commonly represented along the x axis. The plane formed by the impact parameter and z-axis is called the *reaction plane*, so that the (x,z) plane is the reaction plane [135, 5]. In theoretical simulations, impact parameter is generated with a probability distribution $d\sigma/db$ which is proportional to b for $b \leq 2R$, where R is the radius of the nuclei, in a symmetric collision. Fig. 2.4 shows the projection of Pb+Pb collision on the transverse (x,y) plane , where the centre of mass energy of the collision is, $\sqrt{s_{NN}} = 5.02$ TeV and impact parameter, $b = 6$ fm. In the overlap region of the two nuclei, the nucleons from each nuclei interact. The nucleons which encounter at least one interaction with the nucleon from other nucleus, are called the *participant nucleons* or *wounded nucleons* [136] and each of such nucleon-nucleon interactions are labeled as *binary collision*.

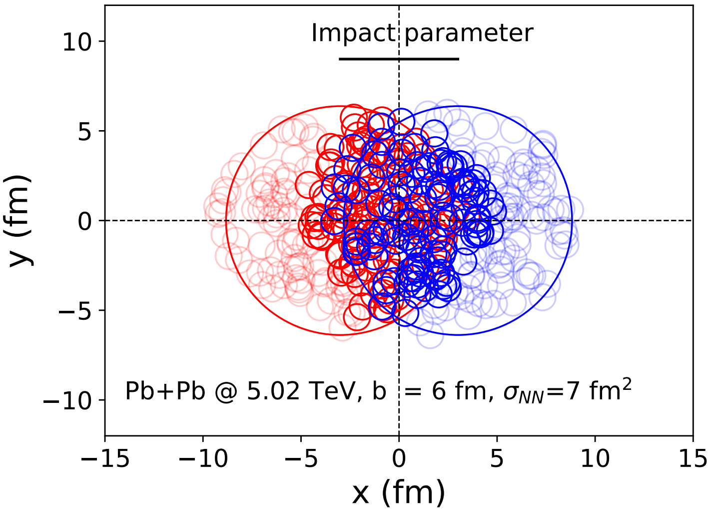

Fig. 2.4 Schematic representation of Pb+Pb collision on the transverse plane at $\sqrt{s_{NN}}$ = 5.02 TeV corresponding to the nucleon-nucleon inelastic cross section, σ_{NN} = 7.2 fm^2. The impact parameter of the collision is b = 6 fm, shown by the black horizontal line on the top. The nucleons from each parent nuclei are shown by corresponding colored (red and blue) circles. The clear solid circles denote the participant nucleons and the blurry circles represent the spectator nucleons. The figure is motivated from [133] and prepared using a MC-Glauber calculation.

The rest of the nucleons which are not involved in any interactions and just pass by are called *spectator nucleons*.

2.2.3 Centrality of the collision

The medium produced in a nucleus-nucleus collision is expected to be a QGP medium and this is more likely if the interaction region during the collision is large. Thus if the collision is closer to *head-on* or in other word more *central*, the overlap area is larger and there is a higher chance of creating a QGP medium. On the other hand, if the collision is more glancing or *peripheral*, it is less likely that the system will achieve the condition for the QGP formation.

Theoretically, the centrality of a collision is defined according to the impact parameter b. However, as a direct measurement of b is not possible, in experiments the centrality of a collision can be estimated according to the total number of charged particles produced in the collision, which is known as *charged particle multiplicity* N_{ch} [68–71] or the transverse energy deposition E_T in the forward calorimeter [72, 73]. The relation between theory and experiment can be understood as the following: if the impact parameter is small (central collision), the volume of the QGP medium is large and the number of participant nucleons is large. On the other hand, N_{ch} and E_T both are increasing with the number of participant nucleons $N_{part}(b)$ [136] (and also the number of binary collisions $N_{coll}(b)$ [137]), which depends on the collision impact parameter [66]. The opposite occurs if the impact parameter is large (peripheral). The dependence of N_{part} (or N_{coll}) on b can be calculated with great precision based on some theoretical models such as the two component *Glauber model* [138]. Thus, although b cannot be directly measured, it can be estimated from the experiments based on the mapping described above. The centrality classified according to the impact parameter is denoted by c_b (sometimes called *b-centrality*) and given by [66, 67],

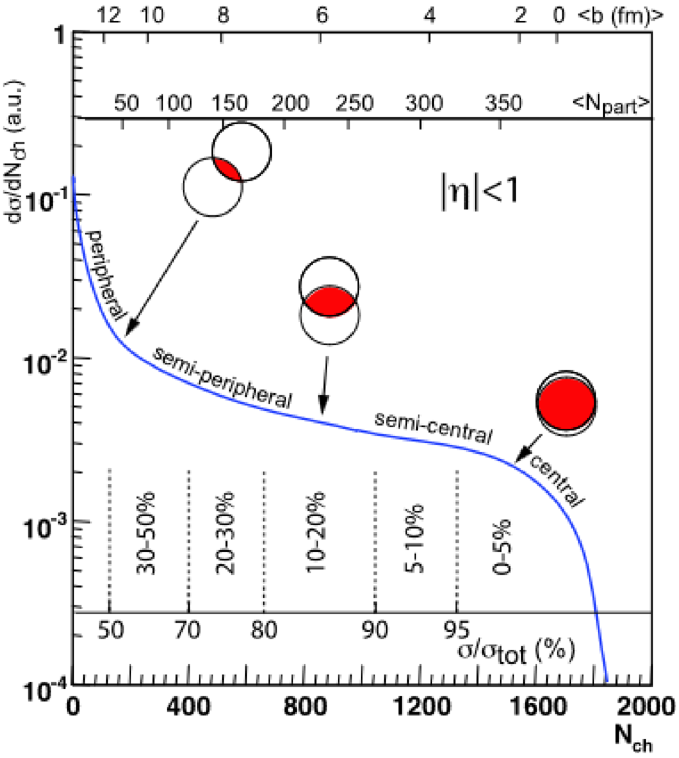

Fig. 2.5 Final state multiplicity distribution (N_{ch}) and centrality classification in experiments. The cartoons of the nucleus-nucleus collision represent corresponding impact parameter in a given centrality class. Figure is taken from [138]

$$c_b = \frac{1}{\sigma_{in}^{AB}} \int_0^b P_{in}(b')2\pi b' db' \;, \tag{2.17}$$

where σ_{in}^{AB} is the inelastic nucleus-nucleus cross section and $P_{in}(b)$ represents the probability that the two nuclei A and B collide at impact parameter b. The probability distribution of c_b is uniform, $P(c_b) = 1$ for $0 < c_b < 1$. On the other hand, in heavy-ion experiments, the centrality is defined as a cumulative distribution of N_{ch} or E_T,

$$c = \int_n^\infty P(n')dn' \qquad (n \equiv N_{ch} \text{ or } E_T) \;. \tag{2.18}$$

Again, the probability distribution of c is uniform, $P(c) = 1$ in $0 < c < 1$. Fig. 2.5 shows the experimental classification of centrality based on the charged particle multiplicity (N_{ch}) and its corresponding mapping to collision impact parameter.

2.3 Glauber modeling in nucleus-nucleus collision

The Glauber model [138–140] serves as a fine theoretical tool to study high-energy nucleus-nucleus collision and it can provide an indirect mapping between the theoretical and experimental classification of collision centrality. In particular, with the help of Glauber model, one can calculate the number of participants ($N_{part}(b)$) and binary collisions ($N_{coll}(b)$) as a function of b in a nucleus-nucleus collision. The model calculation can be based on a classical view of the quantum mechanical framework involving full multiple scattering integrals [136, 141, 142], known as the *optical limit* of Glauber model. However, it can be also calculated based on numerical Monte Carlo simulation [143, 144], which is known as *Monte Carlo Glauber or MC-Glauber* approach.

2.3.1 Optical Glauber model

The Galuber Model treats the nucleus-nucleus collision in terms of independent interactions of the constituent nucleons [138] and assumes that at sufficiently high energies, the nucleons have momentum large enough that their trajectories are essentially undeflected, while travelling on a straight line independent of other nucleons. The individual nucleon-nucleon cross section is obtained from the phase shift using the *optical theorem* [145, 146] and the overall phase shift of the incoming wave associated to each nuclei is assumed to be the sum over all possible two-nucleon phase shifts. The model also assumes that the size of the nucleus is larger than the range of nucleon-nucleon interaction. Such assumptions make possible a simple calculation of the nucleus-nucleus cross section, or of the number of participant nucleons and binary collisions in terms of the nucleon-nucleon cross section.

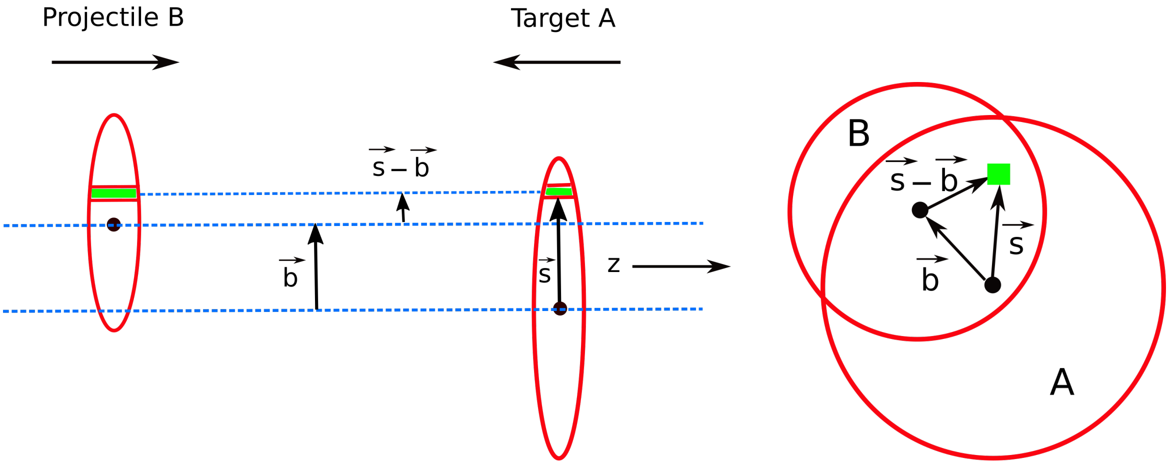

(a) Side view

(b) Beam-line view

Fig. 2.6 Schematic representation of the geometry of optical Glauber model with longitudinal (b) and transverse (a) views. Two nuclei denoted by red curves collide along z axis at an impact parameter $\vec{\mathbf{b}}$ and the green colored region represents the overlap area during the collision. The figure is a modification from [138].

Fig. 2.6 shows the collision of two heavy nuclei A (say *projectile*) and B (*target*) along the z axis, colliding with a relativistic speed at an impact parameter $\vec{\mathbf{b}}$. Let us consider a flux-tube located at a displacement $\vec{\mathbf{s}}$ from the centre of the target nucleus and at a distance $\vec{\mathbf{s}}-\vec{\mathbf{b}}$ from the centre of projectile. The vector $\vec{\mathbf{s}}$ represents the transverse position vector $\vec{\mathbf{s}}(x,y)$. At the time of collision, these two tubes overlap on each other. The probability of a given nucleon of being located within the target flux tube per transverse area is given by the *thickness function*,

$$T_A(\vec{\mathbf{s}}) = \int \rho_A(\vec{\mathbf{s}},z_A)\ dz_A\ , \tag{2.19}$$

where $\rho_A(\vec{\mathbf{s}},z)$ is the nuclear density distribution at $\vec{\mathbf{r}} = (x,y,z)$ given by Eq. (2.15). Similarly, the probability of finding a nucleon in the projectile flux tube per transverse area,

$$T_B(\vec{\mathbf{s}}-\vec{\mathbf{b}}) = \int \rho_B(\vec{\mathbf{s}}-\vec{\mathbf{b}},z_B)\ \ dz_B\ . \tag{2.20}$$

The product of the two, $T_A(\vec{\mathbf{s}})T_B(\vec{\mathbf{s}}-\vec{\mathbf{b}})$ represents the joint probability density per unit area of finding a nucleon from A and a nucleon from B at the overlap region with the collision impact parameter $\vec{\mathbf{b}}$. One can then define the *overlap function* $T(\vec{\mathbf{b}})$ by integrating over all $\vec{\mathbf{s}}$,

$$T(\vec{\mathbf{b}}) = \int T_A(\vec{\mathbf{s}})\ T_B(\vec{\mathbf{s}}-\vec{\mathbf{b}})\ \ d^2s\ . \tag{2.21}$$

Please note, $T(\vec{\mathbf{b}})$ has the unit of inverse area. The thickness function represents the effective overlap area between a particular nucleon from A and a given nucleon from B at the interaction region. The probability of such an interaction is given by $T(\vec{\mathbf{b}})\sigma_{in}^{NN}$, where σ_{in}^{NN} is the nucleon-nucleon inelastic cross section[1]. The probability of n such interactions between the nucleus A (let us say has A nucleons) and the nucleus B (having B nucleons) is given by the binomial distribution,

$$P(n,\vec{\mathbf{b}}) = \begin{pmatrix} AB \\ n \end{pmatrix} [T_{AB}(\vec{\mathbf{b}})\sigma_{in}^{NN}]^n\ [1-T_{AB}(\vec{\mathbf{b}})\sigma_{in}^{NN}]^{AB-n}\ , \tag{2.22}$$

where in the above expression, the first term denotes the number of combinations in which n nucleon-nucleon collisions out of AB collisions occur, the second term represents the probability of exactly n collisions, and the last term gives the probability that $AB-n$ collisions do not occur. The total probability of an interaction between nuclei A and B is,

$$P_{in}^{AB}(\vec{\mathbf{b}}) = \frac{d^2\sigma_{in}^{AB}}{db^2} = \sum_{n=1}^{AB} P(n,\vec{\mathbf{b}}) = 1-[1-T_{AB}(\vec{\mathbf{b}})\sigma_{in}^{NN}]^{AB}\ . \tag{2.23}$$

---

[1] Note that the elastic nucleon-nucleon collisions encounter very little energy loss and hence do not contribute to the Glauber model calculation

The total inelastic cross section of A-B collision can be found by integrating the above equation over impact parameter[2],

$$\sigma_{in}^{AB} = \int_0^\infty [1 - [1 - T_{AB}(b)\sigma_{in}^{NN}]^{AB}]\, 2\pi b db\ . \tag{2.24}$$

The mean number of binary nucleon-nucleon collision is,

$$N_{coll}(b) = \sum_{n=1}^{AB} nP(n,b) = ABT_{AB}(b)\sigma_{in}^{NN} \tag{2.25}$$

and the number of participants at impact parameter b is given by,

$$\begin{aligned} N_{part}(b) &= A\int T_A(\vec{\mathbf{s}})P_{in}^{NB}(\vec{\mathbf{s}}-\vec{\mathbf{b}})\ d^2s + B\int T_B(\vec{\mathbf{s}}-\vec{\mathbf{b}})P_{in}^{NA}(\vec{\mathbf{s}})\ d^2s \\ &= A\int T_A(\vec{\mathbf{s}})\left\{1-[1-T_B(\vec{\mathbf{s}}-\vec{\mathbf{b}})\sigma_{in}^{NN}]^B\right\} d^2s \\ &\quad + B\int T_B(\vec{\mathbf{s}}-\vec{\mathbf{b}})\left\{1-[1-T_A(\vec{\mathbf{s}})\sigma_{in}^{NN}]^A\right\} d^2s\ , \end{aligned} \tag{2.26}$$

where $P_{in}^{NA(B)}$ represents the probability of a nucleon-nucleus collision. Note that the total cross section of a nucleon-nucleus collision can be written as,

$$\sigma_{in}^{NA(B)} = \int \left\{1-[1-T_{A(B)}(\vec{\mathbf{s}})\sigma_{in}^{NN}]^{A(B)}\right\} d^2s\ . \tag{2.27}$$

As the Glauber model calculation of σ_{in}^{AB}, N_{part} and N_{coll} depends on the nucleon-nucleon cross section, it is important to mention the measurement of σ_{in}^{NN} in different experiments and collision energies. From the energy dependence of σ_{in}^{NN} on $\sqrt{s_{NN}}$ [147], it can be estimated that at the SPS energy ($\sqrt{s_{NN}}$ = 20 GeV), $\sigma_{in}^{NN} \simeq 3$ fm^2, at the top RHIC energy ($\sqrt{s_{NN}}$ = 200 GeV), $\sigma_{in}^{NN} \simeq 4.2$ fm^2 [148] and at the LHC energies, $\sigma_{in}^{NN} \simeq 6.4$ fm^2 [149] ($\sqrt{s_{NN}}$ = 2.76 TeV) and 7.0 fm^2 [150] ($\sqrt{s_{NN}}$ = 5.02 TeV).

2.3.2 Monte Carlo Glauber model

The optical Glauber model deals with the continuous distribution of nucleon density and does not really locate the nucleons at locations with specific spatial coordinates inside the nuclei. This is exactly the case in Monte Carlo approach of the Glauber model. The main feature of this method is that the quantities like N_{part}, N_{coll} are calculated by colliding two nuclei event-by-event through computer simulation. Both models give very close results for the averaged quantities, $\langle N_{part}(b)\rangle$ and $\langle N_{coll}(b)\rangle$, where $\langle\dots\rangle$ denotes average over events. However, for the quantities where event-by-event fluctuations (as we will discuss later) are important, the two

---

[2] The scalar distance can be used instead of vector impact parameter if the colliding nuclei are not polarized.

models give different results. Moreover, in the Monte Carlo Glauber approach, one can simulate the observables event-by-event (in a minimum bias way), which are measured in the experiment, such as multiplicity N_{ch} and its distribution can be compared with the experimental distribution to classify similar centrality cuts as in the data. In the Glauber Monte Carlo approach [138], first the nucleons are distributed in the two colliding nuclei A and B, in 3D coordinate space, according to the nucleon density distribution in Eq. (2.15). Next, a random impact parameter is generated according to the impact parameter distribution: $d\sigma/db = 2\pi b$ (where, $0 \leq b \leq R_max$, with $R_{max} > R_A + R_B$). Then, the collision between the two nuclei is assumed as a sequence of independent nucleon-nucleon collisions. It is assumed that the nucleons traverse through a straight line and in each collision, nucleon-nucleon cross section is independent of the collision history of the colliding nucleons. Next, in the simplest scenario, two nucleons are treated to have collided if they satisfy the following condition:

$$d_{NN} \leq \sqrt{\sigma_{in}^{NN}/\pi} \ , \tag{2.28}$$

where d_{NN} is the transverse distance (on the plane perpendicular to beam-axis) between the two nucleons at the time of collision. This criterion is known as *hard-sphere wounding* and could be described for symmetric collisions, by the collision probability:

$$p(d_{NN}) = \Theta(R - d_{NN}) \qquad \text{with} \qquad \sigma_{in}^{NN} = \pi R^2 \ . \tag{2.29}$$

A *Gaussian-wounding* probability is also possible [151](i.e. the nucleons are wounded with respect to a Gaussian probability distribution):

$$p(d_{NN}) = C\ e^{\frac{-\pi\ Cd_{NN}^2}{\sigma_{in}^{NN}}} \ , \tag{2.30}$$

where C is a constant fitted to data. In Fig. 2.4, the solid colored circles denote the wounded nucleons selected according to the hard-sphere condition in Eq. (2.28), for one Pb+Pb collision.

2.4 Relativistic hydrodynamics

The relativistic hydrodynamic description of the evolution and the dynamics of the QGP medium produced in ultrarelativistic heavy-ion collision is a useful way to model the collision dynamics [17–24, 26]. The hot dense droplet of fluid-like QGP medium consists of strongly interacting quarks and gluons (*partons*). A formal physical description of such a system should be based on some rigorous microscopic theory. However, a microscopic description of a system consisting of many interacting particles (many degrees of freedom) is not a trivial task. In such situations, one looks for an effective description of the dynamics of the system, based on some macroscopic theory which considers only those degrees of freedom which are relevant at the larger length and time scales. This works because most of the microscopic variables encounter rapid fluctuations on a small length and time scale, which does not have a significant effect on the macroscopic observables measured in the experiments, only the average quantities on the macroscopic scale matter. On the contrary, the conserved quantities which vary slowly during the dynamical evolution of the system play a crucial role in the effective theory. *Hydrodynamics* (or *fluid dynamics*) is a perfect example of such a macroscopic theory which can provide an effective description of the dynamics of the QGP medium.

Physically, a *fluid* can be described as a continuous system of infinitesimal volume elements, called *fluid elements*. In hydrodynamics, it is assumed that each of these fluid elements is in local thermodynamic equilibrium during its space-time evolution i.e. they are homogeneous without any spatial gradients and can be characterized by thermodynamic relations. This means that the fluid cells are large enough in comparison to the microscopic scale so that a local thermodynamic equilibrium can be defined and at the same time they are small enough in comparison to the macroscopic scale that the continuum (infinitesimal volume) limit is satisfied. We will assume the above criteria for the description of the QGP medium as a nearly fluid-like medium are fulfilled. The following discussions presented in this section is a general short review of some published literature on the theory of relativistic hydrodynamics in heavy-ion collision [25, 152–164].

2.4.1 Thermodynamics

Thermodynamics is a macroscopic theory describing the bulk properties and state of matter. It only deals with the average properties of the microscopic constituents (which are quite large in number) of a system and its fundamental basis lies in statistical mechanics which could be used to derive its basic laws. Here, we will briefly go through the thermodynamic identities and relations which are important and often used in a hydrodynamic model.

A thermodynamic system is usually characterized by a set of few extensive variables such as volume (V), pressure (P), total energy (E), entropy (S) and the number of particles (N) in the system. The differential change in the total internal energy is given by,

$$dE = dQ - PdV + \mu dN \ , \tag{2.31}$$

which is basically the *first law of thermodynamics*. On the right hand side, dQ is the heat exchange, the second term is the work done and the third term is rather difficult to interpret. In a situation where particle is exchanged between two systems at same pressure and temperature but different number density, it represents the thermodynamic potential. However, it is important to note that N is usually the number of particles if the system is non-relativistic. In a relativistic system, N is no longer the number of particles as it is not conserved anymore. In a relativistic system, particles can be produced at the expense of energy or can be destroyed to produce energy. In such systems, N represents some conserved quantities e.g. *baryon number*. If there are more than one conserved quantity, the term μdN is replaced by $\sum_i \mu_i dN_i$, where μ_i is the chemical potential corresponding to the conserved quantity N_i. However, here we will use N to denote baryon number only.

For a reversible thermodynamic process, Eq. (2.31) takes the form,

$$dE = TdS - PdV + \mu dN \,, \tag{2.32}$$

where the heat transfer is related to the change in entropy of the system. Using the above equation one can find the extensive variables,

$$\left.\frac{\partial E}{\partial S}\right|_{V,N} = T, \quad \left.\frac{\partial E}{\partial V}\right|_{S,N} = -P \quad \text{and} \quad \left.\frac{\partial E}{\partial N}\right|_{S,V} = \mu \,, \tag{2.33}$$

which lead to the relation between the thermodynamic variables,

$$E = -PV + TS + \mu N \,, \tag{2.34}$$

known as the *Euler's equation*. Differentiating the above equation one gets the *Gibbs-Duhem relation*,

$$VdP = SdT + Nd\mu \,. \tag{2.35}$$

In the context of hydrodynamics, these thermodynamic quantities are expressed in terms of densities i.e. the energy density $\varepsilon = E/V$, the entropy density $s = S/V$ and the baryon number density $n = N/V$, which are intensive quantities. In terms of densities, Eqs. (2.34) and (2.35) can be written as,

$$\varepsilon = -P + Ts + \mu n \tag{2.36}$$

and

$$dP = sdT + nd\mu \,. \tag{2.37}$$

The thermodynamic equilibrium : It is the thermodynamic state of a system where the system is in a stationary state and where the extensive and intensive variables defining the stationary state do not change with time. For example, the entropy of a system is known to either increase or remain constant from the *second law of thermodynamics*. If a system is in equilibrium, its entropy remains constant in time. But, if the system is in an out of equilibrium state, its entropy increases.

2.4.2 Relativistic ideal hydrodynamics

We start with the dynamics of an ideal relativistic fluid [157, 153, 25]. For an ideal fluid, the system is assumed to be in local thermal equilibrium i.e all of its fluid elements maintain a thermodynamic equilibrium state with each other. This implies that at each of the space-time coordinates $x \equiv x^{\mu}$ of the fluid, one can characterize the local temperature $T(x)$, chemical potential $\mu(x)$ and the *collective four-velocity* $u^{\mu}(x)$ defined as,

$$u^{\mu}(x) = \frac{dx^{\mu}}{d\tau} = \gamma(1,\vec{v}) \,, \tag{2.38}$$

where τ is the proper time, $\gamma = 1/\sqrt{1-\vec{v}^2}$ and $\vec{v} = \frac{d\vec{x}}{dt}$ is the spatial velocity of the fluid.

The state of a relativistic fluid is described with the local energy-momentum tensor $T^{\mu\nu}$ and particle number current N^{μ}. In the *local rest frame (LRF)* of the fluid, $\vec{v} = 0$, making $u^{\mu}_{LRF} = (1,0)$ and the energy-momentum tensor takes the form,

$$T^{\mu\nu}_{LRF} = \begin{pmatrix} \varepsilon & 0 & 0 & 0 \\ 0 & P & 0 & 0 \\ 0 & 0 & P & 0 \\ 0 & 0 & 0 & P \end{pmatrix} , \tag{2.39}$$

where ε is the energy density and P is the pressure of the fluid. In the laboratory frame, the energy momentum tensor is given by,

$$T^{\mu\nu}_{(0)} = (\varepsilon + P)u^{\mu}u^{\nu} - g^{\mu\nu}P \,, \tag{2.40}$$

for an ideal (denoted by "(0)") relativistic fluid. Similarly, the net particle number current and the entropy current are given by,

$$N^{\mu}_{(0)} = nu^{\mu} \quad \text{and} \quad S^{\mu}_{(0)} = su^{\mu} \,. \tag{2.41}$$

Hydrodynamic equations of motion

The equations governing the motion of an ideal fluid, encoding its dynamical description are the hydrodynamic equations of motion, which arise from the conservation laws during the time evolution. The energy-momentum conservation and the net baryon number conservation are given by,

$$\partial_{\mu}T^{\mu\nu} = 0 \quad \text{and} \quad \partial_{\mu}N^{\mu} = 0 \,, \tag{2.42}$$

where $\partial_{\mu} \equiv \frac{\partial}{\partial x^{\mu}}$ and $N^{\mu} = (n, \vec{j})$, with $\vec{j}$ as the particle current vector.

In the laboratory frame, the hydrodynamic equations of motion are obtained by projecting the conservation equations in Eq. (2.42) along and orthogonal to the fluid velocity u^{μ}. Projecting the energy-momentum conservation equation along u^{μ} gives the first equation of ideal hydrodynamics :

$$\frac{d\varepsilon}{d\tau} = -(\varepsilon + P)\theta \quad \text{or} \quad D\varepsilon + (\varepsilon + P)\theta = 0 \,, \tag{2.43}$$

where

$$D \equiv u^\mu \partial_\mu = \frac{d}{d\tau} \quad \text{and} \quad \theta \equiv \partial_\mu u^\mu \ . \tag{2.44}$$

D is known as *hydro-derivative* or *convective derivative* which represents the projection of ∂_μ along u^μ, and θ is called the *expansion scalar*. Similarly, taking the projection orthogonal to u^μ, one obtains another three hydro-equations :

$$a_\lambda = \frac{1}{\varepsilon + P} \nabla_\lambda P \quad \text{or} \quad (\varepsilon + P) D u_\lambda - \nabla_\lambda P = 0 \ , \tag{2.45}$$

where

$$a_\mu = D u_\mu = \frac{d u_\mu}{d\tau}, \qquad \nabla_\mu \equiv \Delta_\mu^\nu \partial_\nu \quad \text{and} \quad \Delta^{\mu\nu} = g^{\mu\nu} - u^\mu u^\nu \ . \tag{2.46}$$

a_μ is called the *four-acceleration*, ∇_μ is the *transverse gradient* and $\Delta^{\mu\nu}$ is known as the *projector*. ∇_μ denotes the projection of ∂_μ orthogonal to u^μ.

Finally, from the conservation equation of particle number current $\partial_\mu N^\mu_{(0)} = 0$, we have the fifth equation for ideal hydrodynamics,

$$\frac{dn}{d\tau} = -n\theta \quad \text{or} \quad Dn + n\theta = 0 \ . \tag{2.47}$$

It is important to note that Eqs. (2.43),(2.45) and (2.47) provide five equations of motion for an ideal fluid but there are six degrees of freedom: ε, P, n and u_μ. The sixth equation comes from the thermodynamic equation of state $P = P(\varepsilon, n)$ which relates the pressure to energy or number density.

In the present context, it is necessary to mention that ideal fluid hydrodynamics is also *isentropic*, which means that the entropy also remain conserved during the hydrodynamic evolution of the fluid. Similar to the particle number conservation, the entropy conservation equation is given by $\partial_\mu S^\mu_{(0)} = 0$ which leads to,

$$Ds + s\theta = 0 \ , \tag{2.48}$$

representing the equation of motion for the entropy current.

2.4.3 Relativistic dissipative hydrodynamics

The formulation of ideal hydrodynamics relies on Lorentz covariance, conservation equations and the crucial assumption that the fluid is in local thermodynamic equilibrium. While the first two principles are quite robust, the assumption of a perfect thermal equilibrium is significantly crude and far for reality. In practice, the fluid elements are never in exact thermodynamic equilibrium due to the dissipative effects originating due to irreversible thermodynamic processes, frictions between the fluid elements during their motion etc. To properly describe the dynamics of a real fluid, these dissipative effects must be taken into account.

The covariant formulation of relativistic dissipative hydrodynamics, known as the *first order theory*, was first given by Eckart [158] and later Landau and Lifshitz [157]. These theories are covariant generalization of the *Navier-Stokes theory*. However, the first order theory has a serious problem in its formulation. The relativistic Navier-Stokes theory is intrinsically unstable [165, 166] because it violates the fundamental causality condition of the relativistic theory [161, 159]. In this theory, signals can travel at an infinite speed or instantaneously, which is not allowed by the principle of causality. Therefore, one needs to resort to the *second order theory* which takes into account the causality principle in its formulation. Among many second order dissipative hydrodynamic theories which addresses the acausal behavior [153, 152, 154, 167, 168], the *Israel-Stewart theory* [153, 152] is the most popular and widely used to describe the hydrodynamic formulation of the QGP.

In relativistic dissipative hydrodynamics, the basic conservation laws for the energy-momentum and the particle number current remains unchanged (Eq. (2.42)). However, for a dissipative fluid, the energy-momentum tensor $T^{\mu\nu}$ and the particle current N^{μ} assume additional terms $\tau^{\mu\nu}$ and dissipative current n^{μ} respectively,

$$\begin{aligned} T^{\mu\nu} &= T^{\mu\nu}_{(0)} + \tau^{\mu\nu} = (\varepsilon + P)u^{\mu}u^{\nu} - g^{\mu\nu}P + \tau^{\mu\nu} = \varepsilon u^{\mu}u^{\nu} - P\Delta^{\mu\nu} + \tau^{\mu\nu} \ , \\ N^{\mu} &= N^{\mu}_{(0)} + n^{\mu} = nu^{\mu} + n^{\mu} \ , \end{aligned} \tag{2.49}$$

where $\tau^{\mu\nu}$ is a symmetric tensor.

Matching conditions

The additional terms in the energy-momentum tensor and number current in Eq. (2.49), disrupt the local thermal equilibrium of the fluid, making the definitions of the thermodynamic variables ambiguous. In order to address this situation, we need to define an equivalent thermodynamic equilibrium so that the definitions of the thermodynamic variables and their relations remain consistent. The total energy density ε and the number density n in the local rest frame of the fluid is defined with respect to the *matching conditions* [157],

$$\varepsilon \equiv u_{\mu}u_{\nu}T^{\mu\nu} \quad \text{and} \quad n \equiv u_{\mu}N^{\mu} \ . \tag{2.50}$$

Irreducible decomposition of dissipative components

In general, any tensor can be decomposed into its irreducible components that can be a scalar or a four-vector or any other tensor of ranking lesser or equal to the original tensor rank. The particle number current N^μ which is a rank-1 tensor can be decomposed in two components,

$$N^\mu = N_\nu g^{\mu\nu} = N_\nu(\Delta^{\mu\nu} + u^\mu u^\nu) = nu^\mu + n^\mu \ , \tag{2.51}$$

where we have used the relation $N_\mu u^\mu = n$ (matching condition in Eq. (2.50)) and $n^\mu = \Delta^{\mu\nu} N_\nu$ which satisfies $n^\mu u_\mu = 0$. Similarly, the energy momentum tensor $T^{\mu\nu}$ which is a second rank tensor can be decomposed as [25],

$$T^{\mu\nu} = \varepsilon u^\mu u^\nu - P\Delta^{\mu\nu} - \Pi\Delta^{\mu\nu} + 2h^{(\mu}u^{\nu)} + \pi^{\mu\nu} \ , \tag{2.52}$$

where,

$$\varepsilon = T_{\alpha\beta}u^\alpha u^\beta, \qquad \Pi = -P - \frac{1}{3}T_{\alpha\beta}\Delta^{\alpha\beta}, \qquad h^\mu = \Delta^{\alpha\mu}u^\beta T_{\alpha\beta} \ . \tag{2.53}$$

Please note that ε has same form as in Eq. (2.50). Π is a scalar, known as the *bulk viscous pressure* , the field h^μ is the *energy diffusion four-current.* The last two terms in Eq. (2.52) are given by,

$$h^{(\mu}u^{\nu)} = \frac{1}{2}(h^\mu u^\nu + h^\nu u^\mu) \quad \text{and} \quad \pi^{\mu\nu} = T^{\alpha\beta}\Delta^{\mu\nu}_{\alpha\beta} \ , \tag{2.54}$$

where $\pi^{\mu\nu}$ is the *shear-stress tensor* which is is traceless and $\Delta^{\mu\nu}_{\alpha\beta}$ is a rank-4 projection operator which is doubly symmetric, traceless and orthogonal to u^μ. $\Delta^{\mu\nu}_{\alpha\beta}$ is expressed in terms of the projectors as,

$$\Delta^{\mu\nu}_{\alpha\beta} = \frac{1}{2}(\Delta^\mu_\alpha\Delta^\nu_\beta + \Delta^\mu_\beta\Delta^\nu_\alpha - \frac{2}{3}\Delta^{\mu\nu}\Delta^{\alpha\beta}) \ . \tag{2.55}$$

Comparing with the energy-momentum tensor for the dissipative fluid in Eq. (2.49), we have the dissipative term $\tau^{\mu\nu}$ in terms of irreducible dissipative components,

$$\tau^{\mu\nu} = -\Pi\Delta^{\mu\nu} + 2h^{(\mu}u^{\nu)} + \pi^{\mu\nu} \ . \tag{2.56}$$

The symmetric tensor $T^{\mu\nu}$ has ten independent components and N^μ has four, which make a total fourteen independent components. The fields n^μ and h^μ have three independent components each (both are orthogonal to u^μ). The stress-tensor $\tau^{\mu\nu}$ being symmetric, traceless and orthogonal to u^μ, has only five independent components. Remaining ε, Π, n and u^μ constitutes another six (ε and P are related by equation of state) independent components. Therefore, in total the irreducible components of $T^{\mu\nu}$ and N^μ have seventeen independent components. There are extra three components, coming from the velocity field u^μ which is not well-defined. The fluid velocity needs to be defined properly by choosing appropriate frame.

Definition of velocity field

For dissipative fluid, there is energy and particle diffusion in the *LRF* of the fluid, which need to be taken into account while defining the velocity. In most of the cases, two possible choices are used:

I. Eckart frame : In this frame [158], it is assumed that there is no net flow of particles or no particle diffusion and that defines the fluid velocity. Using Eq. (2.51),

$$n^{\mu} = 0 \qquad \Rightarrow \qquad N^{\mu} = n u^{\mu} \ . \tag{2.57}$$

II. Landau frame : In this frame [157], the velocity is defined in a way such that there is no energy diffusion or no net flow of total energy. Using Eq. (2.53),

$$h^{\mu} = 0 \qquad \Rightarrow \qquad u_{\nu} T^{\mu\nu} = \varepsilon u^{\mu} \ . \tag{2.58}$$

It should be noted that either of the choices reduces three independent components. In the following discussions, we will use the Landau frame to define the fluid velocity, under which the conserved currents become,

$$T^{\mu\nu} = \varepsilon u^{\mu} u^{\nu} - (P + \Pi)\Delta^{\mu\nu} + \pi^{\mu\nu} \quad \text{and} \quad N^{\mu} = n u^{\mu} + n^{\mu} \ . \tag{2.59}$$

Hydrodynamic equations for dissipative fluid

Similar to ideal fluids, we need to project the conservation equations (Eq. (2.42)) along and orthogonal to the velocity field u^{μ}, in order to find the equations of motion. We use the expressions in Eq. (2.59) and using similar contractions we get [25]:

$$\begin{aligned} u_{\nu}\partial_{\mu} T^{\mu\nu} = 0 \qquad &\Rightarrow \qquad \dot{\varepsilon} + (\varepsilon + P + \Pi)\theta - \pi^{\mu\nu}\sigma_{\mu\nu} = 0 \ , \\ \Delta^{\alpha}_{\nu}\partial_{\nu} T^{\mu\nu} = 0 \qquad &\Rightarrow \qquad (\varepsilon + P + \Pi)\dot{u}^{\alpha} - \nabla^{\alpha}(P + \Pi) + \nabla^{\alpha}_{\nu}\partial_{\mu}\pi^{\mu\nu} = 0 \ , \\ \partial_{\mu} N^{\mu} = 0 \qquad &\Rightarrow \qquad \dot{n} + n\theta + \partial_{\mu} n^{\mu} = 0 \ , \end{aligned} \tag{2.60}$$

where $\dot{a} = Da = u^{\mu}\partial_{\mu} a$ and $\sigma^{\mu\nu}$ is called *shear tensor*, defined as, $\sigma^{\mu\nu} \equiv \nabla^{\langle\mu} u^{\nu\rangle} = \Delta^{\mu\nu}_{\alpha\beta}\nabla^{\alpha} u^{\beta}$. Eq. (2.60) gives us five equations for the relativistic viscous hydrodynamics, whereas $T^{\mu\nu}$ and N^{μ} have fourteen independent components. Therefore, we need nine more equations for a complete set, which are obtained from the dissipative terms i.e. the diffusion current n^{μ}, the shear term $\pi^{\mu\nu}$ and the bulk term Π. The evolution equations for the dissipative terms are obtained from the second order Israel-Stewart theory which we discuss below.

Israel-Stewart theory for viscous hydrodynamics

The Israel-Stewart theory [153, 152, 154] of relativistic dissipative fluid is a second order theory which does not violate causality. In this theory, the entropy four-current for the fluid at non-equilibrium, is assumed to be a function of the dissipative currents in addition to the primary fluid-dynamic variables [25],

$$S^{\mu} = P\beta^{\mu} + \beta_{\nu}T^{\mu\nu} - \alpha N^{\mu} - Q^{\mu}(\delta N^{\mu}, \delta T^{\mu\nu}) \ , \tag{2.61}$$

where $\beta^{\mu} = u^{\mu}/T$, $\beta = 1/T$, $\alpha = \mu/T$ with μ as the chemical potential and Q^{μ} is a function of the deviation of dissipative currents from equilibrium: $\delta N^{\mu} = N^{\mu} - N^{\mu}_{(0)}$ and $\delta T^{\mu\nu} = T^{\mu\nu} - T^{\mu\nu}_{(0)}$. Expanding Q^{μ} in Taylor's series up to the second order in dissipative flux (second order in δ), we have [160, 25],

$$\begin{aligned} S^{\mu} = su^{\mu} - \alpha n^{\mu} - \frac{\beta}{2}(\beta_0\Pi^2 - \beta_1 n_{\nu}n^{\nu} + \beta_2\pi_{\rho\sigma}\pi^{\rho\sigma})u^{\mu} \\ -\beta(\alpha_0\Pi\Delta^{\mu\nu} + \alpha_1\pi^{\mu\nu})n_{\nu} + \mathcal{O}(\delta^3)) \ , \end{aligned} \tag{2.62}$$

where the coefficients β_i and α_i are the thermodynamics coefficients of Taylor's series expansion, which depend on temperature and chemical potential. The next step would be to generate entropy by taking divergence $\partial_{\mu}S^{\mu}$ and then one applies the second law of thermodynamics for each fluid element i.e the entropy production always remains positive: $\partial_{\mu}S^{\mu} \geq 0$. This results in dynamical equations for the dissipative currents, which are of relaxation-type [25]:

$$\begin{aligned} \dot{\Pi} + \frac{\Pi}{\tau_{\Pi}} &= -\frac{1}{\beta_0}[\theta + \beta_{\Pi\Pi}\Pi\theta + \psi\alpha_{n\Pi}n_{\mu}\dot{u}^{\mu} + \alpha_0\nabla_{\mu}n^{\mu} + \psi\alpha_{\Pi n}n_{\mu}\nabla^{\mu}\alpha] \ , \\ \dot{n}^{\langle\mu\rangle} + \frac{n^{\mu}}{\tau_n} &= -\frac{1}{\beta_1}[T\nabla_{\mu}\alpha - \beta_{nn}n_{\mu}\theta + \alpha_0\nabla_{\mu}\Pi + \alpha_1\nabla_{\nu}\pi^{\nu}_{\mu} + \tilde{\psi}\alpha_{n\Pi}\Pi\dot{u}_{\mu} + \\ &\qquad \tilde{\psi}\alpha_{\Pi n}\Pi\nabla_{\mu}\alpha + \tilde{\chi}\alpha_{\pi n}\pi^{\nu}_{\mu}\nabla_{\nu}\alpha + \tilde{\chi}\alpha_{n\pi}\pi^{\nu}_{\mu}\dot{u}_{\nu}] \ , \\ \dot{\pi}^{\mu\nu} + \frac{\pi^{\mu\nu}}{\tau_{\pi}} &= -\frac{1}{\beta_2}[\sigma_{\mu\nu} - \beta_{\pi\pi}\theta\pi_{\mu\nu} - \alpha_1\nabla_{\langle\mu}n_{\nu\rangle} - \chi\alpha_{\pi n}n_{\langle\mu}\nabla_{\nu\rangle}\alpha - \\ &\qquad \chi\alpha_{n\pi}n_{\langle\mu}\dot{u}_{\nu\rangle}] \ , \end{aligned} \tag{2.63}$$

where $\lambda \equiv \kappa/T$ and the coefficients ζ, κ and η are called bulk viscosity, particle diffusion and shear viscosity of the fluid, respectively. The parameters

$$\tau_{\Pi} \equiv \zeta\beta_0, \qquad \tau_n \equiv \lambda\beta_1 = \kappa\beta_1/T \quad \text{and} \quad \tau_{\pi} \equiv 2\eta\beta_2 \tag{2.64}$$

are positive and can be interpreted as relaxation times. Therefore, the coefficients β_0, β_1, and β_2 must also be positive.

The presence of the relaxation time indicates that the hydrodynamic response to the dissipative currents occur within a time scale given by τ, instead of an instantaneous effect i.e.

the theory satisfies the causality requirement of the relativistic theory. However, the theory introduces five new parameters: β_0, β_1, β_2, α_0 and α_1, which can be obtained from more fundamental microscopic theory such as *relativistic kinetic theory* using the framework of Boltzman transport.

2.4.4 Relativistic kinetic theory

In relativistic kinetic theory, the macroscopic properties of a system can be expressed in the framework of statistical mechanics using a *single particle phase-space distribution function* $f(x,p)$. At each space-time point x^μ, the quantity $f(x,p)\Delta^3 x \Delta^3 p$ denotes the average number of particles within the volume $\Delta^3 x$ and having momenta between $\vec{p}$ and $\vec{p}+\Delta\vec{p}$. In terms of the distribution function $f(x,p)$, the particle number four-current or the *four-flow* is given by,

$$N^\mu(x) = \int \frac{d^3p}{p^0}\, p^\mu\, f(x,p)\ , \tag{2.65}$$

and the energy-momentum tensor as,

$$T^{\mu\nu}(x) = \int \frac{d^3p}{p^0}\, p^\mu\, p^\nu\, f(x,p)\ , \tag{2.66}$$

which is symmetric and involves the second moment of the distribution function. Furthermore, using Boltzmann's H-theorem, the general form of the entropy four current (or *entropy four-flow*) can be written as,

$$S^\mu(x) = -\int \frac{d^3p}{p^0}\, p^\mu\, [f(x,p)\ln f(x,p) + r\tilde{f}(x,p)\ln \tilde{f}(x,p)]\ , \tag{2.67}$$

where $\tilde{f}(x,p) = 1 - rf(x,p)$ and $r = 0$ (Maxwell-Boltzmann statistics), $+1$ (Fermi-Dirac statistics) or -1 (Bose-Einstein statistics).

If the system is in equilibrium, the distribution function is given by,

$$f(x,p) \equiv f_0(x,p) = \frac{1}{\exp(\beta p^\mu u_\mu - \alpha) + r}\ . \tag{2.68}$$

But if the system is in a non-equilibrium state, the distribution function can be written as a small deviation from the equilibrium distribution function: $f = f_0 + \delta f$, where δf is the non-equilibrium correction. Furthermore, using the non-equilibrium distribution function in Eq. (2.59), one can find the expressions for the dissipative quantities i.e. the bulk pressure, the particle diffusion current and the shear-stress tensor, in terms of the correction δf as [25],

$$\begin{aligned} \Pi &= -\frac{1}{3}\Delta_{\mu\nu}\int \frac{d^3p}{p^0}\, p^\mu\, p^\nu\, \delta f\,, \\ n^\mu &= \Delta^{\mu\nu}\int \frac{d^3p}{p^0}\, p_\nu\, \delta f\,, \\ \pi^{\mu\nu} &= \Delta^{\mu\nu}_{\alpha\beta}\int \frac{d^3p}{p^0}\, p^\alpha\, p^\beta\, \delta f\,. \end{aligned} \tag{2.69}$$

Dissipative hydrodynamics from relativistic kinetic theory

Israel-Stewart theory for the relativistic viscous hydrodynamics introduced five new parameters: β_0, β_1, β_2, α_0 and α_1, in the evolution equation for the dissipative currents (Eq. (2.63)). These parameters can now be derived from the evolution equations obtained by solving the relativistic Boltzmann equation for the distribution function,

$$p^\mu \partial_\mu f = C[f] \tag{2.70}$$

under the *relaxation time approximation* (RTA),

$$C[f] = -u_\mu p^\mu \frac{\delta f}{\tau_R}\,, \tag{2.71}$$

where $C[f]$ is called *collision functional* and τ_R is the relaxation time. However, for this one needs to assume some approximated form for δf. One of the most popular method is the *Grad's 14-moment approximation method.*

Grad's 14-moment approximation method : In this method, originally proposed by Grad [154], the correction δf is obtained by expanding the distribution in Taylor's series around its local equilibrium in the power of momenta (truncating in second moment of momenta) [153, 155, 169, 160, 162, 164, 163],

$$\delta f = f_0\tilde{f}_0[\varepsilon(x) + \varepsilon_a(x)p^\alpha + \varepsilon_{\alpha\beta}(x)p^\alpha p^\beta] + \mathcal{O}(p^3)\,, \tag{2.72}$$

which involves 14-unknowns to be determined in order to obtain the distribution, hence called 14-moment approximation. While Israel-Stewart used second moment of Boltzmann equation [153], a more consistent approach was proposed by Denicol-Koide-Rischke (DKR) in [155] to obtain the evolution equation for the dissipative quantities [155, 169],

$$
\begin{aligned}
\dot{\Pi} &= -\frac{\Pi}{\tau_\Pi} - \beta_\Pi\theta - \ell_{\Pi n}\partial\cdot n - \tau_{\Pi n} n\cdot\dot{u} - \delta_{\Pi\Pi}\Pi\theta - \lambda_{\Pi n} n\cdot\nabla\alpha_0 + \lambda_{\Pi\pi}\pi^{\mu\nu}\sigma_{\mu\nu}\ , \\
\dot{n}^{\langle\mu\rangle} &= -\frac{n^\mu}{\tau_n} + \beta_n\nabla^\mu\alpha_0 - n_\nu w^{\nu\mu} - \delta_{nn}n^\mu\theta - \ell_{n\Pi}\nabla^\mu\Pi + \ell_{n\pi}\Delta^{\mu\nu}\partial_\lambda\pi^\lambda_\nu \\
&\quad + \tau_{n\Pi}\Pi\dot{u}^\mu - \tau_{n\pi}\pi^\mu_\nu\dot{u}^\nu - \lambda_{nn}n^\nu\sigma^\mu_\nu + \lambda_{n\Pi}\Pi\nabla^\mu\alpha_0 - \lambda_{n\pi}\pi^{\mu\nu}\nabla_\nu\alpha_0\ , \\
\dot{\pi}^{\langle\mu\nu\rangle} &= -\frac{\pi^{\mu\nu}}{\tau_\pi} + 2\beta_\pi\sigma^{\mu\nu} + 2\pi_\alpha^{\langle\mu}w^{\nu\rangle\alpha} - \tau_{\pi n}n^{\langle\mu}\dot{u}^{\nu\rangle} + \ell_{\pi n}\nabla^{\langle\mu}n^{\nu\rangle} - \delta_{\pi\pi}\pi^{\mu\nu}\theta \\
&\quad - \tau_{\pi\pi}\pi_\alpha^{\langle\mu}\sigma^{\nu\rangle\alpha} + \lambda_{\pi n}n^{\langle\mu}\nabla^{\nu\rangle}\alpha_0 + \lambda_{\pi\Pi}\Pi\sigma^{\mu\nu}\ ,
\end{aligned}
\tag{2.73}
$$

where $w^{\mu\nu} = (\nabla^\mu u^\nu - \nabla^\nu u^\mu)/2$ is the vorticity tensor. The above derived equations contain 25 transport coefficients in general, among which three coefficients are shown below [155],

$$
\begin{aligned}
\beta_\Pi &= (\frac{1}{3} - c_s^2)(\varepsilon + P) - \frac{2}{9}(\varepsilon - 3P) - \frac{m^4}{9}\langle(u\cdot p)^{-2}\rangle_0\ , \\
\beta_n &= -\frac{n^2}{\beta(\varepsilon+P)} + \frac{2\langle 1\rangle_0}{3\beta} + \frac{m^2}{3\beta}\langle(u\cdot p)^{-2}\rangle_0\ , \\
\beta_\pi &= \frac{4P}{5} + \frac{\varepsilon - 3P}{15} - \frac{m^4}{15}\langle(u\cdot p)^{-2}\rangle_0\ ,
\end{aligned}
\tag{2.74}
$$

where $\langle\ldots\rangle_0 = \int dp(\ldots)f_0$ and $c_s^2 = (dP/d\varepsilon)_{s/n}$ is the speed of sound squared within the medium, which we discuss later.

Besides, there exist another commonly used method to obtain the equations for the dissipative quantities, namely the *Chapman-Enskog expansion*, where the particle distribution function is expanded in powers of the space-time gradient around its equilibrium value in order to find an approximate expression for δf. For details see [156].

2.5 Quantum Chromodynamics (QCD) : theory of strong interaction

The QGP medium created in the heavy-ion collision is a strongly interacting medium of quarks and gluons which are expected to be weekly coupled in the QGP state at asymptotically large temperature (only). The fundamental theory governing this strong interaction is Quantum Chromodynamics or QCD which deals with the quarks and gluons field and their interactions. The theory explains two fundamental phenomena : i) quarks and gluons cannot exist as free particles in nature. They are always found as bound states (hadrons), this phenomena is known as the *color confinement* ii) the interaction between quarks and gluons becomes weaker at short distance and stronger at longer distance, a phenomenon known as *asymptotic freedom*. We first discuss one of the most interesting feature of this theory; the existence of *color degrees of freedom or color charges* of quarks.

Color degrees of freedom : The first hint of color charges came when people encountered problem to explain the wave function of strange baryons e.g. Δ^{++}, Ω^- etc. For example, Ω^- hyperon consists of three s-quarks and has spin $3/2$. As a result, the spin and flavour wave function of Ω is symmetric with respect to the change of identical valance s-quarks. According to the Pauli's exclusion principle, the full wave function of a particle containing three identical quarks must be antisymmetric. Therefore, it demands that the spatial wave-function of Ω^- has to be antisymetric. However, Ω^- is a stable particle and the ground state of a three $s-$quark system; its total wave function has to be symmetric. To solve this puzzle, people came up with a new quantum number associated with the Ω^- hyperon, which should have at least three different values corresponding to the three quarks within Ω^-. This new quantum number is known as *color*, which is an additional degree of freedom of the quarks and gluons, the fundamental basis of QCD theory.

2.5.1 The QCD Lagrangian

Quantum chromodynamics is a SU(3) gauge theory, known as Yang-Mills gauge theory [170]. The QCD Langrangian density is given by [9, 14, 15, 10],

$$\mathcal{L}_{QCD} = \bar{\psi}_q^i(x)\ [i\gamma^\mu D_\mu - m_q]_{ij}\psi_q^j(x) - \frac{1}{4}F^a_{\mu\nu}F^{a\mu\nu}\ , \tag{2.75}$$

where, $\psi_q^i(x)$ and $\bar{\psi}_q^i(x)$ are the spin-1/2 Dirac fields for quark and antiquark respectively, having color i, flavor q, and mass m_q, with $\bar{\psi} = \psi^\dagger\gamma^0$. The gluons are represented by a field A^a_μ, which has spin equal to 1, zero mass and color index a corresponding to the adjoint representation in SU(3) gauge group. In Eq. (2.75), it is assumed that there is a summation over repeated color and Lorentz indices. The indices $i, j = 1,2,3$ correspond to three possible colors for quarks whereas $a = 1,\ldots,8$ represent the colors for eight gluon fields corresponding to the 8 generators of SU(3) group. The covariant derivative D_μ is defined as,

$$D_\mu = \partial_\mu - igA_\mu = \partial_\mu - igt^aA^a_\mu\ , \tag{2.76}$$

where t^a are the 8 generators of SU(3), given by $t^a = \lambda^a/2$, where λ^a are the Gell-Mann matrices [9]. $F^a_{\mu\nu}$ are the non-abelian gluon field strength tensor, defined by,

$$F^a_{\mu\nu} = \partial_\mu A^a_\nu - \partial_\nu A^a_\mu + gf^{abc}A^b_\mu A^c_\nu \quad \text{or} \quad F_{\mu\nu} = t^aF^a_{\mu\nu} = \frac{i}{g}[D_\mu, D_\nu]\ , \tag{2.77}$$

where f^{abc} are the structure constants of color SU(3) gauge group. The underlying gauge symmetry means that the Lagrangian is invariant under the local gauge transformation,

$$\psi(x) \to \chi(x)\psi(x), \qquad A_\mu(x) \to \chi(x)A_\mu(x)\chi^{-1}(x) - \frac{i}{g}[\partial_\mu \chi(x)]\chi^{-1}(x) \,, \tag{2.78}$$

where $\chi(x) = e^{i\alpha^a(x)t^a}$. The Lagrangian in Eq. (2.75) is based on two fundamental assumptions which are confirmed by experimental observations : all hadrons consist of quarks and quarks are not observed as free particles. These two assumptions demand that there exists a particle which mediates the interaction between the quarks to form the bound state. This interaction has to be attractive i.e. it should depend on the quark colors which requires the mediating particle to be a vector boson of spin 1. In addition to that, the fact that quarks cannot exist as free particles, requires the force of attraction to be stronger at larger distance, which essentially needs the mediating particle to be massless. Thus the particle responsible for strong interaction is a non-Abelian massless vector boson, a gluon.

2.5.2 Asymptotic freedom and confinement

Another very interesting and remarkable feature of QCD is the *asymptotic freedom* which tells us that the QCD coupling strength gets weaker at shorter distances i.e corresponding to larger values of four-momentum squared $q^2 = -Q^2$, where Q is a real number. The running coupling constant of QCD governing the interactions is given by [14, 171],

$$\alpha_s(Q^2) = \frac{\alpha_s(\mu^2)}{1 + \alpha_s(\mu^2)\, \beta_2 \, \ln(Q^2/\mu^2)} \tag{2.79}$$

where,

$$\beta_2 = \frac{11N_c - 2N_q}{12\pi} \quad \text{and} \quad \beta_{QCD}(\alpha) = -\beta_2\alpha^2 + \mathcal{O}(\alpha^3) \,. \tag{2.80}$$

β_{QCD} is known as QCD beta function, N_c is the number of colors and N_q is the number of quark flavors. While $N_q = 6$ in the Standard Model, the effective numbers of flavor depend on the momentum scale Q and in principle could be smaller than six. Eq. (2.79) clearly suggests that as $Q \to \infty$, the coupling constant $\alpha_s(Q^2) \to 0$. This means that the strong interaction between the quarks and gluons become smaller at larger momentum or asymptotically short distance, called the asymptotic freedom. Such a behavior is in striking contrast to other categories of interactions e.g. Quantum Electrodynamics or QED. In QED, β_2 is negative and as a result the QED coupling constant becomes stronger at the shorter distance or larger Q^2. The quantity μ in Eq. (2.79) represents an arbitrary scale, known as the *renormalization point*. Eq. (2.79) can be rewritten as,

$$\alpha_s(Q^2) = \frac{1}{\beta_2 \, \ln(Q^2/\Lambda^2_{QCD})} \,, \tag{2.81}$$

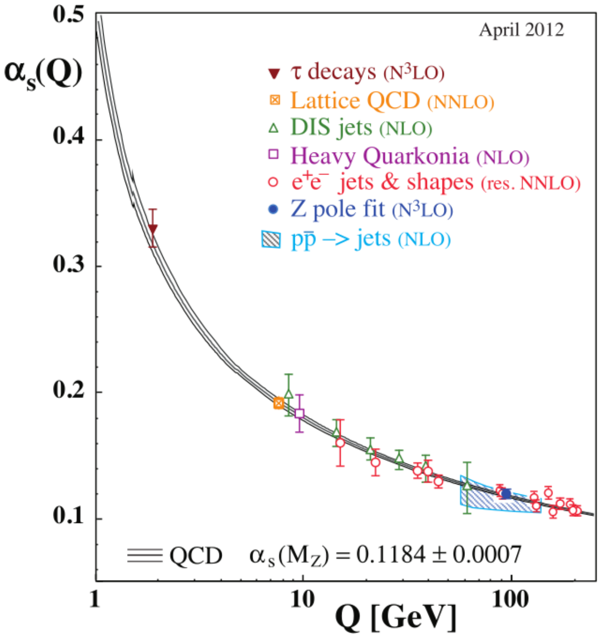

Fig. 2.7 The running coupling of QCD, as a function of energy (momentum) scale Q, illustrating the asymptotic freedom. The figure shows a summary of different measurements of α_s at the respective energy scale. Figure is taken from [172]

where Λ_{QCD} is the fundamental scale of QCD, having value $\simeq 200-300$ MeV. The exact value of Λ_{QCD} depends on the method of renormalization. The strong coupling constant $\alpha_s(Q^2)$ become large when $Q \sim \Lambda_{QCD}$, which makes the interaction between quarks and gluons stronger leading to the confinement of the quarks and gluons inside hadrons. Fig. 2.7 shows the dependence of the running coupling constant $\alpha_s(Q^2)$ on the energy scale (Q), depicting the asymptotic freedom.

Deconfinement and formation of QGP

The asymptotic freedom discussed above suggests that when the momentum-transfer squared is very large (($Q^2 \gg 1$)) i.e. when the collision energy is very high, the coupling strength of the strong interaction between the constituent partons become very week ($\alpha_s(Q^2) \to 0$). At asymptotically large temperature, the interaction strength between the partons become so week that within the hot dense matter, the quarks and gluons become asymptotically free and a new degrees of freedom (color) enters into the picture. This phenomena is called *color deconfinement* which is responsible for the formation of the Quark-Gluon-Plasma (QGP). The experimental program of heavy-ion collision aims at creating this hot and dense droplet of matter where this particular phenomenon of deconfinement transition takes place.

In the present context, it is important to mention another useful description of QCD theory, known as *Lattice QCD* (LQCD) which is used to calculate the QCD Equation of State (EoS) for the QGP medium at high temperature as well as to obtain the QCD phase diagram. Below we briefly discuss this.

2.5.3 QCD Equation of State and Lattice QCD

The Equation of State (EoS) of a system is defined as the relationship between the thermodynamic variables (state variables) of the system, i.e. pressure (P) or number density (n) to the energy density (ε). EoS is extremely important because it describes the equilibrium properties of the QCD matter. To close the hydrodynamic set of equations, one needs an additional equation which is provided by the equation of state of the system, hence it is an important input for hydrodynamics.

If we treat the QGP medium as an ideal gas of massless quarks and gluons having zero net chemical potential ($\mu_B = 0$), then thermodynamic quantities of the system can be calculated from the partition function $Z(T,V)$ of the system,

$$\begin{aligned} \text{energy density,} \qquad & \varepsilon_{QGP} = \nu_{QGP}\frac{\pi^2}{30}T^4 \ , \\ \text{pressure,} \qquad & P_{QGP} = \nu_{QGP}\frac{\pi^2}{90}T^4 \ , \\ \text{number density,} \qquad & n_{QGP} \approx \nu_{QGP}\frac{1}{\pi^2}T^4 \ , \end{aligned} \tag{2.82}$$

where ν_{QGP} is the total number of degrees of freedom of the system, given by,

$$\nu_{QGP} = 16 + \frac{21}{2}N_f \ , \tag{2.83}$$

where N_f is the number of quark flavours. Then in the massless ideal gas limit, one has the EoS of the system: $P = \frac{1}{3}\varepsilon$, the EoS for the ideal gas.

Speed of sound in QGP : In this context, it is important to discuss the speed of sound within the QGP medium. Sound is defined as a small disturbance that propagates through a uniform fluid at rest. For a QGP medium with pressure P and energy density ε, the speed of sound squared is defined as,

$$c_s^2 = \frac{\partial P}{\partial \varepsilon} \ . \tag{2.84}$$

Therefore, for a massless gas of quarks and gluons, $c_s^2 = \frac{1}{3}$. In the case of a baryon less QGP medium ($\mu_B = 0$), using Eqs. (2.37) and the relation between the densities, the speed of sound within the medium can be also written in terms of temperature and entropy density as [20, 173],

$$c_s^2 = \frac{d\ln T}{d\ln s} \ . \tag{2.85}$$

However, in reality the quarks have mass and interact strongly. Matter created after the heavy-ion collision exhibit two phases (as we will describe later) during the hydrodynamic evolution : the QGP phase at high temperature and as the temperature drops, it gradually enters into the *hadron resonance gas* (HRG) phase. As a result, in the heavy-ion community it is a common practice to use Lattice QCD (LQCD) calculation at high temperature and HRG model at low temperature for the EoS with vanishing baryon chemical potential ($\mu_B = 0$) [174].

At zero baryon chemical potential ($\mu_B = 0$), there exist many methods, a combination of which could give us a good understanding of EoS at all temperatures. At extremely high temperature ($\alpha_s \ll 1$) i.e. in the pure QGP phase, EoS can be obtained by the perturbative QCD calculations [175–177]. On the other hand, at the low temperature (α_s large), i.e. in the hadron gas phase EoS is calculated from HRG model [174]. Lattice QCD (LQCD) bridges the gap between the two calculations and captures the transition between the QGP and the hadron gas phase [178]. In the non-perturbative region, where α_s is not so small, LQCD calculation serves as the major tool to investigate equilibrium properties of QCD. In lattice QCD calculations, a discretized 3+1D lattice space is created and through Monte Carlo approach, the partition function (Z) is evaluated on the lattice through path integral method. Once the partition function is defined, all the thermodynamic quantities can be calculated at $\mu_B = 0$ and for any temperature T, eventually providing the QCD EoS [179, 178, 180] at $\mu_B = 0$. In the case of finite baryon chemical potential ($\mu_B \neq 0$), the EoS is usually obtained through some approximation using Taylor series expansion around $\mu_B = 0$ [181–184]. LQCD calculation is used to obtain the equation of state at high temperatures and HRG model is used at low temperatures, with an interpolation procedure in between [174, 25].

2.6 Different stages of HI collision : hydrodynamic framework

An ultrarelativistic nucleus-nucleus collision at the LHC or RHIC produces hundreds or thousands of particles. From the time of the collision to the time of the detection of the produced particles, the time span is very short (few fm/c). However, within that little span of time, there exist different stages that the system undergoes before ending up as particles at the detectors [185, 25, 27, 28]. Fig 2.8 shows the schematic representation and timeline of different stages of a heavy-ion collision event, which we briefly describe below :

- At $t = 0$ fm/c, two incoming nuclei collide and at the overlap area of collision they deposit energy (or entropy), which serves as the *initial state* of the collision.
- The fireball created at the collision does not achieve thermal equilibrium immediately after the collision, rather it takes some time for its constituents to interact between each other so

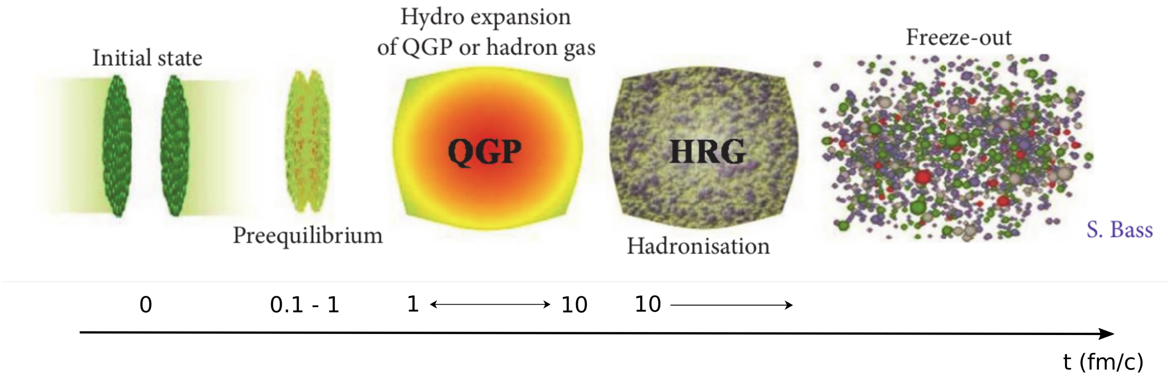

Fig. 2.8 Schematic representation of different stages in heavy-ion collision along with the timeline for the stages. Figure is taken from [25].

that the system gradually approach the equilibrium. This is known as the *pre-equilibrium state* which survives for $t \simeq 0.1 - 1$ fm/c.

- At around $t \lesssim 1$ fm/c, the system is usually considered to have partially achieved thermodynamic equilibrium. Next the system of deconfined quarks and gluons starts to expand collectively staying close to the local thermal equilibrium and simultaneously cools down. At this stage, the QGP medium can be treated as a fluid medium so that it can be evolved through *hydrodynamics*. This phase lasts approximately until $t \sim 10$ fm/c.

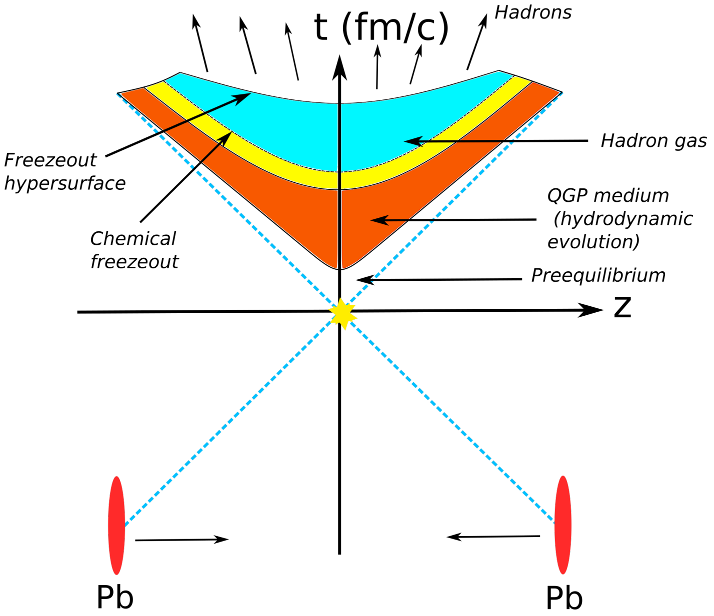

Fig. 2.9 Space-time diagram of different stages of heavy-ion collision. There exist a preequilibrium phase denoted by the white space. Next, there is a QGP phase, where hydrodynamic evolution occurs, denoted by the orange color. The hadron gas phase is denoted by the combination of yellow and blue colors, where at the end of the yellow region chemical freezeout occurs.

- After the hydrodynamic evolution of the QGP medium ($t \sim 10$ fm/c), when the system temperature drops below the phase-transition temperature (T_c) which is around 150 MeV, the system encounters a phase transition, where the medium constituents or the partons combine with each other to produce hadrons. This is called *hadronization*[3] in which many hadrons and resonance particles are produced forming a system of hadrons, *the hadron-resonance gas* (HRG). At this stage, the produced hadrons undergo resonance decay and elastic or inelastic interactions with each other until they reach a certain point where the system ceases to produce new particles, known as the *chemical freezeout*. After chemical freezeout, the produced stable hadrons still undergo elastic interactions with each other until the system reach a certain state where the elastic interactions between the hadrons also stop, called the *kinetic freezeout*[4]. It is expected that the kinetic freezeout occurs later than chemical freezeout so that the temperature for chemical freezeout is always larger ($T_{ch} > T_{kin}$). After kinetic freezeout, hadrons are free to stream towards the detector.
- When the system reaches the state of kinetic freezeout, the space-time hypersurface of the system is called the *freezeout hypersurface*. The momentum space distribution of the final identified hadrons is then obtained by converting the fluid dynamical information from each hypersurface cell into the local phase-space distributions of hadrons, through *particlization* method.

Fig 2.9 shows the space-time evolution and different stages of heavy-ion collision. It is clearly visible that in the hadron gas phase there exists checmical and kinetic freezeout separately.

It should be noted that after the hydrodynamic evolution, when the system reaches the freezeout state, the hadrons particlized from the freezeout hypersurface, can again undergo secondary elastic or inelastic interactions and cascade decays before finally hitting the detectors. Such interactions and cascade decays can redistribute the momentum distribution of the identified particles. Therefore, modern hydrodynamic simulations take these into account by carrying out hydrodynamic evolution followed by a hadron-cascade stage, where the latter is implemented through a *after-burner*. We will revisit this fact at the end of this chapter.

2.6.1 Initial conditions

At the time of the collision, two nuclei deposit energy (or entropy) at the overlap region which serves as the initial state for the collision event. The initial state condition is of practical importance in heavy-ion collision, in the sense that many final state observables depend largely on the initial state properties [186, 128, 187, 92, 97]. A full 3D initial condition would involve a

---

[3] not to be confused with *particlization* which occur at later time

[4] Please note until this stage the system is still evolving through hydrodynamics as the fluid picture was still valid. In reality, the precise time for the hydrodynamic evolution to stop is not accurately defined, one only knows that it has to stop at some point.

2D density profile on the transverse plane along with the space-time rapidity (η_s) distribution of those transverse profiles [188, 49, 189, 190]. However, as long as we restrict ourselves to the central rapidity region, the space-time evolution of the system can be assumed to be a boost-invariant, homogeneous (or uniform) longitudinal expansion, known as the *Bjorken flow* which is a very simplistic yet effective assumption of hydrodynamic expansion first proposed by J.D. Bjorken [191], which will be again discussed later. In the Bjorken picture, the boost-invariance ensures that most of the knowledges about the transverse collective properties of the system can be obtained using a 2+1 D hydrodynamic expansion of the system, which will be our primary topic of discussion in this document. For the initial conditions of such boost-invariant hydrodynamic evolution, the two dimensional density profiles are sufficient. This initial density could be obtained from some state of the art initial state models e.g. 2D Glauber model (discussed in Sec. 2.3), saturation based *color glass condensate* model (Kharzeev-Levin-Nardi(KLN) model [137, 192], IP-Glasma model [94, 193]), parametric Glauber-like model (TRENTo model [194]) etc. In this document we will mostly use the Glauber model which we have already discussed in Sec. 2.3 and the parametric TRENTo model to generate 2D initial conditions for hydro-evolution, which we briefly discuss below.

Two-component Glauber model

Although in Sec. 2.3, we discussed the basic features of the optical and MC Glauber model, we did not discuss the particle production i.e. how the final state multiplicity scales according to the number of participants or binary collisions. In the simplest picture, the multiplicity of hadrons per unit rapidity in an event scales according to the soft processes i.e. the total number of participants or the number of wounded nucleons : $\frac{dN_{ch}}{d\eta} = N_{pp}\frac{N_{part}}{2}$, known as the *wounded-nucleon model* [136], where N_{pp} is the average multiplicity in p+p collision. However, later the experimental data have suggested that the total multiplicity in a nucleus-nucleus collision gets contribution from both hard and soft processes. In particular, the multiplicity per unit pseudo-rapidity has two components: the ‘soft’ part is proportional to the number of participants N_{part} and the ‘hard’ part is proportional to the number of binary collisions N_{coll} [137],

$$\frac{dNch}{d\eta} = (1-\alpha)\, N_{pp}\, \frac{N_{part}}{2} + \alpha\, N_{pp}\, N_{coll}\ , \tag{2.86}$$

where $0 < \alpha < 1$. The above two models are implemented within *GLISSANDO* [144].

TRENTo model

TRENTo which reads as *Reduced Thickness Event-by-event Nuclear Topology*, is a parametric non-dynamical effective model for generating initial conditions directly at the thermalization time (τ_0) in high-energy nucleus-nucleus, proton-nucleus and proton-proton collisions [194].

Let us first consider, two protons A and B, separated by an impact parameter b along x-axis, collide with each other having nuclear densities,

$$\rho_{A,B} = \rho_{proton}(x \pm b/2, y, z) \ . \tag{2.87}$$

Then the participant thickness associated with each projectile is given by,

$$T_{A,B}(x,y) = \int dz \ \rho_{A,B}(x,y,z) \ . \tag{2.88}$$

The incoming two protons collide with a probability [195],

$$P_{coll} = 1 - \exp\left[-\sigma_{NN} \int dx \ dy \int dz \rho_A \int dz \rho_B \right] , \tag{2.89}$$

where the above integral represents the overlap integral of proton thickness function and σ_{NN} is the proton-proton inelastic cross-section. To introduce additional event-by-event fluctuations, each proton is assigned a *fluctuating* thickness,

$$T_{A,B}(x,y) = \omega_{A,B} \ \int dz \ \rho_{A,B}(x,y,z)] \ , \tag{2.90}$$

where $\omega_{A,B}$ represent independent random weights which are sampled from a gamma distribution with unit mean,

$$P_k(\omega) = \frac{k^k}{\Gamma(k)} \omega^{k-1} e^{-k\omega} \ . \tag{2.91}$$

The additional multiplicity fluctuations are introduced by the above gamma weights.

Next come two primary postulates for the entropy production in this model:

- In the collision, the entropy production occurs through the eikonal overlap of T_A and T_B.
- There exist a scalar field $f(T_A, T_B)$ which converts the projectile thicknesses into entropy deposition i.e $f \propto dS/dy|_{\tau=\tau_0}$, where $dS/dy|_{\tau=\tau_0}$ is the entropy deposited per unit rapidity at the hydrodynamic thermalization time τ_0.

In the TRENTo model, f represents the *reduced thickness* having the functional form,

$$f = T_R(p; T_A, T_B) \equiv \left(\frac{T_A^p + T_B^p}{2} \right)^{\frac{1}{p}} , \tag{2.92}$$

named accordingly because the above function takes two thicknesses T_A, T_B and ‘reduces’ them to a third thickness, similar to the reduced mass. The above functional form represents the

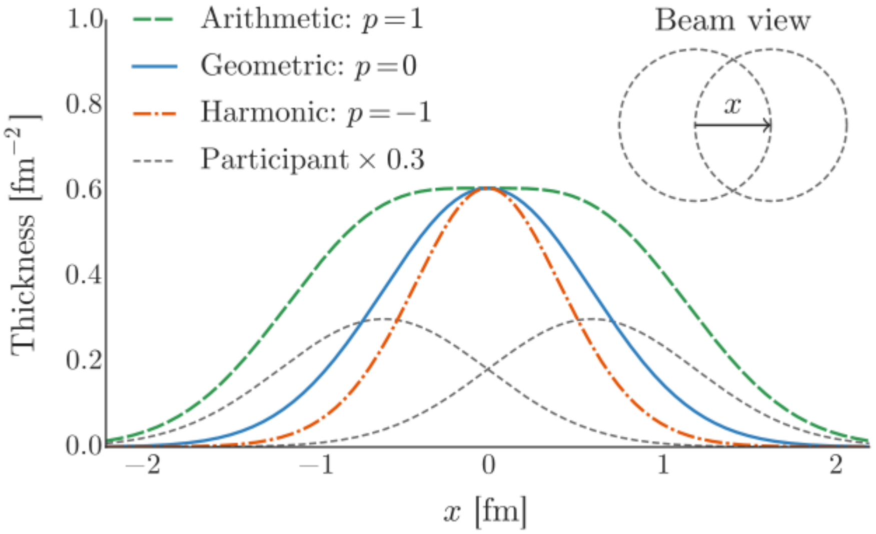

Fig. 2.10 Reduced thickness in the collision of two nucleons at some non-zero impact parameter along x-axis for different values of p. The plot shows the cross-sectional view of the overlap of thicknesses. Figure taken from [194].

generalized mean which depending on the value of the parameter p, reduces to

$$T_R = \begin{cases} \max(T_A, T_B), & p \to +\infty \\ (T_A + T_B)/2, & p = +1 \text{ (arithmetic mean)} \\ \sqrt{T_A T_B}, & p = 0 \text{ (geometric mean)} \\ 2T_A T_B/(T_A + T_B), & p = -1 \text{ (harmonic mean)} \\ \min(T_A, T_B)\ . & p \to -\infty \end{cases} \tag{2.93}$$

Please note that with $p = 1$, the reduced thickness become equivalent to the wounded nucleon model. Fig. 2.10 shows the reduced thickness as a function of the impact parameter for two colliding nucleons for different values of p.

Similarly, proton-nucleus and nucleus-nucleus collisions can be treated as a superposition of proton-proton collisions. Let us consider now two colliding nuclei A and B. The position of the nucleons in each projectile is obtained by sampling a nuclear distribution e.g. Woods-Saxon distribution (Sec. 2.2.1) and then collision probability is sampled for each pair of nucleons from the two projectiles. The nucleons which collide at least once with another nucleon from the other projectile, are called the 'participants' and the rest of the nucleons are spectators hence not relevant. Then the fluctuating thickness function of two nuclei reads,

$$T_{A,B}(x,y) = \sum_{i=1}^{N_{part}^{A,B}} \omega_i \int dz\, \rho_{A,B}^{proton}(x - x_i, y - y_i, z - z_i). \tag{2.94}$$

where ω_i is the weight corresponding to i^{th} participant. Once we have the participant thickness T_A and T_B, we can calculate $T_R(p;T_A,T_B)$ using Eq. (2.92) and the initial transverse entropy deposition per unit rapidity is given by up to an overall normalization factor,

$$\frac{dS}{dy}|_{\tau=\tau_0} \propto T_R(p;T_A,T_B) \; . \tag{2.95}$$

The average charged particle multiplicity (N_{ch}) produced in the final state after the hydrodynamic evolution, is to a good approximation, proportional to the average total initial entropy [196] and so to the integrated reduced thickness[5],

$$\frac{dN_{ch}}{dy'} \propto \int dx\, dy\, \frac{dS}{dy'}|_{\tau=\tau_0} \equiv \int dx\, dy\, T_R \; . \tag{2.96}$$

The default value of the parameter p is 0, the parameter k in Eq. (2.91) is called the shape parameter having a default value $k = 1$. Small values of k $(0 < k < 1)$ correspond to larger multiplicity fluctuations and if $k \gg 1$ then it suppresses the fluctuations. The proton thickness function in Eq. (2.94) is given by a Gaussian density,

$$\int dz\, \rho_{proton} = \frac{1}{2\pi w^2} \exp\left(-\frac{x^2+y^2}{2w^2} \right) , \tag{2.97}$$

where w^2 is the effective area, having a default value $w = 0.6$ fm. The latest version of TRENTo also includes the option to work with the constituents (partons) and hence the Gaussian constituent width v [197].

2.6.2 Pre-equilibrium

Once we have the initial condition in a heavy-ion collision event, the next step is the hydrodynamic evolution of the system once it achieves thermal equilibrium. However, the thermalization is not achieved immediately after the collision, rather there exist a finite time interval between the time of collision ($\tau = 0$) and the thermalization time ($\tau = \tau_0$), called the pre-equilibrium phase. In this time interval, the constituents (partons) of the created system just after collision, involve in rapid interaction with each other in order to achieve the equilibrium state. In principle, there could be two limiting cases for the coupling strength inside the QGP medium [27]: infinitely week coupling where the secondary partons created in the collision free-stream without any interaction and infinitely strong coupling where the inter-particle mean free path becomes extremely small, eventually resulting in a fluid-like system.

In reality, the initial parton interactions in the preequilibrium phase is governed by a coupling strength lying between the above two extremes, while the system continues to evolve. The simplest choice for the dynamical evolution of the system in pre-equilibrium phase is

---

[5] denoting here rapidity as y'.

the free-streaming of partons, governed by the collision-free Boltzmann equation [27, 28] : $p^{\mu}\partial_{\mu}f(x,p) = 0$. Usually the free-streaming time is taken to be $0 < \tau_{fs} \lesssim 1$ fm/c. IP-Glasma [94, 193] is the one of the most popular state-of-the-art models which takes into account the pre-equilibrium dynamics until hydrodynamics begin. The IP-Glasma model is a CGC based [198–203], impact parameter dependent saturation model (IP-Sat) which provides the initial condition for heavy-ion collision by taking into account not only the fluctuations in nucleons' positions but also the quantum fluctuations of color charges. Besides, there are other transport models e.g. URQMD [204–206], AMPT [36, 37, 207, 208], KoMPoST [209] and relativistic ADS/CFT models [210] which also incorporate the pre-equilibrium dynamics.

2.6.3 Hydrodynamic evolution

Once the QGP system reaches thermalized state, the hydrodynamic evolution can be started from the thermalization time (τ_0) assuming the system as a fluid-like medium. The hydrodynamic evolution of the system is governed by the hydrodynamic equations of motion described in Sec. 2.4, as well as the equation of state of the system. In reality, this evolution is a fully three dimensional evolution in space-time, but a boost-invariant two dimensional transverse evolution also works as a good approximation, which stems from the Bjorken picture of the hydrodynamic evolution. In this thesis, all the results in the following chapters are based on a boost-invariant two dimensional evolution, where the underlying assumption is the Bjorken flow that we discuss below.

Bjorken flow

Bjorken flow describes the longitudinal expansion (along the beam-axis) of the fluid medium created in heavy-ion collision, first proposed by J.D. Bjorken [191]. Bjorken proposed that in a central collision of two large nuclei, the fluid medium near the collision axis expand homogeneously (or uniformly) in the longitudinal direction (along z-axis). It means that at a given longitudinal distance z, all points on the fluid move with a longitudinal velocity $\beta_z = v_z = z/t$ at a given time t in the lab frame, while the pancake-like nuclei recede in opposite directions and the fluid in the midway stays at rest. The velocity is uniform and the expansion is boost-invariant under Lorentz transformation in a sense that if someone boosts the system (say with velocity v) along the z-direction, all three quantities v_z, z, t change in the new frame but $v_z = z/t$ still hold in the new frame or in other words, in the new frame the fluid expands with a uniform velocity $v_z' = z'/t'$ in the longitudinal direction. Bjorken's prescription for hydrodynamic expansion is supported by the experimentally observed plateau in the distribution of produced particles in rapidity[6] [73, 149, 211]. In the Bjorken picture, one works with the proper time coordinates

---

[6] In experiment one often measures the charged particle multiplicity distribution in pseudo-rapidity rather than rapidity

(Eq. 2.4) or the so called *Milne coordinates* given by,

$$\tau = \sqrt{t^2 - z^2} \quad \text{and} \quad \eta_s = \frac{1}{2}\ln\frac{t+z}{t-z}\,, \tag{2.98}$$

where τ is the proper time and η_s is the space-time rapidity. Conversely, t and z are given in terms of Milne coordinates as,

$$t = \tau\,\cosh\eta_s \quad \text{and} \quad z = \tau\,\sinh\eta_s\,. \tag{2.99}$$

Under the Bjorken scaling $v_z = z/t$, the fluid rapidity y in Eq. (2.5) becomes equal to space-time rapidity η_s,

$$\eta_s = \frac{1}{2}\ln\frac{t+z}{t-z} = \frac{1}{2}\ln\frac{1+z/t}{1-z/t} = \frac{1}{2}\ln\frac{1+v_z}{1-v_z} = \frac{1}{2}\ln\frac{1+p_z/E}{1-p_z/E} = y. \tag{2.100}$$

Under the Lorentz boost along z-axis, τ remains constant, y and η_s shift by a constant. With the Bjorken's prescription, initial conditions are usually specified at a given proper time $\tau = \tau_0$, rather than a given time $t = t_0$ and the solution of the hydrodynamic equations becomes much simpler.

Solution of hydrodynamic equations in the Bjorken picture

Bjorken picture of hydrodynamic expansion describes only one-dimensional flow in the longitudinal direction and no transverse flow[7]. However, it is important for the assumption of boost-invariant expansion of the fluid. The fluid four-velocity in Bjorken picture becomes,

$$u^\mu = \gamma(1, v_z), \quad \text{with} \quad v_z = \frac{z}{t},\ \gamma = \frac{1}{\sqrt{1-v_z^2}} = \frac{t}{\tau}\,. \tag{2.101}$$

In terms of Milne coordinates,

$$(t, z) = \tau\ (\cosh\eta_s, \sinh\eta_s) \Rightarrow u^\mu = (\cosh\eta_s, \sinh\eta_s). \tag{2.102}$$

For an ideal relativistic fluid, we recall the hydro-equations in Eq. (2.43) and Eq. (2.47),

$$D\varepsilon + (\varepsilon + P)\theta = 0 \quad \text{and} \quad Dn + n\theta = 0\,, \tag{2.103}$$

where $D = u^\mu \partial_\mu$ and $\theta = \partial_\mu u^\mu$. In terms of Milne coordinates they become,

$$D \equiv \frac{\partial}{\partial\tau} \quad \text{and} \quad \theta = \frac{1}{\tau}\,. \tag{2.104}$$

---

[7] It should be noted that the Bjorken flow is an oversimplification of the hydrodynamic expansion. In reality, the fluid expands in all possible directions. However, the transverse expansion sets in at a later time leading to the transverse anisotropic flow and most distinctive collective behaviour of the fluid observed in the final state.

With this, the hydro equations become,

$$\frac{\partial \varepsilon}{\partial \tau} = -\frac{\varepsilon + P}{\tau} \quad \text{and} \quad \frac{\partial n}{\partial \tau} = -\frac{n}{\tau} \, . \tag{2.105}$$

Assuming that the hydrodynamic evolution starts at time $\tau = \tau_0$, when the initial energy density is $\varepsilon = \varepsilon_0$ and using the EoS, $P = c_s^2 \varepsilon$, the first equation in Eq. (2.105) gives,

$$\frac{\partial \varepsilon}{\partial \tau} + (1 + c_s^2)\frac{\varepsilon}{\tau} = 0 \qquad \Longrightarrow \qquad \varepsilon_{Bjorken} = \varepsilon_0 \left(\frac{\tau_0}{\tau}\right)^{1+c_s^2} \, . \tag{2.106}$$

Similar to the second part of Eq. (2.105), Eq. (2.48) gives the equation for entropy density,

$$\frac{\partial s}{\partial \tau} = -\frac{s}{\tau} \qquad \Longrightarrow \qquad s = \frac{s_0 \tau_0}{\tau} \tag{2.107}$$

and so the pressure of the system would evolve as, $P \propto \frac{1}{\tau^{1+c_s^2}}$. For the evolution of the temperature, we use Eq. (2.36) with zero baryon chemical potential,

$$\varepsilon = -P + Ts \qquad \Longrightarrow \qquad T \propto \frac{1}{\tau^{c_s^2}} \, . \tag{2.108}$$

If we consider the medium as a gas of massless quarks and gluons, then $c_s^2 = 1/3$ leads to the relation :

$$P \propto T^{1+\frac{1}{c_s^2}} = T^4, \qquad \varepsilon \propto T^4 \quad \text{and} \quad s \propto T^3 \, , \tag{2.109}$$

which we find for an ideal gas.

2.6.4 Hadronization and freezeout : QCD phase transition

Towards the end of hydrodynamic evolution, when the QGP medium has cooled down sufficiently ($T \sim 150$ MeV), the interaction strength between the constituent partons become large enough that they couple with each other to form bound states or hadrons. At this stage, the system undergoes a smooth phase-transition from the decoupled QGP phase to a strongly coupled hadronic phase, producing a gas of stable hadrons and their unstable resonance particle, called *hadron resonance gas* (HRG). This is known as the so-called QCD phase transition [29, 212, 30–33, 213, 34] and the corresponding phase diagram is shown in Fig. 2.11. Please note that the type of phase transition depends on the collision energy which translates into the temperature and baryon chemical potential. It is expected that a smooth transition occurs at a vanishing baryon chemical potential ($\mu_B \sim 0$) in the *crossover region*, which is the case for collisions at the LHC and highest RHIC energies.

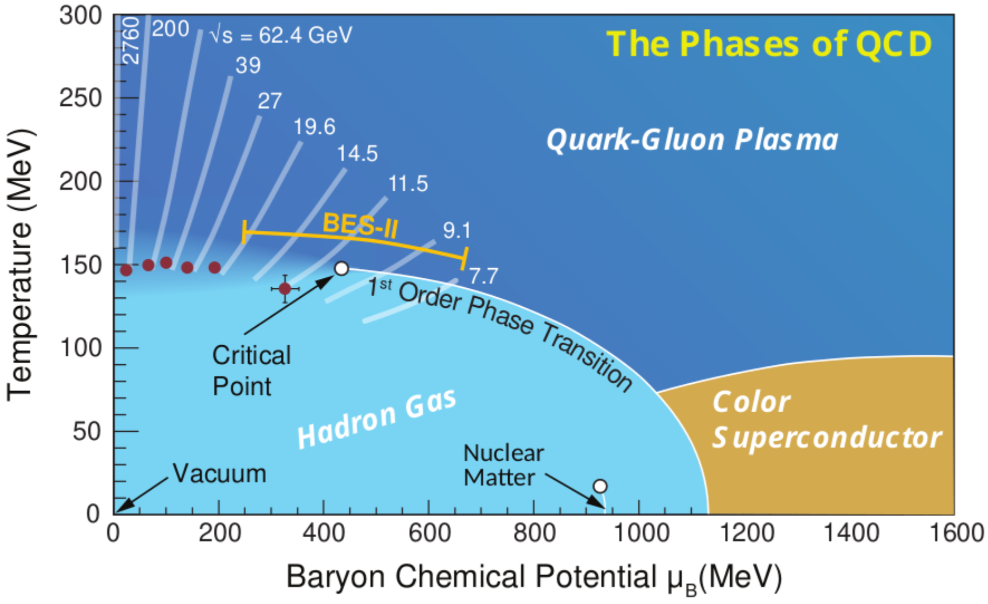

Fig. 2.11 Schematic representation of the QCD phase diagram. It is shown that the phase transition and its type depend on the collision energy, probing different (T, μ_B) regions. The solid curve separating the QGP phase and HRG phase, denotes the *first order transition*, and the point where it ends is called *critical point or critical end point*. After the critical point there exist a smooth transition region, called the *crossover region*. At the LHC or highest RHIC energies, the phase transition from QGP to hadron gas occurs towards the end of the crossover region where $T \sim 150$ MeV and $\mu_B \sim 0$. Figure taken from [214].

Freezeout

In the HRG phase, many stable and unstable hadrons are produced, which are further involved in elastic or inelastic collisions and resonance decays. These produce further particles until the system reach a certain state where the production of new particles stops. This is called *chemical freezeout*. After chemical freezeout, the system of stable hadrons still interact with each other via elastic collisions until the system reach another state where the elastic collisions also cease and that is known as *kinetic freezeout*. When the system reach kinetic freezeout, the space-time hypersurface at that point is called *freezeout hypersurface* and the hydrodynamic evolution stops at this stage. The most popular choices for the freeze-out criterion are the constant temperature or constant energy density hypersurface.

Particlization: Cooper-Frye prescription

Once the system reaches the kinetic freezeout condition (temperature $T = T_{fo}$ or energy density ε_{fo}), stable hadrons stream towards the detector. Therefore, at freezeout one needs to change the description of the system from the 'fluid picture' to 'particle picture', because at the end those particles are detected by the detectors. We need a method to obtain the momentum distribution of the particles from the freezeout hypersurface at constant temperature or energy density. This is called *particlization* and it is commonly given by Cooper-Frye formula [215], where the basic assumption is that towards the end of the hydrodynamic expansion, the momentum distribution of the outgoing particles is essentially the momentum distribution of the particles within the fluid, which are treated as independent particles [20]. In the Cooper-Frye prescription, the momentum distribution of hadron species i with degeneracy g_i is given by [8],

$$E\frac{dN}{d^3p} = \frac{dN}{dyp_Tdp_Td\phi_p} = \frac{g_i}{(2\pi)^3}\int_\Sigma f(x,p)p^\mu d^3\Sigma_\mu \ , \tag{2.110}$$

where $f(x,p) = f_0(x,p) + \delta f(x,p)$ is the distribution function consisting of the equilibrium part and the dissipative correction. Σ is the four dimensional freeze-out hypersurface at T_{fo} (or ε_{fo}) given by,

$$\Sigma_\mu = (\tau_f \cosh\eta_s, x, y, \tau_f sinh\eta_s) \ , \tag{2.111}$$

where τ_f is the freeze-out time (also called *switching time*) determined by the fall of temperature (or energy density) below T_{fo} (or ε_{fo}). $d^3\Sigma_\mu$ is the differential freezeout hypersurface element. The equilibrium distribution function is given by Eq. (2.68),

$$f(x,p) = \frac{1}{\exp((p^\mu u_\mu - \mu_i)/T_{fo}) \pm 1} \ , \tag{2.112}$$

where the ± sign depends on whether the distribution is Bose-Einstein or Fermi-Dirac distribution, depending on the spin of the hadronic species. The fluid velocity at the hypersurface, resulting from longitudinal and transverse flow is taken into account through the invariant expression $E \equiv E(x) = p^\mu u_\mu$, denoting the local energy of the hypersurface. The dissipative correction could be obtained from different prescriptions [218, 219, 189, 28]. Among them the most extensively used methods are Grad's 14-moment approximation and Chapman-Enskog expansion discussed in Sec.2.4.4. If the dissipative effect is considered only due to shear viscosity, then Grad's approximation gives,

$$\delta f(x,p)_{\text{shear}} = \frac{f_0\tilde{f}_0}{2(\varepsilon+P)T^2}p^\mu p^\nu \pi_{\mu\nu} \tag{2.113}$$

and the Chapman-Enskog expansion gives,

$$\delta f(x,p)_{\text{shear}} = \frac{5f_0\tilde{f}_0}{2(\varepsilon+P)T}\frac{1}{u\cdot p}p^\mu p^\nu \pi_{\mu\nu} \ . \tag{2.114}$$

---

[8] It should be noted that the Cooper-Frye formula presented here, which involves an integral over the hypersurface, is used only on a smooth surface producing directly the spectra of a particle according to Eq. (2.110). We particularly use this formalism in our simulation, as implemented in MUSIC[216] hydrodynamics code. This is not exactly *particlization* in a literal sense but equivalent to that. Instead of a continuous integral (Eq. ((2.110)) particles can be sampled from from the hypersurface in a discretized way according to particle's momentum through a sampler such as iSS [217], where the true sense of particlization is realized.

In our analysis and the results presented in the subsequent chapters, we limit ourselves to the study of the effect of shear viscosity on the observables under consideration. Therefore, we only need to include the dissipative corrections due to the shear viscosity (δf_{shear}) at freezeout. We use relativistic viscous hydrodynamics code MUSIC for our simulation, where the correction due to shear viscosity, at the freezeout, is implemented using the Grad's 14-moment approximation method in Eq. (2.113) [216, 220].

After the freezeout process, the resulting hadrons could be considered to stream freely to the detector. However, in the modern practice of simulating heavy-ion collision through hydrodynamic framework, instead of particlization from the freezeout hypersurface, people particlize the hypersurface at some temperature, called the *particlization temperature* [221] or the *switching temperature* (T_{sw}) [9]. Then to take into account further inelastic collisions, resonance decays and elastic interactions, known as *hadron re-scattering* or *hadron cascade*, the produced particles are fed into some hadronic transport models called *after burner*. The mean free path between the produced particles is quite large at this stage and the system is evolved through the Boltzman transport equation with collision terms. There exist several state-of-the-art models to take into account hadron rescattering effect or hadronic transport separately, e.g UrQMD [204, 205], AMPT [36, 37], SMASH [222] etc. for the particlized hadrons, to incorporate the hadron cascade until the kinetic freezeout before experimental detection of the particles.

In this chapter, we have shortly presented a complete picture of ultrarelativistic heavy-ion collision experiments covering the physics behind it, theoretical tools to study it and a description of the hydrodynamic framework which will be the main underlying theory for the results that will be presented in the following chapters. We conclude this chapter by briefly describing the simulation set-up for the results presented in this manuscript.

Simulation set-up

An ultrarelativistic heavy-ion collision comprises many stages and each of these stages can be well described by a certain model. As a result, nowadays it is a common practice in the heavy-ion community to use a hybrid-model-approach to simulate the hydrodynamic framework in heavy-ion collisions. In those approaches, different models corresponding to the different stages are clubbed together [223–225, 28] to properly simulate the collision e.g. initial condition + pre-equilibrium + hydrodynamic evolution + Cooper-Frye freezeout + hadronic transport ≡ IP-Glasma [94] / Glauber [143, 144] / TRENTo [197] + free streaming [28] / KOMPOST [209] + MUSIC [216] / VISH2+1 [226] / v-USPhydro [227] + iSS [217] + UrQMD [204] / SMASH [222]. However, the inclusion of all these intermediate stages is not always essential

---

[9] For many such calculations, people take the chemical freezeout tempearture as the particlization temperature T_{sw}

for describing the collective behavior of the final state particles i.e. collective flow, fluctuations and correlation between them.

In our hydrodynamic simulation of ultrarelativistic heavy-ion collision, we do not take into account the pre-equilibrium phase and the rescattering or hadronic transport through a hadronic cascade after-burner. While the effect of a pre-equillibirum phase could be negligible, there could be some effect in the final state from hadronic transport. However, in all our analysis presented in the subsequent chapters we will be mostly dealing with the charged hadrons, rather than any particular species of identified particles. Moreover, we will be always dealing with the event averaged quantity or sometimes the ratio of the observables. In such cases, the effect of hadronic transport is small. One can just follow hydrodynamic freezeout and Cooper-Frye prescription at the final freezeout. We take the initial condition at some thermalization time $\tau_0 \sim 0.6 fm/c$ as the input for hydrodynamic evolution and free streaming after the computation of thermal spectra or momentum distribution, following Cooper-Frye formula at the freezeout temperature (T_{fo}). However, we take into account the resonance decays. Our simulations are centered at the LHC and RHIC energies and all the results presented in the subsequent chapters are based on the boost-invariant 2+1D hydrodynamic simulation. The initial conditions for our simulation are generated from the Glauber model [144] or TRENTo [197] model and for the hydrodynamic simulation we use MUSIC [216, 220] hydro code. MUSIC is a simulation package which can simulate both 3+1D and 2+1D hydrodynamic evolution and it can also operate in different modes. In our calculation, MUSIC does everything from the start of the hydrodynamic evolution to the Cooper-Frye freezeout. We use the default values of the parameter set in the input file of MUSIC [228] unless otherwise stated for some specific studies. So, our simulation set-up reads Glauber / TRENTo + MUSIC.

Chapter 3

Collective flow and its fluctuations in heavy-ion collision

One of the most peculiar and spectacular phenomena observed in high energy heavy-ion collision, is the collective behavior of the final state particles produced in the collisions. This collective nature has been studied extensively and with immense dedication over the past 30 years in theory, as well as in the experiments. The most distinctive feature of this collective phenomena is the *collective flow*, specifically the *anisotropic flow* [40], which has been the central focus for these theoretical studies [40–43, 45, 44, 46, 188, 47, 23, 48–51, 229, 61, 62, 57, 7, 58] and experimental measurements [63, 52, 64, 53–56, 59, 60]. The measurement of the anisotropic flow was the first evidence of the thermalized QGP medium produced in heavy-ion collisions. The anisotropic flow originates from the spatial anisotropy in the initial state of the collision leading to a pressure gradient of the fireball, which then translates into the momentum anisotropy of the final state particles. Collective flow can be analyzed or measured through different approaches [41, 43, 230–239]. Another very interesting and exotic characteristic of heavy ion collisions is the *event-by-event fluctuations* of the collective flow of particles in the final state [74–76, 240, 77, 78, 241, 79, 80, 242, 243, 81, 244, 125, 245, 130, 246, 247, 82, 248, 83–86, 249, 87, 250], stemming from event-by-event fluctuations in the initial state [88, 251, 89–91, 252, 253, 92–94]. In this chapter, we will discuss the basic phenomenology of collective flow: its origin, relation to the final state, its centrality dependence, transverse momentum dependence and most importantly its event-by-event fluctuations.

3.1 Anisotropic flow : from spatial anisotropy to momentum anisotropy

In a heavy-ion collision, two colliding nuclei deposit energy in the overlap area, creating a transverse density profile at the initial state. The spatial distribution of this initial energy or entropy density in the transverse plane is not isotropic, which creates an anisotropy in the pressure of the fluid. As a result, there exist a pressure gradient ∇P on the QGP fireball created in the collision. This pressure is propagated to the final state through the viscous hydrodynamic evolution of the fireball, resulting in larger transverse momentum of the particles originating from part of the fluid having larger ∇P and vice versa. This leads to an anisotropy in the transverse momentum distribution of the final state particles and such flow of particles is known as *anisotropic flow* [40, 41, 43]. Thus anisotropic flow is a characteristic signature of the momentum space azimuthal anisotropy of final state particles. Fig. 3.1 shows the formation of the fireball in a non-central heavy-ion collision and the translation of spatial anisotropy or non-uniform pressure gradient in the initial state, to the azimuthal anisotropy of momentum distribution of final state particles. Before we move into the quantification of anisotropic flow, we need to have knowledge about the characteristic properties of the initial state.

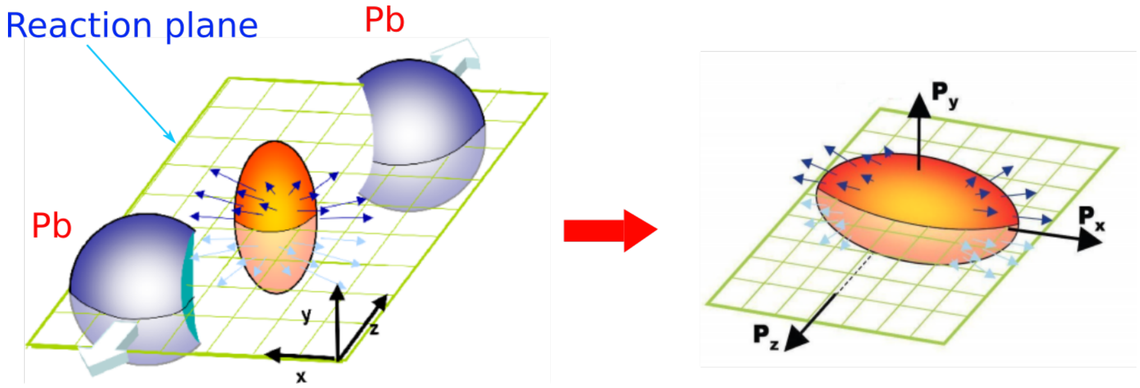

Fig. 3.1 Schematic representation of the almond shaped fireball formation in a non-central Pb+Pb collision and development of momentum anisotropy at the final state. Figure taken from [254] and BNL.

3.1.1 Initial state properties

The nature of the anisotropic flow is largely determined by the initial energy density or entropy density, shape and size of the overlap region at the initial state. In a non-central collision of two identical heavy-nuclei, the overlap area assumes an almond-like shape (Fig. 3.5) and the spatial anisotropy of entropy density distribution on the transverse plane (x,y) is characterized with respect to the reaction plane, spanned by the impact parameter and z-axis. Let us denote the initial energy density by $\varepsilon(x,y)$ and the entropy density by $s(x,y)$[1]. In this manuscript, we will always consider entropy density for our calculations and hydro inputs. The spatial anisotropy of the entropy density distribution can be identified in terms of standard eccentricity [255, 256],

$$\epsilon_{std}=\frac{\{y^2-x^2\}}{\{y^2+x^2\}}, \quad \text{with} \quad \{\dots\}=\int \dots\, s(x,y)\, dx\, dy\,. \tag{3.1}$$

---

[1] In general the initial energy density or entropy density are taken at the thermalization time or at the onset of hydrodynamics, denoted by $s_0(x,y) \equiv s(x,y,\tau_0)$ or $\varepsilon_0(x,y) \equiv \varepsilon(x,y,\tau_0)$.

In the initial years of flow study, it was believed that the standard eccentricity ϵ_{std} of the initial state leads to the formation of anisotropic flow, specifically *elliptic flow*, as we will explain later, originating from the ellipsoidal shape in non-central collisions. However, later it was seen that the elliptic flow did not disappear even in central collision especially in small collision systems (e.g. Cu+Cu), where ϵ_{std} is small. The reason behind this puzzling behavior was rooted in the fact that event-by-event fluctuations of the initial state geometry are important in central collision to explain the anisotropic flow [133]. This phenomena is even more significant in case of *triangular flow* [48]. In this regard, instead of the almond shaped overlap area of the two nuclei, the region formed by the participant nucleons in each event is more relevant. The plane formed by the principal axis of the *participant zone* and the z-axis is called the *participant plane* (Fig. 3.2) which is different than reaction plane and its orientation fluctuates event-by-event with respect to reaction plane. The spatial eccentricity which drives the elliptic flow is not the standard eccentricity, rather the eccentricity defined with respect to the participant plane, called *participant eccentricity* [48],

$$\epsilon_2^{part} = \frac{\sqrt{(\{y^2\} - \{x^2\})^2 + 4\{xy\}^2}}{\{y^2\} + \{x^2\}} \ . \tag{3.2}$$

It is defined with respect to a coordinate system where $\{x\} = 0$ and $\{y\} = 0$. In terms of polar coordinates (r, ϕ), the above equation takes the form,

$$\epsilon_2^{part} = \frac{\sqrt{\{r^2 \cos(2\phi)\}^2 + \{r^2 \sin(2\phi)\}^2}}{\{r^2\}} \ , \tag{3.3}$$

where ϕ denotes the azimuthal angle of the participant nucleon. The elliptic asymmetry of

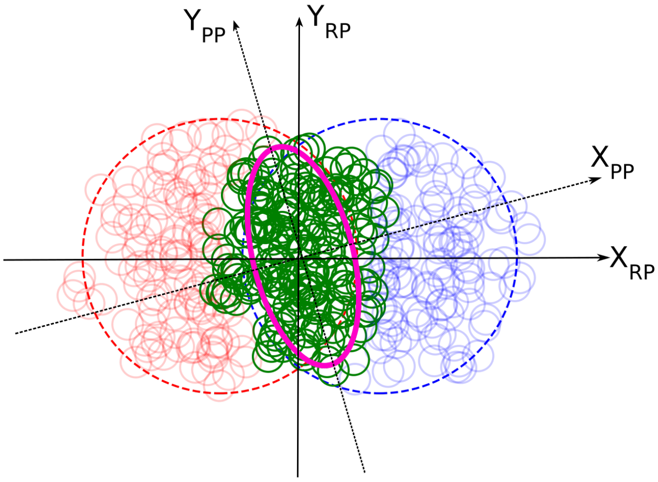

Fig. 3.2 Pictorial depiction of the reaction plane and participant plane in a collision. The area with green circles denote the *participant zone* whose principle axis is different than the principle axis of the almond shaped overlap area.

the participant zone, quantified by ϵ_2, drives the elliptic flow at the final state. Similarly, the triangular asymmetry, which is largely induced by fluctuations, leads to the triangular flow at the final state, for which analogously we can define *participant triangularity* [48, 251],

$$\epsilon_3^{part} = \frac{\sqrt{\{r^2\cos(3\phi)\}^2 + \{r^2\sin(3\phi)\}^2}}{\{r^2\}} . \tag{3.4}$$

In a generalized way, the eccentricity harmonic coefficients associated with the spatial anisotropy of the participant region can be formulated through the cumulant expansion method [90, 92],

$$\epsilon_{m,n}\, e^{\Phi_{m,n}} = -\frac{\{r^m e^{in\phi}\}}{\{r^m\}}, \tag{3.5}$$

which accounts for different order moments of r associated with n^{th} harmonic. In this definition, ϵ_2=$\epsilon_{2,2}$ and ϵ_3=$\epsilon_{2,3}$. However, it has been found that using the moment of r^3 works as a better estimator than r^2 for the triangular flow [92], so that ϵ_3=$\epsilon_{3,3}$. In general, the conventional eccentricity coefficients are given by [256, 7],

$$\epsilon_1\, e^{i\Phi_1} = -\frac{\{r^3 e^{i\phi_1}\}}{\{r^3\}} \quad \text{and} \quad \epsilon_n\, e^{in\Phi_n} = -\frac{\{r^n e^{in\phi}\}}{\{r^n\}} \quad \text{for} \quad n > 1, \tag{3.6}$$

where ϵ_1 is known as *dipole asymmetry* [44], which turns out to be responsible for the *directed flow*, ϵ_2 is the *quadrupole asymmetry* or ellipticity, ϵ_3 is the *octupole asymmetry* or triangularity of the initial transverse density profile and so on. Φ_n is the n^{th} order participant plane angle or orientation angle.

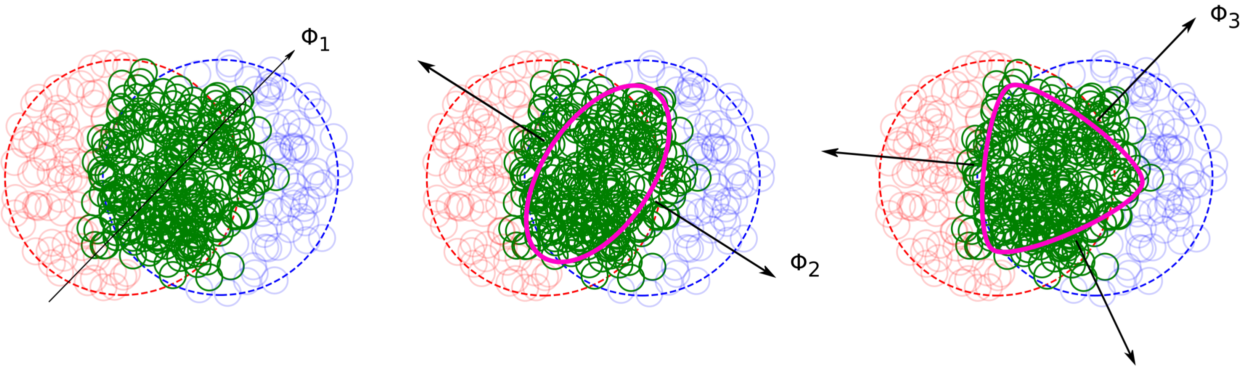

Fig. 3.3 Pictorial representation of the participant eccentricity harmonics. The principal axes or participant plane angles corresponding to the dipole (left), elliptic (middle) and triangular asymmetry (right) are shown.

The total entropy and energy per unit rapidity at the initial state is given by,

$$S \propto \int s(r,\phi)\, r\, dr\, d\phi \quad \text{and} \quad E_i \propto \int \varepsilon(r,\phi)\, r\, dr\, d\phi \ , \tag{3.7}$$

and the transverse size of the fireball is quantified by the RMS radius,

$$R^2 = \frac{\int r^2\, s(r,\phi)\; r\, dr\, d\phi}{\int s(r,\phi)\; r\, dr\, d\phi}\ . \tag{3.8}$$

3.1.2 Particle spectra

To make a quantitative description of the anisotropic flow, first we need to discuss the particle spectra, as it includes a collective effect of all the particles in the final state. At the end of the hydrodynamic evolution, from the freeze-out hypersurface, we obtain the transverse momentum (p_T) distribution of the particles through Cooper-Frye freezeout method. In principle, the distribution could be obtained for individual particle species (identified particles), but in this document we will only consider the charged particles ($\pi^+, \pi^-, K^+, K^-, p, \bar{p}$). The distribution is given by,

$$f(p_T,\phi) = \frac{dN}{p_T dp_T d\phi}, \tag{3.9}$$

which serves as the probability distribution for the particles carrying transverse momentum $\vec{p_T}$, and ϕ ($\equiv \phi_p$) is the azimuthal angle corresponding to the transverse momentum p_T. The charged particle spectra from ALICE [257] and ATLAS [258] collaboration for Pb+Pb collision at $\sqrt{s_{NN}}$=5.02 TeV, are shown in Fig. 3.4. In experiments, the charged particle spectra are calculated in pseudorapidity bins[2] i.e. $\frac{dN}{p_T dp_T d\phi d\eta}$, whereas in our hydro-calculation we use rapidity bins for the spectra i.e. $\frac{dN}{p_T dp_T d\phi dy}$. For the charged particle spectra, these two have similar meaning and the difference is negligible. However, for the identified particle spectra these two differ because y depends on the mass of the particle whereas η does not. For this reason, in experiments the identified particle spectra are usually measured in rapidity bins [259, 260].

The charged particle spectra can be used to calculate the total charged particle multiplicity in an event,

$$N_{ch} \equiv N = \int p_T dp_T d\phi f(p_T,\phi) = \int_{p_{min}}^{p_{max}} dp_T\, \frac{dN}{dp_T}. \tag{3.10}$$

Another very important collective observable is the mean transverse momentum per particle in an event, which we denote as $[p_T]$ and it is defined as,

$$[p_T] = \frac{1}{N}\int_{p_{min}}^{p_{max}} dp_T\; p_T\, \frac{dN}{dp_T}\ . \tag{3.11}$$

Event-by-event fluctuations of $[p_T]$ are also of great importance and contain interesting information of the QGP, which we will study in detail in the next chapter.

---

[2] Although in Eq. (3.9) we present the two dimensional spectra or just the transverse momentum spectra, which is relevant for boost invariant calculations and description of anisotropic flow, in practice we need to consider the full phase-space (y or η, p_T ϕ) or the full spectra obtained from the freeze-out hypersurface i.e. the spectra is calculated in either rapidity or pseudo-rapidity bins

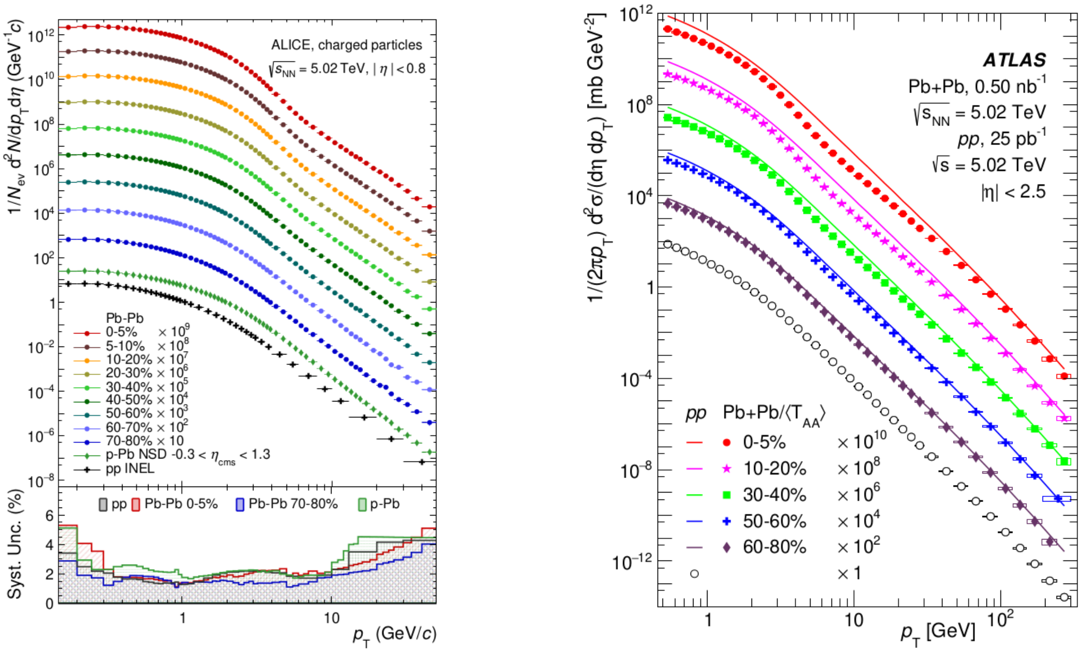

Fig. 3.4 Event-averaged charged-particle multiplicity spectra measured by the ALICE (left) and ATLAS (right) collaboration for Pb+Pb collision at 5.02 TeV is shown. Figure taken from [257] and [258] respectively.

Radial flow

In the present context, it will be useful to mention another type of flow, called the *radial flow*, which does not originate from the anisotropy of the initial density profile, but is due to rotationally symmetric collective transverse fluid motion. In the case of rotational symmetric and baryonless fluid, the transverse momentum distribution at zero rapidity ($p_z = 0$), for any particle species is given by the Cooper-Frye formula [20],

$$\frac{dN}{2\pi p_T dp_T} \propto \exp\left(-\frac{E^*}{T_{fo}}\right) = \exp\left(-\frac{p^\mu u_\mu}{T_{fo}}\right) = \exp\left(-\frac{m_T u_0 + p_T v}{T_{fo}}\right), \tag{3.12}$$

where we consider the Maxwell-Boltzman statistics for simplicity. E^* is the energy of the particles in the lab frame, v is the maximum transverse velocity of the fluid at zero-rapidity according to Bjorken scaling and m_T is the transverse mass of the particles eventually depicting the energy of the particles in fluid rest frame with $p_z = 0$. If the fluid is at rest in lab frame, $v = 0$ and $u_0 = 1$, which makes the spectra exponential in m_T with slope $1/T_{fo}$ i.e. $\propto \exp(\frac{-m_T}{T_{fo}})$. This means that the particle-spectra are scaled according to the transverse mass of each species but having the same slope $1/T_{fo}$. This describes only the thermal motion of the particles. However, if the fluid moves with a transverse velocity v, then on top of the thermal motion, the particles have a collective velocity (the fluid velocity) v, which increases the overall kinetic energy of the particles. Due to the collective motion, the heavier particles attain larger kinetic energy and this breaks the m_T-scaling of the spectra, because for a given m_T, heavier particles have smaller p_T. As a result, the slope of the m_T-spectra becomes flatter for heavier particles [261, 262, 46]. Such transverse collective flow is known as the radial flow, named because of the radial or axial symmetry.

3.1.3 Flow harmonics

In section 3.1.2, we have identified the magnitude of the transverse momentum in terms of mean transverse momentum per particle in an event $[p_T]$. Now we want to characterize the directions or the azimuths associated with p_T, as the anisotropic flow originates from the anisotropy of the azimuthal distribution of the particles. The azimuthal distribution of the particles is quantified event-by-event in terms of Fourier expansion with respect to the azimuthal angle [41, 43, 5, 125, 128],

$$\frac{dN}{p_T dp_T d\phi} = \frac{dN}{2\pi p_T dp_T}\left(1 + 2\sum_{n=1}^{\infty} V_n(p_T)e^{-in\phi}\right), \tag{3.13}$$

where the Fourier coefficients V_n are known as n^{th} order *harmonic flow coefficients*, which depend on p_T i.e. $V_n = V_n(p_T)$. It could be decomposed as $V_n(p_T) = v_n(p_T)e^{in\Psi_n(p_T)}$ such that $V_n(p_T)$ is interpreted as *flow vector* with *flow magnitude* $v_n(p_T)$ and *flow angle* $\Psi_n(p_T)$[3]. The angle ϕ is the azimuthal angle of the particles and Ψ_n is known as the *event plane angle* [256, 7, 8] which serves as a proxy or an estimate of the reaction plane (orientation of which is not known experimentally) in each event and could be determined independently for each harmonic of anisotropic flow.

Differential and integrated flow

The harmonic flow coefficient in Eq. (3.13), $V_n(p_T)$ is a function of the transverse momentum p_T in an event and it also depends on the pseudo-rapidity(η) i.e. $V_n(p_T, \eta)$, when full three dimensional spectra are considered. In that case, it is called p_T-differential or η-differential flow or in general *differential flow*. To calculate the flow harmonics over the whole phase space in the transverse plane, $V_n(p_T)$ should be integrated with respect to the distribution,

$$V_n = \frac{1}{N}\int_{p_{min}}^{p_{max}} dp_T\ V_n(p_T)\ \frac{dN}{dp_T}, \tag{3.14}$$

where V_n is known as *integrated flow* or specifically p_T-integrated flow in an event. In Fig. 3.8, differential and integrated elliptic and triangular flow for various centralities in Pb+Pb collision have been shown.

---

[3] Please note that v_n and Ψ_n depend on both p_T and η i.e. $v_n = v_n(p_T, \eta)$ and $\Psi_n = \Psi_n(p_T, \eta)$, if instead of only on the transverse plane, we consider full 3D distribution, $\frac{dN}{p_T dp_T d\phi d\eta}$

3.1.4 Different types of flow and their relation to initial anisotropy

For different order n, we get different type of flow e.g. v_2 is called *elliptic flow* , v_3 is called *triangular flow*, v_4 is known as *quadrangular flow*, v_5 is called *pentagonal flow* etc, which are driven by participant eccentricities ϵ_n at the initial state. For $n = 1$, the flow is known as *directed flow* v_1 which at the mid-rapidity is driven by dipole asymmetry [90] ϵ_1 of the initial state.

Elliptic flow

Elliptic flow, originally proposed by J-Y. Ollitrault [40], is identified as one of the most peculiar and significant signature of the collective flow [42, 43, 46, 44]. It originates mainly due to the ellipsoidal geometry at the initial state of the collision or quadrupole asymmetry of the initial density profile. If the fireball is elliptic shaped, then it develops a pressure gradients ∇P which results in larger transverse momentum of the particles that are emitted in the direction of reaction plane because of the larger fluid velocity in that direction (larger pressure gradient results in larger force : $\vec{F} = -\nabla P$), and smaller momentum for the particles which are emitted in the direction perpendicular to the reaction plane (Fig. 3.5). This azimuthal anisotropy of the transverse momentum is reflected through the elliptic flow of particles and identified by the harmonic coefficient v_2. In non-central collision, the elliptic flow v_2 is mainly due to the elliptic geometry of the initial state, which is characterized by the eccentricity or ellipticity ϵ_2 (Eq. (3.6)). There exist direct phenomenological relation between the two [48, 92],

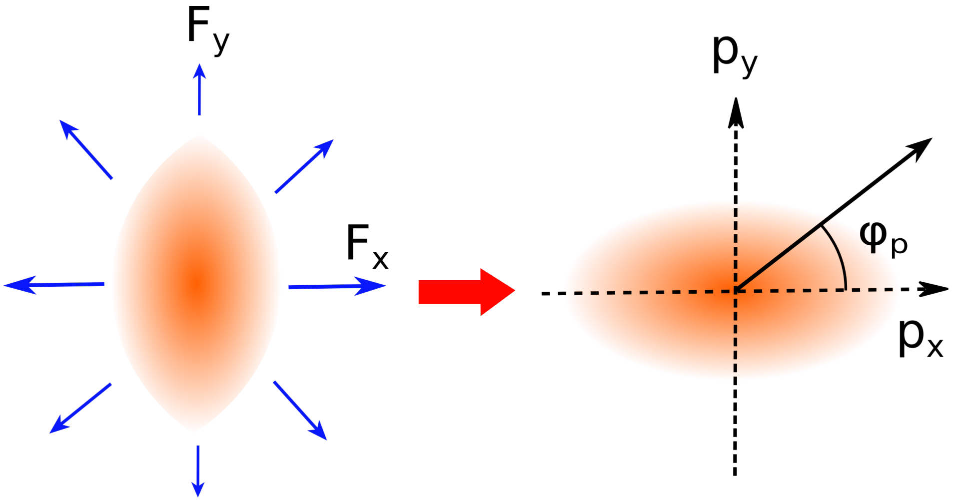

Fig. 3.5 Schematic representation of the origin of elliptic flow in a non central heavy-ion collision. The left hand side shows the formation of almond shaped or elliptic geometry at the initial state, creating a pressure gradient and hence an anisotropic outward force. The right hand side shows the development of the momentum anisotropy at the final state due to the pressure gradient, leading to the elliptic flow of particles.

$$v_2 e^{2i\Psi_2} = k_2\, \epsilon_2\, e^{2i\Phi_2} \qquad \Rightarrow \qquad v_2 \simeq k_2\, \epsilon_2\,, \tag{3.15}$$

where it is assumed that the event plane Ψ_2 approximately coincides with the participant plane Φ_2. The coefficient k_2 is the *hydrodynamic response coefficient*, which depends on the properties of the QGP medium.

However, in central collisions (say, $0-5$ %), in addition to the elliptic geometry, event-by-event fluctuations of the initial state plays a major role in contributing to the quadrupole asymmetry ϵ_2, generating elliptic flow in central collision, and this effect become dominant in ultracentral collisions ($0-1$ %). This might not be obvious at first instance when one thinks of v_2 in a single event, however in practice only the event-averaged quantities are important, where fluctuations and its contributions play a crucial role. Generally in central collision, event-by-event fluctuations of ϵ_2, fluctuations of Ψ_2 around Φ_2 and even fluctuations of v_2 for a given ε_2, all contribute to the event averaged v_2. We will explain this fact while discussing experimental method for the measurement of v_2. The scatter plot between v_2^2 and ϵ_2^2 for central and semi-central Pb+Pb collision at 5.02 TeV are shown in Fig. 3.6. As discussed, the correlation is stronger in case of semi-central collision ($30-40\%$) where elliptic geometry of the overlap are dominates, whereas the central collision shows significant effect of event-by-event fluctuations.

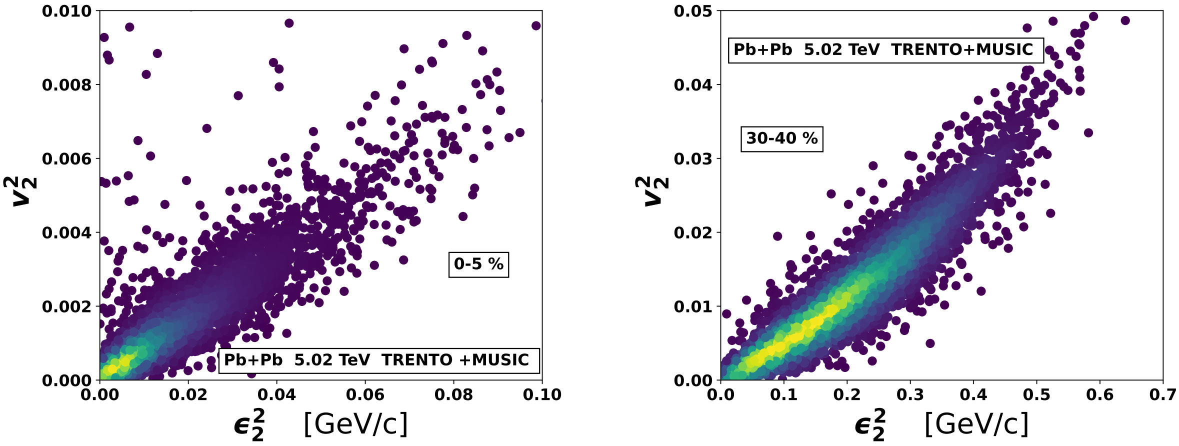

Fig. 3.6 Scatter plot between v_2^2 and ϵ_2^2 for $0-5\%$ (left) and $30-40\%$ (right) centrality in Pb+Pb collision at 5.02 TeV with TRENTO initial condition.

Triangular flow

Similar to the elliptic flow, the triangular flow v_3 originates from the third order participant eccentricity or triangualrity ϵ_3 [48, 11], defined in (Eq. (3.6)). It also follows the approximated phenomenological relation,

$$v_3 \simeq k_3\, \epsilon_3, \tag{3.16}$$

where k_3 is the hydro-response coefficient for the triangular flow. The value of the response

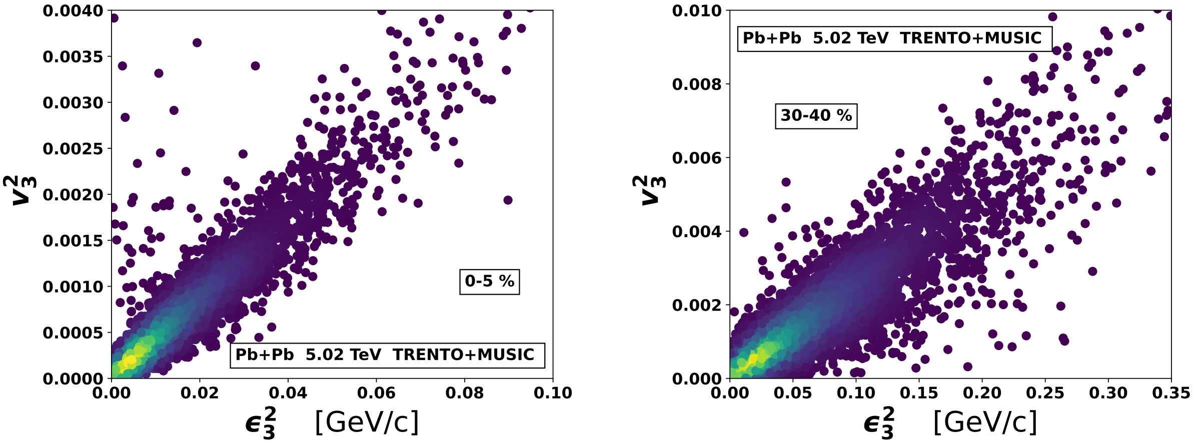

Fig. 3.7 Scatter plot between v_3^2 and ϵ_3^2 for $0-5\%$ (left) and $30-40\%$ (right) centrality in Pb+Pb collision at 5.02 TeV with TRENTO initial condition.

coefficients k_n can be estimated using the linear relationship between flow and eccentricity [92],

$$v_n e^{in\Psi_n} = k_n\, \epsilon_n\, e^{in\Phi_n} \qquad \Rightarrow \qquad k_n = \frac{\langle v_n\, \epsilon_n \cos(n(\Psi_n - \Phi_n))\rangle}{\langle \epsilon_n^2 \rangle}\,, \tag{3.17}$$

where the angular bracket $\langle \dots \rangle$ denotes the average over all events[4]. Unlike elliptic flow, the triangularity or octupole asymmetry ϵ_3, driving the triangular flow v_3, is largely dominated by the contribution from event-by-event fluctuations of the initial density profile, even in non-central collision and especially in central collision, as depicted in Fig. 3.7. Fluctuations at the initial state are more important for the triangular flow.

Quadrangular and pentagonal flow

The fourth order ($n = 4$) harmonic flow is called quadrangular flow, v_4. Similar to the elliptic and triangular flow one could expect that v_4 also originates from fourth order harmonic eccentricity of the initial state, ϵ_4. However, it has been observed that the estimator is only valid for central collision but fails to predict v_4 for peripheral events. This happens because in the peripheral collisions, due to the elliptic shape of the participant area, the second order moment ϵ_2 becomes very dominant or much larger in comparison to higher order moments such as ϵ_4 [92]. As a result, there exist a possibility of non-linear contributions from lower order eccentricities to the flow harmonic v_4. The first choice of such contribution would be ϵ_2^2 by symmetry[5], so that the actual predictor for v_4 is given by,

$$v_4 e^{4i\Psi_4} = k_4\, \epsilon_4\, e^{4i\Phi_4} + k_4'\, \epsilon_2^2\, e^{4i\Phi_2}, \tag{3.18}$$

---

[4] It should be noted that Eq. (3.15) and Eq. (3.16) only imply a strong correlation (linear) between v_n and ϵ_n for $n = 2, 3$. The ratio v_n/ϵ_n (even if they are event averaged values) should never be taken as an estimation of k_n which should always be estimated by Eq. (3.17).

[5] Here we mean rotational symmetry i.e. the quantity $\langle V_4(\epsilon_n\, e^{-in\Phi_n})^m \rangle$ must be invariant under rotation.

which serves as a very good estimator for all centralities. For central collisions, both ϵ_4 and ϵ_2 are driven by fluctuations and so they are small. As a result, the contribution of ϵ_4 dominates in terms of eccentricities.

For $n = 5$, the flow is is called pentagonal flow, v_5 which also assumes non-linear contribution from the initial state anisotropies, even for central collision. In addition to ϵ_5, by symmetry the non-linear contribution comes from $\epsilon_2\epsilon_3$ and the estimator for v_5 reads [92],

$$v_5 e^{5i\Psi_5} = k_5\, \epsilon_5\, e^{5i\Phi_5} + k_5'\, \epsilon_2\, e^{2i\Phi_2}\, \epsilon_3\, e^{3i\Phi_3}, \tag{3.19}$$

which serves as a very good predictor for v_5 for all centralities.

Directed flow

For $n = 1$ the flow is known as directed flow v_1 which could be separated into two parts depending on rapidity of the particles y : *rapidity-odd* directed flow and *rapidity-even* directed flow[263]. The rapidity odd v_1 is the usual directed flow [264–266] which largely depends on the space-time rapidity profile (η_s) of the fireball, driven by the tilt of the fireball at the initial phase of the evolution [50, 267–269]. On the other hand, the rapidity-even v_1, which shows a little dependence on y, is interesting at the mid-rapidity and it originates from the dipole asymmetry of the initial transverse density profile, characterized by ϵ_1 [90].

Event-by-event fluctuations of the initial geometry break the symmetry of the transverse density profile and make it steepest in a particular direction, which is quantified as the dipole asymmetry [90, 270],

$$\epsilon_1\, e^{i\Phi_1} = -\frac{\{r^3 e^{i\phi_1}\}}{\{r^3\}}, \tag{3.20}$$

contributing to v_1 in a similar manner as fluctuation-induced quadrupole asymmetry ϵ_2 contributes to v_2 and octupole asymmetry ϵ_3 contributes to v_3. The dipole asymmetry creates a gradient in the transverse density profile, resulting in largest fluid velocity along the direction of the steepest gradient having azimuth Φ_1. As a result, the particles with larger p_T are emitted along the direction of Φ_1 and the small-p_T particles are emitted in the opposite direction [270]. Due to the conservation of total transverse momentum, v_1 is positive for high-p_T particles and negative for small-p_T particles giving rise to a specific pattern for the p_T dependence of v_1 [90, 270].

3.1.5 Methods of flow analysis

Anisotropic flow is originally defined as the azimuthal correlation of the outgoing particles with the reaction plane. But experimentally the reaction plane orientation cannot be measured. That is why the flow is represented in terms of event plane angle which we also call the flow angle. If we drop the p_T dependence for a moment or just consider the integrated flow, then we can write only the azimuthal distribution of the particles from Eq. (3.13) as,

$$f(\phi) = \frac{dN}{d\phi} \propto \left[1 + 2\sum_{n=1}^{\infty} v_n e^{in(\phi - \Psi_n)} \right], \tag{3.21}$$

where ϕ is the azimuthal angle of the particle and Ψ_n is the event-plane angle. Then the flow harmonics v_n can be estimated as [43, 230],

$$v_n = \langle \cos[n(\phi - \Psi_n)] \rangle, \tag{3.22}$$

where the angular bracket $\langle \dots \rangle$ denotes the average over all particles and over all events. The sine term does not appear because of the reflection symmetry and it cancels out when averaged over events. This method of estimating flow harmonics is called the *event-plane method* which is obsolete and no longer in use. Modern experimental methods of flow analysis in heavy-ion collision use the *cumulant method* involving multi-particle azimuthal correlations. Below we discuss the theoretical background and experimental implementation of the method [230, 231, 235].

Cumulant method: multi-particle correlations

As the actual orientation of the reaction plane is unknown in experiments, instead of considering a single particle, if we consider the relative azimuthal angles between the outgoing particles, then it could capture the correlation with the reaction plane and eventually provide an estimate of the flow [230, 231]. The simplest case would be a two-particle azimuthal correlation which could be expressed as,

$$\langle \cos[n(\phi_1 - \phi_2)] \rangle \equiv \langle e^{in(\phi_1 - \phi_2)} \rangle, \tag{3.23}$$

which comes from the two-particle azimuthal distribution in an event $f(\phi_1, \phi_2) \equiv \frac{dN}{d\phi_1 d\phi_2}$ and the angular bracket has the similar meaning as before i.e. first an average over all the pairs of particle in an event and then the average over all the events. The two-particle distribution in an event can be decomposed as,

$$f(\phi_1, \phi_2) = f(\phi_1) f(\phi_2) + f_c(\phi_1, \phi_2), \tag{3.24}$$

where the first term on the r.h.s. represents the product of the uncorrelated distributions and the second term denotes the correlated distribution. Accordingly, Eq. (3.23) can be decomposed as,

$$\langle e^{in(\phi_1 - \phi_2)} \rangle = \langle e^{in\phi_1} \rangle \langle e^{in\phi_2} \rangle + \langle\!\langle e^{in(\phi_1 - \phi_2)} \rangle\!\rangle \ . \tag{3.25}$$

The terms $\langle e^{in\phi_1} \rangle$ and $\langle e^{in\phi_2} \rangle$ vanishes because the angles ϕ_1 and ϕ_2 are measured in the laboratory frame, assuming that the detector is a ‘perfect detector’ covering the entire acceptance region[6]. The second term $\langle\langle e^{in(\phi_1-\phi_2)}\rangle\rangle$ represents the *genuine* two-particle correlation which can include contribution from anisotropic flow as well as from other sources e.g. due to global momentum conservation, resonance decay (in which the decay products are correlated), final state coulomb, strong or quantum interactions etc. [271, 272], called the *non-flow correlations* or 'direct' correlations. If the source was isotropic, $\langle\langle e^{in(\phi_1-\phi_2)}\rangle\rangle$ would represent only the non-flow correlations.

The quantity $\langle\langle e^{in(\phi_1-\phi_2)}\rangle\rangle$ is known as *cumulant* or specifically *two-particle cumulant*, which can be obtained using a generalized cumulant expansion method from the cumulant generating function [230, 231] and written as,

$$c_n\{2\} \equiv \langle\langle e^{in(\phi_1-\phi_2)}\rangle\rangle \ . \tag{3.26}$$

The contribution of the flow to the two-particle cumulant is given by [231],

$$v_n\{2\}^2 = c_n\{2\} \qquad \Rightarrow \qquad v_n\{2\} = \sqrt{c_n\{2\}}, \tag{3.27}$$

where $v_n\{2\}$ represents the n^{th} order harmonic flow estimated from two-particle cumulant. The advantage of this method lies in its ability to reduce the non-flow correlation, which is achieved by constructing higher order cumulants or multi-particle cumulants. For example, similar to Eq. (3.23), if we consider four particle azimuthal correlation, then corresponding four-particle cumulant could be written as [230, 231],

$$\begin{aligned}
c_n\{4\} &\equiv \langle\langle e^{in(\phi_1+\phi_2-\phi_3-\phi_4)}\rangle\rangle \\
&= \langle e^{in(\phi_1+\phi_2-\phi_3-\phi_4)}\rangle - \langle e^{in(\phi_1-\phi_3)}\rangle\langle e^{in(\phi_2-\phi_4)}\rangle - \langle e^{in(\phi_1-\phi_4)}\rangle\langle e^{in(\phi_2-\phi_3)}\rangle \\
&= \langle e^{in(\phi_1+\phi_2-\phi_3-\phi_4)}\rangle - 2\langle e^{in(\phi_1-\phi_3)}\rangle^2 \ ,
\end{aligned} \tag{3.28}$$

where the simplification at the last step is due to the symmetry between ϕ_1 and ϕ_2. Please note, in the final expression of $c_n\{4\}$ on the r.h.s, both the first and second term include two-particle non-flow (direct) correlation which is eliminated by the subtraction. Thus by constructing higher order cumulants, we can eliminate the non-flow correlation of sub-leading orders. Similarly one can construct six-particle cumulant $c_n\{6\}$ and corresponding contributions of the flow are given by[231],

$$\begin{aligned}
-v_n\{4\}^4 &= c_n\{4\} \qquad \Rightarrow \qquad v_n\{4\} = (-c_n\{4\})^{1/4}, \\
\text{and} \quad 4v_n\{6\}^6 &= c_n\{6\} \qquad \Rightarrow \qquad v_n\{6\} = (\frac{c_n\{6\}}{4})^{1/6},
\end{aligned} \tag{3.29}$$

where $v_n\{4\}$ and $v_n\{6\}$ represent the flow estimated from four-particle and six-particle cumulants respectively[7].

---

[6] As the azimuths of the particles are randomly oriented, average over all the events give zero

[7] Please note, as 2-particle estimation of flow is non-flow contaminated, it is always larger than 4- or 6-particle estimation. In general the trend follows: $v_n\{2\} > v_n\{4\} \simeq v_n\{6\}$.

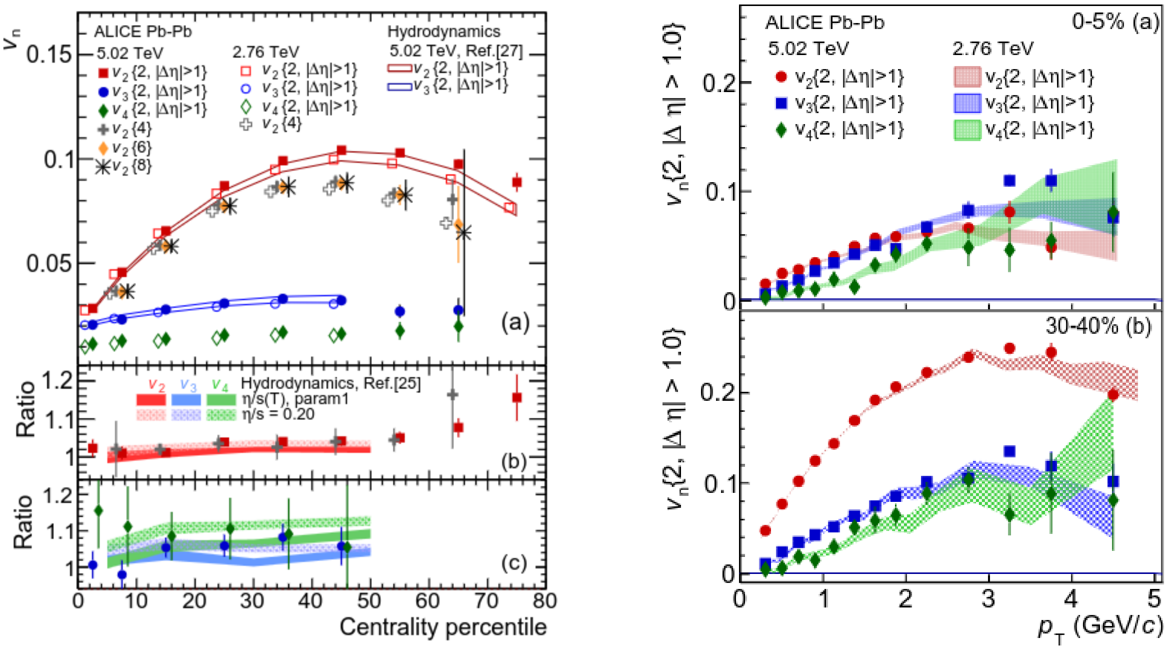

Fig. 3.8 Measurement of differential and integrated flow using multi-particle cumulant method. The left hand side shows the centrality dependence of the integrated flow cumulants while the right hand side shows differential flow cumulants corresponding to different order harmonics. Figure taken from [59].

Experimental method : Q-vector

Experimentally, the above mentioned cumulant method is used for the estimation of flow harmonics, but in a slightly different way. In experiments, the cumulants are expressed in terms of the moments of the flow vector Q_n, called $Q-vector$, in an event, which is defined as [235],

$$Q_n \equiv \sum_{i=1}^{M} e^{in\phi_i} , \tag{3.30}$$

where M is the number of particles in the event, used for the analysis. This way, the method is not biased by the interference of various harmonics, does not involve the approximation as used in formalism involving the generating function [230] and can also disentangle the detector effect more efficiently; ideal for experimental realization. As in this approach, the cumulants are calculated without any approximation, directly from the data using the $Q-vector$, it is sometimes referred as the *direct cumulant* or *Q-cumulant* method [235] which is the experimental implementation of the cumulant method discussed just before.

In the experimental method, first the *average* two-particle or four-particle azimuthal correlation are found in a *single event*, defined as,

$$
\begin{aligned}
\overline{2} = \overline{e^{in(\phi_1-\phi_2)}} &= \frac{1}{M(M-1)} \sum_{i\neq j=1}^{M} e^{in(\phi_i-\phi_j)}, \\
\overline{4} = \overline{e^{in(\phi_1+\phi_2-\phi_3-\phi_4)}} &= \frac{1}{M(M-1)(M-2)(M-3)} \sum_{i\neq j\neq k\neq l=1}^{M} e^{in(\phi_i+\phi_j-\phi_k-\phi_l)},
\end{aligned}
\tag{3.31}
$$

where the unequal signs between the sum indices denote the removal of self-correlation between the particles and the factor sitting before the sum could be expressed for general k-particle correlator as $\frac{(M-k)!}{M!}$. Then the above correlators are expressed in terms of the moments of the magnitude of Q_n-vectors. For example, in case of 2-particle correlator,

$$
|Q_n|^2 = Q_n Q_n^* = \sum_{i,j=1}^{M} e^{in(\phi_i-\phi_j)} = M + \sum_{i\neq j}^{M} e^{in(\phi_i-\phi_j)}
\tag{3.32}
$$

and then using Eq. (3.31), we can write,

$$
\overline{2} = \frac{|Q_n|^2 - M}{M(M-1)} \; .
\tag{3.33}
$$

Then the average over all events [235] is found, which gives the two-particle cumulant,

$$
c_n\{2\} \equiv \langle \cos n(\phi_1 - \phi_2) \rangle = \langle \frac{1}{M(M-1)} \sum_{i\neq j=1}^{M} e^{in(\phi_i-\phi_j)} \rangle = \langle \overline{2} \rangle \; ,
\tag{3.34}
$$

from which flow harmonics $v_n\{2\}$ can be estimated using Eq. (3.27) and which would be of course non-flow contaminated. Please note, here the angular bracket denotes only average over events. Similarly, the fourth moment of the magnitude of Q_n can be written as,

$$
|Q_n|^4 = Q_n Q_n Q_n^* Q_n^* = \sum_{i,j,k,l=1}^{M} e^{in(\phi_i+\phi_j-\phi_k-\phi_l)} \; ,
\tag{3.35}
$$

which could involve four different cases for the indices i, j, k and l : i) all are different (4-particle correlator in Eq. (3.31)), ii) three are different iii) two are different and iv) all are same. Expanding all the cases one can obtain [235],

$$
\overline{4} = \frac{|Q_n|^4 + |Q_{2n}|^2 - 2Re[Q_{2n} Q_n^* Q_n^*] - 4(M-2)|Q_n|^2 + 2M(M-3)}{M(M-1)(M-2)(M-3)} \; .
\tag{3.36}
$$

Then after taking the average over all events i.e. $\langle \overline{4} \rangle$, the four-particle cumulant can be found following Eq. (3.28),

$$
c_n\{4\} = \langle \overline{4} \rangle - 2\langle \overline{2} \rangle^2 \; .
\tag{3.37}
$$

and the six-particle cumulant can be obtained in a similar way as [230, 235],

$$c_n\{6\} = \langle\overline{6}\rangle - 9\langle\overline{2}\rangle\langle\overline{4}\rangle + 12\langle\overline{2}\rangle^3. \tag{3.38}$$

Finally, the flow harmonics $v_n\{4\}$ and $v_n\{6\}$ can be obtained using Eq. (3.29), which are non-flow subtracted.

In the present context, let us mention that the $2k$-particle cumulants $c_n\{2k\}$ discussed above, can be expressed as the event average of different powers of the magnitude of harmonic flow v_n. Let us consider the 2-particle cumulant from Eq.(3.34) and Eq. (3.31),

$$c_n\{2\} = \langle\overline{2}\rangle = \langle \frac{1}{M(M-1)} \sum_{i\neq j=1}^{M} e^{in(\phi_i-\phi_j)} \rangle. \tag{3.39}$$

Using the definition of flow vector $V_n = v_n e^{in\Psi_n}$ in an event as described in Eq. (3.21), we can write the quantity within bracket on the r.h.s. of the above equation, as a *scalar product* of two flow-vectors in an event,

$$\frac{1}{M(M-1)} \sum_{i\neq j=1}^{M} e^{in(\phi_i-\phi_j)} = V_n V_n^* = v_n^2, \tag{3.40}$$

where the self-correlation between the particles have been omitted while calculating the scalar product. Then from Eq. (3.39) we can write,

$$c_n\{2\} = \langle v_n^2 \rangle \ . \tag{3.41}$$

Similarly, using Eqs. (3.37) and (3.38) the 4-particle and 6-particle cumulants can be expressed as [273],

$$\begin{aligned} & c_n\{4\} = \langle v_n^4\rangle - 2\langle v_n^2\rangle^2, \\ \text{and} \qquad & c_n\{6\} = \langle v_n^6\rangle - 9\langle v_n^2\rangle\langle v_n^4\rangle + 12\langle v_n^2\rangle^3 \ . \end{aligned} \tag{3.42}$$

Similar methods could be applied to obtain the differential flow harmonics [231, 235]. Fig. 3.8 shows the measured differential and integrated flow using cumulant method.

Flow analysis in our simulation:

Let us also mention the approach we use for flow analysis in simulation, based on which we present results in the current and in the subsequent chapters. In our simulation set-up which uses MUSIC [216] hydro code, we obtain the spectra $dN/2\pi p_T dp_T dy$ and the differential harmonic flow vectors $V_n(p_T)$ event-by-event as a function of p_T. Then in each event we can calculate the integrated flow vector V_n, mean transverse momentum per particle $[p_T]$ and number of charged particle N_{ch} using Eqs.(3.14), (3.11) and (3.10) respectively. Then the event averaged flow is calculated using,

$$v_n\{2\} = \sqrt{\langle V_n V_n^* \rangle} = \sqrt{\langle v_n^2 \rangle}, \tag{3.43}$$

where the angular bracket denotes the average over all events.

3.2 Fluctuations of harmonic flow

One of the most exotic and distinctive features of the anisotropic flow is the event-by-event fluctuations which have served as a phenomenon of sheer interest in both theoretical [74–76, 240, 77, 78, 241, 79, 80, 242, 243, 81, 244, 125, 245, 130, 246, 247] and experimental [82–86, 249, 87, 250] studies. In these studies, a wide range of aspects and potential probes of the flow-fluctuation have been explored. The primary reason behind the flow-fluctuations are the event-by-event fluctuations of the initial state [88, 251, 89–91, 252, 253, 92–94] (as shown in Fig. 3.9), providing the source of the anisotropic flow in each event, along with the other sources e.g. thermal fluctuations. Fluctuations in the initial state can originate from different sources e.g. geometry fluctuations or shape fluctuations, quantum fluctuations in the overlap of the wavefunctions of the colliding nucleons etc. Here our primary focus is to discuss event-by-event fluctuations of the harmonic flow coefficients v_n and possible effects of fluctuations in terms of physical observables which could potentially probe the fluctuations. One way to probe such flow fluctuations is to study the ratio of the multi-particle cumulants which in turn could probe the initial state fluctuations in terms of eccentricity cumulants [274, 55]. Another very interesting observable which is our primary focus in this chapter, to study flow-fluctuation, is the *flow-factorization breaking coefficient* or simply *factorization-breaking coefficient* [240, 81, 244, 125, 245, 130], accounting for the breaking of the factorization between the flow harmonics in two different kinematic bins (p_T or η bins), which we discuss below.

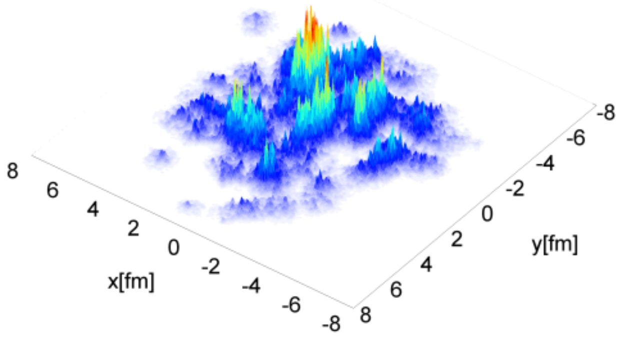

Fig. 3.9 Pictorial representation of fluctuations at the initial state, generated from the MC Glauber model. Figure taken from [94].

3.2.1 Factorization-breaking coefficients

As discussed in the previous sections, the harmonic flow coefficients v_n can be measured through two-particle correlations at the lowest order, which eventually measure the flow harmonic square v_n^2 as given in Eq. (3.27). If the two particles are measured in two different p_T bins p_1 and p_2 (for simplicity we use $p_T \equiv p$), then the factorization between the flow harmonics in those two bins would imply [240],

$$C_n(p_1, p_2) \equiv \langle \cos n(\phi_1 - \phi_2) \rangle \overset{\text{(factorization)}}{=} v_n\{2\}(p_1) \times v_n\{2\}(p_2), \tag{3.44}$$

where $C_n(p_1, p_2)$ is the event averaged correlation matrix, ϕ_1 and ϕ_2 are the azimuthal angles of the two particles in two transverse momentum bins p_1 and p_2, and the bracket has the usual meaning as in Eq. (3.23). In the earlier years of flow-analysis, the factorization relation in Eq. (3.44) was assumed to hold and was investigated in experiments [248, 82, 55]. However, in practice even if we do not consider any non-flow correlation (which naturally breaks the factorization), there is still considerable factorization-breaking between the flow harmonics in two different kinematic bins [240, 81, 244, 83, 85, 86], due to event-by-event fluctuations of the flow harmonics originating from the fluctuations of the initial state. Here we will restrict our discussions to transverse momentum dependent flow-fluctuations.

In the case of integrated (p_T-averaged) flow, the flow harmonics are obtained from the flow vector $V_n = v_n e^{in\Psi_n}$ using the standard 'two-particle cumulant' formula in (Eqs. (3.27) and Eq. (3.41)),

$$v_n\{2\} = \sqrt{c_n\{2\}} = \sqrt{\langle V_n V_n^* \rangle} = \sqrt{\langle v_n^2 \rangle}\,, \tag{3.45}$$

where the angular bracket denotes the average over all events. Similarly one can define the transverse momentum dependent flow vector (i.e. flow vector measured in a transverse momentum bin), $V_n(p) = v_n(p) e^{in\Psi_n(p)}$, where both *flow magnitude* $v_n(p)$ and *flow angle* (event-plane angle) $\Psi_n(p)$ depend on the transverse momentum which we write as p in the present context. Then the transverse momentum dependent or the differential measure of the harmonic flow is given by [231, 235, 130],

$$v_n\{2\}(p) = \frac{\langle V_n V_n^*(p) \rangle}{v_n\{2\}} = \frac{\langle V_n V_n^*(p) \rangle}{\sqrt{\langle V_n V_n^* \rangle}}, \tag{3.46}$$

which is the definition used in the experimental analysis for differential flow, where one particle is taken from a particular transverse momentum bin p and the other particle is taken from the entire p_T-acceptance region or *all* the particles detected in the event. Here the flow V_n serves as the *reference flow* [235] for studying p_T-dependent differential flow. However, an alternative definition for the differential flow could be used, which is given by [78, 130],

$$v_n[2](p) = \sqrt{\langle V_n(p) V_n^*(p) \rangle} = \sqrt{\langle v_n(p)^2 \rangle}, \tag{3.47}$$

where both particles are taken within the same transverse momentum bin p. Although in principle this definition could be used for the theoretical study, but it is not suitable for the experimental analysis as it might be difficult to find two particles within the same p_T-bin at larger p_T , due to limited statistics[8]. This concept will be extremely useful for the upcoming discussions in this section.

Let us consider two particles in two different transverse momentum bins p_1 and p_2. Then the event averaged correlation matrix $C_n(p_1,p_2)$ given in Eq. (3.44) should satisfy two conditions: first, its diagonal elements should be positive and second, the off-diagonal elements must satisfy the Cauchy-Schwarz inequality,

$$C_n(p_1,p_1) \geq 0 \quad \text{and} \quad C_n(p_1,p_2)^2 \leq C_n(p_1,p_1)C_n(p_2,p_2)\,. \tag{3.48}$$

If there is factorization between the flow harmonics in different p_T-bins, then the inequality saturates to equality condition. In other words, based on this inequality condition, we can construct a correlation coefficient which can quantify the amount of factorization breaking [240],

$$r_n = \frac{C_n(p_1,p_2)}{\sqrt{C_n(p_1,p_1)C_n(p_2,p_2)}}, \tag{3.49}$$

which could be written explicitly in terms of the event flow in two bins $V_n(p_1)$ and $V_n(p_2)$ as [240, 244],

$$r_n(p_1,p_2) = \frac{\langle V_n(p_1)V_n^*(p_2)\rangle}{\sqrt{\langle v_n^2(p_1)\rangle\langle v_n^2(p_2)\rangle}}\,. \tag{3.50}$$

If there is factorization, $r_n = 1$, which is the limiting case and any deviation of r_n from 1 will correspond to the breaking of the factorization. The correlation coefficient $r_n(p_1,p_2)$ is known as *factorization-breaking coefficient*.

The factorization-breaking coefficient in Eq. (3.50) is defined as the linear correlation coefficient between two flow vectors which are complex numbers. The effect of event-by-event flow fluctuations is the *decorrelation* between these harmonic flow vectors in two different p_T-bins. In each event, $V_n(p)$ is a smooth function of p. In general, it is expected that the correlation is stronger when $p_1 \simeq p_2$ and it decreases as the difference between p_1 and p_2 increases i.e there is decorrelation which is understood as the deviation of the factorization-breaking coefficient $r_n(p_1,p_2)$ from 1. The decorrelation occurs due to decoherence between the flow vectors, induced by the quantum fluctuations in the wavefunctions of the incoming nucleons, in the initial state. The factorization-breaking coefficient $r_n(p_1,p_2)$ has been studied in models [240, 275–277, 244] and measured in the experiments [278, 279, 83]. In Fig. 3.10, we show the results for $r_2(p_1,p_2)$ as a function of the difference $p_1 - p_2$, calculated in our model for Pb+Pb collision at 5.02 TeV, where the flow vector in one p_T-bin is kept fixed and correlated

---

[8] From the particle spectra it is obvious that there are less and less number of particles as we go higher in p_T

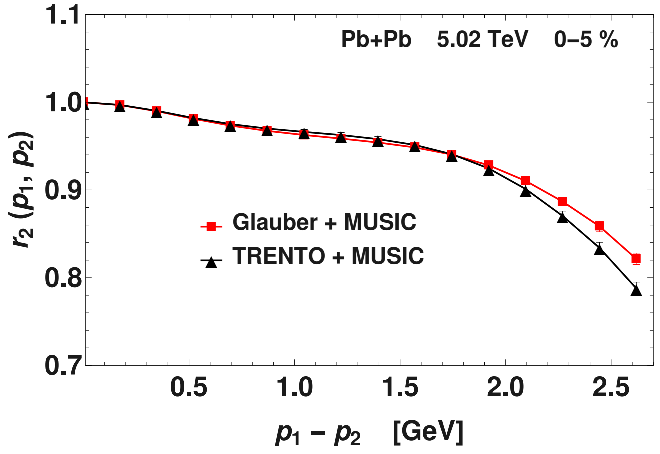

Fig. 3.10 The factorization-breaking coefficient between elliptic flow vectors in two different transverse momentum bins p_1 and p_2, plotted as a function of $p_1 - p_2$ for Pb+Pb collision at 5.02 TeV in $0-5\%$ centrality. The red squares and the black triangles denote the results obtained in hydrodynamic simulations with Glauber and TRENTO initial conditions respectively.

with the flow vectors in other bins. As expected, the correlation $r_n \to 1$ as p_1 and p_2 are closer to each other and it gradually deviates from 1 i.e. the decorrelation increases as the difference $p_1 - p_2$ increases.

It should be noted that all the results reported in this and following sections are obtained using a boost invariant viscous hydrodynamic model MUSIC [216] for Pb+Pb collisions at $\sqrt{s_{NN}} =$ 5.02 TeV. The density distributions in the initial state, used as an input for the hydrodynamic evolution, are obtained from two initial-state models: a two-component Glauber Monte Carlo model [280] and the TRENTO model [194]. Unless otherwise stated, we use a constant shear viscosity to entropy density ratio $\eta/s = 0.08$.

The flow vector $V_n(p) = v_n(p)e^{in\Psi_n(p)}$ has two parts: flow magnitude $v_n(p)$ and flow angle $\Psi_n(p)$, both of which fluctuate event-by-event depending on transverse momentum. Naturally, one would expect flow magnitude factorization breaking (decorrelation) and flow angle decorrelation, where the latter represents the event-by-event difference in the flow angles $\Psi_n(p_1)$ and $\Psi_n(p_2)$ (event-plane angle) at two transverse momenta. The decorrelation between the flow magnitudes at two transverse momentum bins is defined as[244],

$$r_n^{v_n}(p_1, p_2) = \frac{\langle |V_n(p_1)||V_n(p_2)| \rangle}{\sqrt{\langle v_n^2(p_1)\rangle \langle v_n^2(p_2)\rangle}} = \frac{\langle v_n(p_1) v_n(p_2) \rangle}{\sqrt{\langle v_n^2(p_1)\rangle \langle v_n^2(p_2)\rangle}} , \tag{3.51}$$

and the corresponding flow angle decorrelation is given by,

$$\langle \cos[n(\Psi_n(p_1) - \Psi_n(p_2))] \rangle . \tag{3.52}$$

In principle, one could study all these three quantities (flow vector, magnitude and angle decorrelation) in models [244]. The decorrelation between harmonic flow vectors at two different momenta involves both the decorrelation of the flow magnitudes and of the flow angles [78, 281, 244]. Therefore, it is natural to expect that the flow vector decorrelation factorizes into flow magnitude and angle decorrelation i.e.

$$\begin{aligned} r_n(p_1,p_2) &= \frac{\langle v_n(p_1)v_n(p_2)\cos[n(\Psi_n(p_1)-\Psi_n(p_2))]\rangle}{\langle v_n^2(p_1)\rangle\langle v_n^2(p_2)\rangle} \\ &\simeq \frac{\langle v_n(p_1)v_n(p_2)\rangle}{\sqrt{\langle v_n^2(p_1)\rangle\langle v_n^2(p_2)\rangle}} \times \langle\cos[n(\Psi_n(p_1)-\Psi_n(p_2))]\rangle, \end{aligned} \tag{3.53}$$

which however does not hold true in practice [244].

Flow angle and flow magnitude factorization breaking : Need for 2nd order

It should be noted that experimentally, flow magnitude and angle decorrelation cannot be measured through the formulae presented in Eqs. (3.51) and (3.52). The reason is that in experiment, we can only measure the scalar product between two flow-vectors, which involves two-particle correlation. As a result, in the *first order* of flow, only flow vector decorrelation (Eq. (3.50)) can be measured, flow magnitude and flow angle decorrelation cannot measured using two-particle correlators. In order to measure the flow magnitude and flow angle decorrelation experimentally, we need to consider four-particle correlators or in other words, we need to construct the factorization-breaking coefficients between the *squares* of the flow. A similar method was applied to estimate separately, the flow magnitude and flow angle decorrelation in pseudorapidity bins, using four-particle correlators [282]. A similar procedure can be used for the correlation between the harmonic flow in two different transverse momentum bins [244].

The factorization-breaking coefficients between two flow vectors *squared* can be defined as,

$$r_{n;2}(p_1,p_2) = \frac{\langle V_n(p_1)^2 V_n^*(p_2)^2\rangle}{\sqrt{\langle v_n^4(p_1)\rangle\langle v_n^4(p_2)\rangle}} \ , \tag{3.54}$$

which is a four-particle correlator, measuring the breaking of the factorization between two flow vectors in two transverse momentum bins, in *second order*. Please note that in the above definition, the four particle correlator is constructed by taking two particles from the same transverse momentum bin p_1 and other two particles from the bin p_2. In a similar manner, the factorization-breaking coefficient between flow magnitude *squared* can be defined as,

$$\begin{aligned} r_{n;2}(p_1,p_2) &= \frac{\langle V_n(p_1)V_n(p_1)^* V_n(p_2)V_n(p_2)^*\rangle}{\sqrt{\langle v_n^4(p_1)\rangle\langle v_n^4(p_2)\rangle}} \equiv \frac{\langle |V_n(p_1)|^2|V_n(p_2)|^2\rangle}{\sqrt{\langle v_n^4(p_1)\rangle\langle v_n^4(p_2)\rangle}} \\ &= \frac{\langle v_n(p_1)^2 v_n^2(p_2)\rangle}{\sqrt{\langle v_n^4(p_1)\rangle\langle v_n^4(p_2)\rangle}}, \end{aligned} \tag{3.55}$$

which in principle can be used in experiments to measure flow magnitude decorrelation. However, it is not possible to define an experimental observable which could directly measure the flow angle correlation between two transverse momentum bins. Only an estimate of the flow angle correlation (or decorrelation) can be obtained by taking the ratio of four-particle flow vector correlator and flow magnitude correlator [282] given by,

$$F_n(p_1,p_2) = \frac{\langle V_n(p_1)^2 V_n^*(p_2)^2 \rangle}{\langle v_n(p_1)^2 v_n(p_2)^2 \rangle}, \tag{3.56}$$

which is the ratio of the flow vector squared (Eq. (3.54)) and flow magnitude squared (Eq. (3.55)) factorization-breaking coefficients.

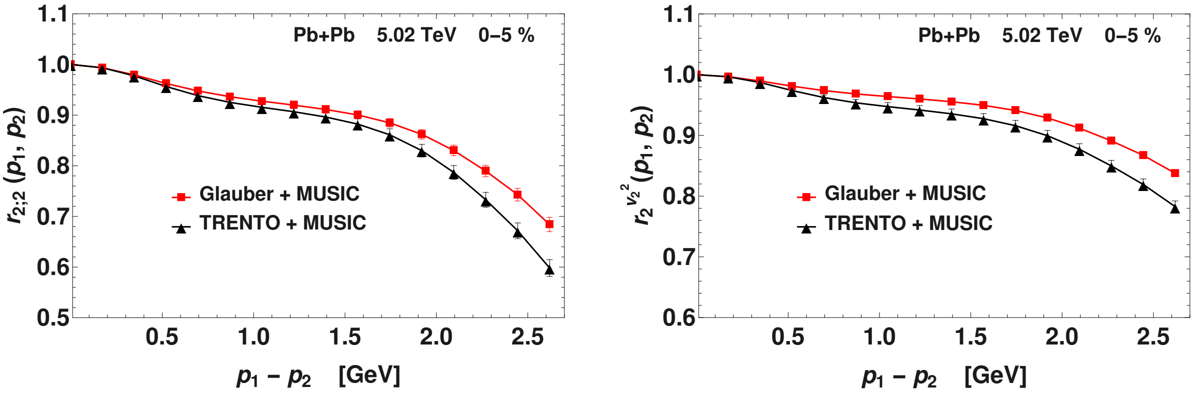

Fig. 3.11 Factorization-breaking coefficients between flow vectors squared (left) and flow magnitude squared (right) between two different bins p_1 and p_2, plotted as a function of $p_1 - p_2$ for the elliptic flow in Pb+Pb collision for $0-5\%$ centrality. The symbols carry similar meaning as Fig. 3.10.

Fig. (3.11) shows the flow vector squared and flow magnitude squared factorization-breaking coefficients for the elliptic flow in our model calculation. It could be seen that the flow magnitude decorrelation is smaller than flow vector decorrelation, because the other part of it is given by the flow angle decorrelation. Although formally possible, the experimental implementation of the formulae in Eqs. (3.54) and (3.55) are not feasible because one needs two particle from the same transverse momentum bin, which become very difficult at larger momenta due to low statistics.

3.2.2 Removing experimental difficulty: Taking one flow p_T-averaged

To ease the experimental measurement, one could take only one transverse momentum bin and can correlate the particles from that particular bin with the particles from the entire acceptance range. This was originally introduced by the measurement from the ALICE collaboration [85, 87, 250]. This way we could partly overcome the limitation from low multiplicity in bins at high transverse momentum. Below we present our model calculations following this method for the factorization-breaking coefficients. The following sections are, for the most part, presentations from the original publications [125, 283], coauthored by the author. In the first order, the

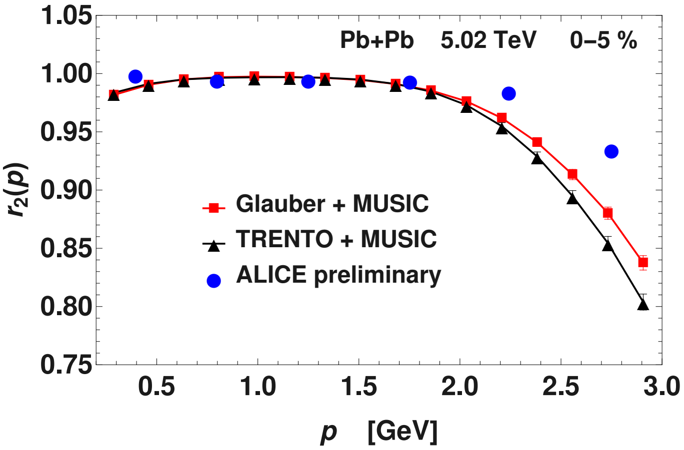

Fig. 3.12 The factorization-breaking coefficient between transverse momentum averaged (V_2) and transverse momentum dependent elliptic flow vector($V_2(p)$) as a function of the transverse momentum p in Pb+Pb collision at 5.02 TeV for $0-5\%$ centrality. The results obtained in hydrodynamic simulations with Glauber and TRENTO initial conditions are represented by the red squares and the black triangles respectively. The blue dots represent the experimental data from the ALICE collaboration [87].

factorization-breaking coefficient can be defined as,

$$r_n(p) = \frac{\langle V_n V_n^*(p) \rangle}{\sqrt{\langle v_n^2 \rangle \langle v_n^2(p) \rangle}} \,, \tag{3.57}$$

which measures the correlation between the harmonic flow vector averaged over transverse momentum (p_T-averaged flow or global flow) and the flow vector in a transverse momentum bin p[9]. The coefficient $r_n(p)$ represents a two-particle correlator, where one particle comes from the transverse-momentum bin p and the second particle comes from anywhere of the full p_T-acceptance range of the detector, which serves as the reference particle (reference flow) much like Eq. (3.46). In fact, the factorization-breaking coefficient $r_n(p)$ could be written using Eq. (3.46) and (3.47) as,

$$r_n(p) = \frac{v_n\{2\}(p)}{v_n[2](p)}, \tag{3.58}$$

which is a measure of the difference between two definitions of the differential harmonic flow coefficient [78]. Fig. (3.12) shows the factorization-breaking coefficient $r_2(p)$ for the elliptic flow calculated in our model, along with the ALICE data. Our model results can reproduce the qualitative nature of the data well, where both results show significant decorrelation at higher transverse momentum. Quantitatively speaking, at large transverse momentum, the decorrelation is stronger in our model than the data, which could be due to the presence of non-flow correlations in the data. We will return to this point shortly after.

We can use the similar idea to define the factorization-breaking coefficient in second order of flow, which is our ultimate goal. In the second order, we can define the factorization-breaking

---

[9] we use $p \equiv p_T$, where p represents a particular p_T-bin

coefficient between the flow vector squared as,

$$r_{n;2}(p) = \frac{\langle V_n^2 V_n^*(p)^2 \rangle}{\sqrt{\langle v_n^4 \rangle \langle v_n^4(p) \rangle}} , \tag{3.59}$$

which is a four-particle correlator, where two of them are from the transverse momentum bin p and the other two are taken globally and eventually represent the correlation coefficient between V_n^2 and $V_n^2(p)$. Figs. 3.13 and 3.14 show the results obtained in the hydrodynamic model, for the factorization-breaking coefficients $r_{n;2}(p)$ in the case of elliptic and triangular flow respectively, for $0-5\%$ and $30-40\%$ centrality in each case. A first observation of the figures reveal that the decorrelation is significantly larger for the centralities where fluctuations dominate i.e. for the elliptic flow in central collisions and for the triangular flow in any centrality. In Fig. 3.13, for the elliptic flow, the model results are similar to the data for $0-5\%$ centrality and there is large decorrelation between the flow vectors at high transverse momentum. On the contrary, for $30-40\%$ centrality (semi-central collisions) the decorrelation is much smaller as there is less fluctuations, but the model results show stronger decorrelation than in the data at high transverse momentum, making the difference prominent for $p > 2.0$ GeV. A possible reason behind this phenomena could be that our model calculation do not include any contributions from non-flow correlations, while in the experimental data non-flow effects are present, which are usually reduced by using larger rapidity gaps between the measured flow vectors. A precise quantification of the contributions of the remaining non-flow correlation and the genuine difference in flow fluctuations between the model and the experiment, to the observed difference between the model results and the data in Fig. 3.13 (right), lies beyond the scope of our present study.

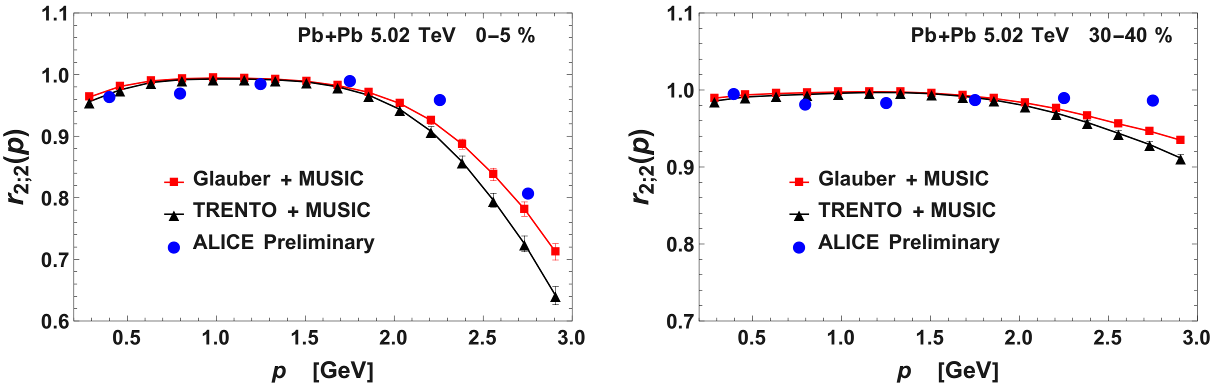

Fig. 3.13 Factorization-breaking coefficients between momentum averaged (V_2^2) and momentum dependent elliptic flow ($V_2(p)^2$) vector squared as a function of the transverse momentum in Pb+Pb collision at 5.02 TeV for $0-5\%$ (left) and $30-40\%$ (right) centrality. The symbols carry similar meaning as Fig. 3.59. The figure is from the original publication [125], coauthored by the author.

The decorrelation between the triangular flow vector squared in Fig. 3.14, is quite strong for both $0-5\%$ and $30-40\%$ centralities due to dominating flow fluctuations. A careful inspection of

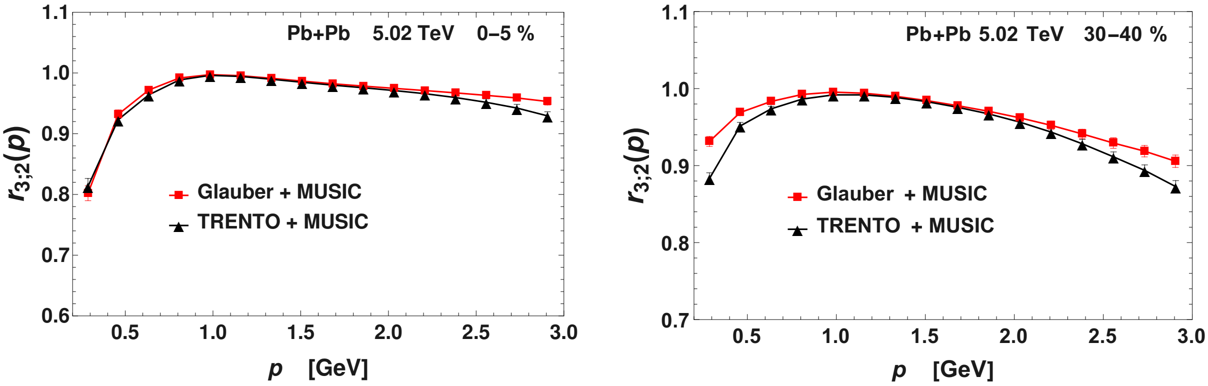

Fig. 3.14 Flow vector squared factorization-breaking coefficients between momentum averaged and momentum dependent triangular flow in Pb+Pb collision at 5.02 TeV for $0-5\%$ (left) and $30-40\%$ (right) centrality. Symbols are same as Fig. 3.13. The right panel is from the original publication [125], coauthored by the author.

the two plots discloses another interesting fact: there is a considerable decorrelation even at low transverse momentum, which is not so noticeable in case of elliptic flow. The origin of this effect lies within the definition of the factorization-breaking coefficient $r_{n;2}(p)$ in Eq. (3.59). Here we correlate the flow vector in a transverse momentum bin $V_n(p)^2$ with the p_T-averaged flow vector V_n which correspond to the average transverse momentum over all events, $\langle p_T \rangle \equiv \langle p \rangle \sim 0.8$ GeV. As the difference between p and $\langle p \rangle$ increases, which could happen for both low and high transverse momentum bins, there could be decorrelations. This effect is small for V_2, but dominant in the case of V_3.

Flow magnitude decorrelation

Similar to Eq. (3.59), through a four-particle correlator we can define the factorization-breaking coefficient between the flow magnitude squared with one flow momentum-averaged and another flow in a momentum bin,

$$r_n^{v_n^2}(p) = \frac{\langle v_n^2 v_n^2(p) \rangle}{\sqrt{\langle v_n^4 \rangle \langle v_n^4(p) \rangle}} , \tag{3.60}$$

which is easier to measure in experiment as compared to Eq. (3.55), because now it requires to find only two particles in a transverse momentum bin p. Fig. 3.15 shows the results obtained in the hydrodynamic model and comparison with the data, for the factorization-breaking coefficients between magnitude squared of elliptic flow, $r_2^{v_2^2}(p)$ for $0-5\%$ and $30-40\%$ centrality. Similar to the flow vector factorization breaking coefficients, the magnitude factorization breaking coefficients show that the experimental data lie above the simulation results at high transverse momentum. This discrepancy can be partly attributed to the contribution of non-flow correlations. The disparity is particularly noticeable for the $30-40\%$ centrality, where certain data points even surpass 1, indicating significant dominance of the non-flow correlations.

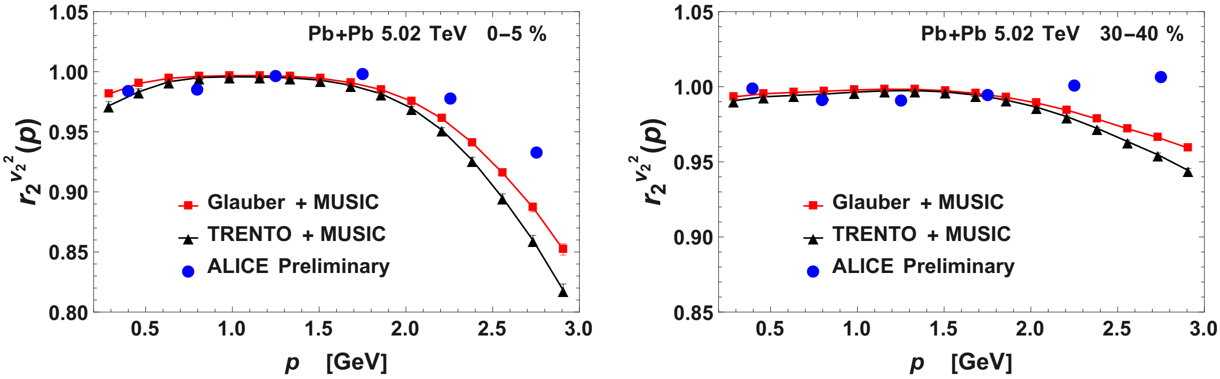

Fig. 3.15 Factorization-breaking coefficients for the flow magnitude squared between transverse momentum averaged and transverse momentum dependent elliptic flow as a function of the transverse momentum in Pb+Pb collisions for 0 – 5% (left) and 30 – 40% (right) centrality. The symbols carry similar meaning as Fig. 3.13. The figure is from the original publication [125], coauthored by the author.

A second observation reveals that the flow magnitude decorrelation accounts for roughly one-half of the flow vector decorrelation, i.e.

$$[1 - r_{n;2}(p)] \simeq 2[1 - r_n^{v_n^2(p)}] \,. \tag{3.61}$$

This suggests that the other half of the flow vector decorrelation can be approximately attributed to the flow-angle decorrelation, as we will see shortly. This relation regarding the flow vector, magnitude and angle decorrelation, as an outcome of the event-by-event flow fluctuations is expected in a random toy model [246](Appendix. A.1). Although it is generally possible to have any proportions of angle and magnitude decorrelation contributing to total vector decorrelation, previous experimental measurements [86] and model calculations [81] have shown that flow decorrelation in rapidity exhibits a roughly equal strength of angle and magnitude decorrelation. The results for the triangular flow are qualitatively similar, which we do not show here.

In the present context, let us point out that the correlation coefficient in Eq. (3.60) which is a measure of the flow magnitude squared factorization-breaking, is not equal to or not to be confused with the Pearson correlation coefficient between v_n^2 and $v_n^2(p)$,

$$\frac{\langle v_n^2 v_n^2(p)\rangle - \langle v_n^2\rangle\langle v_n^2(p)\rangle}{\sqrt{(\langle v_n^4\rangle - \langle v_n^2\rangle^2)(\langle v_n^4(p)\rangle - \langle v_n^2(p)\rangle^2)}} \,. \tag{3.62}$$

Fig. 3.16 shows the comparison between these two definitions of the correlation coefficient for elliptic flow, along with the data for flow magnitude decorrelation. It could be clearly seen that the correlation coefficient in Eq. (3.60) follows the trend of the data and much closer to it, hence provide true measure of flow magnitude decorrelation, whereas the Pearson correlation coefficient in Eq. (3.62) shows completely different behavior and huge departure from the data.

Please note that the extraction of the flow vectors squared and flow magnitudes squared factorization breaking coefficients from the experimental data of the ALICE collaboration,

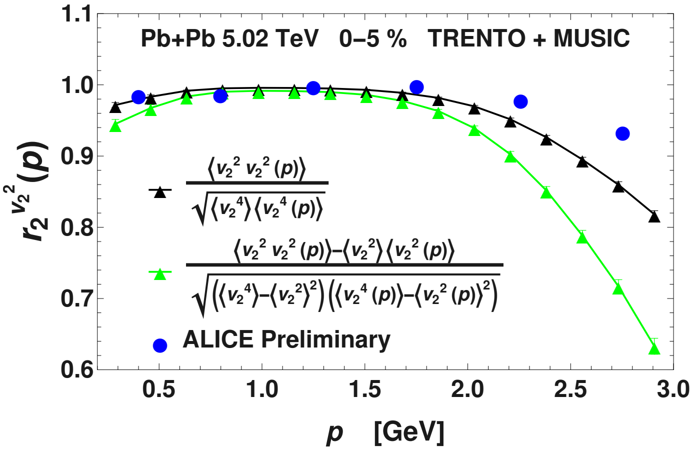

Fig. 3.16 Comparison between different definitions of flow magnitude factorization-breaking coefficient for the elliptic flow, in Pb+Pb collision at 5.02 TeV in $0-5\%$ centrality with TRENTO initial condition. The black triangles represent our usual definition of flow magnitude squared factorization-breaking coefficients given in Eq. 3.60, while the green triangles denote the Pearson correlation coefficient between v_2^2 and $v_2^2(p)$. The blue dots represent the ALICE data for the flow magnitude decorrelation.

involves several considerations. The experiment does not directly measure these flow vector and flow magnitude factorization coefficients (Eq. 3.59 and 3.60) [284, 87, 250]. The primary challenge lies in extracting the four-particle correlator $\langle v_n^4(p)\rangle$, sitting at the denominator of the correlation formulae, because all four particles are from a narrow transverse momentum bin. On the other hand, the fourth moment $\langle v_n^4\rangle$ which involves four particles from anywhere in the full acceptance, can be measured. The results presented by the ALICE Collaboration for the correlators, are with different scaling [284][10], e.g. for flow magnitude squared correlations,

$$\frac{\langle v_n^2 v_n^2(p)\rangle}{\langle v_n^2\rangle\langle v_n^2(p)\rangle} \,. \tag{3.63}$$

Upon dividing this scaled correlator by $\langle v_n^4\rangle/\langle v_n^2\rangle^2$ [284], an estimate of the flow magnitude squared factorization-breaking coefficient,

$$r_n^{v_n^2}(p) \simeq \frac{\langle v_n^2 v_n^2(p)\rangle\langle v_n^2\rangle}{\langle v_n^4\rangle\langle v_n^2(p)\rangle}, \tag{3.64}$$

or the flow vector squared factorization-breaking coefficient,

$$r_{n;2}(p) \simeq \frac{\langle V_n^2 V_n^\star(p)^2\rangle\langle v_n^2\rangle}{\langle v_n^4\rangle\langle v_n^2(p)\rangle} \tag{3.65}$$

---

[10] Please note that when we performed our analysis, the data from the ALICE collaboration was in the preliminary form, as presented in the IS2021 conference in Rehovot [284]. In the original publication [87], which came after our publication [125], the data for magnitude squared correlation was presented with the scaling presented in Eq. (3.64), so is followed in a recent preprint with more systematic study [250]

can be obtained. The difference between Eqs. (3.65) and (3.64) and the factorization-breaking coefficients defined in Eqs. (3.59) and (3.60) is a factor,

$$\sqrt{\frac{\langle v_n^4(p)\rangle\langle v_n^2\rangle^2}{\langle v_n^4\rangle\langle v_n^2(p)\rangle^2}} \ . \tag{3.66}$$

In our hydrodynamic simulations, we have verified that the deviation of this factor from unity is less than 6×10^{-3} for transverse moemntum ranging from 0.5 GeV to 3.0 GeV. The experimental values for the flow vector and magnitude squared correlations depicted in the figures are determined using the formulae given in Eqs. (3.65) and (3.64).

Flow angle decorrelation

As discussed earlier, an experimental observable which could directly measure the flow angle correlation (or decorrelation) cannot be defined. Therefore, the flow angle decorrelation between the momentum averaged flow and momentum dependent flow could be defined following the similar prescription as in Eq. (3.56), i.e. by taking the ratio of flow vector squared (Eq. 3.59) and flow magnitude squared (Eq. 3.60) factorization-breaking coefficients,

$$F_n(p) = \frac{r_{n;2}(p)}{r_n^{v_n^2}(p)} = \frac{\langle V_n^2 V_n^*(p)^2\rangle}{\langle v_n^2 v_n(p)^2\rangle} \ , \tag{3.67}$$

which could be easily measured in the experiments.

Figs. 3.17 and 3.18 show the results for the flow angle decorrelation obtained in hydrodynamic simulations compared to the ALICE data, for elliptic and triangular flow respectively. The model simulations predict a noticeable flow angle decorrelation between the global flow V_n and the differential, momentum dependent flow $V_n(p)$, for both the elliptic and triangular flow. For the elliptic flow in central collision ($0-5\%$), the simulation results are consistent with the preliminary data from the ALICE collaboration. However, for the centrality $30-40\%$, both the model results and experimental data show a smaller angle decorrelation in comparison to the central collision. Once again, this can be linked to the unavoidable presence of the non-flow correlations which are expected to be relatively more important in off-central collisions. The difference in the decorrelation strength between the central and semi-central collisions arises from the global correlation of the elliptic flow with the initial geometry in non-central collisions.

Moreover, as claimed earlier, from Fig. 3.17 it could be seen that the flow angle decorrelation is roughly one half of the flow vector decorrelation (Fig. 3.13). Therefore, it is quite safe to infer the following theorem (at least for the central collisions) based on our analysis,

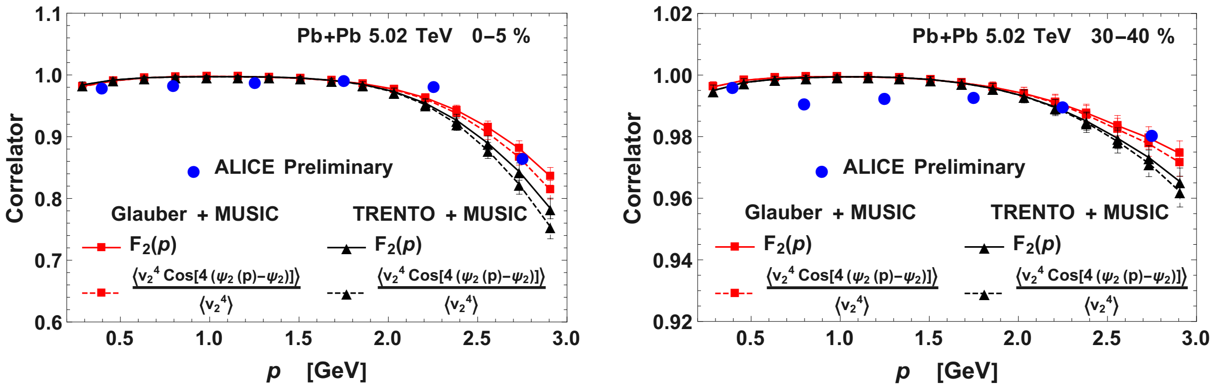

Fig. 3.17 Flow angle decorrelation as a function of the transverse momentum for the elliptic flow in Pb+Pb collision at 5.02 TeV for $0-5\%$ (left) and $30-40\%$ (right) centrality. The red squares and black triangles denote the results obtained with the initial conditions from the Glauber and TRENTO model respectively. The solid lines denote the estimate of the flow angle correlation (or decorrelation) that can be measured in experiments while the dashed lines denote the actual flow-angle correlation. The blue dots represent the corresponding ALICE data for flow angle decorrelation. The figure is from the original publication [125], coauthored by the author.

Transverse momentum dependent flow vector decorrelation approximately amounts to the summation of flow magnitude and flow angle decorrelation (Appendix. A.1) :

$$[1-r_{n;2}(p)] \simeq [1-r_n^{v_n^2(p)}]+[1-F_n(p)] \ . \tag{3.68}$$

In Fig. 3.18, similar to the past situations, there exist flow decorrelation on either side of the average transverse momentum ($\langle p \rangle$), indicating the peculiar characteristics of the triangular flow, coming from the dominance of fluctuations.

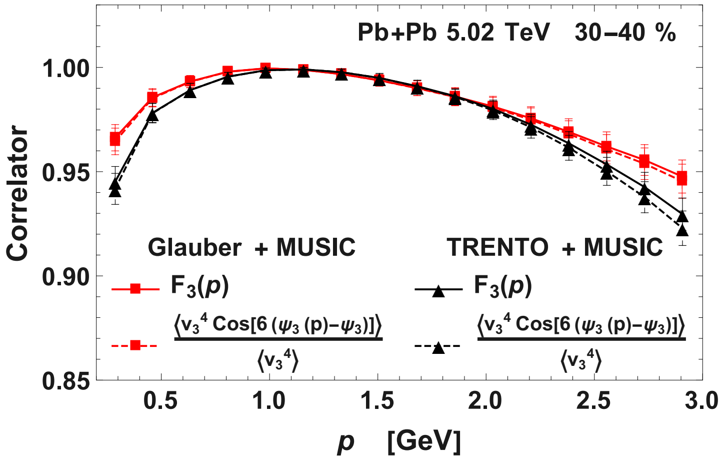

Fig. 3.18 Flow angle decorrelation for the triangular flow with $30-40\%$ centrality in Pb+Pb collision at 5.02 TeV. The symbols have similar meaning as Fig. 3.17. The figure is from the original publication [125], coauthored by the author.

The formula in Eq. (3.67) provides a way to estimate the flow angle decorrelation in experiments. It measures the quantity,

$$\frac{\langle v_n^2 v_n(p)^2 \cos[2n(\Psi_n(p)-\Psi_n)]\rangle}{\langle v_n^2 v_n(p)^2\rangle}, \tag{3.69}$$

providing an estimate of the true measure of the flow angle decorrelation,

$$\frac{\langle v_n^4 \cos[2n(\Psi_n(p)-\Psi_n)]\rangle}{\langle v_n^4\rangle}, \tag{3.70}$$

which involves only the angle decorrelation. The above expression for the actual flow angle decorrelation is based on the implicit assumption that the decorrelations between the flow magnitudes in the numerator and the denominator cancel out. In other words, the transverse momentum dependence of the flow magnitudes in Eq. (3.69) vanishes, so that we could get,

$$F_n(p) \approx \frac{\langle v_n^4 \cos[2n(\Psi_n(p)-\Psi_n)]\rangle}{\langle v_n^4\rangle} \; . \tag{3.71}$$

The above formula (Eq. (3.70)) cannot be directly applied in experimental analysis. However, in our model, we can assess the similarity between the results obtained with the two formulae in Eqs. (3.69) and (3.70), specifically addressing the validity of Eq. (3.71). This is equivalent of examining whether the momentum dependence of the magnitude and flow angle in the numerator of Eq. (3.69) factorizes in the hydrodynamic model simulations. The results from hydrodynamic model calculated using both formulae are presented in Figs. 3.17 and 3.18. It can be clearly seen that the two formulae produce similar results, which implies that the experimental measure (Eq. (3.67)) can be used to estimate the *weighted* flow angle decorrelation. It should be noted that the angle correlation is weighted by the fourth power of flow magnitude i.e. only the v_n^4 weighted or *magnitude weighted* flow angle decorrelation can be measured in the experiment.

Another interesting fact in the present context is that the simple average of the cosine between the angles,

$$\langle \cos[2n(\Psi_n(p)-\Psi_n)]\rangle \tag{3.72}$$

is not a measure of the angle decorrelation. Fig. (3.19) (left) shows the comparison between different definitions of the angle decorrelation compared with the ALICE data. It can be seen that Eq. (3.72) provides very different results. However, such results are quite expected. In events where flow harmonics are large (large $|V_n|$ and large $|V_n(p)|$), the random decorrelation between two vectors is relatively small, making the angle decorrelation minimal. For a detailed discussion of the effect we refer interested readers to Ref. [81].

It is to be noted that in the experiment, only the angle decorrelation between the flow vectors *squared* can be measured. However, in the model one can check how it is related to the angle

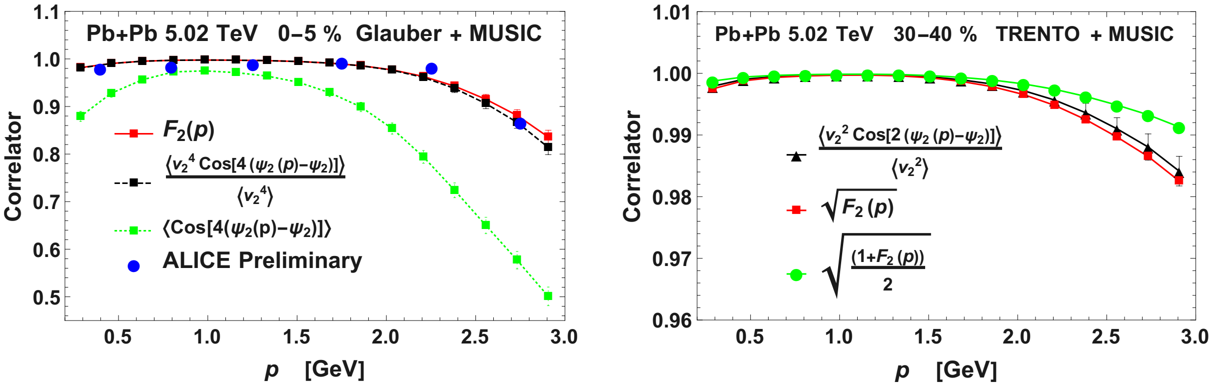

Fig. 3.19 Left: Comparison between different definitions of flow angle correlation along with the data for Pb+Pb collision in centrality $0-5\%$. The red and black squares denote the experimental measure and actual flow angle correlations respectively. The green squares represent the simple angle correlation without any weights of flow magnitudes. The blue dots denote the ALICE data. Right: The flow angle correlation between the first moment of flow vectors $V_2(p)$ and V_2 as a function of the transverse momentum for centrality $30-40\%$ (black triangles), compared to its approximation by $\sqrt{F_2(p)}$ (red squares) and its upper limit $\sqrt{(1+F_2(p))/2}$ (green dots). The figure is from the original publications [125, 283], coauthored by the author.

correlation between first order of flow i.e. between first moments of flow vectors :

$$\frac{\langle v_n^2 \cos[n(\Psi_n(p)-\Psi_n)]\rangle}{\langle v_n^2\rangle} . \tag{3.73}$$

In Fig. 3.19 (right), we show the hydrodynamic model results for the flow angle correlation between the first moments and we find that it can be approximated as the square root of the angle decorrelation between the flow vectors squared $F_n(p)$, i.e.

$$\frac{\langle v_n^2 \cos[n(\Psi_n(p)-\Psi_n)]\rangle}{\langle v_n^2\rangle} \simeq \sqrt{F_n(p)} . \tag{3.74}$$

A similar relation was found for the correlators of higher moments of flow vectors in pseudorapidity bins [86]. In Fig. 3.19 (right), we also show the upper limit for the flow angle correlation, given by $\sqrt{(1+F_n(p))/2}$, as proposed by the ALICE Collaboration [284, 87].

3.2.3 Mixed-flow factorization-breaking: measure of non-linearity

It is a general characteristic of flow harmonics V_n that as we go higher order in n ($n>2$), the flow vectors get contributions from the subsequent lower orders of flow, identified as the non-linear flow correlation [93, 285]. The major contributing factors behind such non-linear behavior in the final state are the similar non-linear relations of the higher order eccentricities to the lower orders (Eqs. (3.18) and (3.19)) at the initial state, as discussed in Sec. 3.1.4. As a natural consequence, the correlations between mixed flow harmonics or specifically, the correlations between the event planes corresponding to different orders of harmonic flow could provide very good measure of nonlinearities in the hydrodynamic expansion, as well as of the correlations in the initial state [93, 285–287, 256, 288, 236, 289–295].

Typically these studies involve correlators between the flow vectors of different orders or moments of flow, which are averaged over transverse momentum. However, the momentum dependent correlation between flow harmonics of different orders could reveal interesting measure of differential non-linear response of the medium and put additional constraints on the initial state models [296, 81]. Such studies involve higher order moments of mixed-flow harmonics in bins of transverse momentum i.e. many-particle correlator in small bins, which again cannot be measured easily in experiments due to limited statistics.

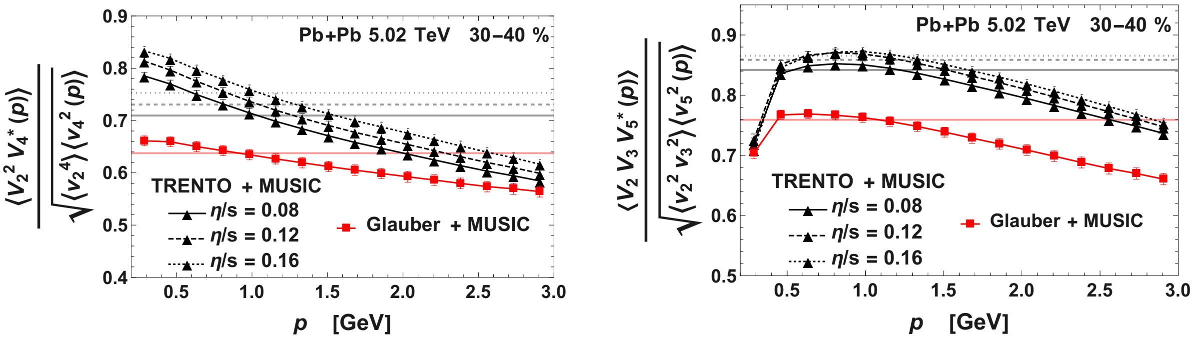

Fig. 3.20 Mixed-flow correlation between V_2^2 and $V_4(p)$ (left), and between V_2V_3 and $V_5(p)$ (right) as a function of transverse momentum in Pb+Pb collision at 5.02 TeV with $30-40\%$ centrality. The results from the hydrodynamic model using Glauber and TRENTO model initial conditions are represented by the red squares and black triangles respectively. The solid, dashed and dotted black lines represent results with $\eta/s = 0.08,\ 0.12,\ 0.16$ respectively for the TRENTO initial conditions. Corresponding correlation coefficients between the momentum averaged flow vector V_2^2 and V_4, and between V_2V_3 and V_5 are denoted by the horizontal lines. The figure is from the original publication [125], coauthored by the author.

Following the similar method as before, we can construct a correlation coefficient (in this context the name correlation coefficient suits more, as used in the literature as well, instead of factorization-breaking coefficient) in the first order, between the mixed flow harmonics, with only one of the flow harmonics restricted to a transverse momentum bin through a generalized formula,

$$\frac{\langle V_k V_l V_m^*(p)\rangle}{\sqrt{\langle v_k^2 v_l^2\rangle\langle v_m^2(p)\rangle}}, \tag{3.75}$$

with $m = k+l$. For $m \neq k+l$, the cumulant in the numerator becomes zero by symmetry and no physical information can be extracted in that case.

Owing to the non-linear relationships described in Eqs. (3.18) and (3.19), we can write the non-linear relationships for the quadrangular and pentagonal flow in terms of elliptic and triangular flow as,

$$V_4 = V_4^L + \chi_{4,22}V_2^2 \quad \text{and} \quad V_5 = V_5^L + \chi_{5,23}V_2V_3\ , \tag{3.76}$$

where V_4^L and V_5^L correspond to the linear contributions with $\chi_{4,22}$ and $\chi_{5,23}$ as the *non-linear response coefficients* respectively. Therefore, we can construct the correlation coefficients between $V_2^2 - V_4$ and $V_2V_3 - V_5$, to measure the non-linearity. In particular, the momentum-dependent correlations would read,

$$\frac{\langle V_2^2 V_4^*(p)\rangle}{\sqrt{\langle v_2^4\rangle\langle v_4^2(p)\rangle}} \quad \text{and} \quad \frac{\langle V_2V_3V_5^*(p)\rangle}{\sqrt{\langle v_2^2v_3^2\rangle\langle v_4^2(p)\rangle}} \, . \tag{3.77}$$

In Fig. 3.20, we show the results for the correlation coefficients measuring the nonlinear coupling between $V_4(p)$ and V_2^2 (left) and between $V_5(p)$ and V_3V_2 (right) as a function of the transverse momentum. We present the correlation coefficients for semi-central $(30-40\%)$ collisions only, where the nonlinear components in V_4 and V_5 have dominant contributions. It could be seen that the correlations are the largest for small transverse momentum and the decorrelation gradually increases with increasing transverse momentum in case of $V_2^2 - V_4(p)$ correlation. For $V_2V_3 - V_5(p)$ correlation, there are decorrelations on the either side of average transverse momentum, similar to the triangular flow. Additionally, for mixed-flow correlations we show results corresponding to different η/s with TRENTO initial conditions. The results show a weak dependence on the shear viscosity of the medium. The transverse momentum dependence of the mixed-flow correlations gives an additional constraint on the initial state and on the hydrodynamic evolution.

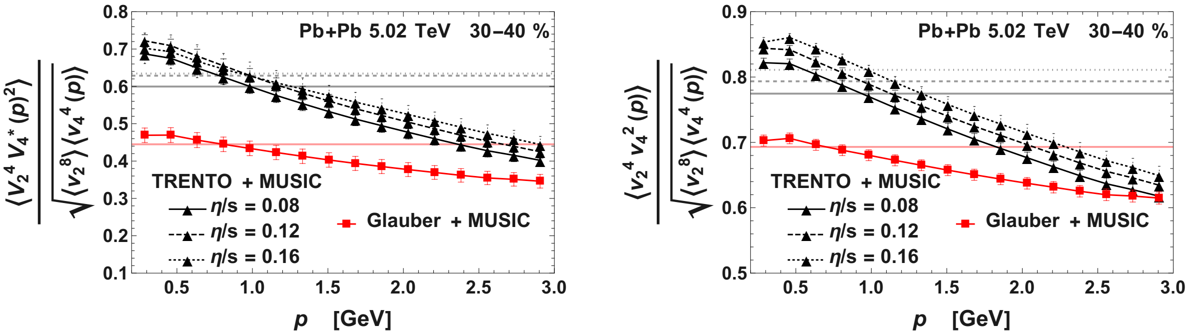

Fig. 3.21 Correlation coefficients between flow vector squared V_2^4 and $V_4^2(p)$ (left) and flow magnitudes squared v_2^4 and $v_4^2(p)$ (right) as a function of the transverse momentum in Pb+Pb collision at 5.02 TeV with $30-40\%$ centrality. The symbols have similar meaning as Fig. 3.20. The figure is from the original publication [125], coauthored by the author.

In order to extract the momentum-dependent flow angle correlation (or event-plane correlation) between mixed flow harmonics, separately from the magnitude decorrelation, similar to the previous methods, correlators involving higher powers of flow harmonics must be taken into account. For example, if we consider the non-linear coupling between V_4 and V_2, the correlation coefficient between the flow vector squared is given by,

$$\frac{\langle V_2^4 V_4^*(p)^2 \rangle}{\sqrt{\langle v_2^8 \rangle \langle v_4^4(p) \rangle}}, \tag{3.78}$$

while the correlation coefficient or factorization-breaking coefficient between the non-linear flow magnitude squared can be constructed as,

$$\frac{\langle v_2^4 v_4(p)^2 \rangle}{\sqrt{\langle v_2^8 \rangle \langle v_4^4(p) \rangle}}, \tag{3.79}$$

and then the flow angle correlation can be estimated from the ratio of the above two as,

$$\frac{\langle V_2^4 V_4^*(p)^2 \rangle}{\langle v_2^4 v_4(p)^2 \rangle} . \tag{3.80}$$

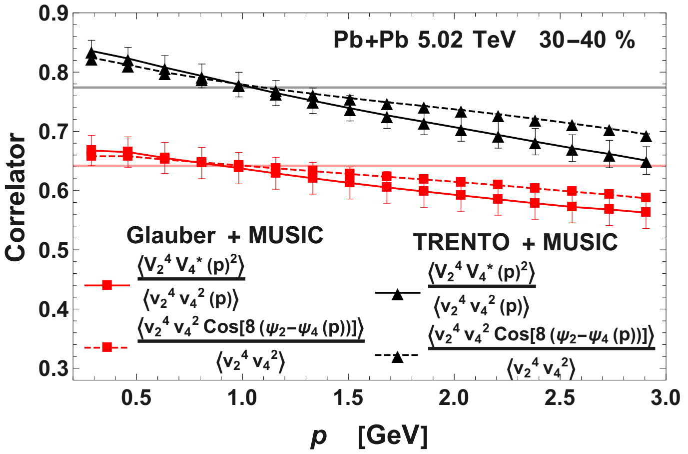

Fig. 3.22 Flow angle decorrelation between V_2^4 and $V_4^2(p)$ as a function of transverse momentum in Pb+Pb collision at 5.02 TeV with $30-40\%$ centrality. The red squares and the black triangles denote the hydrodynamic results obtained with Glauber and TRENTO model initial conditions respectively. The solid lines denote the estimate of the flow angle decorrelation while the dashed lines represent the actual measure of flow angle correlation between the mixed harmonics. Corresponding angle correlations between the momentum-averaged flow V_2^4 and V_4^2, are indicated by the horizontal lines. The figure is from the original publication [125], coauthored by the author.

The correlation coefficients between flow vector and magnitude squared are shown in Fig. 3.21. It should be noted that the correlation between higher powers of the flow vectors (Fig. 3.21 (left)) is smaller than between the lower powers of the respective flow vectors (Fig. 3.20 (left)). Moreover, it could be seen that the flow magnitude decorrelation accounts for about one half of the flow vector decorrelation shown in Fig. 3.21. Therefore, the relation described by Eq. (3.61) is also valid for non-linear mixed-flow correlators.

In Fig. (3.22), we show results for the flow-angle correlation for mixed-harmonics, which involve six-particle correlators and could be extracted from the experimental data. It could be observed that the flow angle decorrelation is again approximately one half of the flow vector decorrelation (Fig. 3.21). We notice that the flow angle correlation (Eq. 3.80) defined as the ratio of the correlation coefficient between flow vectors and of the factorization breaking coefficient between the flow magnitudes, serves as a good approximation for the flow angle correlation weighted with the powers of flow magnitudes,

$$\frac{\langle v_4^2 v_2^4 \cos[8(\Psi_4(p)-\Psi_2)]\rangle}{\langle v_4^2 v_2^4\rangle}, \tag{3.81}$$

which is the true measure of the flow angle correlation as discussed previously. For completeness, in Fig. 3.23, we show the centrality dependence of flow angle decorrelation between momentum averaged flow vectors V_4^2 and V_2^4. Alongside the momentum dependent flow angle correlation depicted in Fig. 3.22, this can serve as an extra experimental observable, showing sensitivity to various models of initial conditions.

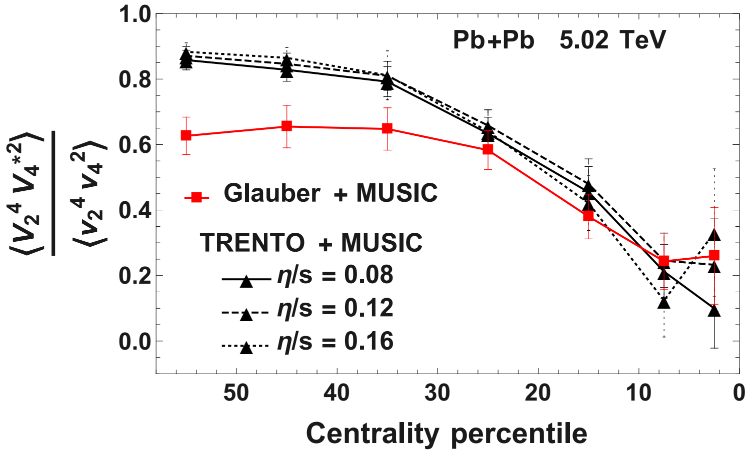

Fig. 3.23 Centrality dependence of the flow angle correlation between V_2^4 and V_4^2 in Pb+Pb collision at 5.02 TeV. The hydrodynamic results with Glauber and TRENTO model are denoted with red squares and black triangles respectively. For the TRENTO model initial conditions, the solid, dashed and dotted lines represent results with the viscosities, $\eta/s = 0.08,\ 0.12$, and 0.16 respectively. The figure is from the original publication [125], coauthored by the author.

3.2.4 Experimental measurements and removing non-flow correlation

As seen in the discussions above, the simulation results for centrality $30-40\%$ do not reproduce the experimental data of the ALICE Collaboration. This is because in semi-central collisions, in general we find stronger decorrelation in our model, while in the experiment the harmonic flow correlation is somewhat larger and sometimes surpassing 1. This might be attributed to a large contribution of non-flow correlations in the measured data.

In order to minimize the non-flow correlations, an estimate of correlation measures can be constructed involving four harmonic flow vectors in separated pseudorapidity bins. For example, using four bins in pseudorapidity located at $-\eta_F, -\eta, \eta, \eta_F$, the factorization coefficient for flow vectors squared can be estimated as,

$$r_{n;2}(p) \simeq \frac{\langle V_n(-\eta_F)V_n^\star(-\eta,p)V_n^\star(\eta,p)V_n(\eta_F)\rangle\langle V_n^\star(-\eta)V_n(\eta)\rangle}{\langle V_n(-\eta_F)V_n^\star(-\eta)V_n^\star(\eta)V_n(\eta_F)\rangle\langle V_n^\star(-\eta,p)V_n(\eta,p)\rangle}\ , \tag{3.82}$$

the factorization breaking coefficient between flow vector magnitudes can be defined as

$$r_{n;2}^{v_n^2}(p) \simeq \frac{\langle V_n(-\eta_F)V_n(-\eta,p)V_n^\star(\eta,p)V_n^\star(\eta_F)\rangle\langle V_n^\star(-\eta)V_n(\eta)\rangle}{\langle V_n(-\eta_F)V_n(-\eta)V_n^\star(\eta)V_n^\star(\eta_F)\rangle\langle V_n^\star(-\eta,p)V_n(\eta,p)\rangle}\ , \tag{3.83}$$

and the flow angle correlation is estimated from the ratio the two quantities above

$$F_n(p) \simeq \frac{\langle V_n(-\eta_F)V_n^\star(-\eta,p)V_n^\star(\eta,p)V_n(\eta_F)\rangle\langle V_n(-\eta_F)V_n(-\eta)V_n^\star(\eta)V_n^\star(\eta_F)\rangle}{\langle V_n(-\eta_F)V_n(-\eta,p)V_n^\star(\eta,p)V_n^\star(\eta_F)\rangle\langle V_n(-\eta_F)V_n^\star(-\eta)V_n^\star(\eta)V_n(\eta_F)\rangle}, \tag{3.84}$$

similar to [86]. The four-particle correlators in these formulae involve flow vectors at different pseudorapidity and transverse momentum. Consequently, in the result we would observe a combination of flow decorrelation in transverse momentum as well as in pseudorapidity. However, assuming the longitudinal decorrelation factorizes from the transverse momentum decorrelation, it eventually cancels between the numerator and the denominator, i.e. we assume,

$$\langle V_n(\eta,p)V_n^*(\eta,p)\rangle \simeq \sqrt{\langle V_n(\eta)V_n^*(\eta)\rangle\langle V_n(p)V_n^*(p)\rangle}\ . \tag{3.85}$$

In the above formulae for experimental measure, we also use the approximation

$$\frac{\sqrt{\langle v_n^4(p)\rangle}}{\langle v_n^2(p)\rangle} \simeq \frac{\sqrt{\langle v_n^4\rangle}}{\langle v_n^2\rangle}\ , \tag{3.86}$$

as discussed earlier in Eq. (3.66). By using this approximation, we remove the difficulty of measuring a four-particle correlator in the experiment, where all flow vectors are defined in a narrow transverse momentum bins, as in the denominators of Eqs. (3.59) and (3.60). Note that the flow vectors at forward and backward rapidities $\pm\eta_F$ do not require the measurement of the transverse momenta of the particles and can be measured using the forward/backward calorimeters. Only the flow vectors $V_n(\pm\eta,p)$ necessitate the measurement of the individual particles' transverse momenta. For this purpose, two bins well separated in pseudorapidity within the central rapidity region of the detector's acceptance can be utilized. Thus employing a simple approximation (Eq. (3.86)) and using well-separated bins in pseudorapidity, the experimental difficulty in measurement of multi-particle correlators due to limited statistics can be surmounted and the influence of non-flow correlations can be substantially reduced.

Chapter 4

Transverse momentum fluctuations in ultracentral collisions

In a heavy-ion collision event, a large number of particles (around 35000 hadrons in a head-on collision of two ^{208}Pb nuclei at 5.02 TeV at the LHC) are emitted at the final state, which share the total energy of the initial fireball in terms of individual momentum, specifically transverse momentum (p_T) which is particularly interesting in the present context. In each such event, one can define a *mean transverse momentum per charged particle*, which we denote as $[p_T]$ and it is defined as $[p_T] \equiv (\sum p_T)/N_{ch}$. Similar to the fluctuations of anisotropic flow, discussed in the previous chapter, event-by-event fluctuations of transverse momentum per particle $[p_T]$, are of great interest and can serve as an excellent and even more direct probe of the QGP matter produced in the collision. For collisions with same N_{ch}, the transverse momentum per particle, $[p_T]$ fluctuates from event to event. There exist of course trivial *statistical* fluctuations of $[p_T]$, due to averaging over finite number of charged particles, but the measured fluctuations are larger than that. The excess fluctuations are known as true *dynamical* fluctuations of $[p_T]$, which we are interested in. They originate due to event-by-event fluctuations of the distribution of the source in the initial state of collisions, known as *shape fluctuation* which could have a geometrical origin as well as a quantum or intrinsic origin reflecting the randomness in positions of the nucleons in colliding nuclei. The dynamical fluctuations of $[p_T]$ have been studied over the years in theoretical models [297–306, 96, 307, 308] and have been measured in experiments [309–314]. In this chapter, we will focus on the characteristics of $[p_T]$ in ultracentral [278, 315–320] Pb+Pb collisions at the LHC. The intriguing behavior of average transverse momentum (which we denote as $\langle p_T \rangle \equiv \langle [p_T] \rangle$, averaged over events) in ultracentral collisions provides a sensitive probe of hydrodynamics and could help in extracting important physical quantities e.g. speed of sound in the QGP medium with utmost precision [173]. After subtracting the trivial statistical fluctuations, the dynamical fluctuations of $[p_T]$ are very small (below 1%) [312]. However, recent measurements by the ATLAS collaboration [102, 321], studying the variation of $[p_T]$ as a function of N_{ch}, shows a very striking and peculiar pattern of

$[p_T]$-fluctuation in the ultracentral (high N_{ch}) regime. This motivated us to perform a meticulous and careful study of $[p_T]$-fluctuation in ultracentral Pb+Pb collisions, which ultimately proves to offer great physical significance and direct probe to the formation of the QGP fluid. The following sections are, for the most part, presentations from the original publications [126, 127], coauthored by the author.

4.1 Variance of $[p_T]$-fluctuation

Fluctuations of the mean transverse momentum per particle $[p_T]$ observed in heavy-ion collisions can have many features. In general, fluctuations can be characterized by different orders of cumulant: mean, variance, skewness, kurtosis etc. Let us first consider the variance, which is the primary quantity when one talks about fluctuations.

4.1.1 Strange behavior of the ATLAS data

We start with the ATLAS data for $[p_T]$-fluctuation [102, 321] presenting the variance as a function of the centrality estimator which can be either the charged particle multiplicity N_{ch} or the transverse energy deposited on the forward calorimeter E_T, shown in Fig. 4.1. The ATLAS collaboration at the LHC detects the charged particles through an inner detector that covers an angular range of approximately $10^\circ < \theta < 170^\circ$ (where θ represents the angle between the collision axis and the particle's direction). The detector measures the transverse momenta of these particles, given by $p_T \equiv p \sin\theta$, where p is the magnitude of total momentum. The analysis includes all charged particles detected in a specific interval of p_T. In particular, results in two p_T intervals: $0.5 < p_T < 5$ GeV$/c$ and $0.5 < p_T < 2$ GeV$/c$ are presented. Let us first consider the results for the interval with larger upper p_T-cut i.e.$0.5 < p_T < 5$ GeV$/c$, the default interval in our analysis. Later we will discuss the effect of p_T-cut dependence of the fluctuations.

A first observation on the plots reveals that after subtracting trivial statistical fluctuations, the remaining dynamical fluctuations [311] are very small, below 1% in central Pb+Pb collisions [312]. We focus on these small dynamical fluctuations in this chapter. The left panel of Fig. 4.1 displays their variance as a function of N_{ch}. It is seen that the variance decreases as N_{ch} increases i.e as we approach towards more central events. The most striking phenomenon is a sudden steep decrease, by a factor of ~ 2, over a narrow interval of N_{ch} around 3700. Other models of the collision in which the Pb+Pb collision is treated as a superposition of independent nucleon-nucleon collisions fail to reproduce this behavior. For example, in the HIJING model [143, 322], the decrease of the variance is found to be proportional to $1/N_{ch}$ [312, 308] for all N_{ch}. In the following, we argue that the impact parameter, b, plays a crucial role behind this phenomenon. It will be shown that the relation between multiplicity N_{ch} and b is not one-to-one, while $[p_T]$ depends on both quantities.

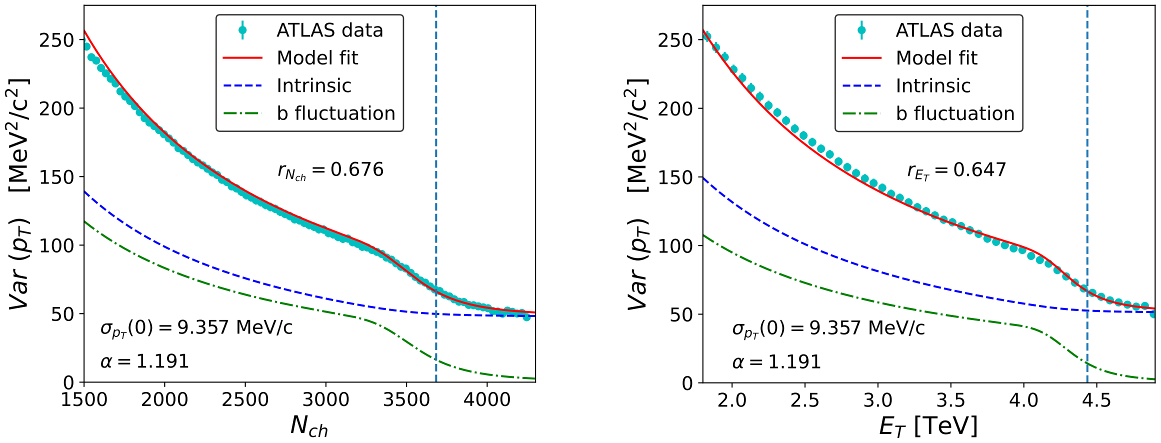

Fig. 4.1 Variance of the transverse momentum per particle $[p_T]$ as a function of the centrality estimators N_{ch} (left) and E_T (right). Symbols represent the ATLAS data [102]. The model fit to the data are represented by the solid red lines. We show separately the two contributions to the variance as per Eq. (4.13) from our model calculation : the contribution from intrinsic and impact parameter fluctuations represented by dashed and dashed-dotted lines respectively. The sum of the two contributions is the solid red line. The figure is from the original publication [126], coauthored by the author.

4.1.2 Hydro vs HIJING results at fixed b

In order to illustrate the dependence of $[p_T]$ on N_{ch}, we simulate 1000 Pb+Pb collisions at 5.02 TeV at fixed impact parameter $b = 0$, using relativistic viscous hydrodynamics, and evaluate N_{ch} and $[p_T]$ for every collision. Our hydro-simulation set up remains same as before and discussed in Appendix. B.1. The right panel of Fig. 4.2 displays the distribution of $[p_T]$ and N_{ch} at $b = 0$. One can see that both the quantities exhibit significant dynamical fluctuations and span finite ranges. In particular, for N_{ch}, the fluctuations around the mean extend up to $\sim 14\%$, whereas it is around $\sim 3\%$ for $[p_T]$. These fluctuations originate from different sources of quantum fluctuations: from the fluctuations in the positions of nucleons at the time of impact [138], from the partonic content of the nucleons [323] as well as from the process of particle production.[1] These fluctuations are taken into account [74] in modern hydrodynamic simulations by implementing a different initial density profile (the initial condition of hydrodynamic equations) for each collision event. The second observation in Fig. 4.2 is that there is a significant positive correlation between $[p_T]$ and N_{ch} in hydrodynamics, which carries a crucial importance in our analysis.

Thermodynamic interpretation of the correlation: The correlation observed in Fig. 4.2 could be interpreted as a natural consequence of local thermalization. Thermalization is an underlying assumption of the hydrodynamic description of the QGP evolution. If we fix the impact parameter b, we essentially fix the collision volume V (left panel of Fig. 4.2). Then at fixed volume, larger N_{ch} implies a larger density N_{ch}/V. In hydrodynamics, as the

---

[1] Please note that we only consider spherical nuclei. For deformed nuclei, the fluctuations in their orientations must be considered, which in turn affect both the multiplicity [119] and the momentum per particle [104].

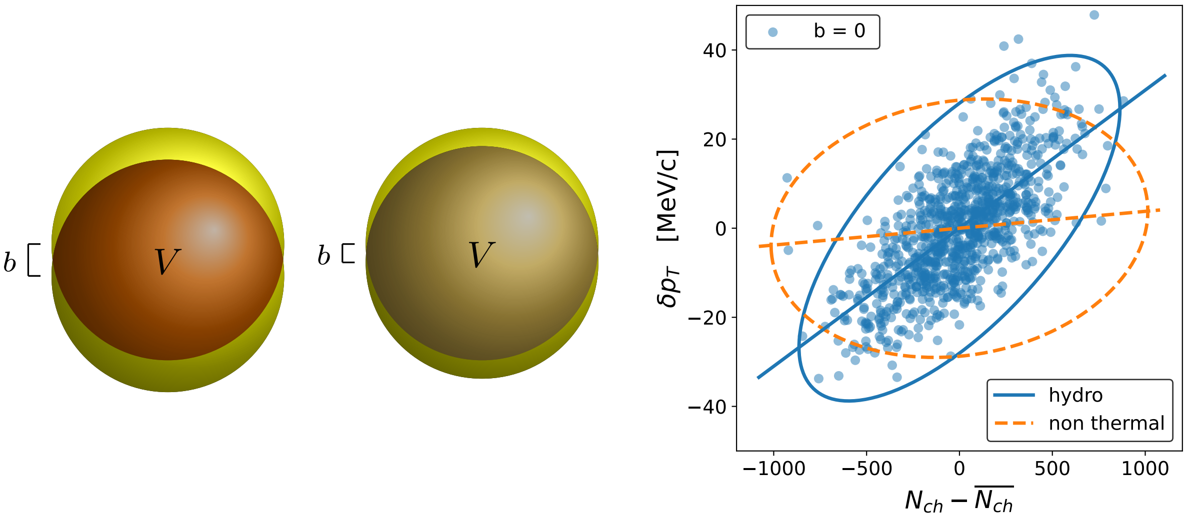

Fig. 4.2 Left: Pictorial depiction of Pb+Pb collisions at fixed multiplicity but different impact parameters: $b = 1.8$ fm (left) and $b = 1.0$ fm (right). The impact parameters correspond to centrality fractions $c_b \simeq 1.5$ % and $c_b \simeq 0.5$ % respectively. The difference between these two values is typically the spread of c_b at fixed multiplicity. A larger value of b corresponds to a smaller collision volume, resulting in a larger density, which we symbolically denote with a darker color. Right: The scatter plot between the charged particle multiplicity N_{ch} and the transverse momentum per particle $[p_T]$ in Pb+Pb collisions at 5.02 TeV and $b = 0$. The symbols and the solid lines represent the results obtained from hydrodynamic simulations for 1000 events. The dashed lines correspond to the results of 1.4×10^6 collisions simulated with HIJING [322] (individual points are not shown). The results are obtained using the same kinematic cuts used in the ATLAS analysis. Instead of plotting N_{ch} and $[p_T]$ themselves, we plot the differences $N_{ch} - \overline{N_{ch}}$ and $\delta p_T \equiv [p_T] - \overline{p_{T0}}$, where $\overline{N_{ch}} = 6662$ and $\overline{p_T} = 1074$ MeV$/c$ are the event averaged values. The straight lines indicate the average value $\overline{\delta p_T}(N_{ch}, b = 0)$ (Eq. 4.13), and the ellipses are 99% confidence ellipses evaluated by assuming that the distribution is a correlated Gaussian using Eq. (4.7). The left panel is from the original publication [127] and the right panel is a modification of the figure in the original publication [126], coauthored by the author.

system is locally thermalized, a larger density corresponds to a higher initial temperature. It should be noted that, relativity plays an essential role in this interpretation. In non-relativistic thermodynamics, density and temperature are independent variables and if we heat a system at constant volume, the density remains unchanged, because the number of particles is conserved. On the other hand, in a relativistic system, particles can be both created (by converting kinetic energy into mass) and destroyed. In that case, a larger temperature implies a higher density. Therefore, a higher density of the system implies a higher temperature, resulting in a higher energy per particle in the final state of hydrodynamic evolution, which eventually means a larger momentum per particle $[p_T]$ [11]. In the previous sentence we mean that the larger energy per entropy in the initial state translates into larger energy per particle in the final state, while maintaining consistency with the thermodynamic picture.

The above phenomenon could be understood from the perspective of collective flow as well. The larger density at fixed collision volume increases the overall magnitude of the outward pressure in the fireball. This is another way of realizing the thermalization of the system manifested through the equation of state (pressure and energy density are related). The larger pressure, through collective flow, results in larger transverse momentum per particle in the final state after the hydrodynamic evolution.

In order to illustrate that the positive correlation between $[p_T]$ and N_{ch} is not trivial but caries a greater physical significance, we also display results of simulations using the HIJING model [322] in the right panel of Fig. 4.2. In HIJING which is a non-thermal model, particles do not interact after they are produced. We see that the corresponding correlation is much smaller (individual points are not shown) by a factor of ~ 10. However, on should note that while thermalization always implies a positive correlation, the converse statement does not hold. As an example, in the color-glass condensate picture of high-energy collisions, such a correlation could be already present at the level of particle production, since both the momentum per particle and the particle density increase with the saturation scale [323]. More details about the analysis of hydrodynamic and HIJING simulations are given in Appendix B.1

$[p_T]$-fluctuation at fixed N_{ch} : Effect of impact parameter fluctuations

Let us now discuss how thermalization plays an important role on the observed $[p_T]$ fluctuations in the data. First, note that the experimental analysis is performed at fixed N_{ch} which is traditionally used as an estimator of centrality, whereas our hydrodynamic simulation is done at fixed b (= 0 to be specific in this case). Both choices are driven by practical considerations. Experimentally, the impact parameter b cannot be measured. On the other hand, in simulations, b can be fixed before starting, and the final multiplicity N_{ch} is obtained only at the end. Therefore, in order to interpret experimental results, we need to provide explanations at fixed N_{ch}, with b varying. Let us understand the phenomenon of thermalization and its effect on $[p_T]$, as explained in the paragraph preceding the last, at fixed N_{ch} and fluctuating b. If N_{ch} is fixed and b fluctuates, then a larger b results in a smaller collision volume V and so a larger density N_{ch}/V, hence larger temperature and eventually larger $[p_T]$ on average in the final state. The opposite scenario occurs if b is smaller, as shown in the left panel of Fig. 4.2. Thus thermalization and collective flow of the QGP medium have direct consequences on $[p_T]$ of the particles and at fixed multiplicity, impact parameter fluctuations contribute to transverse momentum fluctuations. This is the main underlying physics behind our analysis, as we will see that the contribution of impact parameter fluctuations gradually disappears in the ultracentral regime causing the sharp decline observed in the data.

4.1.3 Modelling the correlation : Two dimensional Gaussian

To understand the data, we first need to model the correlation between $[p_T]$ and N_{ch} as seen in Fig. 4.2. The figure shows that even both b and N_{ch} are fixed, $[p_T]$ can still fluctuate. Instead of b, let us use the centrality fraction $c_b \simeq \pi b^2/\sigma_{\text{Pb}}$ [67] (where σ_{Pb} is the inelastic cross section of the Pb+Pb collision) as an equivalent variable throughout this chapter, where c_b lies between 0 and 1. We assume that the joint probability distribution of N_{ch} and $[p_T]$ at fixed c_b, given by $P([p_T],N_{ch}|c_b)$, is a two dimensional correlated Gaussian. The choice of this Gaussian ansatz can be justified through the following arguments. Within a hydrodynamic model, fluctuations in N_{ch} and $[p_T]$ originate from fluctuations in the initial density profile. When the impact parameter is fixed, these density fluctuations stem from quantum fluctuations which may occur either in the wave functions of colliding nuclei [324, 138, 323] or in the dynamics of the collision. At ultrarelativistic energies, the fluctuations at different locations on the transverse plane are independent due to causality. Therefore, it can be thought that a large number of such independent contributions result in the fluctuations of N_{ch} and $[p_T]$. According to the central limit theorem, these fluctuations can be treated as approximately Gaussian.

The two-dimensional Gaussian distribution (as will be shown shortly) is characterized by five parameters: The mean and variance (or equivalently standard deviation) of N_{ch} and of $[p_T]$, which we denote by $\overline{p_T}(c_b)$, $\overline{N_{ch}}(c_b)$, $\mathrm{Var}(p_T|c_b)$, $\mathrm{Var}(N_{ch}|c_b)$ respectively and the Pearson correlation coefficient (or the covariance) $r_{N_{ch}}(c_b)$ between $[p_T]$ and N_{ch}. We expect this correlation to be positive as shown in Fig. 4.2. We now explain how they are obtained.

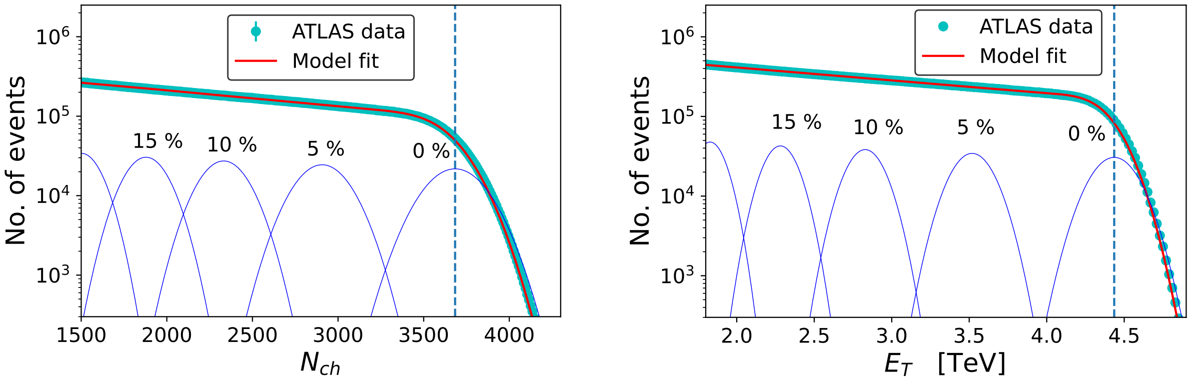

Fig. 4.3 Histogram of the charge particle multiplicity N_{ch} (left), measured by ATLAS, and of transverse energy E_T (right), deposited at the forward and backward calorimeters. The fits using superposition of Gaussians are denoted by the solid lines (Eqs. (4.2) and (4.3)). Contributions of collisions at fixed impact parameter b, given by Eq. (4.2) are shown corresponding to centrality fractions 0, 5%, 10%, 15% by thin blue lines. The "knee" is denoted the vertical dashed line, defined as the average value of N_{ch} or E_T at $b = 0$. The figure is from the original publication [126], coauthored by the author.

Constructing "knee" of the N_{ch}-distribution

Let us discuss how we obtain $\overline{N_{ch}}(c_b)$ and $\sigma_{N_{ch}}(c_b)$. First, without any microscopic modeling, precise information can be obtained about the probability distribution of impact parameter at fixed N_{ch}, given by $P(c_b|N_{ch})$ [67]. To achieve this, we first solve the inverse problem: Finding the probability distribution of N_{ch} at fixed c_b, given by $P(N_{ch}|c_b)$. Then we apply Bayes' theorem:

$$P(c_b|N_{ch})P(N_{ch}) = P(N_{ch}|c_b)P(c_b) \;\;\Rightarrow\;\; P(c_b|N_{ch}) = \frac{P(N_{ch}|c_b)P(c_b)}{P(N_{ch})} \;, \tag{4.1}$$

where $P(c_b) \simeq 2\pi b/\sigma_{Pb}$ depicting the probability distribution of b. As explained earlier, collisions at the same impact parameter vary due to quantum fluctuations, which result in fluctuations of N_{ch}. In nucleus-nucleus collisions, these fluctuations are sufficiently small to be approximated as Gaussian. The Gaussian distribution is characterized by the mean, $\overline{N_{ch}}(c_b)$, and the variance, $\mathrm{Var}(N_{ch}|c_b)$ (or equivalently $\sigma_{N_{ch}}(c_b)$). The distribution is given by,

$$P(N_{ch}|c_b) = \frac{1}{\sqrt{2\pi \mathrm{Var}(N_{ch}|b)}} \exp\left(- \frac{\left(N_{ch} - \overline{N_{ch}}(c_b)\right)^2}{2\mathrm{Var}(N_{ch}|c_b)} \right) . \tag{4.2}$$

In experiment, one measures the marginal distribution $P(N_{ch})$ which is obtained after integrating Eq. (4.2) over c_b within $0 < c_b < 1$:

$$P(N_{ch}) = \int_0^1 P(N_{ch}|c_b) dc_b \;, \tag{4.3}$$

shown in Fig. 4.3 (left). In the figures, we display values of N_{ch} larger than some threshold that corresponds to 20% centrality, which can be considered as fairly central collisions on which our analyses focus. The distribution $P(N_{ch})$ shows a mild variation up to $N_{ch} \sim 3500$, after which it declines sharply. We assume that $\overline{N_{ch}}(c_b)$ is a smooth function of c_b, and parametrize it as the exponential of a polynomial. A third-degree polynomial provides an excellent fit to $P(N_{ch})$ within this range:

$$\overline{N_{ch}}(c_b) = \overline{N_{ch}}(0) \exp\left(- \sum_{k=1}^{3} a_k c_b^k \right) . \tag{4.4}$$

Similarly, we assume that the variance $\mathrm{Var}(N_{ch}|c_b)$ encounters a smooth variation with c_b. The parameters are obtained by fitting Eq. (4.3) as a superposition of Gaussians, to the distribution $P(N_{ch})$ measured by ATLAS in Pb+Pb collisions. The fit is shown in Fig. 4.3. We normalize the probability distribution $P(N_{ch})$ using the centrality calibration provided by the ATLAS collaboration, that 40% of events have $N_{ch} > 705$. The fit is in agreement with data within 2%.

Through fitting we can precisely reconstruct $\overline{N_{ch}}(c_b)$ and $\mathrm{Var}(N_{ch}|c_b = 0)$ [325]. The *knee* of the distribution, representing the mean value of N_{ch} for collisions at $c_b = 0$, is accurately reconstructed, and denoted with a vertical line on Fig. 4.3. Above this knee, the rapid decline of $P(N_{ch})$ provides direct access to $\mathrm{Var}(N_{ch}|c_b = 0)$. It is important to note that the variance can only be reconstructed at $c_b = 0$, and we assume $\mathrm{Var}(N_{ch}|c_b)/\overline{N_{ch}}(c_b)$ to be constant by default. Additionally, we have tested two alternative scenarios: one assuming constant $\mathrm{Var}(N_{ch}|c_b)$ and another assuming constant $\mathrm{Var}(N_{ch}|c_b)/\overline{N_{ch}}(c_b)^2$. We have checked the robustness of our results with respect to these assumptions; the quality of the fit remains equally good and the

N	N_{ch}	E_T
$\overline{N}(b=0)$	3683 ± 4	4.435 ± 0.003 TeV
$\sqrt{\mathrm{Var}(N\|b=0)}$	168.1 ± 0.1	0.1433 ± 0.0001 TeV
a_1	4.31 ± 0.02	4.18 ± 0.01
a_2	-4.19 ± 0.03	-3.45 ± 0.01
a_3	10.21 ± 0.09	8.54 ± 0.05

Table 4.1 Values of the fit parameters for Pb+Pb collisions at $\sqrt{s_{NN}} = 5.02$ TeV. The central value for each parameter is obtained with the assumption that the variance is proportional to the mean. The error bars reflect the changes after considering alternate scenario with the variance being constant, or proportional to the square of the mean.

fit parameters are essentially unchanged, as summarized in Table 4.1. Thus performing the fit to the N_{ch} distribution, along with our assumption, we obtain two parameters: $\overline{N_{ch}}(c_b)$ and $\mathrm{Var}(N_{ch}|c_b)$, out of the five parameters of the correlated Gaussian.

In our analysis, the events with multiplicities above the knee are termed as ultracentral collisions [326, 278]. These events constitute a small fraction of the total, approximately 0.35%. However, ATLAS has observed enough collisions that for a few events N_{ch} exceeds the knee by 20%, corresponding to 4 standard deviations. It should be noted that the Poisson fluctuations contribute only by 15% to the variance [325], indicating that N_{ch} fluctuations are predominantly due to dynamical factors.

The main source of error in determining the impact parameter from data lies in the global normalization, due to the difficulty in experimentally estimating which fraction of the cross-section is detected [71]. Since we are interested in ultracentral collisions, this issue can be ignored. When we mention using the 20% most central events, we refer to the 20% most central of the events that are actually observed in the detector. The overlapping circles in Fig. 4.4 are pictorial depictions of the colliding Pb nuclei, having a radius $R = 6.62$ fm. The values of b are calculated from the inelastic cross section of Pb+Pb collisions, $\sigma_{PbPb} = 767$ fm^2. Using Eqs. (4.2) and (4.3), the probability distribution of the impact parameter at fixed N_{ch} is obtained from Eq.(4.1):

$$P(c_b|N_{ch}) = \frac{1}{P(N_{ch})} P(N_{ch}|c_b), \tag{4.5}$$

where $P(c_b) = 1$ have been used, because the probability distribution of c_b is uniform by construction. The distributions $P(c_b|N_{ch})$ becomes narrower as we move towards ultracentral collisions, illustrated in Ref. [67].

Impact parameter dependence of other parameters: For the 30% most central collisions, the average transverse momentum is largely independent of centrality [327]. Therefore, we assume $\overline{p_T}(c_b)$ is independent of c_b, and we denote its value by $\overline{p_{T0}}$ ($\equiv \langle p_T \rangle$). We decompose $[p_T] = \overline{p_{T0}} + \delta p_T$, and we only model the distribution of δp_T, as we show below. Since we only consider fluctuations around $\overline{p_{T0}}$, our results are independent of its value. The variance

$\text{Var}(p_T|c_b)$ may vary with the impact parameter, but this dependence should be smooth. For statistical fluctuations, the variance is proportional to $1/N_{ch}$. For the c_b dependence, we assume a more general form for $\text{Var}(p_T|c_b)$ which behaves like a power law of the mean multiplicity:

$$\text{Var}(p_T|c_b) \equiv \sigma^2_{p_T}(c_b) = \sigma^2_{p_T}(0)\left(\frac{\overline{N_{ch}}(0)}{\overline{N_{ch}}(c_b)}\right)^{\alpha}\ , \tag{4.6}$$

where $\sigma_{p_T}(0)$ and α are constants. Finally, for the sake of simplicity, we also assume that the correlation coefficient $r_{N_{ch}}$ does not vary with impact parameter.

4.1.4 $\text{Var}(\text{p}_\text{T}|\text{N}_\text{ch})$ from the correlated Gaussian :

Once we fix the impact parameter dependence of the parameters of correlated Gaussian distribution, we can fit the remaining three parameters ($\overline{N_{ch}}(c_b)$ and $\text{Var}(N_{ch}|c_b)$ are already fixed) $\sigma_{p_T}(0)$,α and $r_{N_{ch}}$ to the ATLAS data for variance. To do so, we need an analytic expression for $\text{Var}(\text{p}_\text{T}|\text{N}_\text{ch})$ which is obtained from the correlated Gaussian distribution at fixed c_b, $P(\delta p_T, N_{ch}|c_b)$ given by,

$$\begin{aligned} P(\delta p_T, N_{ch}|c_b) = &\frac{1}{2\pi\sqrt{(1-r^2)\text{Var}(p_T)\text{Var}(N_{ch})}} \\ &\times \exp\left[\frac{1}{1-r^2}\left(-\frac{(\delta p_T)^2}{2\text{Var}(p_T)} - \frac{\left(N_{ch}-\overline{N_{ch}}\right)^2}{2\text{Var}(N_{ch})} + \frac{r\left(N_{ch}-\overline{N_{ch}}\right)\delta p_T}{\sqrt{\text{Var}(N_{ch})\text{Var}(p_T)}}\right)\right], \end{aligned} \tag{4.7}$$

where the impact parameter (c_b) dependence on the right hand side is implicit, we have used r to represent $r_{N_{ch}}$ and as explained above instead of $[p_T]$, we use $\delta p_T \equiv [p_T] - \overline{p_{T0}}$. The linear correlation between $[p_T]$ and N_{ch} can be understood as,

$$\int_{-\infty}^{\infty}\int_{-\infty}^{\infty} \delta p_T (N_{ch} - \overline{N_{ch}}) P(\delta p_T, N_{ch}) dN_{ch} d\delta p_T = r\sqrt{\text{Var}(N_{ch})\text{Var}(p_T)}\ . \tag{4.8}$$

A characteristic of the two-dimensional Gaussian distribution is that its marginal distributions which are obtained by integrating over one of the variables, are also Gaussians. Integrating Eq. (4.1.3) over δp_T, one recovers Eq. (4.2). Similarly, integrating Eq. (4.1.3) over N_{ch}, one obtains the distribution of δp_T at fixed c_b:

$$P(\delta p_T|c_b) = \frac{1}{\sqrt{2\pi \text{Var}(p_T|c_b)}} \exp\left(-\frac{(\delta p_T)^2}{2\text{Var}(p_T|c_b)}\right)\ . \tag{4.9}$$

Another interesting property of the two-dimensional Gaussian is that if one of the variables is fixed, let us say N_{ch}, the distribution of the other variable, e.g. δp_T, is also Gaussian. The distribution of δp_T at fixed N_{ch} and c_b is defined by,

$$\begin{aligned}
P(\delta p_T|N_{ch},c_b) &= \frac{P(\delta p_T,N_{ch}|c_b)}{P(N_{ch}|c_b)} \\
&= \frac{1}{\sqrt{2\pi\kappa_2(c_b)}}\exp\left[-\frac{(\delta p_T-\kappa_1(c_b))^2}{2\kappa_2(c_b)}\right],
\end{aligned} \tag{4.10}$$

where we omit the dependence on N_{ch} in the right-hand side. The coefficients $\kappa_1(c_b)$ and $\kappa_2(c_b)$ represent the mean and the variance of δp_T at fixed N_{ch} *and* c_b, given by:

$$\begin{aligned}
\kappa_1(c_b) \equiv \overline{\delta p_T}(N_{ch},c_b) &= r\sqrt{\frac{\mathrm{Var}(p_T|c_b)}{\mathrm{Var}(N_{ch}|c_b)}}\left(N_{ch}-\overline{N_{ch}}(c_b)\right) \\
&\equiv r\frac{\sigma_{p_T}(c_b)}{\sigma_{N_{ch}}(c_b)}\left(N_{ch}-\overline{N_{ch}}(c_b)\right) , \\
\text{and} \quad \kappa_2(c_b) \equiv \mathrm{Var}(p_T|N_{ch},c_b) &= \left(1-r^2\right)\mathrm{Var}(p_T|c_b) \equiv \left(1-r^2\right)\sigma^2_{p_T}(c_b) ,
\end{aligned} \tag{4.11}$$

where we omit c_b-dependence of r as per our assumption.

The n^{th} order moment is obtained by multiplying Eq. (4.10) with δp_T^n and integrating over δp_T. The first and second order moments are given by :

$$\langle \delta p_T \rangle = \kappa_1 \quad \text{and} \quad \langle \delta p_T^2 \rangle = \kappa_1^2 + \kappa_2 , \tag{4.12}$$

where the dependencies on c_b and N_{ch} are implicit. These moments are then averaged over c_b, to obtain only the N_{ch}-dependence which can be compared to the data. The mean and variance of p_T at fixed N_{ch} are finally constructed using the c_b-average of the moments in Eq. (4.12) as,

$$\begin{aligned}
\langle \delta p_T|N_{ch}\rangle &= \langle \kappa_1\rangle_{c_b} = \langle \overline{\delta p_T}(N_{ch},c_b)\rangle_{c_b} , \\
\mathrm{Var}(p_T|N_{ch}) &= \langle \kappa_1^2+\kappa_2\rangle_{c_b} - \langle\kappa_1\rangle_{c_b}^2 = \left(\langle\kappa_1^2\rangle_{c_b} - \langle\kappa_1\rangle_{c_b}^2\right) + \langle\kappa_2\rangle_{c_b} \\
&= \left(\langle \overline{\delta p_T}(N_{ch},c_b)^2\rangle_{c_b} - \langle \overline{\delta p_T}(N_{ch},c_b)\rangle_{c_b}^2\right) + \langle \mathrm{Var}(p_T|N_{ch},c_b)\rangle_{c_b} ,
\end{aligned} \tag{4.13}$$

with,

$$\langle \ldots \rangle_{c_b} \equiv \int_0^1 \ldots P(c_b|N_{ch})dc_b = \frac{1}{P(N_{ch})}\int_0^1 \ldots P(N_{ch}|c_b)dc_b , \tag{4.14}$$

where we have used Eq. (4.1)[2] in the last line. Putting the explicit expressions of $\overline{\delta p_T}(N_{ch},c_b)$ and $\mathrm{Var}(p_T|N_{ch},c_b)$ from Eq. (4.11) into Eq. (4.13), we obtain the multiplicity dependence of mean (average) of δp_T and variance of p_T. The first term of the expression for variance in Eq. (4.13), denoted within bracket, stems from the variation of $\overline{\delta p_T}(N_{ch},c_b)$ with impact

---

[2] c_b is the cumulative distribution of b, therefore, $P(c_b) = 1$ by construction.

parameter, reflecting the contribution of b-fluctuation to $[p_T]$-fluctuation. We refer to the second term as the intrinsic variance (or intrinsic fluctuations), in the sense that it is not a by-product of impact parameter fluctuations. We will see that both terms are of comparable magnitudes below the knee, and most importantly the first term explains the peculiar pattern (steep fall) observed for large N_{ch}. The variance $\mathrm{Var}(p_T|N_{ch})$ is fitted to the ATLAS data in Fig. 4.1 (left) with three parameters $\sigma_{p_T}(0)$, α and $r_{N_{ch}}$, details of which are provided in Appendix B.2. The fitted values of these parameters are shown on the figure.

4.1.5 Fit results: Thermalization and predictions for mean $\langle \delta p_T \rangle$

Let us first examine the distribution of δp_T and N_{ch} returned by our fit, shown in the left panel of Fig. 4.4. The white curves represent 99% confidence ellipses at fixed impact parameter [325], which are drawn using the probability given by Eq. (4.9). It can be seen that they are tilted with respect to the horizontal axis, similar to the hydrodynamic calculation of Fig. 4.2. This tilt reflects the positive correlation between δp_T and N_{ch}, parameterized by $r_{N_{ch}}$. As explained above, this correlation is a natural consequence of thermalization. The width of the δp_T distribution for fixed N_{ch} can be attributed to two contributions. A part of it comes from the fact that several ellipses contribute for a given N_{ch} (first term in Eq. (4.13)), and the rest is due to the vertical width of a single ellipse (second term in Eq. (4.13)).

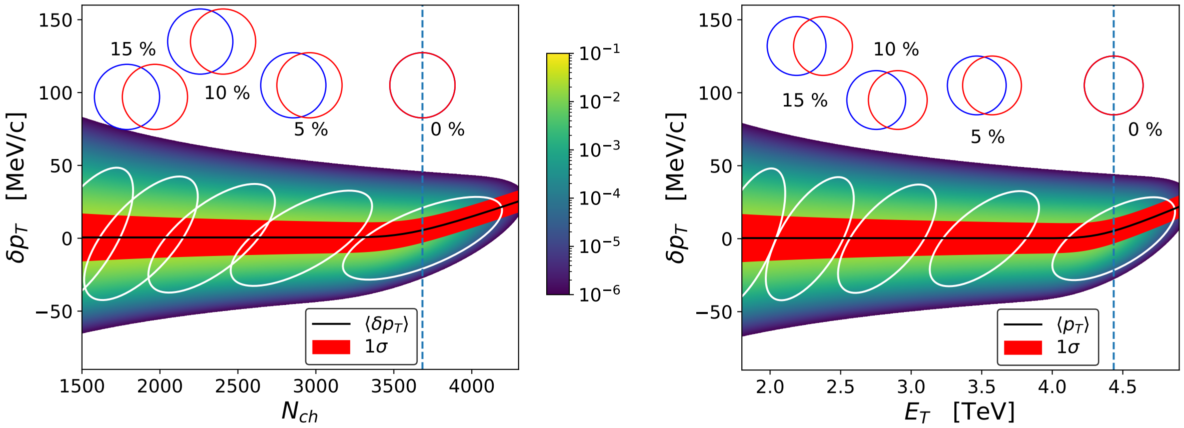

Fig. 4.4 Joint distribution of δp_T and N_{ch} (left) or E_T (right), obtained from the fit of our model and integrating Eq. (4.7) over c_b. The white curves are 99% confidence ellipses at fixed impact parameters, obtained from the correlated Gaussian distribution in Eq. (4.1.3) at fixed values of c_b. Schematic representation of two nuclei colliding with these impact parameters are also shown. The black line is the mean value of δp_T (Eq. (4.13)), and the red band is the 1-σ band, representing square-root of the red line in Fig. 4.1. The figure is from the original publication [126], coauthored by the author.

The left panel of Fig. 4.1 displays the data and the model fit, along with the two terms of Eq. (4.13). There exist equal contributions from the two terms below knee. However, above knee the first term (b-fluctuation) gradually disappears. Thus our model precisely explains the observed steep decrease of the variance around the knee which comes from the first term, namely, from impact parameter fluctuations at fixed N_{ch}, whose effect becomes negligible in ultracentral collisions. The magnitude of this term is essentially determined by the correlation coefficient $r_{N_{ch}}$, which is thus constrained by data.

As a corollary, we also predict a small increase in the average transverse momentum $\langle \delta p_T \rangle$, represented by a black line in Fig. 4.4, in ultracentral collisions. This effect had been predicted a while ago [173, 328] and has recently been observed by CMS collaboration [329]. Note that our model calculation quantitatively predicts this increase.

Using different centrality estimator: Transverse energy E_T

A particularity of the ATLAS analysis is the use of an alternative centrality estimator, in addition to N_{ch}: the transverse energy E_T[3]. This is defined as energy multiplied by $\sin\theta$ and is measured in two calorimeters located symmetrically on either side of the collision point, covering approximately the angular ranges $1° < \theta < 5°$ and $175° < \theta < 179°$. Our analyses and results are presented for the observables of interest with both centrality estimators N_{ch} and E_T, presented on the left and right panel of the figures respectively. The variance analysis can be repeated by selecting events based on E_T, rather than N_{ch}, as illustrated in the right panel of Fig. 4.3. Similarly, our model calculation can be repeated by replacing N_{ch} with E_T everywhere. This serves as a valuable and rigorous check for the validity of our approach.

Although the distributions of N_{ch} and E_T are similar in shape (Fig. 4.3 (right)), it could be seen that the decline above the knee is steeper for E_T than for N_{ch}. Please also note, only 0.26% of events fall above the knee for E_T, while for N_{ch} it is 0.35%. It is interesting to note, despite this difference, the observed decrease in variance around the knee remains consistent for both estimators, as measured by ATLAS (Fig. 4.3 (right)). The parameters $\sigma_{p_T}(0)$ and α, determining the impact parameter dependence of the variance of $[p_T]$, should not depend on whether the events are classified according to N_{ch} or E_T. Therefore, we find the values that show best simultaneous agreement with N_{ch} and E_T-based data, discussed in detail in Appendix B.2.

However, the Pearson correlation coefficient r_{E_T} between $[p_T]$ and E_T is independently fitted and does not necessarily match $r_{N_{ch}}$. Note that the correlation $r_{N_{ch}}$ pertains to the correlation between $[p_T]$ and N_{ch} for the *same* particles, whereas r_{E_T} pertains to the correlation between $[p_T]$ and the E_T measured in different angular windows separated by rapidity interval. Therefore we expect $r_{E_T} < r_{N_{ch}}$, which is confirmed by the fit from our analysis. The similarity in the values indicates that particle depositions in different θ windows are strongly correlated.

4.1.6 Effect of p_T interval on variance

Another peculiar aspect of the ATLAS analysis is its study of how $[p_T]$-fluctuations change with the p_T interval. The default analysis involves all particles in the range $0.5 < p_T < 5$ GeV/c

---

[3] The quantity used as the centrality estimator can be generically denoted as N, can be either N_{ch} or E_T.

(particles with $p_T < 0.5$ GeV$/c$ are not detected, and those with $p_T > 5$ GeV$/c$ are likely to be associated with jets, and not relevant to the collective behavior). Additionally, in this section we present results for the particles in the range $0.5 < p_T < 2$ GeV$/c$, which excludes about 7% of the particles as considered in the previous case. The remarkable effect is that the variance decreases by a factor ~ 4, when comparing these intervals in Figs. 4.1 and 4.5. Strikingly, the phenomenon is also observed in the hydrodynamic simulations, where the magnitude of δp_T is reduced by a factor of approximately 2 for the smaller p_T-interval (see Fig. 4.6). Numerically, the variance representing the average value of δp_T^2, decreases by a factor 4.3 ± 0.2, aligning with the ATLAS result.

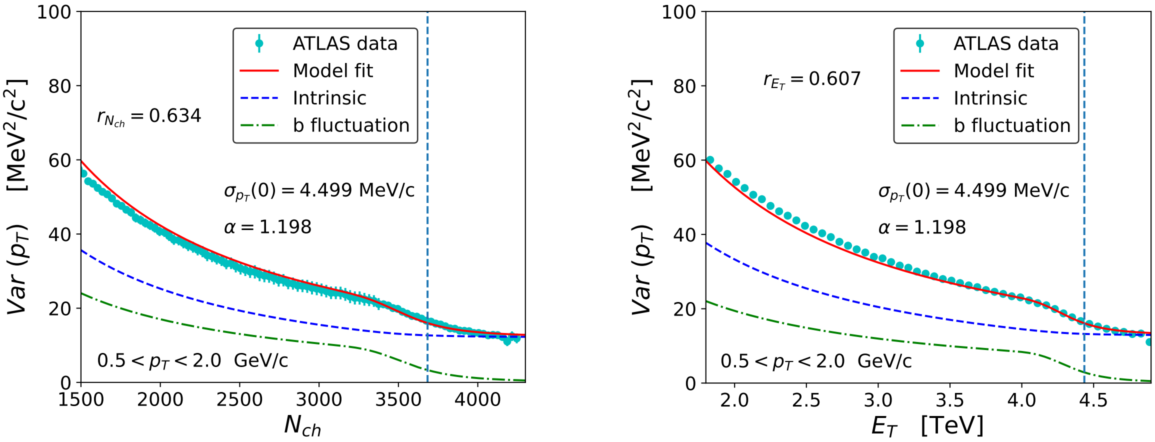

Fig. 4.5 Same as Fig. 4.1, but for the the transverse momentum range of the particles in: $0.5 < p_T < 2$ GeV$/c$. One sees that there is a factor of ~ 4 reduction in the magnitude of variance in comparison to Fig. 4.1 with $0.5 < p_T < 5$ GeV$/c$, thus showing the effect of p_T interval on p_T-fluctuation.

We provide an estimate how the variance depends on the p_T selection. Fluctuations in fluid velocity cause global fluctuations in the p_T distribution, where the tail of the distribution is largely affected. Thus in hydrodynamics, event-by-event $[p_T]$ fluctuations arise from transverse fluid velocity fluctuations. The momentum distribution of particles follows a boosted Boltzmann distribution, where p_T appears in the exponent. Thus relative change in the p_T distribution $f(p_T) \equiv \frac{dN}{dp_T}$ due to a small change in the fluid velocity is linear in p_T [330]:

$$f(p_T) = \langle f(p_T)\rangle \Big(1 + x(p_T - \langle p_T\rangle)\Big), \tag{4.15}$$

where $\langle f(p_T)\rangle$ denotes the event average of the p_T distributions, and $\langle p_T\rangle \equiv \langle [p_T]\rangle$ given by,

$$\langle p_T\rangle \equiv \frac{\int p_T \langle f(p_T)\rangle dp_T}{\int \langle f(p_T)\rangle dp_T} \tag{4.16}$$

is the average p_T. Here x is a random variable fluctuating event to event around zero. For a class of events with the same multiplicity, the integral of $f(p_T) - \langle f(p_T)\rangle$ must vanish, making the

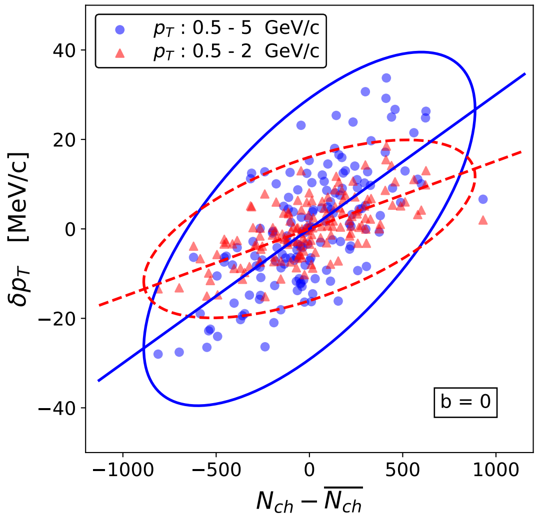

Fig. 4.6 Distribution of δp_T and N_{ch} for two different p_T-intervals: $0.5 < p_T < 2.0$ GeV and $0.5 < p_T < 5.0$ GeV, denoted by red and blue symbols respectively, similar to Fig. 4.2. The results are shown for 150 events in Pb+Pb collision at 5.02 TeV and $b = 0$ obtained from hydrodynamics. The solid and red curves denote the 99% confidence ellipses. For the interval $0.5 - 5$ GeV$/c$, the value of the average (Eq. (4.16)) $\overline{p_{T0}}$ is 1074 MeV$/c$. As one removes particles with higher values of p_T, the average value $\overline{p_{T0}}$ decreases to 970 MeV$/c$ for $0.5 - 2$ GeV$/c$ interval. The straight lines indicate the average value $\overline{\delta p_T}(N_{ch}, b = 0)$. The values of the standard deviations (Eq. (4.17)) obtained for the two intervals are 6 MeV/c and 13 MeV/c for $0.5 - 2$ GeV$/c$ and $0.5 - 5$ GeV$/c$ respectively, showing factor of 2 increase (i.e. factor of 4 increase in variance) and reflecting consistency with ATLAS data.

relative fluctuation proportional to $p_T - \langle p_T \rangle$, instead of just p_T. The fluctuations in transverse momentum per particle are obtained by integrating the spectrum (4.15) over the p_T range used in the analysis:

$$\sigma_{p_T} = x \frac{\int_{p_{\min}}^{p_{\max}} (p_T - \langle p_T \rangle)^2 \langle f(p_T) \rangle dp_T}{\int_{p_{\min}}^{p_{\max}} \langle f(p_T) \rangle dp_T} \,. \tag{4.17}$$

We assume the fluctuations are small enough to replace $f(p_T)$ with the average distribution $\langle f(p_T) \rangle$ in the denominator.

The dependence of the right-hand side of Eq. (4.17) on the upper bound $p_{\max}$ can be evaluated using spectra measured by ALICE in central Pb+Pb collisions at the same energy [257], in place of $\langle f(p_T) \rangle$. We find that lowering $p_{\max}$ from 5 down to 2 GeV$/c$ reduces the right-hand side of Eq. (4.17) by a factor 2.05, leading to a decrease in variance by a factor 4.23, consistent with ATLAS observations.

One should note, in this model, the only variable parameter in Eq. (4.17) is the overall factor x, which sets the fluctuation magnitude. This can be checked in hydrodynamics. First, it could be checked by eye that in Fig. 4.6, symbols of different types appear in pairs with the same N_{ch}. Each pair represents one collision event, and the proportionality factor x in Eq. (4.17) fluctuates event-by-event. The change in δp_T [4] from one symbol to the another in the same pair

---

[4] Please note that $\langle \delta p_T \rangle$ is the average shown in Fig. 4.4.

is roughly the same for all events, as suggested by Eq. (4.17). More quantitatively, the Pearson correlation between the two δp_T values for each event (i.e. between $\delta p_T(0.5 < p_T < 5)$ and $\delta p_T(0.5 < p_T < 2)$) is about ~ 0.97, close to its maximum value 1, implied by Eq. (4.17). The observed dependence of the variance on the p_T selection is another layer of evidence supporting the hydrodynamic origin of $[p_T]$ fluctuations.

Importance of b-fluctuation

It is interesting to note that the impact parameter is a classical quantity. One can calculate its quantum uncertainty which is negligible: Heisenberg's principle gives $\delta b \equiv \hbar/P \sim 4 \times 10^{-7}$ fm for a Pb+Pb collision at the LHC, insignificant compared to the range spanned by b, of order 15 fm.[5] The *only* classical quantity characterizing a collision is the impact parameter, and collisions with the same impact parameter differ only by quantum fluctuations. As the collision occurs at high energy, a single quantum fluctuation can produce a large number of particles, which promotes such fluctuations to the status of a classical fluctuations. (Elliptic flow in central collisions [324] and triangular flow [48] are driven by a similar mechanism.) The effect studied here, involves a subtle interplay between classical fluctuations of impact parameter, and quantum fluctuations of the collision multiplicity.

4.2 Non-Gaussian features of $[p_T]$-fluctuation : Skewness and Kurtosis

In the previous section, we discussed the leading order cumulant of $[p_T]$-fluctuation i.e. variance. However, one could also think of higher order cumulants, namely skewness and kurtosis of $[p_T]$-fluctuation, which can also exhibit interesting features in ultracentral collisions. The observed decrease in the variance above the knee is caused by the decrease of impact parameter fluctuations with the increase in multiplicity at the ultracentral regime. In this section, we will show that the same mechanism is also responsible for strong non-Gaussian characteristics of the fluctuations of $[p_T]$ in ultracentral collisions.[6] Using the same model of $[p_T]$ fluctuations outlined above, we present robust quantitative, parameter-independent predictions for skewness and excess kurtosis, which characterize standard measures of the non-Gaussianity.

---

[5] Note that in event-by-event simulations, the impact parameter is correctly defined only if each nucleus is recentered after randomly drawing nucleon positions. The recentering correction is larger by orders of magnitude than the quantum uncertainty. It is however *not* implemented in the simulations shown in Fig. 4.2, but this does not alter the conclusions we draw from the figure.

[6] It has already been observed that hydrodynamic calculations imply a significant skewness of $[p_T]$ fluctuations [307], but the crucial role of impact parameter has not been studied.

4.2.1 Non-Gaussianity from a simplified model

We begin by explaining the origin of non-Gaussian fluctuations based on a simplified model, in which $[p_T]$ is a single-valued function of N_{ch} and c_b. In other words, $[p_T]$ does not fluctuate if we fix both N_{ch} and c_b. Given that the variation of c_b at fixed N_{ch} is small, the dependence of $[p_T]$ on c_b can be linearized:[7]

$$[p_T] = p_T^{\min} + \lambda c_b, \tag{4.18}$$

where $p_T^{\min}$ and λ depend on N_{ch}. This approximation in turn means that the correlation coefficient between $[p_T]$ and N_{ch}, r assumes a value close to 1 [8]. The probability distribution of $[p_T]$ at fixed N_{ch}, is then determined by the probability distribution of c_b at fixed N_{ch}. The latter one, denoted by $P(c_b|N_{ch})$, is obtained using Eq. (4.1) and from the probability distribution of N_{ch} at fixed c_b (Eq. (4.2)), which we have assumed above to be Gaussian. For ultracentral collisions where $c_b \ll 1$, one can neglect the dependence of $\sigma_{N_{ch}}$ on c_b, and then the variation of the mean can be linearized as:

$$\overline{N_{ch}}(c_b) = N_{\text{knee}} - \beta c_b, \tag{4.19}$$

where $N_{\text{knee}} \equiv \overline{N_{ch}}(0)$ and β determines how mean multiplicity decreases with centrality. As was done earlier, the values of these parameters can be obtained by fitting the measured distribution of N_{ch}, $P(N_{ch})$(Fig. (4.3)). From the numerical fit, we obtain the values of the parameters as: $N_{\text{knee}} = 3680$, $\sigma_{N_{ch}} = 168$, $\beta = 18300$, similar to Table 4.1.

With the linear approximation, the probability distribution of c_b for fixed N_{ch} is then given by,

$$P(c_b|N_{ch}) = \frac{P(N_{ch}|c_b)}{P(N_{ch})} \propto \exp\left(-\frac{(N_{ch} - N_{\text{knee}} + \beta c_b)^2}{2\sigma_{N_{ch}}^2}\right), \tag{4.20}$$

where we have used Eqs. (4.1) and (4.19). Eq. (4.20) indicates that the distribution of c_b is Gaussian, with a width $\sigma_{N_{ch}}/\beta \simeq 0.9\%$. However, this distribution is not a full Gaussian, but rather a *truncated* Gaussian distribution, which is truncated on the left because of the boundary condition $c_b \geq 0$ [66, 67]. Consequently, Eq. 4.18 suggests that the probability distribution of $[p_T]$ is also a truncated Gaussian, subject to the boundary condition $[p_T] \geq p_T^{\min}$. The truncated Gaussian distribution for $[p_T]$ is obtained from Eq. (4.20), with the condition that $[p_T]$ is given by Eq. (4.18). This results in the solid curves shown in Fig. 4.7, which are truncated on the left due to the lower limit of $[p_T]$ (c_b).

This truncation has several effects which lead to peculiar patterns for the cumulants of $[p_T]$-fluctuation in the ultracentral regime. First, the distribution of $[p_T]$ becomes narrower (Fig. 4.7), which results in a decrease of the variance, which we have discussed and is reflected

---

[7] Note that observables depend quadratically on c_b for small b due to symmetry reasons [331], which percludes a dependence of the type $\sqrt{c_b}$ for small b.

[8] This could be understood if we consider the hydro results in Fig. 4.2 (right). If $[p_T]$ (or equivalently δp_T) does not fluctuate at fixed c_b and N_{ch}, then the values of δp_T coincides with the average $\overline{\delta p_T}(N_{ch}, c_b)$ given in Eq. (4.11) making $r \to 1$.

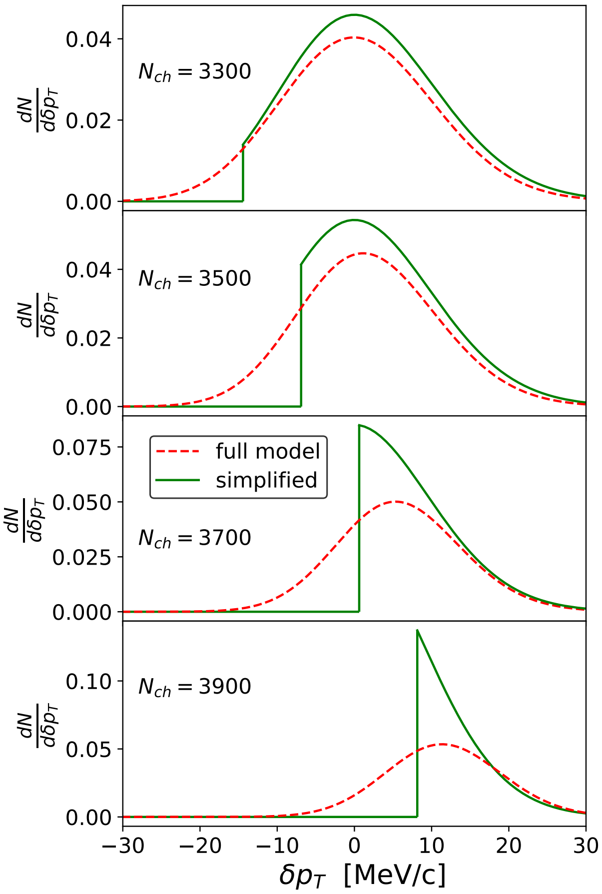

Fig. 4.7 Probability distribution of $[p_T]$ at fixed multiplicity N_{ch}, for various values of N_{ch}. If the centrality is defined according to N_{ch}, these values of N_{ch} correspond to the centrality fractions, from top to bottom, 2.2%, 1.1%, 0.3% and 0.04%. Similar to previous figures, we plot the distribution of δp_T rather than $[p_T]$. The distributions obtained with the simplified model are denoted by the solid lines, where $[p_T]$ only depends on N_{ch} and impact parameter (Eq. (4.19)) and it does not fluctuate if both are fixed. The results with a more realistic model are represented by the dashed lines, assuming Gaussian fluctuations of $[p_T]$ at fixed N_{ch} and c_b, obtained from Eq. (4.21), which is referred as "full model" on the figure. The figure is from the original publication [127], coauthored by the author.

in Figs. 4.1 and 4.5. Second, the truncation gives rise to non-Gaussian features such as skewness and kurtosis, which we discuss below.

4.2.2 Skewness and kurtosis from the full model

In reality, in addition to the effect of impact parameter fluctuations, $[p_T]$ fluctuates even if both c_b and N_{ch} are fixed, as seen in Fig. 4.2 and expressed via Eq. (4.10), which we referred as the intrinsic fluctuations previously. The distribution of δp_T at fixed N_{ch} is obtained by averaging

Eq. (4.10) over the impact parameter:

$$\begin{aligned} P(\delta p_T|N_{ch}) &= \int_0^1 P(\delta p_T|N_{ch},c_b)P(c_b|N_{ch})dc_b \\ &= \frac{1}{P(N_{ch})}\int_0^1 P(\delta p_T,N_{ch}|c_b)dc_b, \end{aligned} \tag{4.21}$$

where we have used Eqs. (4.1) and (4.10) to arrive at the last line. The distributions $P(\delta p_T|N_{ch})$ are shown by the dashed lines in Fig. 4.7 for selected values of N_{ch} close to the knee. The solid lines in this figure, representing the truncated Gaussian, are obtained by setting the correlation coefficient to its maximum value $r = 1$, corresponding to the simplified model in Eq. (4.19). Note that when $r \to 1$, the variance $\kappa_2(c_b)$ approaches zero and $P(\delta p_T|N_{ch},c_b)$ collapses into a Dirac delta function $\delta(\delta p_T - \kappa_1(c_b))$, which implies that δp_T is solely determined by N_{ch} and c_b.

Similar to Eq. (4.12), the third and fourth moment of δp_T is obtained by multiplying Eq. (4.9) with δp_T^3 and δp_T^4 respectively and integrating over δp_T:

$$\begin{aligned} \langle \delta p_T^3\rangle &= \kappa_1^3 + 3\kappa_2\kappa_1\ , \\ \langle \delta p_T^4\rangle &= \kappa_1^4 + 6\kappa_2\kappa_1^2 + 3\kappa_2^2, \end{aligned} \tag{4.22}$$

where again the dependence on c_b on the right-hand side is implicit. Averaging the above moments over c_b and using the third and fourth order cumulant formula we find the skewness and kurtosis [9]:

$$\begin{aligned} \mathrm{Skew}(p_T|N_{ch}) &= \Big(\langle\kappa_1^3\rangle - 3\langle\kappa_1^2\rangle\langle\kappa_1\rangle + 2\langle\kappa_1\rangle^3\Big) + 3\Big(\langle\kappa_2\kappa_1\rangle - \langle\kappa_2\rangle\langle\kappa_1\rangle\Big)\ , \\ \mathrm{Kurt}(p_T|N_{ch}) &= \Big(\langle\kappa_1^4\rangle - 4\langle\kappa_1^3\rangle\langle\kappa_1\rangle + 6\langle\kappa_1^2\rangle\langle\kappa_1\rangle^2 - 3\langle\kappa_1\rangle^4\Big) \\ &\quad + 6\Big(\langle\kappa_2\kappa_1^2\rangle - \langle\kappa_2\rangle\langle\kappa_1^2\rangle - 2\langle\kappa_2\kappa_1\rangle\langle\kappa_1\rangle + 2\langle\kappa_2\rangle\langle\kappa_1\rangle^2\Big) \\ &\quad + 3\Big(\langle\kappa_2^2\rangle - \langle\kappa_2\rangle^2\Big)\ , \end{aligned} \tag{4.23}$$

where angular brackets denote averages over c_b : $\langle\ldots\rangle \equiv \langle\ldots\rangle_{c_b}$ and the N_{ch} dependence on the right hand side has been omitted. The expression for skewness has two terms: the first term involves κ_1 only, and the second term is proportional to the correlation between κ_1 and κ_2. The excess kurtosis has three terms: two of which are similar to skewness and the third term is proportional to the variance of κ_2. The skewness and the kurtosis capture the non-Gaussian characteristics of the event-by-event fluctuations of $[p_T]$. In our model, we assume

---

[9] Note we do not consider intrinsic skewness and consider only excess kurtosis, because our model is based on a Gaussian fluctuation model of b. For a Gaussian distribution (Eq. (4.10)), skewness ($\kappa_3(c_b,N_{ch})$) is zero and kurtosis ($\kappa_4(c_b,N_{ch})$) is 3. Therefore, our results represent an underestimation of these quantities and will always lie below the measured values.

Gaussian fluctuations for a fixed impact parameter. Therefore, any non-Gaussianities in our model results originate from fluctuations in the impact parameter. In the absence of impact parameter fluctuations, each term in the above expressions of Skew(p_T) and Kurt(p_T) would be zero.

Two parametrization : DUKE vs JETSCAPE

Similar to the analysis of variance, the dependence of the mean multiplicity, $\overline{N_{ch}}(c_b)$ and the standard deviation $\sigma_{N_{ch}(c_b)}$ on c_b can be inferred from the experimental distribution $P(N_{ch})$(Fig. 4.3). However, because existing data do not constrain the c_b dependence of $\sigma_{N_{ch}}$, we avoid making assumptions, and instead adopt a more realistic approach. We borrow information from state-of-the-art models tuned to experimental data via Bayesian analyses. Specifically, we use the Maximum A Posteriori parameter sets from two sources: one from the Duke group [27] and another from the JETSCAPE collaboration (which use the Grad viscous correction to the distribution function at freezeout) [28]. The JETSCAPE analysis, tuned to a larger dataset that includes several collision energies, differ from the Duke analysis which is particularly tuned to 5.02 TeV data (the same energy used in our analysis) and accounts for the nucleon substructure, which may potentially affect the fluctuations. We evaluate $\sigma_{N_{ch}}(c_b)$ based on both models, the method of which is explained in detail in Appendix B.3. The prediction by the DUKE parametrization is an increase in $\sigma_{N_{ch}}$ between $b = 0$ and $b = 3.5$ fm, whereas the JETSCAPE model predicts a slight decrease. The difference between these two models provides an estimate of the errors in our predictions.

4.2.3 Results : Predictions for skewness and kurtosis

We find quantitative predictions for the skewness and kurtosis of $[p_T]$-fluctuations based on Eq. (4.23) and using the fit parameters obtained by fitting the variance data in Fig. 4.1. Our quantitative predictions are displayed in Figs. 4.8 and 4.9. Note that the fit parameters $\sigma_{p_T}(0)$ and α are not the same as Fig. 4.1, because here we take different c_b dependence for $\sigma_{N_{ch}}$ based on the two different parametrizations: DUKE and JETSCAPE. However the correlation coefficient r remain unchanged in Figs. 4.1 and 4.8. One can see that, the results on the skewness and the kurtosis exhibit sharp variations around the knee. In particular, our model predicts an increase of the skewness below the knee (such an increase has already been seen by the ALICE collaboration [332], as will be discussed below), followed by a steep decrease above the knee. The kurtosis, on the other hand, has first a minimum below the knee, followed by a maximum roughly at the knee and then it encounters sharp decrease. It is interesting to note that, these peculiar patterns come from the terms involving κ_1, also caused the sharp decrease in variance around knee, and are actually inherited from the truncated Gaussian, reflecting the effect of b-fluctuation at the ultracentral regime. Note that it is possible to calculate

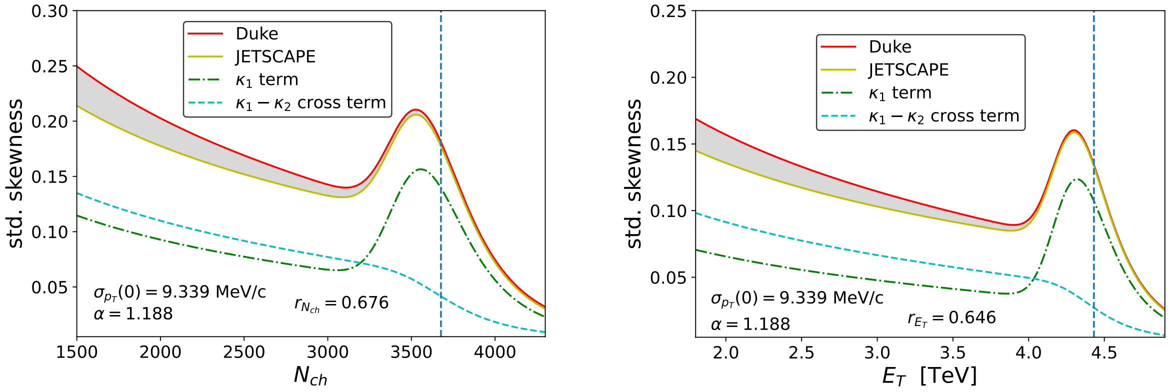

Fig. 4.8 Predictions for the standardized skewness as a function of N_{ch}(left) and E_T(right), based on our model fit to the variance data from ATLAS, and using the Duke and JETSCAPE parametrizations of the centrality dependence of $\sigma_{N_{ch}}$ (Appendix B.3). The difference between the two parametrization is sizable and it is shown as a gray shaded band, thereof serves as error in our prediction. The various terms in Eq. (4.23), contributing to skewness, are shown for the Duke parametrization only. The figure is from the original publication [127], coauthored by the author.

the cumulants of the truncated Gaussian (Fig. 4.7) analytically. Quantitatively speaking, the maximum skewness occurs around $N_{ch} \simeq N_{\text{knee}} - \sigma_{N_{ch}} \simeq 3510$, while the kurtosis reaches a minimum at $N_{ch} \simeq N_{\text{knee}} - 2\sigma_{N_{ch}} \simeq 3340$, followed by a maximum at $N_{ch} \simeq N_{\text{knee}} \simeq 3680$. These numerical values correspond to the structures seen in our model results.

Our predictions show a little dependency on whether one adopts the Duke or JETSCAPE parametrization to characterize the centrality dependence of the multiplicity fluctuations. In fact, the primary limitation of our model lies in assuming a Gaussian distribution for $[p_T]$ at fixed N_{ch} and b. Since $[p_T]$ is inherently positive, it naturally exhibits a positive skewness κ_3 and a positive excess kurtosis κ_4. These factors additionally give positive contributions to $\text{Skew}(p_T|N_{ch})$ and $\text{Kurt}(p_T|N_{ch})$ in Eq. (4.23), in the form of $\langle\kappa_3\rangle$ and $\langle\kappa_4\rangle$. One should consider our predictions as lower bounds both for the skewness and for the kurtosis. Precise quantitative predictions of the values of these additional terms would require extensive hydrodynamic simulations with high statistics. However, we can safely comment that these additional contributions should have a smooth dependence on N_{ch}, resulting in a positive offset from our predictions. The sharp *variations* of the skewness and kurtosis around the knee in Figs. 4.8 and 4.9 are robust, quantitative predictions.

Like the results for the variance, here also we present predictions based on both centrality estimators N_{ch}(left) and E_T(right). However, E_T turns out to be a better centrality estimator than N_{ch}, because of having smaller impact parameter fluctuations [331, 325]. In our model, all the non-Gaussianities arise from the impact parameter fluctuations and hence, both the skewness and the kurtosis are expected to be smaller if the centrality is determined by E_T instead of N_{ch}. This is exactly seen in our predictions (Figs. 4.8 and 4.9). Experimental verification of these predictions will be essential in assessing the importance of impact parameter fluctuations.

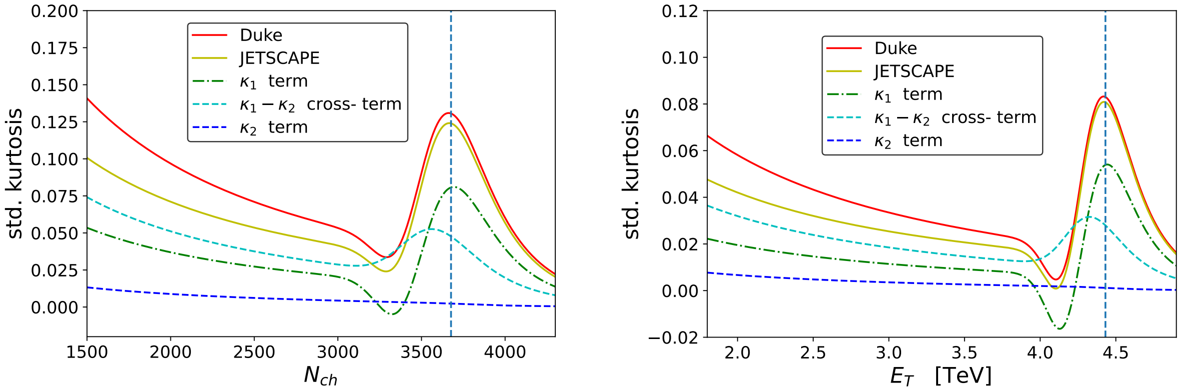

Fig. 4.9 Same as Fig. 4.8 but for the predictions for the standardized excess kurtosis. The figure is from the original publication [127], coauthored by the author.

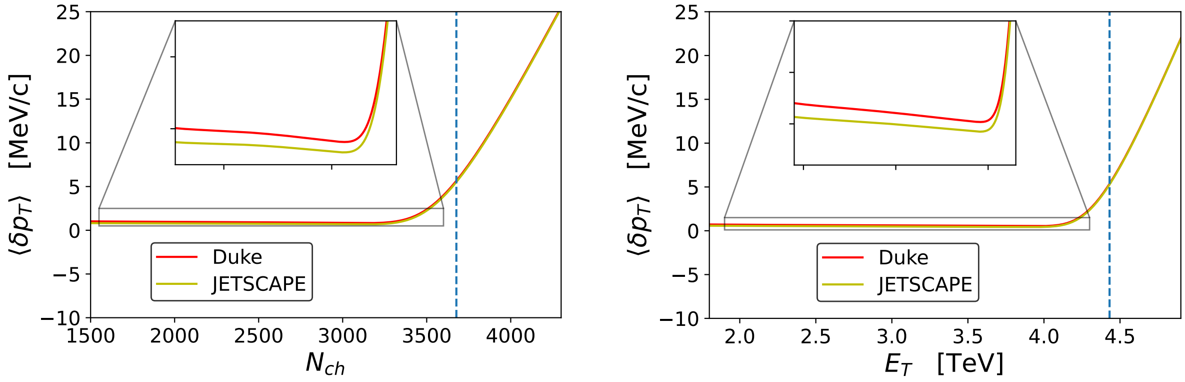

Fig. 4.10 Predictions for average $\langle \delta p_T \rangle$, based on our model, using DUKE and JETSCAPE parametrization. The difference is negligible for the mean, unlike skewness and kurtosis. The figure is from the original publication [127], coauthored by the author.

Similar to Fig. 4.4, here also we present predictions on the increase of the average $\langle \delta p_T \rangle$ based on two different parameterizations displayed in Fig. 4.10.

Comparison with ALICE measurements

Finally, let us compare our results with the recent results on the skewness and kurtosis from the ALICE collaboration [314]. ALICE collaboration uses the amplitude deposited in scintillators located at forward rapidities as the centrality estimator. This is qualitatively similar to the E_T-based centrality determination by ATLAS. The skewness measurements are performed in the central pseudorapidity (η) region, again analogous to the ATLAS analysis but with a narrower η interval. The centrality binning by ALICE is significantly coarser compared to ATLAS, with each point covering a 5% interval. Our analysis focuses on approximately the 20% most central collisions. Therefore, our predictions can only be compared with the last four data points from ALICE, corresponding to the ranges (in TeV) $1.6 < E_T < 2.1$, $2.1 < E_T < 2.7$, $2.7 < E_T < 3.5$, and $E_T > 3.5$.

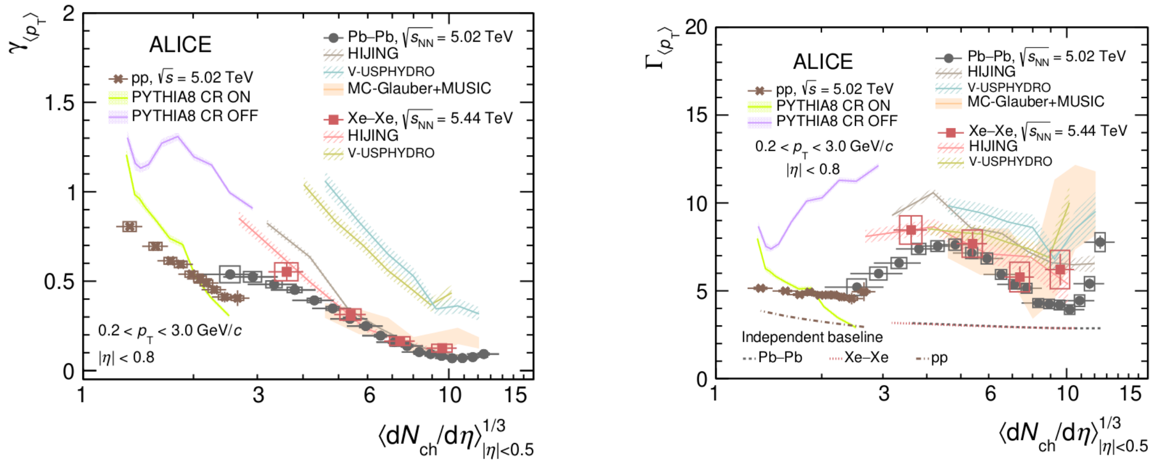

Fig. 4.11 Measurement of the standardized (left) and intensive (right) skewness of $[p_T]$-fluctuation by ALICE for Pb+Pb. Figure taken from [314].

The quantities shown by ALICE are both standardized and intensive skewness [307] shown in Fig. 4.11. The standardized skewness measured by ALICE for the last four points (ultracentral, centrality range of our analysis) is within $0-0.1$, with a slight increase for the last data point, consistent with our prediction. In our prediction, the skewness starts to rise after $E_T \sim 4.0$ TeV, for which data from ALICE is not available. The intensive skewness, on the other hand, is obtained by multiplying the standardized skewness with the average value, $\langle p_T \rangle$, and normalizing by the standard deviation $\mathrm{Var}(p_T)^{1/2}$. We have not evaluated this quantity because we are not provided with the values of $\langle p_T \rangle$ by the ATLAS collaboration. Given the p_T range covered by ATLAS, an approximate estimate for $\langle p_T \rangle$ might be around ~ 1 GeV/c. We then predict that the intensive skewness remains relatively constant and approaches approximately 10 within the interval $1.8 < E_T < 3.5$ TeV. In comparison, ALICE reports the values for the intensive skewness (Fig. 4.11, right) that rise from (slightly below) 4 to (slightly above) 5 over a similar range. It is important to note that direct comparison of the absolute values is not straightforward due to the difference in the p_T coverage: ALICE covers $0.2 < p_T < 3$ GeV/c, whereas ATLAS considers $0.5 < p_T < 5$ GeV/c [10].

Interestingly in the ALICE data, the intensive skewness is close to 8, in the most central bin, which is significantly higher than in the previous bins. This last point of the ALICE data corresponds to the E_T interval: $E_T > 3.5$ TeV, over which our model predicts a rise followed by a fall of the intensive skewness, peaking at a value ~ 18, below the knee. ALICE measurements (not shown) on standardized kurtosis (lies between 3.02 - 3.07 for the right most four points) are consistent with our predictions for excess kurtosis. It is tempting to interpret the ALICE

---

[10] The dependence of $\sigma_{p_T}(c_b)$ on the p_T interval is not trivial. How fluctuations of the p_T spectrum depends on p_T is at present not known, and assessing it would require to measure the quantity $v_0(p_T)$ introduced in Ref. [96]. Recently we have found that the observable $v_0(p_T)$ carries much more significance in relation to $[p_T]$-fluctuation. One can actually capture the p_T-interval dependence of the fluctuations through $v_0(p_T)$. Work on this particular phenomenon is in progress.

results corroborating with our predictions and possibly as a first confirmation. It will be useful if the ALICE analysis is repeated in finer centrality bins, specifying the values of the centrality estimator in each bin and if they can provide measurements for more ultracentral events.

Chapter 5

Transverse momentum-harmonic flow correlations

In Chapter 3, we discussed fluctuations of harmonic flow (v_n) and in Chapter 4, we discussed fluctuations of the mean transverse momentum per particle ($[p_T]$) in heavy-ion collisions. We have seen that both of these final state quantities are largely determined by the properties of the initial state. The harmonic flow is directly related to the initial spatial anisotropy or eccentricities (ϵ_n)[48, 92], whereas the mean transverse momentum of the particles is related to the size of the initial fireball (R) [303, 96]. Events with a smaller size of the interaction region have larger energy density gradients, resulting in a larger transverse push during the expansion and hence larger $[p_T]$ at the final state. As a result, the event-by-event fluctuations of v_n and $[p_T]$ are governed by the event-by-event fluctuations of the initial state. The fluctuations of the harmonic flow coefficients could be due to fluctuations of the shape of the initial fireball, as well as due to dynamical fluctuations in the expansion dynamics. Analogously, fluctuations of $[p_T]$ can be related to the fluctuations of the size of the fireball as well as fluctuations of the initial entropy or energy (S or E_i) [97, 128]. Therefore, naturally one can expect that these two final state quantities, $[p_T]$ and v_n are correlated.

The Pearson correlation coefficient between the mean transverse momentum per particle and harmonic flow coefficient, $\rho([p_T], v_n^2)$, first introduced by P. Bożek [95], hence sometimes referred as Bożek coefficient [106], serves as an excellent tool to study the correlation between collective observables at the final state and a fine probe to the correlation present in the initial state [186, 96, 97, 225, 128]. Another significant importance of this correlator ρ is that it can be used as a fine tool to study nuclear structure and deformation in high energy heavy-ion collisions [110, 106, 108, 98], which we will discuss in detail in the next chapter. Moreover it can be used in Bayesian analysis to put precise constraints on the initial state and medium properties of the QGP [333, 28, 334]. The observable $\rho([p_T], v_n^2)$ has been measured in experiments [100–102, 335, 336] and been studied extensively in models over the past few years [186, 96–98, 225, 128, 337–340].

In this chapter, at first we discuss the centrality dependence of $\rho([p_T],v_n^2)$ and higher order correlations between transverse momentum and different orders of harmonic flow through normalized symmetric cumulants [237, 99, 273] which put additional constraints on the initial state properties and correlations. In the second part, we include momentum dependence within the harmonic flow and construct the correlation coefficient between $[p_T]$ and differential flow $v_n(q)$[1]. This provides the momentum dependent measure of the correlation coefficient and further constrain the initial state parameters. The following sections are, for the most part, presentations from the original publications [128, 129], coauthored by the author.

5.1 Correlation between $[p_T]$ and integrated flow v_n

Let us first consider the correlation between mean transverse momentum per particle $[p_T]$ and squares of the harmonic flow v_n^2, which could be constructed as Pearson correlation coefficient [95, 186] at the lowest order or as higher order correlations involving different orders of flow through the *symmetric cumulants* [99, 273].

5.1.1 Pearson correlation coefficient : $\rho([p_T],v_n^2)$

The Pearson correlation coefficient, first proposed in [95], between the mean transverse momentum per particle and the harmonic flow, can be used to measure the event-by-event correlation and it is defined as,

$$\rho([p_T],v_n^2) = \frac{Cov([p_T],v_n^2)}{\sqrt{Var([p_T])Var(v_n^2)}} , \tag{5.1}$$

where the covariance is given by,

$$Cov([p_T],v_n^2) = \langle [p_T] V_n V_n^\star \rangle - \langle [p_T] \rangle \langle V_n V_n^\star \rangle , \tag{5.2}$$

and the variances in the denominator as,

$$Var([p_T]) = \langle [p_T]^2 \rangle - \langle [p_T] \rangle^2 \quad \text{and} \quad Var(v_n^2) = \langle (V_n V_n^\star)^2 \rangle - \langle V_n V_n^\star \rangle^2 . \tag{5.3}$$

The Pearson correlation coefficient $\rho([p_T],v_n^2)$ is particularly robust as it does not depend on the hydrodynamic response coefficient k_n and essentially insensitive to the medium properties. Moreover, it is insensitive to statistical fluctuations and picks up only genuine correlation between mean transverse momentum and harmonic flow coefficients. The covariance in the numerator of the correlation coefficient in Eq. (5.1) involves three particle correlations, whereas the variance of the flow harmonic in Eq. (5.3) is a four particle correlator. The experimental

---

[1] We do not use the notation p here and use q instead, to denote transverse momentum bins to avoid confusion.

measurement for the covariance and the variances in Eq. (5.1) involves up to three or four sums over particles in the event, with self-correlations excluded, as discussed in [95].

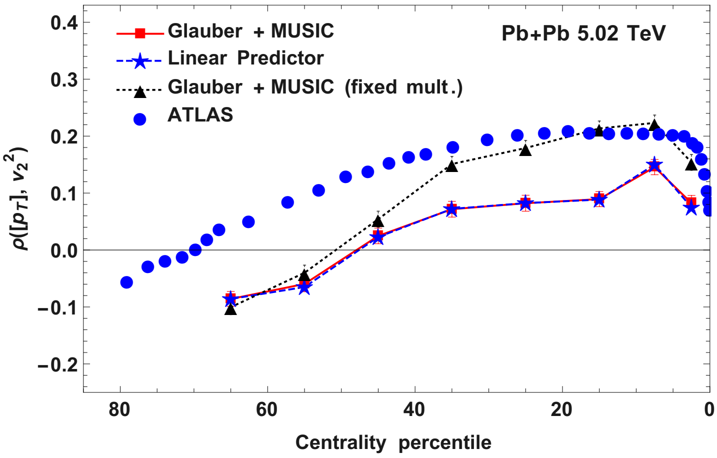

Fig. 5.1 The Pearson correlation coefficient between the mean transverse momentum per particle $[p_T]$ and the elliptic flow squared v_2^2 in Pb+Pb collisions at 5.02 TeV as a function of centrality. The experimental data shown are from the ATLAS collaboration [102] (blue points). The results of the hydrodynamic simulations with Glauber initial conditions are denoted by the red squares, the black triangles represent the results for the correlation coefficient corrected for multiplicity fluctuations (Eq. 5.5) and the star symbols with the blue dashed line represent the correlation coefficient obtained from the linear predictor (Eq. 5.6). The figure is from the original publication [128], coauthored by the author.

To calculate these quantities in our model, here also we simulate Pb+Pb collisions at $\sqrt{s_{NN}} = 5.02$ TeV using the boost invariant version of MUSIC [216] with the initial energy densities obtained from the two-component Glauber Monte Carlo model [280] in each event. The details of the model for the initial density can be found in [95]. Unless otherwise specified, we use a constant shear viscosity to entropy ratio $\eta/s = 0.08$ for the hydrodynamic evolution.

Fig. 5.1 shows the model results for the centrality dependence of the transverse momentum-elliptic flow correlation coefficient $\rho([p_T], v_2^2)$ along with the experimental data from the ATLAS collaboration [102]. The model calculations for $\rho([p_T], v_2^2)$ follow a qualitatively similar centrality dependence as compared to the ATLAS data [102]. In particular, the correlation coefficient $\rho([p_T], v_2^2)$ decreases in the most central collisions as well as in peripheral collisions. Both the data and the model calculations show a sign change in peripheral collisions. However, It can be seen that the change of sign for $\rho([p_T], v_2^2)$ occurs at different centralities, with the model calculation changing sign in more central collisions as compared to the data.

The correlation coefficient for the triangular flow $\rho([p_T], v_3^2)$ and the quadrangular flow $\rho([p_T], v_4^2)$ are shown in Fig. 5.2. The measured correlation $\rho([p_T], v_3^2)$ is small as compared to our model results. Moreover, our simulation results cannot describe the full features of the experimental data. Such discrepancies observed between the data and simulations results for $\rho([p_T], v_n^2)$ may stem from some underlying physics of the dynamics in the model or it could indicate that we are missing in our model calculations some essential correlations present in the initial state. For peripheral collisions with very low multiplicities, some correlations may be

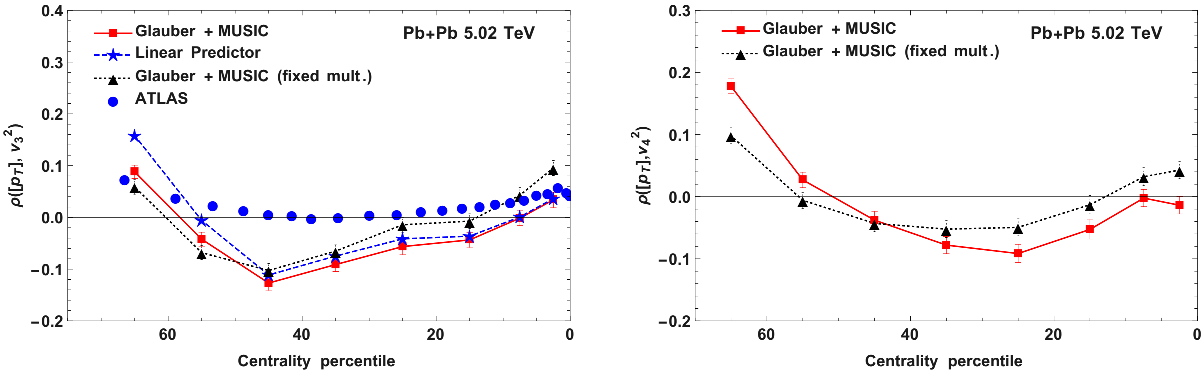

Fig. 5.2 Left: The Pearson correlation coefficient between the mean transverse momentum per particle and the triangular flow in Pb+Pb collisions at 5.02 TeV as a function of centrality. Right: The same for quadrangular flow. The symbols are same as Fig. 5.1. The left panel of the figure is from the original publication [128], coauthored by the author.

attributed to the presence of non-flow contributions and/or the initial flow, but why a significant discrepancy for $\rho([p_T], v_n^2)$ occur at the mid-central collisions, is unclear. The correlation coefficient $\rho([p_T], v_4^2)$ is the prediction based on our model.

Correction for multiplicity fluctuations: Partial correlation

Along with the mean transverse momentum per particle and harmonic flow, the multiplicity also fluctuates event-by-event. As a result, the correlation between $[p_T]$ and v_n^2 may partially originate from the correlations of these quantities with the event multiplicity N (We denote multiplicity in an event by $N \equiv N_{ch}$). Usually the experimental analysis is performed in narrow bins of centrality, where such residual correlation can be significantly reduced. To tackle this effect in model calculations, the dependence of the variance or covariance of the observables of interest on the fluctuations of a third variable, (e.g. here the multiplicity) are taken into account by calculating the partial variance or covariance [341]. The *partial correlation coefficient* between $[p_T]$ and v_n^2 is given by,

$$\rho([p_T], v_n^2 \bullet N) = \frac{\rho([p_T], v_n^2) - \rho([p_T], N)\rho(N, v_n^2)}{\sqrt{1-\rho([p_T], N)^2}\sqrt{1-\rho(v_n^2, N)^2}} \, , \tag{5.4}$$

which provides an estimate of the correlation coefficient in a centrality bin at fixed multiplicity [280]. Figs. 5.1 and 5.2 show the results for the partial correlation coefficients, denoted by black dashed line. One can see that there is sizable correction due to multiplicity fluctuations for the elliptic flow. Moreover, the model results obtained for $\rho([p_T], v_2^2)$ after correcting for multiplicity, is closer to the experimental data in comparison to the uncorrected one (red solid lines). However, for $\rho([p_T], v_3^2)$ and $\rho([p_T], v_4^2)$, the correction are not so significant and both of the calculations lie close to each other.

In general, if an observable O has an approximately linear dependence on the multiplicity in a given bin, then the correction for multiplicity fluctuations to O can be implemented as [96],

$$\tilde{O} = O - \frac{Cov(O,N)}{Var(N)} (N - \langle N \rangle) \ , \tag{5.5}$$

where $\tilde{O}$ denotes the multiplicity-corrected observable. In principle, one can use the above equation for $[p_T]$ and v_n^2 and calculate $\rho([p_T], v_n^2)$. This is equivalent of using the formula for the partial correlation coefficient presented in Eq. (5.4). Later in this section, we use the corrected observables $\tilde{O}$ while estimating the higher order cumulants/correlations to remove the effects of multiplicity fluctuations.

In order to compare with the experimental data, obtained in narrow bins of multiplicity, the model calculations should always be corrected for the multiplicity fluctuations and only then it should be compared. If the experimental multiplicity bins are wide or a different centrality estimator (as discussed in the previous chapter) is used for defining centrality bins, a correction for the observables using Eq. (5.5) should be done (where N will denote the centrality estimator) in order to establish a consistent description of correlations and cumulants between different experiments and model calculations.

5.1.2 Mapping to initial state: Linear predictor

The collective observables in the final state of heavy-ion collisions are largely determined by the initial conditions of the collision. In particular, the mean transverse momentum per particle $[p_T]$ and the harmonic flow coefficients v_n are strongly correlated to these properties of the initial state[92, 76, 187, 303]. As discussed in Chapter 3, the harmonic flow coefficients can be mapped to the spatial anisotropy or eccentricities ϵ_n of the initial density distribution (Eqs. (3.15),(3.16) and (3.18)), therefore resulting in a strong correlation as seen in Figs. 3.6 and 3.7. The mean transverse momentum per particle, on the other hand, can be related to the the RMS size of the transverse profile R (Eq. 3.8) [342, 305], the total initial entropy S (Eq. 3.7) as well as the initial eccentricities. Fig. 5.3 shows the scatter plot between the mean transverse momentum and transverse size R on the left, and between mean transverse momentum and total entropy per unit elliptic area S/A_e on the right, where $A_e = \pi R^2 \sqrt{1 - \varepsilon_2^2}$ denoting the elliptic area of the initial transverse profile. The figure shows a strong correlation (negative) between $[p_T]$ and R, as well as a significant correlation (positive) with the total entropy S and ellipticity of the initial state ε_2.

The anti-correlation between the mean transverse momentum per particle $[p_T]$ and the transverse size R observed in Fig. 5.3 (left) can be understood by the same thermodynamic argument presented in Chapter-4. If we fix the multiplicity (i.e. initial entropy), then a smaller transverse size implies a smaller collision volume, and hence larger density. Then by relativistic thermodynamics, it means larger temperature and eventually larger pressure gradients which results in larger energy per particle or larger transverse momentum per particle $[p_T]$. The reverse scenario occurs when R is large which produce smaller $[p_T]$. Similar argument can be made for explaining the positive correlation between $[p_T]$ and S at fixed collision volume, this is equivalent to dividing the event-by-event total entropy by the transverse area. At fixed collision volume, a larger entropy means a larger density and hence by the same principle of relativistic thermodynamics, it produces larger transverse momentum per particle at the final state resulting in the strong positive correlation observed in Fig. 5.3 (right). As an alternative way, $[p_T]$ can be also predicted from the initial energy per rapidity (E_i) [97] or the energy weighted entropy [96].

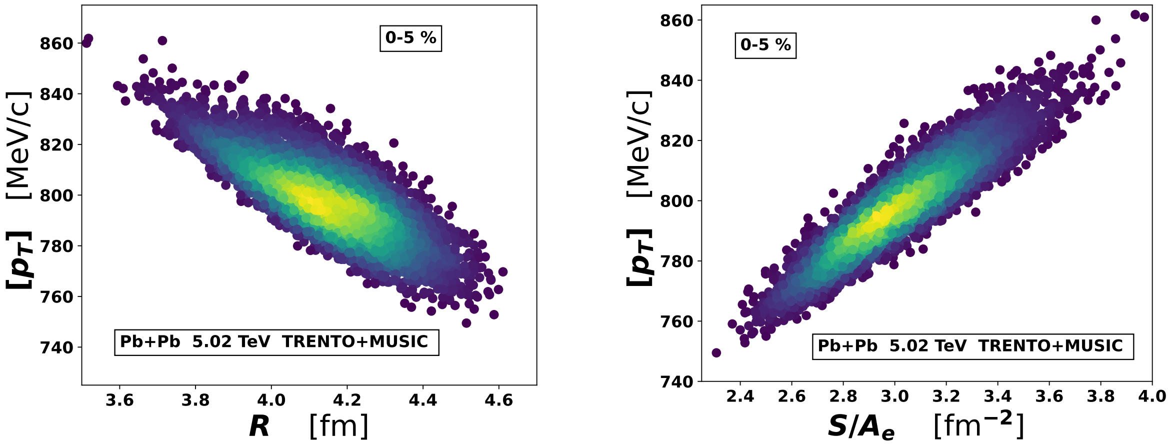

Fig. 5.3 Left: Scatter plot between event-by-event mean transverse momentum per particle and transverse size of the initial source for $0-5\%$ centrality in Pb+Pb collision at 5.02 TeV obtained with TRENTO initial condition. Right: Similar scatter plot between mean transverse momentum per particle and total entropy per unit elliptic area.

The correlation present in the initial state between these quantities can be captured by constructing an appropriate predictor for $[p_T]$ and v_n. It was proposed [186] that in order to construct a predictor for the Pearson correlation coefficient between the mean transverse momentum per particle and the elliptic or triangular flow, the initial state eccentricities should also be included in the predictor for the transverse momentum $[p_T]$. According to Ref. [186], such an *improved predictor* can well describe the transverse momentum-harmonic flow correlation $\rho([p_T], v_n^2)$, in connection to the full hydrodynamic simulation. Therefore, for our analysis we use general linear predictors for $[p_T]$ and v_n, based on moments of the initial density[2], given by

$$\begin{aligned}
\hat{v}_2^2 &= k_2\varepsilon_2^2 + \alpha_2\delta R + \beta_2\delta S \\
\hat{v}_3^2 &= k_3\varepsilon_3^2 + \alpha_3\delta R + \beta_3\delta S \ , \\
[\hat{p}_T] &= \langle[\hat{p}_T]\rangle + \alpha_p\delta R + \beta_p\delta S + \gamma_p\delta\varepsilon_2^2 + \lambda_p\delta\varepsilon_3^2 \quad ,
\end{aligned} \tag{5.6}$$

---

[2] Please note $[p_T]$ can be simultaneously related to R, S and also ε_n. In Fig. 5.3 (right), we show the correlation between $[p_T]$ and S/A_e which contains all of these quantities in terms of entropy density and hence the correlation is remarkably strong. But in Eq. (5.6) we construct a general predictor from individual quantities, in order to capture the genuine correlations between them through the Pearson's correlation coefficient and the symmetric cumulants.

where the *hat* symbol is used to denote the observables predicted from initial state in order to distinguish from the one obtained from hydrodynamic simulations. For any observable O, we have $\delta O = O - \langle O \rangle$, where $\langle \ldots \rangle$ denotes the event average of the observable and the coefficients sitting before each moments can be thought as hydrodynamic response coefficients. One can also write the linear predictor in Eq. (5.6) in a generalized form,

$$\delta \hat{O}_i = L_i^j \delta M_j \ , \tag{5.7}$$

where M_i is a set of moments of the initial density and L_i^j are the response coefficients. In our analysis we optimize each of the observables in Eq. (5.6) separately. Only after the parameters or the response coefficients are fixed for a linear predictor, the cumulants and correlation are calculated between the predicted observables. Using Eq. (5.7), the covariance or the correlations between the final state observables can be expressed as a linear transformation of the correlation at the initial state,

$$\langle \delta O_i \ldots \delta O_j \rangle = L_i^s \ldots L_j^k \langle \delta M_s \ldots \delta M_k \rangle \ . \tag{5.8}$$

Figs. 5.1 and 5.2 show the results for the correlation $\rho([p_T], v_n^2)$ calculated using the linear predictors in Eq. (5.6), presented by blue lines. The results are in fair agreement with the corresponding correlations calculated from hydrodynamic simulations. This shows the robustness of the linear predictors and how well it can capture the initial state correlations. This also establishes the fact that the Pearson correlation coefficient (and aslo the higher order cumulants, as we will see shortly) involving the final state observables can be understood as a linear hydrodynamic response of the correlations present in the initial state. Note that the correlation $\rho([p_T], v_4^2)$ cannot be predicted using the set of linear predictor used in our analysis. Therefore in Fig. 5.2 (right), we only present the results obtained from hydrodynamics.

5.1.3 Higher order correlations: Symmetric cumulants

Pearson correlation coefficient $\rho([p_T], v_n^2)$ represents the leading (lowest) order correlation between mean transverse momentum per particle and the harmonic flow coefficient, and it involves flow harmonic of a specific order. However, in order to understand additional information on such correlations and interplay between transverse momentum and different orders of flow harmonics, one needs to look into higher order correlations. Study of such higher order correlation coefficient is also useful to understand the higher order and mixed correlations present in the initial state. A correlation of order larger than 2, between mean transverse momentum and flow harmonics cannot be constructed using Pearson correlation coefficient and one needs to resort different constructions such as *symmetric cumulants (SC)*. Such symmetric cumulants between the magnitudes of the harmonic flow of different orders have been studied [237]. We adopt similar methodology in order to construct SC between $[p_T]$ and $v_n's$.

2nd order normalized symmetric cumulants (NSC)

We start with the second order symmetric cumulants in analogy to the Pearson correlation coefficients. The second order SC is simply the covariance between two observables

$$SC(A,B) = \langle AB\rangle - \langle A\rangle\langle B\rangle \equiv Cov(A,B)\ . \tag{5.9}$$

Then the *normalized symmetric cumulant* (NSC) is obtained by scaling the above equation by the individual mean of the observables involved in SC. In case of correlation between transverse momentum and harmonic flow of a particular order, NSC can be defined as,

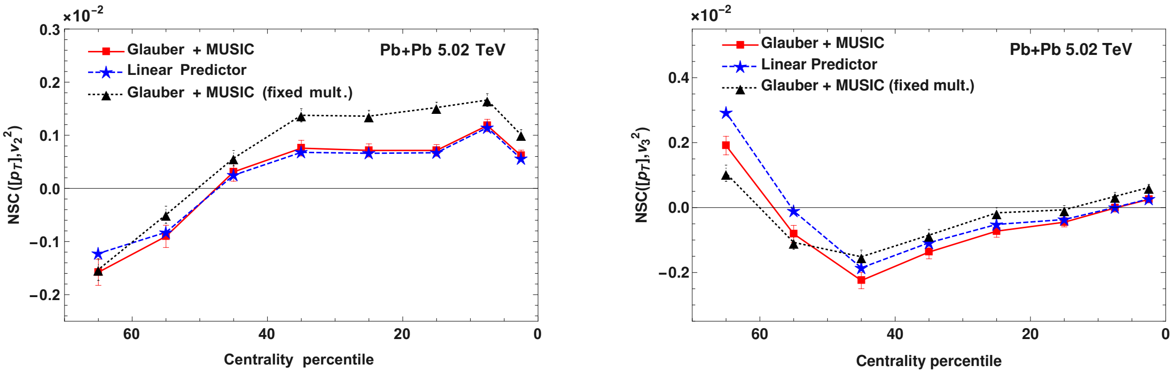

Fig. 5.4 Left: Normalized symmetric cumulant between mean transverse momentum per particle and elliptic flow coefficient in Pb+Pb collision at 5.02 TeV as a function of centrality. The red squares denote the results obtained from hydrodynamics and the black triangles denote the results corrected for multiplicity fluctuations. The blue stars represent the cumulant obtained from the linear predictor. Right: Same for the triangular flow.

$$NSC([p_T],v_n^2) = \frac{\langle [p_T]v_n^2\rangle - \langle [p_T]\rangle\langle v_n^2\rangle}{\langle [p_T]\rangle\langle v_n^2\rangle}\ . \tag{5.10}$$

The normalized symmetric cumulants $NSC([p_T],v_n^2)$ for the elliptic and triangular flow are shown in Fig. 5.4 . $NSC([p_T],v_n^2)$ represents the event by event correlations between the mean transverse momentum and the harmonic flow and this information is contained in the covariance of the two observables in the numerator. This implies that $NSC([p_T],v_n^2)$ basically carries the same information as the correlation coefficient $\rho(p_T,v_n^2)$, which is reflected in the results of Fig. 5.4. However, the orders of magnitude of the correlation are changed because of the changed normalization. Furthermore, it should be noted that the experimental extraction of normalized symmetric cumulant is simpler than the Pearson correlation coefficient ρ. This is because the denominator of Eq. (5.10) involves at most a two particle correlator, whereas the denominator in Eq. (5.1) requires the measurement of three or four particle correlators. The definition in Eq. (5.10) is favourable by experiments and also methods for reducing non-flow effects can be implemented, even in small collision systems [337].

Third and fourth order NSC

Next, we move to the constructions of higher order NSC, which may contain additional information on correlations between mean transverse momentum and harmonic flow. Such higher order cumulants of only harmonic flow of different orders have been studied [237, 99, 273]. We implement the same methodology for cumulants of $[p_T]$ and v_n^2. In general, the n-th order normalized symmetric cumulant involves only the genuine correlation between n observables, where all the lower order correlations are subtracted. This way it is similar to the construction of multi-particle flow cumulants discussed in Chapter-3. The third and fourth order symmetric cumulants for scalar observables are defined as [99],

$$\begin{aligned}
SC(A,B,C) &= \langle ABC\rangle - \langle AB\rangle\langle C\rangle - \langle AC\rangle\langle B\rangle - \langle BC\rangle\langle A\rangle + 2\langle A\rangle\langle B\rangle\langle C\rangle \;, \\
\text{and} \quad SC(A,B,C,D) &= \langle ABCD\rangle - \langle ABC\rangle\langle D\rangle - \langle ABD\rangle\langle C\rangle - \langle ACD\rangle\langle B\rangle - \langle BCD\rangle\langle A\rangle \\
&\quad - \langle AB\rangle\langle CD\rangle - \langle AC\rangle\langle BD\rangle - \langle BC\rangle\langle AD\rangle \\
&\quad + 2\Big(\langle AB\rangle\langle C\rangle\langle D\rangle + \langle AC\rangle\langle B\rangle\langle D\rangle + \langle AD\rangle\langle C\rangle\langle B\rangle \\
&\quad + \langle BC\rangle\langle A\rangle\langle D\rangle + \langle BD\rangle\langle A\rangle\langle C\rangle + \langle CD\rangle\langle A\rangle\langle B\rangle\Big) \\
&\quad - 6\langle A\rangle\langle B\rangle\langle C\rangle\langle D\rangle \;,
\end{aligned} \tag{5.11}$$

and the corresponding normalized symmetric cumulants are given by

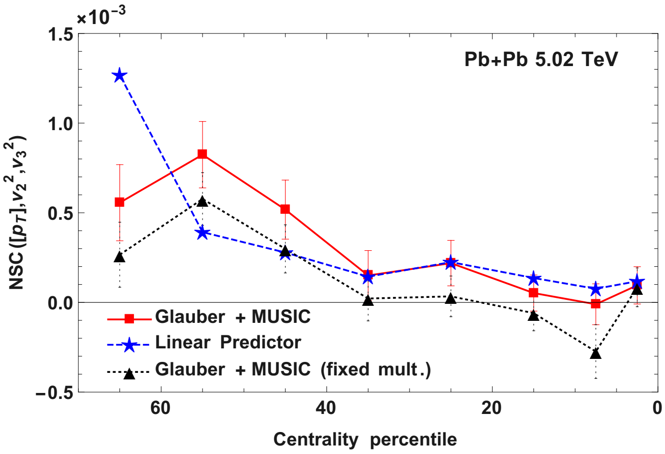

Fig. 5.5 Third order normalized symmetric cumulant between mean transverse momentum per particle, elliptic flow and triangular flow coefficient in Pb+Pb collision at 5.02 TeV as a function of centrality. The symbols carry similar meaning as Fig. 5.10. The figure is from the original publication [128], coauthored by the author.

$$NSC(A,B,C) = \frac{SC(A,B,C)}{\langle A\rangle\langle B\rangle\langle C\rangle} \quad \text{and} \quad NSC(A,B,C,D) = \frac{SC(A,B,C,D)}{\langle A\rangle\langle B\rangle\langle C\rangle\langle D\rangle} \;. \tag{5.12}$$

In Figs. 5.5 and 5.6, the simulation results for the third order normalized symmetric cumulants $NSC([p_T],v_2^2,v_3^2)$, $NSC([p_T],v_2^2,v_4^2)$ and $NSC([p_T],v_3^2,v_4^2)$ are presented. As noted earlier, for the higher order symmetric cumulants, the effect of multiplicity fluctuations is reduced by correcting the observables for multiplicity using Eq. (5.5). A first observation is that for all the third order normalized symmetric cumulants, the magnitude of the correlation is much smaller as compared to ρ, which confirms the fact that it measures only genuine third order correlations. The cumulants $NSC(p_T,v_2^2,v_3^2)$ and $NSC(p_T,v_2^2,v_4^2)$ increase for the peripheral collisions, whereas the cumulant $NSC(p_T,v_3^2,v_4^2)$ show a decrease in peripheral collisions. For $NSC(p_T,v_2^2,v_3^2)$, the linear predictor (5.6), based on the initial correlations only, describes the full hydrodynamic calculation within centrality range: 0-50%. Like in the previous case, the cumulants involving v_4 cannot be predicted using our linear predictor, so that we only present the hydro results for them and they could serve as a precise measure of nonlinearities between harmonic flow of different orders with subtle interplay between average transverse momentum and flow. The fourth order normalized symmetric cumulant $NSC(p_T,v_2^2,v_3^2,v_4^2)$ is presented in Fig. 5.7. The results are compatible with zero within the statistical accuracy of our calculation.

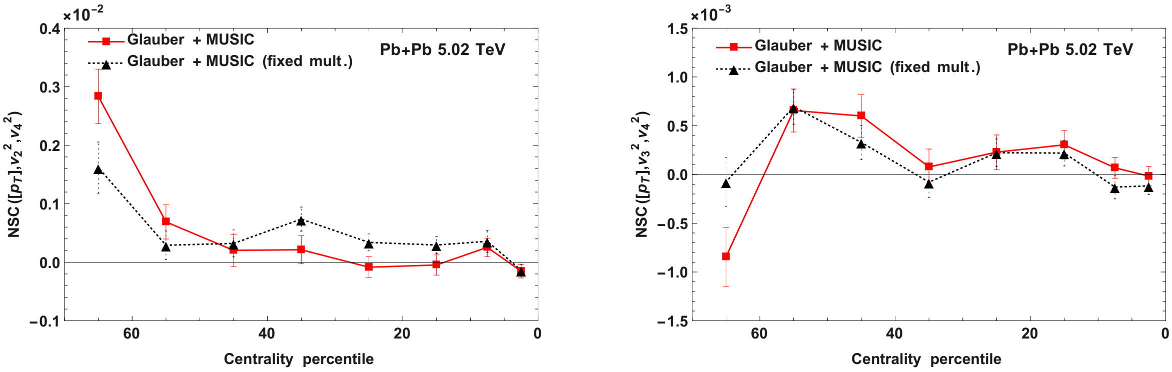

Fig. 5.6 Third order normalized symmetric cumulant between $[p_T]$, v_2^2 and v_4^2 in the left and between $[p_T]$, v_3^2 and v_4^2 in the right for Pb+Pb collision at 5.02 TeV as a function of collision centrality. The red squares and black triangles denote the results obtained from the hydrodynamic simulation without and with corrections for multiplicity fluctuations respectively. The figure is from the original publication [128], coauthored by the author.

For completeness, we also study the third and fourth order NSC between $[p_T]$, N and v_n^2, the results of which are shown in Fig. 5.8. Such correlations involving the multiplicity (or any centrality estimator) as one of the observable could be sensitive to the fluctuations in the entropy deposition at the initial state and the correlation of it with its moments. Our simulation results and the linear predictor show opposite behavior for the peripheral collisions which opens the scope for further investigation of the peripheral behavior of such higher order cumulants. Please note that the results presented in this case, for the observables $[p_T]$ and v_n^2, are not corrected for multiplicity fluctuations, because the cumulant involve multiplicity as an observable within itself. Normalized symmetric cumulants involving multiplicity might not carry much significance for spherical nuclei collisions but have a greater importance for deformed nuclei collisions, where

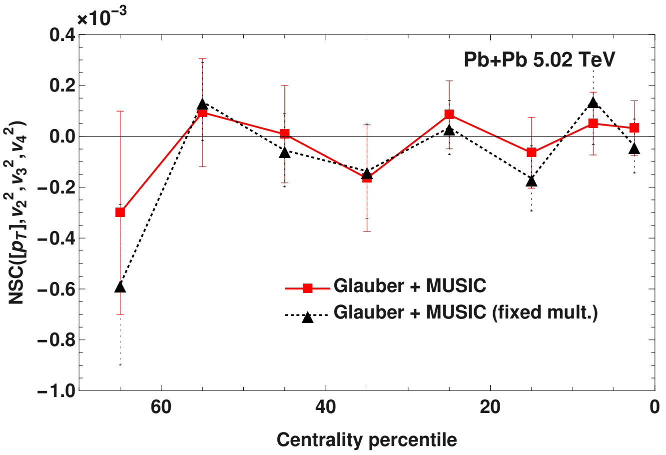

Fig. 5.7 Fourth order normalized symmetric cumulant between $[p_T]$, v_2^2, v_3^2 and v_4^2 in Pb+Pb collision at 5.02 TeV as a function of centrality. The symbols have similar meaning as Fig. 5.6.

fluctuations of multiplicity is more significant and can probe deformed structure of the nucleus. Such effects will be discussed in detail in the next chapter.

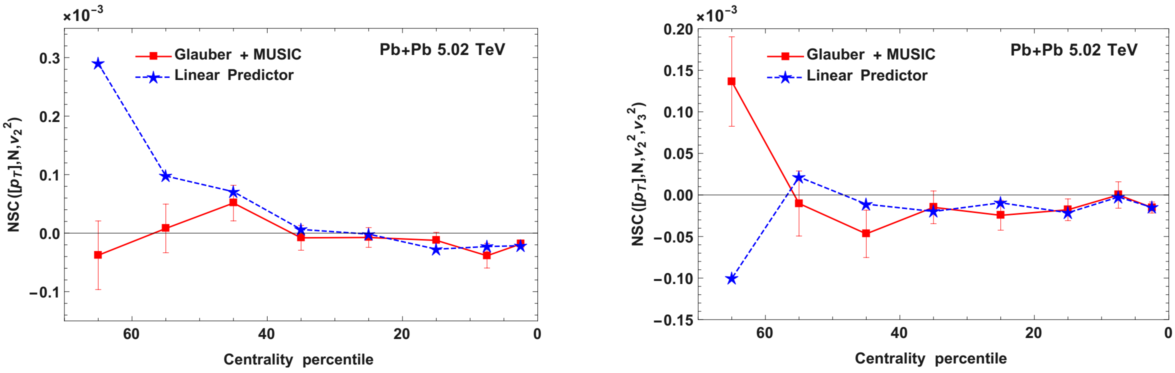

Fig. 5.8 Left: Third order normalized symmetric cumulant between mean transverse momentum per particle, multiplicity and elliptic flow coefficients in Pb+Pb collision at 5.02 TeV as a function of centrality. The red squares and blue stars represent the results obtained from the hydrodynamic simulation and the linear predictor respectively. Right: Fourth order normalized symmetric cumulant between $[p_T]$, N, v_2^2 and v_3^2. with symbols carrying same meaning.

Change of normalization: Scaled symmetric cumulants (SSC)

The denominator of the normalized symmetric cumulants in Eq. (5.12) involve averages of the observables for which the cumulant is calculated. However, with such definitions the interpretation of the results become less obvious than the Pearson correlation coefficient ρ. The average transverse momentum in a collision can depend on many factors [304] such as the freeze-out procedure, the bulk viscosity, the preequilibrium flow and even the experimental range for transverse momentum. Moreover, the linear predictor for the mean transverse momentum per particle in an event Eq. (5.6) can only predict the deviations from the average and the absolute

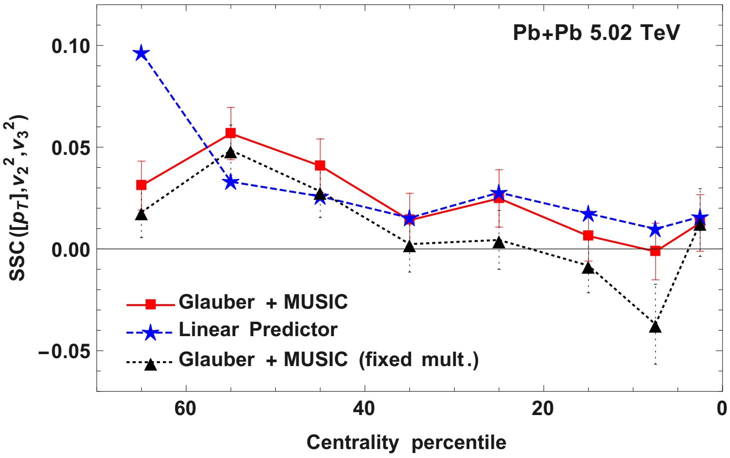

Fig. 5.9 Third order scaled symmetric cumulant between mean transverse momentum per particle, elliptic flow and triangular flow coefficients in Pb+Pb collision at 5.02 TeV as a function of centrality. Symbols have similar meaning as Fig. 5.5. The figure is from the original publication [128], coauthored by the author.

value for the average transverse momentum is not provided by the experiments. To overcome all these limitations, a modification for the normalization of the SC could be necessary.

Such an alternative normalization for the symmetric cumulants can be the standard deviations of the observables involved in the denominator instead of mean. With that, we construct the *scaled symmetric cumulants* given by,

$$\begin{aligned} SSC(A,B,C) &= \frac{SC(A,B,C)}{\sqrt{Var(A)Var(B)Var(C)}} \, , \\ \text{and} \quad SSC(A,B,C,D) &= \frac{SC(A,B,C,D)}{\sqrt{Var(A)Var(B)Var(C)Var(D)}} \, . \end{aligned} \tag{5.13}$$

The scaled symmetric cumulant has two-fold advantages. First the prediction of SSC from the initial state does not require the input on the value of the average transverse momentum, which is sometimes not known from either the simulations or the experiments. Second, the values of the scaled symmetric cumulants can be relatively well predicted using the linear hydrodynamic response (Eq. (5.6)).

Fig. 5.9 shows results for the scaled symmetric cumulant between $[p_T]$, v_2^2 and v_3^2. The results display a very similar behavior as the normalized symmetric cumulants presented in Fig. 5.5. The only noticeable difference is in the order of magnitudes. The numerical values for SSC are larger as compared to NSC because of the change in normalization. It could be noted that the sole change of the normalization from the average (mean) transverse momentum to its standard deviation results in a change by a factor in the range[3]: $20-100$.

---

[3] This effect can be related to the 1% relative dynamical fluctuations of $[p_T]$ discussed in the last chapter

5.2 Momentum dependent correlation: Between $[p_T]$ and differential flow $v_n(q)$

In the previous section, we discussed the correlations and cumulants between mean transverse momentum per particle $[p_T]$ and *integrated* flow v_n. One can think of generalizing this class of observables to momentum dependent correlation coefficients, by introducing transverse momentum dependence within the flow harmonics. In particular, such correlation coefficient would read as a correlation between mean transverse momentum per particle in an event $[p_T]$ and the harmonic flow coefficient in a transverse momentum bin, denoted by $v_n(q)$ (here, q denotes a particular transverse momentum bin). Such momentum dependent correlations can provide useful insights in many aspects. Apart from providing a complementary statistical information of the event-by-event distribution of those particular observables, $[p_T]-v_n(q)$ correlations could shed light on several interesting issues related to heavy-ion collisions, which serve as motivating factors for engaging in such studies, as outlined below. The momentum dependent correlation coefficient between mean transverse momentum and differential harmonic flow

- could help us to understand the observed p_T-cut dependence of the correlation coefficients such as $\rho([p_T],v_n^2)$ [100],
- could provide useful insights on specific modes in the initial state which can be related to the final state transverse momentum and harmonic flow [342],
- could show sensitivity to nucleon width or *granularity* in the initial state [98], which plays a significant role for momentum dependent flow.
- could provide a measure of the correlation between transverses momentum and harmonic flow independent of the shape of the momentum dependence of the particular flow harmonics,
- if used for identified particles, it could also test the hadronization mechanism and its possible dependence on the transverse expansion.
- or, could help in identifying the correlations between mean transverse momentum and harmonic flow from other models such as the color glass condensate dynamics [343].

In this section, we propose possible definitions for the momentum dependent correlation coefficient between the mean transverse momentum and the harmonic flow. We mostly focus on the momentum dependent construction for Pearson correlation coefficients. Similar momentum dependent higher order cumulants can also be studied but lies beyond the scope of our current study. We also explore the sensitivity of such correlation coefficients to the granularity in the initial state and medium properties (e.g. shear viscosity), and propose new covariance that could be measured in experiments. We propose alternate simplified expressions for the momentum dependent correlation that could be used in experimental analyses with lesser difficulty. Like the previous cases, the simulation results are presented for Pb+Pb collisions at 5.02 TeV energy, which are obtained from the boost invariant relativistic viscous hydrodynamics code MUSIC, with initial conditions generated from the TRENTO or Glauber initial condition model.

5.2.1 Pearson correlator: $\rho([p_T], v_n(q)^2) \equiv \rho([p_T], V_n(q)V_n(q)^\star)$

The momentum dependent construction for the Pearson correlation coefficient between mean transverse momentum per particle and the harmonic flow coefficient in a transverse momentum bin can be defined as,

$$\rho\left([p_T], V_n(q)V_n(q)^\star\right) = \frac{Cov\left([p_T], V_n(q)V_n(q)^\star\right)}{\sqrt{Var\left([p_T]\right) Var\left(V_n(q)V_n(q)^\star\right)}} , \tag{5.14}$$

where the covariance and variance in the above expression are defined similarly as Eqs. (5.2) and (5.3). The correlation coefficient in Eq. (5.14) is a function of the transverse momentum, denoted by q in order to distinguish from $[p_T]$ which is not a variable. The quantity $V_n(q)V_n(q)^\star$ denotes the differential harmonic flow in the transverse momentum bin q in an event and is equivalent to $v_n(q)^2$ (Eq. 3.47). We write it explicitly in order to distinguish it from $V_n V_n(q)^\star$ (Eq. 3.46) which will be discussed shortly.

Figs. 5.10 and 5.11 (left) show the results for the correlation coefficient $\rho([p_T], V_n(q)V_n(q)^\star)$ for the elliptic and the triangular flow. For the elliptic flow, the results are shown for three centralities: $0-5\%$, $30-40\%$ and $60-70\%$, whereas for the triangular flow results are shown only for $0-5\%$. In the figures, the hydrodynamic results are presented only up to $q = 2$ GeV, where hydrodynamics is more applicable. However, it should be noted that the measurements at higher q could be interesting to study non-flow effects, correlations originating from the color-glass condensate etc. Please also note, in order to maintain clarity, the error bars are shown on the figures for specific points to show statistical errors in our simulation results. Fig. 5.10 shows that for the elliptic flow, the correlation coefficients $\rho([p_T], V_2(q)V_2(q)^\star)$ display strong dependence on the transverse momentum q in all centralities. This momentum dependence can be attributed to experimentally observed dependence of the momentum independent correlation coefficient, $\rho([p_T], v_2^2)$, on the transverse momentum cuts [100]. Similar dependence on q for triangular flow in Fig. 5.11 is weak as compared to the elliptic flow. The momentum dependent coefficient, $\rho\left([p_T], V_n(q)V_n(q)^\star\right)$, measures the correlation between the mean transverse momentum per particle and the fraction of total (momentum averaged or integrated) harmonic flow at a definite transverse momentum q in an event. Therefore, it does not depend on the specific shape of the q-dependence of the event averaged harmonic flow (Eq. (3.47)) given by $\langle v_n(q)^2 \rangle$. The importance of this momentum dependent construction of the Pearson correlation coefficient

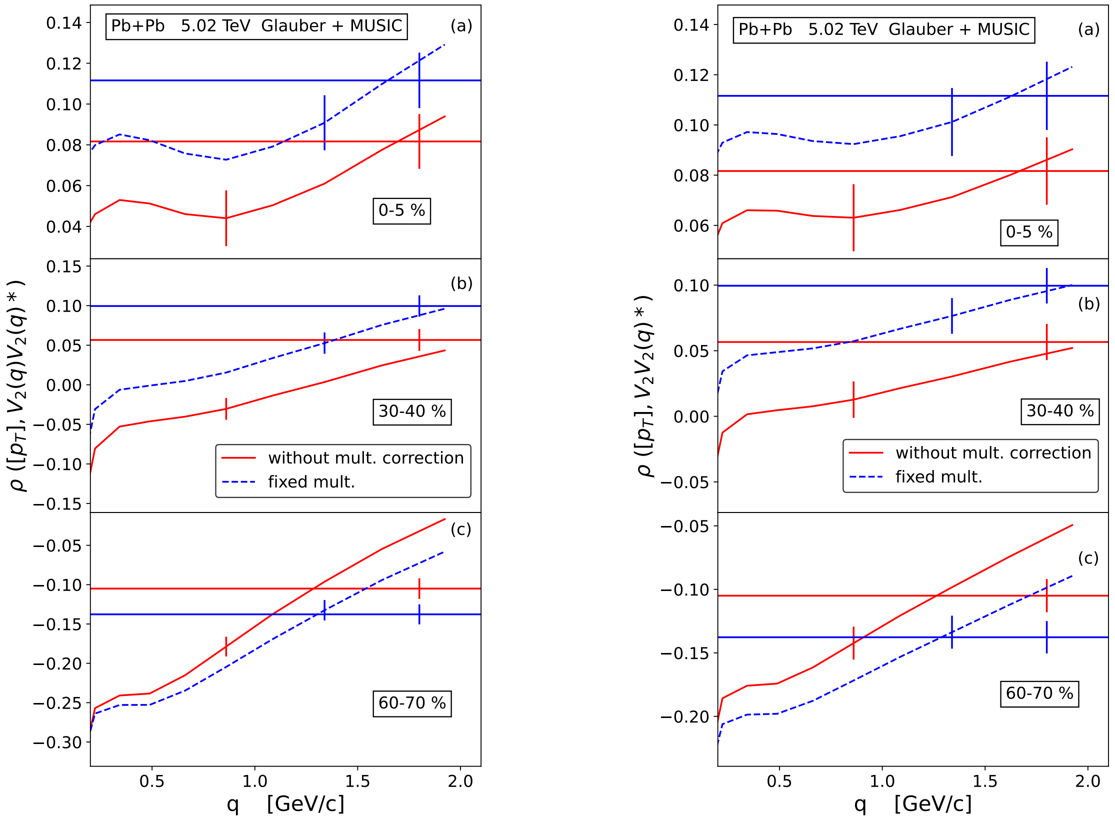

Fig. 5.10 Left: Momentum dependent Pearson correlation between mean transverse momentum per particle and elliptic flow, $\rho([p_T], V_2(q)V_2(q)^\star)$ in Pb+Pb collision at 5.02 TeV for three different centralities: 0-5 %, 30-40 % and 60-70 %. The red solid lines denote the results obtained from hydrodynamic simulations with Galuber initial condition and the blue dashed lines represent the results corrected for multiplicity fluctuations. The horizontal lines denote the correlation coefficients between the momentum averaged flow, $\rho([p_T], v_2^2)$, serving as the baselines for the momentum dependent curves. Right: Same but for the other definition of the momentum dependent correlation $\rho([p_T], V_2V_2(q)^\star)$, where one of the flow harmonics is momentum averaged. The lines and symbols have same meaning as left plot. The figure is from the original publication [129], coauthored by the author.

is that it removes two significant limitations: dependence on transverse momentum cuts and q-dependence of harmonic flow (averaged over events).

For completeness, in those figures we also present results for the momentum independent correlation coefficient $\rho([p_T], v_n^2)$, plotted as the horizontal solid lines, serving as the baselines for the momentum dependent coefficients. It is important to note that the correlation coefficient for the momentum averaged or integrated flow, $\rho([p_T], v_n^2)$, is not simply equal to the momentum average of the correlation coefficient for momentum dependent or differential flow $\rho\left([p_T], V_n(q)V_n(q)^\star\right)$. In particular, it turns out that the observed q-dependence of the correlation coefficient as seen in Figs. 5.10 and 5.11 is due to its construction which involves the ratio of two average quantities, namely the covariance and the variance, which are individually momentum dependent. Later in this section, we discuss this in detail by directly comparing the two covariances, $Cov\left([p_T], V_n(q)V_n(q)^\star\right)$ and $Cov\left([p_T], v_n^2\right)$.

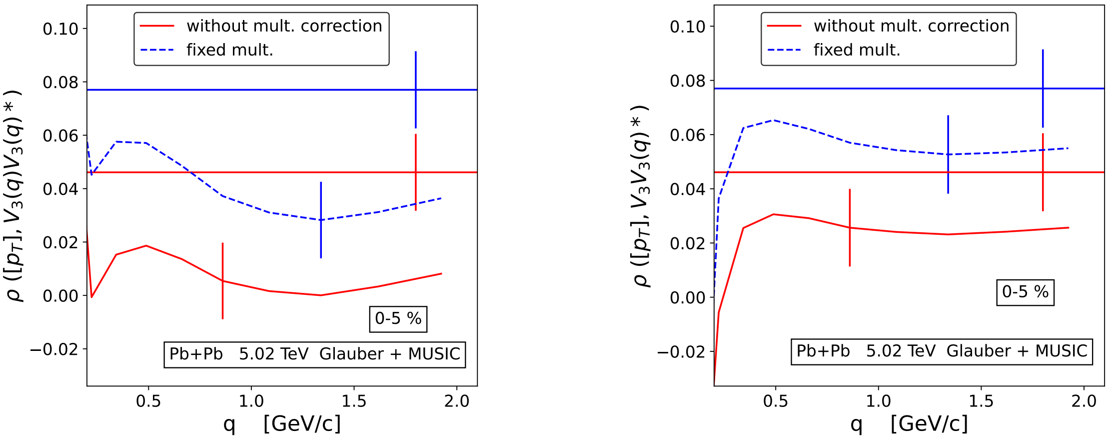

Fig. 5.11 Same as Fig. 5.10 but for the triangular flow and only for 0-5 % centrality. The figure is from the original publication [129], coauthored by the author.

Like the momentum averaged case, the momentum dependent Pearson correlation coefficient between mean transverse momentum and harmonic flow is impacted by the multiplicity fluctuations in a specific centrality bin, as in our calculation we use wide bins of centrality. Therefore, we correct both quantities $[p_T]$ and $V_n(q)V_n(q)^\star$ for the multiplicity fluctuations in each centrality bin using Eq. (5.5). In Figs. 5.10 and 5.11, we also show the results for the correlation coefficient after multiplicity-correction or at fixed multiplicity, denoted by the dashed lines. It is seen that the corresponding correction is numerically sizable and hence once again emphasizes the necessity of such corrections whenever studying similar correlation coefficients. In the following parts, unless otherwise specified, we always use quantities corrected for multiplicity fluctuations.

Experimental definition : $\rho([p_T], V_nV_n(q)^\star)$

The correlation coefficient in Eq. (5.14) is difficult to use in experiments. An alternative definition for the momentum dependent correlation coefficient between the mean transverse momentum and the harmonic flow can be,

$$\rho\left([p_T], V_nV_n(q)^\star\right) = \frac{Cov\left([p_T], V_nV_n(q)^\star\right)}{\sqrt{Var\left([p_T]\right)Var\left(V_nV_n(q)^\star\right)}} , \qquad (5.15)$$

which is constructed in analogy to the experimental definition of transverse momentum dependent harmonic flow (Eq. (3.46)). The difference between the correlation coefficients in Eq. (5.14) and Eq. (5.15) is similar to the difference between Eq. (3.47) and Eq. (3.46). The above correlation coefficient $\rho([p_T], V_nV_n(q)^\star)$ is relatively easier to measure experimentally. The denominator of Eq. (5.15), $Var\left(V_nV_n(q)^\star\right)$ is a four particle correlator where only two of them are restricted to a particular transverse momentum bin, unlike $Var\left(V_n(q)V_n(q)^\star\right)$, where all the four particles are from same bin hence more difficult to measure in experiment especially for larger value of q. However, the correlation coefficient in Eq. (5.15) does not have such a simple interpretation as the coefficient in Eq. (5.14). The results for $\rho([p_T], V_n V_n(q)^\star)$, from hydrodynamic simulations, are presented in the right panels of Figs. 5.10 and 5.11. The qualitative behavior of the transverse momentum dependence for the correlation coefficient remains similar to Eq. (5.14) for all centralities with, however, weaker dependence for $\rho\left([p_T], V_n V_n(q)^\star\right)$, in comparison to $\rho\left([p_T], V_n(q) V_n(q)^\star\right)$. This shows that even though we change the definition for the momentum dependent correlation coefficient for the sake of experimental measurement, there is no significant effect on the overall results.

5.2.2 Constraining granularity in the initial state

Granularity in the initial state is defined by the nucleon width w and it is identified by the size of the region where the nucleons deposit energy (entropy) at the time of the collision. If w is small then the initial state is more granular and a larger w indicates a less granular initial state. The information on w is important because it defines the nucleon wave function which is considered as Gaussian as discussed in Chapter-2. It has been seen that the correlation coefficient between the mean transverse momentum and harmonic flow is sensitive to the nucleon width or the granularity of the initial state for the hydrodynamic evolution [95, 98]. Therefore, we study the same thing for momentum dependent correlation coefficient between transverse momentum and harmonic flow, where granularity of initial state can have more significant effect. In models, the granularity of the initial state can be modified by changing the nucleon size, defined by the wave function of the nucleon. In our analysis, we use TRENTO model to obtain the initial state for this particular study, where the granularity is changed by changing the 2D Gaussian width w (described in 2.6.1) associated to each nucleon in TRENTO. Experimental results suggest that the size of the region where the nucleon deposit energy is small, which corresponds to an initial state with high granularity [98]. In our analysis, we study this size dependence by changing the nucleon width in TRENTO with three different values: $w = 0.3$, 0.5, and 0.8 fm.

Fig. 5.12 (left) shows the results for the momentum dependent correlation coefficient $\rho([p_T], V_n(q) V_n(q)^\star)$, for 20-30% centrality for different nucleon widths. For the elliptic flow, the correlation coefficient shows a strong dependence on the transverse momentum q for all granularity. However, the increase of the correlation coefficient with q is less steep for the initial state with a more granularity i.e. with smaller w. The effect becomes dominant for the triangular flow (panel (b). For triangular flow, the correlation even decreases with q for most granular state having $w = 0.3$ fm. Specifically, the correlation coefficient shows different patterns of transverse momentum dependence within the range: $q = 0$-1.5 GeV for different w. The momentum independent correlation coefficients (baselines), on the other hand, follow a particular dependence on the granularity; the correlation decreases as w increases or the granularity decreases.

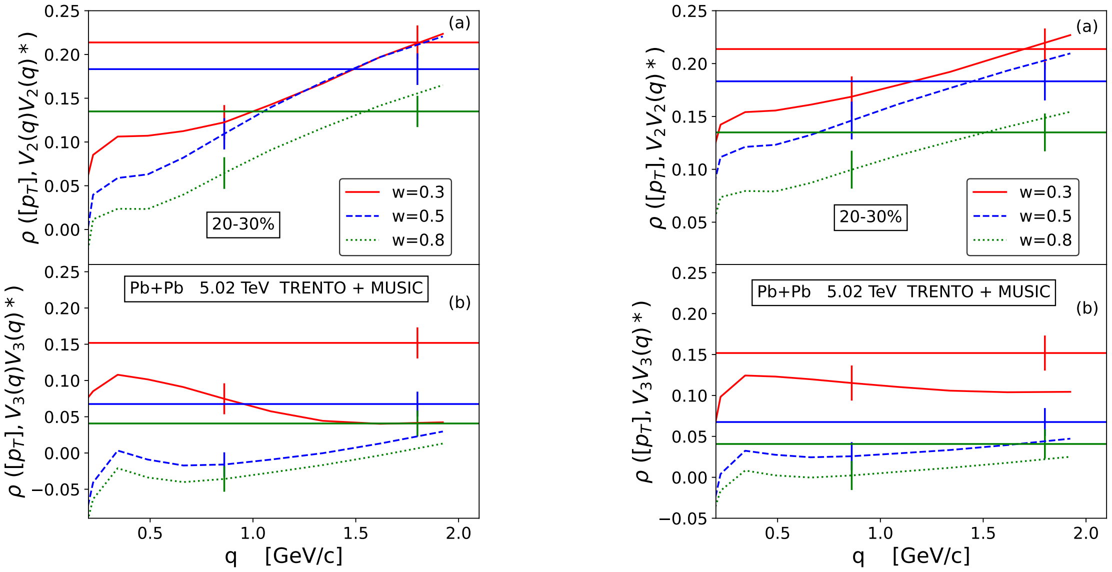

Fig. 5.12 Left: Pearson correlation coefficient $\rho([p_T],V_n(q)V_n(q)\star)$ between the mean transverse momentum per particle and momentum dependent elliptic flow (a) and triangular flow (b) obtained with TRENTO initial condition in Pb+Pb collision at 5.02 TeV with 20-30 % centrality for different granularity of the initial state: $w = 0.3, 0.5$ fm and 0.8 fm denoted by red, blue and green colors respectively. The horizontal lines denote the baselines corresponding to the correlation between the momentum averaged flow. Right: Same but for the other definition of momentum dependent correlation : $\rho([p_T],V_nV_n(q)\star)$. The figure is from the original publication [129], coauthored by the author.

The correlation coefficients, $\rho([p_T],V_nV_n(q)^\star)$, is shown on the right panel of Fig. 5.12. The coefficients show a quite similar behavior for the transverse momentum dependence as $\rho([p_T],V_n(q)V_n(q)^\star)$. Again for the triangular flow, the initial state with higher granularity shows less steep dependence on q and furthermore for this correlation coefficient the difference between the initial states with different w is the strongest in the range $q = 0$-1.5 GeV. Therefore, it would be interesting to verify our model predictions in experiments, particularly for these correlation coefficient $\rho([p_T],V_n(q)V_n(q)^\star)$ or $\rho([p_T],V_nV_n(q)^\star)$, which will put precise constraints on the parameters of the initial state in the hydrodynamic modeling of heavy-ion collisions [98]. A comparison of the results in Fig. 5.12 indicates that the momentum dependent correlation coefficient $\rho([p_T],V_nV_n(q)^\star)$ serves as a better candidate to probe the granularity whereas its experimental measurement is easier than $\rho([p_T],V_n(q)V_n(q)^\star)$. We will again come to the effect of granularity later while discussing the momentum dependent covariances.

Viscosity dependence

In order to present a comprehensive picture, discussing the dependence of this momentum dependent correlation coefficient on medium properties such as shear or bulk viscosity remain indispensable. In Fig. 5.13, the correlation coefficients for three different values of the shear viscosity to entropy density ratio η/s are presented for both definitions and for both elliptic

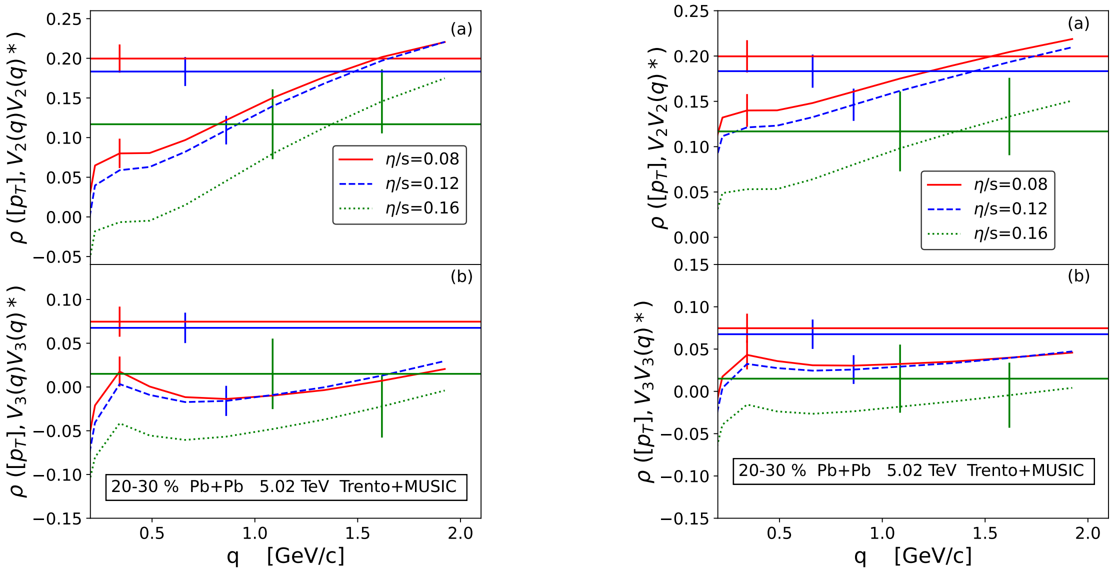

Fig. 5.13 Same as Fig. 5.12 but for the comparison of three different values of shear viscosity to entropy density ratio η/s: 0.08, 0.12, 0.16 denoted by red, blue and green colors respectively. The figure is from the original publication [129], coauthored by the author.

and triangular flow. The qualitative nature of the transverse momentum dependence of the correlation coefficient remain similar for different values of shear viscosity. The dependence on the shear viscosity is rather much weaker in comparison to the granularity. The change in shear viscosity causes a overall shift of the curves, without altering the specific shape for the momentum dependence. The shift is, however, much smaller in magnitude; there is practically not much difference between $\eta/s = 0.08$ and $\eta/s = 0.12$ for both momentum dependent correlation coefficients and their baselines. Therefore, the momentum dependent correlation coefficient is not specifically sensitive to shear viscosity according to Fig. (5.13); the shape of the curves are similar for different values of shear viscosity. The correlation coefficient between mean transverse momentum and the harmonic flow might not be an ideal candidate to probe the viscosity of the QGP medium. We have checked that the momentum dependence on the bulk viscosity of the considered correlation coefficients is similar as the dependence on shear viscosity.

5.2.3 Addressing experimental challenges: Alternative definitions

The experimental measurement of the momentum dependent correlation coefficient, $\rho([p_T], V_n(q)V_n(q)^\star)$ is difficult for low statistics at large q. The estimation of $\rho([p_T], V_nV_n(q)^\star)$ is relatively easier but still sufficiently difficult in comparison to the momentum independent correlation coefficient, $\rho([p_T], V_nV_n^\star)$. The main experimental difficulty lies in estimating the variances in the denominators i.e. $Var(V_n(q)V_n(q)^\star)$ or $Var(V_nV_n(q)^\star)$. These quantities require the measurement of a four (or two) particle correlator in the same transverse momentum bin, which turn out challenging for the bins with large q due to limited statistics. Below we propose alternate and approximated choice for the momentum dependent correlation coefficients that could be easily used in experiments.

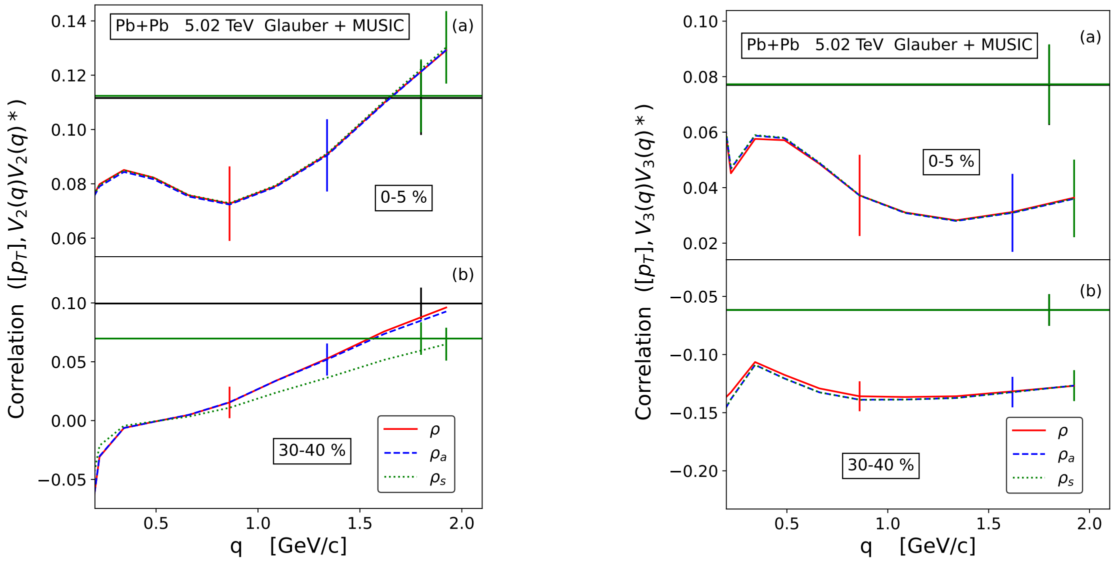

Fig. 5.14 Momentum dependent correlation coefficient between $[p_T]$ and $V_n(q)V_n(q)^\star$ for 0-5 % (panel (a)) and 30-40 % (panel (b)) centrality in Pb+Pb collision at 5.02 TeV for the elliptic (left) and triangular (right) flow coefficient. The red lines denote the original definition in Eq. (5.14). The blue dashed lines denote the approximated definition for the correlation in Eq. (5.16) and the green dotted line denotes the results obtained with the scaled correlation coefficient in Eq. (5.20). The figure is from the original publication [129], coauthored by the author.

One of the possibilities would be to use the momentum averaged or integrated variance, $Var(v_n^2)$, in the denominator within the square root of the correlation coefficient, because it would be much easier to estimate a four particle correlator in the full transverse momentum acceptance. But then at the same time we need to divide the new construction with $\frac{\langle V_n(q)V_n(q)^\star\rangle}{\langle v_n^2\rangle}$ (or $\frac{\langle V_n(q)V_n^\star\rangle}{\langle v_n^2\rangle}$) in order to properly retain the momentum dependence. With this, the new modified approximate formula for the momentum dependent correlation coefficients would read,

$$\rho_a([p_T], V_n(q)V_n(q)^\star) = \frac{Cov([p_T], V_n(q)V_n(q)^\star)\langle v_n^2\rangle}{\sqrt{Var([p_T])\,Var(v_n^2)\langle V_n(q)V_n(q)^\star\rangle}} \tag{5.16}$$

and

$$\rho_a([p_T], V_nV_n(q)^\star) = \frac{Cov([p_T], V_nV_n(q)^\star)\langle v_n^2\rangle}{\sqrt{Var([p_T])\,Var(v_n^2)\langle V_nV_n(q)^\star\rangle}}\ . \tag{5.17}$$

The approximate formulae in Eqs. (5.16) and (5.17) are expected to reproduce very close results as of the original momentum dependent correlation coefficients in Eqs. (5.14) and (5.15), because if we take the ratios of the new formulae to the original ones then the factors

$$\frac{\sqrt{Var(V_n(q)V_n(q)^\star)}\langle v_n^2\rangle}{\sqrt{Var(v_n^2)}\langle V_n(q)V_n(q)^\star\rangle} \tag{5.18}$$

and

$$\frac{\sqrt{Var(V_nV_n(q)^\star)}\langle v_n^2\rangle}{\sqrt{Var(v_n^2)}\langle V_nV_n(q)^\star\rangle} \tag{5.19}$$

are consistent with 1 as discussed in Chapter-3 [125].

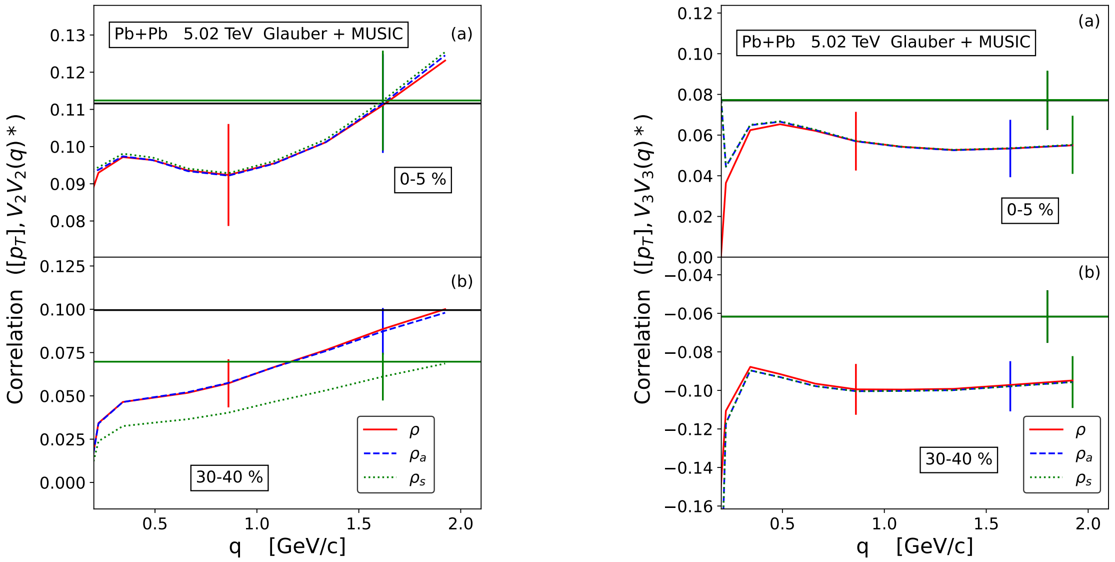

Fig. 5.15 Same as Fig. 5.14 but for the correlation coefficient between $[p_T]$ and $V_nV_n(q)^\star$. The figure is from the original publication [129], coauthored by the author.

Another possibility to re-construct the correlation coefficients would be to scale the covariance between the mean transverse momentum and the harmonic flow sitting at the numerator of those expressions, by the average of momentum dependent harmonic flow squared instead of the standard deviation. Such modifications are expected to rescale the magnitudes of the correlation coefficient without changing its specific momentum dependence. The formulae for the scaled correlation coefficients are given by,

$$\rho_s([p_T], V_n(q)V_n(q)^\star) = \frac{Cov([p_T], V_n(q)V_n(q)^\star)}{\sqrt{Var([p_T])}\langle V_n(q)V_n(q)^\star\rangle)} \tag{5.20}$$

and

$$\rho_s([p_T], V_nV_n(q)^\star) = \frac{Cov([p_T], V_nV_n(q)^\star)}{\sqrt{Var([p_T])}\langle V_nV_n(q)^\star\rangle} \ . \tag{5.21}$$

The scaled correlation coefficients, ρ_s, are expected to appear as a good approximation of the original correlation coefficients ρ when the harmonic flow is dominated by fluctuations i.e when $\sqrt{Var(V_n(q)V_n(q)^\star)} \simeq \langle V_n(q)V_n(q)^\star\rangle$ and $\sqrt{Var(V_nV_n(q)^\star)} \simeq \langle V_nV_n(q)^\star\rangle$. According to the discussions in Chapter-3, this happens in case of elliptic flow in central collision and triangular flow in all centralities. For completeness, the momentum independent version of the scaled correlation coefficient would be,

$$\rho_s\big([p_T], v_2^2\big) = \frac{Cov\big([p_T], v_2^2\big)}{\sqrt{Var([p_T])}\langle v_2^2\rangle} , \tag{5.22}$$

which is almost same as the normalized symmetric cumulant between the mean transverse momentum $[p_T]$ and the harmonic flow v_n^2 as discussed earlier. Moreover, STAR collaboration has used Eq. (5.22) for studying the nuclear deformation in relativistic Au+Au and U+U collisions systems [344].

Figs. 5.14 and 5.15 show the comparison between the original momentum dependent correlation coefficient and the approximated definitions for the momentum dependent correlation coefficient $\rho\left([p_T], V_n(q)V_n(q)^\star\right)$ and $\rho\left([p_T], V_nV_n(q)^\star\right)$ respectively for $0-5\%$ and $30-40\%$ centralities and for the elliptic and triangular flow. It could be seen that almost in every cases, within the range $q < 2$ GeV, the results with the approximated expressions coincide with the original formula for the correlation coefficient. In particular, the correlation coefficient ρ_a is very close to the correlation coefficient ρ in all cases and therefore could serve as a good experimental estimate of the momentum dependent correlation between mean transverse momentum and harmonic flow. The scaled correlation coefficient ρ_s also provides equally good approximation except for the elliptic flow in peripheral collisions where fluctuations have less importance than the geometry. Therefore, ρ_s can be used in experiment for the triangular flow and for the elliptic flow in central collisions where fluctuations dominated harmonic flow exists. It should be noted that all of these approximated formulae represent well-defined measures for the momentum dependent correlation coefficients between $[p_T]$ and momentum dependent flow harmonics, and they could be measured in the experiments and compared to the models, although they are not exactly the Pearson correlation coefficients.

5.2.4 Scaled covariance

As an extension of our study, we also study the momentum dependence of the covariance between the mean transverse momentum and momentum dependent harmonic flow. The covariance appears at the numerator of the momentum dependent correlation coefficients, $\rho\left([p_T], V_n(q)V_n(q)^\star\right)$ or $\rho\left([p_T], V_nV_n(q)^\star\right)$, and significantly contribute to their strong dependence on the transverse momentum q. Therefore, it would be interesting to look directly at the momentum dependent covariances between the mean transverse momentum and the harmonic flow, which itself is an as good observable as the correlation coefficient and remove the momentum dependence of the denominator. But of course we have to normalize the covariance

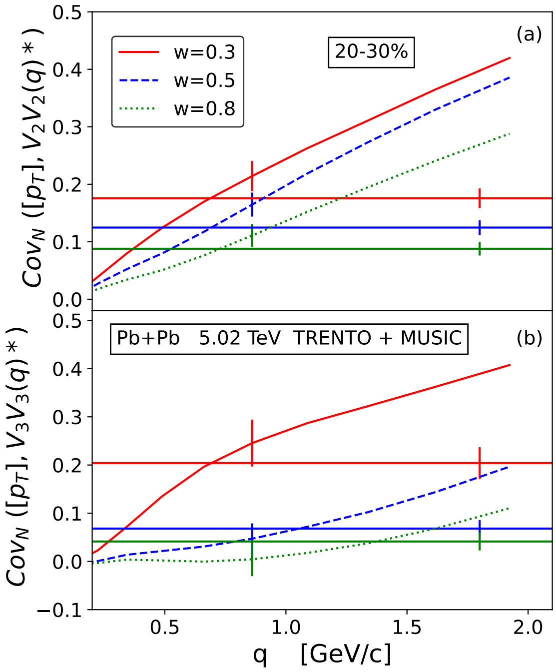

Fig. 5.16 Normalized covariance between mean transverse momentum $[p_T]$ and momentum dependent harmonic flow $V_nV_n(q)^\star$ for 20-30 % centrality in Pb+Pb collision at 5.02 TeV with TRENTO initial condition for three different values of w: 0.3, 0.5 and 0.8 fm denoted by red, blue and green colors respectively. Panel (a) and (b) represent the results for the elliptic and triangular flow respectively. The figure is from the original publication [129], coauthored by the author.

properly. In particular, momentum dependent normalized covariance can be defined as,

$$Cov_N\left([p_T], V_n(q)V_n(q)^\star\right) = \frac{Cov\left([p_T], V_n(q)V_n(q)^\star\right)}{\sqrt{Var([p_T])}\langle v_n^2\rangle} . \tag{5.23}$$

and

$$Cov_N\left([p_T], V_nV_n(q)^\star\right) = \frac{Cov\left([p_T], V_nV_n(q)^\star\right)}{\sqrt{Var([p_T])}\langle v_n^2\rangle} , \tag{5.24}$$

where the normalization is chosen in a similar way as for the normalized symmetric cumulants between the mean transverse momentum and the harmonic flow coefficients discussed earlier. It is interesting to note that the baselines for both $Cov_N\left([p_T], V_n(q)V_n(q)^\star\right)$ and $Cov_N\left([p_T], V_nV_n(q)^\star\right)$ are given by $\rho_s\left([p_T], v_2^2\right)$ given in Eq (5.22). Such normalized covariances can be useful to constrain the granularity of the initial state in better way, in the sense that it is relatively easier to measure in experiment in comparison to the full correlation coefficient. It can also pick up the robust sensitivity of such momentum dependent observable between $[p_T]$ and harmonic flow, which does not get partially washed out by the similar dependence in the denominator.

Fig. 5.16 shows the normalized covariance in Eqs. (5.23) and (5.24) for the elliptic and triangular flow in 20-30% centrality. It is clearly visible that the normalized covariance between the mean transverse momentum and the momentum dependent harmonic flow shows a strong dependence on the transverse momentum q and a remarkable sensitivity to the granularity of initial state or the nucleon width w, showing a significant separation between three cases. This occur due to the absence of momentum dependence in the denominator. The effect is particularly pronounced for the triangular flow, where a steepest dependence on q is observed for $w = 0.3$ fm in the range of transverse momentum $q < 1$ GeV, along with a striking difference from the other two cases. Therefore, the normalized covariance in Eqs. (5.23) and (5.24) could serve as an ideal candidate to constrain the granularity in the initial state of heavy-ion collision upon successful verification of our results in the experiments.

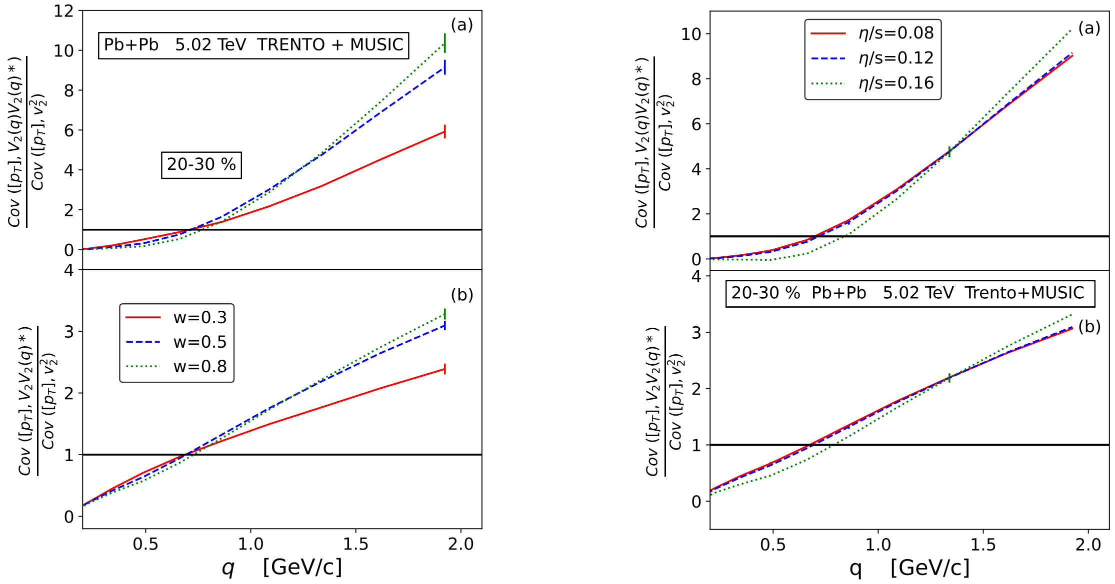

Fig. 5.17 Left: Ratio of the momentum dependent and momentum independent covariance between mean transverse momentum per particle and harmonic flow coefficients for 20-30 % centrality in Pb+Pb collision at 5.02 TeV for three different values for granularity in the initial state : w= 0.3 (red), 0.5 (blue) and 0.8 (green) fm. In the upper and lower panel, the numerators of the ratios are with momentum dependent flow $V_n(q)V_n(q)^\star$ and $V_nV_n(q)^\star$ respectively. Right: Same as left plot but for three different values of shear viscosity to entropy ratio η/s: 0.08 (red), 0.12 (blue) and 0.16 (green). The figure is from the original publication [129], coauthored by the author.

An alternative way to look into the momentum dependence of the covariance would be directly studying the ratio of momentum dependent and momentum averaged (independent) covariance, given by,

$$\frac{Cov\left([p_T],V_n(q)V_n(q)^\star\right)}{Cov\left([p_T],V_nV_n^\star\right)} \tag{5.25}$$

and

$$\frac{Cov\left([p_T],V_nV_n(q)^\star\right)}{Cov\left([p_T],V_nV_n^\star\right)}\,. \tag{5.26}$$

The construction of such observables is possible whenever the denominator is not close to zero otherwise it will make the ratio to diverge. In Fig. 5.17 (left), the simulation results for the covariance ratios in Eqs. (5.25) and (5.26) are shown for three different values of granularity parameter w in collisions with 20-30 % centrality. The covariance ratios show even more spectacular transverse momentum dependence. For both of the covariance ratios, all lines cross the baseline of 1, at the average transverse momentum $q \simeq \langle [p_T] \rangle$. Then the lines split at higher momenta depending on the granularity of the initial state given by w and especially showing a remarkable difference for $q \simeq$ 1-2 GeV. Thus the covariance ratio also shows outstanding sensitivity on the granularity and could be measured in experiment to constrain w with great precision.

To complete the picture, the right panel of Fig. 5.17 shows the shear viscosity dependence of the covariance ratios for different values of η/s in the same centrality. The results suggest that the momentum dependence of the covariance ratio has a weak dependence on the value of shear viscosity. The particular shapes of the momentum dependence of such observable could be used as an additional constraint on the value of shear viscosity in Bayesian analysis of model simulation and experimental data [333, 28, 334].

Chapter 6

Nuclear deformation through heavy-ion collisions

Nuclear structure is primarily studied in low energy theoretical and experimental nuclear physics. As we have seen that the information on the nuclear density profile and the Woods-Saxon parameters are particularly important to sample nucleon positions in a nucleus. Such information on nuclear structure can be obtained from low energy electron scattering experiments. So far in our discussions, we were limited to the collision of spherical nuclei i.e. ^{208}Pb+^{208}Pb. However, the majority of atomic nuclei in their ground state are not spherical and posses an intrinsic deformation having in the leading order an axially quadrupole or ellipsoidal structure. Such deformations result in non-zero electric multipole moments of the nucleus with respect to the nuclear wave function. The deformation is quantified by a dimensionless deformation parameter β_n [345–347]. Examples of such deformed nuclei are uranium (^{238}U), xenon (^{129}Xe) etc. which posses a significant non-zero quadrupole deformation β_2.

In low energy experiments, information on these deformation parameters are obtained by measuring the electric multipole transition probability of the nucleus from the ground state to excited states [345, 346]. In low energy theory and simulations, the structure and deformation parameters are estimated through *ab-initio* calculations [348–351]. On the other hand, high-energy nuclear experiments or relativistic heavy-ion collisions can serve as an excellent platform for nuclear structure and deformation studies [347, 104, 106, 109, 119, 122]. In particular, over the last few years, there have been numerous theoretical [103, 347, 104–118, 352, 353] and experimental [119–123, 101, 102, 124] efforts to study deformed nuclear structure of heavy nuclei through high energy relativistic heavy-ion collisions at RHIC and the LHC energies. At RHIC, most of these studies have focused on the structures of nuclei such as ^{238}U, ^{197}Au and isobars such as ^{96}Ru and ^{96}Zr. At the LHC, the study of collisions with the deformed xenon nucleus ^{129}Xe along with its comparison to spherical lead nuclei ^{208}Pb, has served as a candidate for nuclear deformation studies.

The deformation of nuclei has a direct impact on the shape and the geometry of the initial state of heavy-ion collisions, leaving a significant effect on fluctuations and correlations of collective observables in the final state. Especially, the quadrupole deformation of the uranium nucleus is found to have a substantial effect on the event-by-event mean transverse momentum per particle $[p_T]$ and harmonic flow coefficients V_n [104, 106]. As a result, the correlations, cumulants and the fluctuation-probing factorization breaking coefficients between those observables are found to exhibit a distinctive behavior [104, 106, 128, 130], paving the path to probe the deformation parameter β_2 through heavy-ion collisions. In this chapter, we will discuss the observables that are discussed in the earlier chapters, for U+U collision at RHIC energy, which could put exclusive constraints on the quadrupole deformation (β_2) of uranium nucleus. The following sections are, for the most part, presentations from the original publications [128, 130], coauthored by the author. We denote the quadupole deformation by β for simplicity, as we will limit our discussion to only quadrupole deformation of uranium nuclei.

6.1 Collision of deformed nuclei

If two deformed nuclei are collided in a collision, then the geometry and shape of the overlap region is directly impacted by the deformed structure of the nuclei. This effect is translated to the final state observables such as mean transverse momentum per particle $[p_T]$ and harmonic flow V_n through hydrodynamic expansion. Therefore, to understand how the deformed structure affect these quantities, first we need to implement the nuclear deformation in the Woods-Saxon density distribution for such nuclei, which is used for sampling the nucleon positions in those nuclei before collision.

Woods-Saxon density distribution for a deformed nucleus:

The mass density distribution for a deformed nucleus with axial symmetry is given by three parameter Fermi distribution function with Woods-Saxon parametrization [347, 134, 104, 109, 116],

$$\rho(r,\theta,\phi) = \frac{\rho_0}{1+\exp[\frac{r-R_0(1+\beta Y_{2,0}(\theta,\phi))}{a}]}, \tag{6.1}$$

where only the leading order *quadrupole deformation* is considered, identified by the dimensionless quadrupole deformation parameter $\beta(\equiv \beta_2)$, which is most relevant for the uranium nuclei. The other parameters R_0, ρ_0 and a carry similar meaning as before (Eq. (2.15)) with $R \equiv R_0$ for a spherical nucleus. The spherical harmonic $Y_{2,0}(\theta,\phi)$ breaks the spherical symmetry of the nucleus and is given by,

$$Y_{2,0}(\theta,\phi) = \sqrt{\frac{5}{16\pi}}(3\cos^2\theta - 1)\ , \tag{6.2}$$

where θ and ϕ are the polar and azimuthal angles in the intrinsic nuclear frame. The quadrupole deformation parameter β, given by[354, 106],

$$\beta \simeq \frac{4\pi}{5} \frac{\int r^2 \rho(r,\theta,\phi) Y_{2,0}(\theta,\phi) d^3\vec{r}}{\int r^2 \rho(r,\theta,\phi) d^3\vec{r}} \tag{6.3}$$

leads to an ellipsoidal structure of the nucleus. If $\beta > 0$ (^{238}U) then the nuclear structure is *prolate* and the nucleus is *oblate* when $\beta < 0$ (^{197}Au).

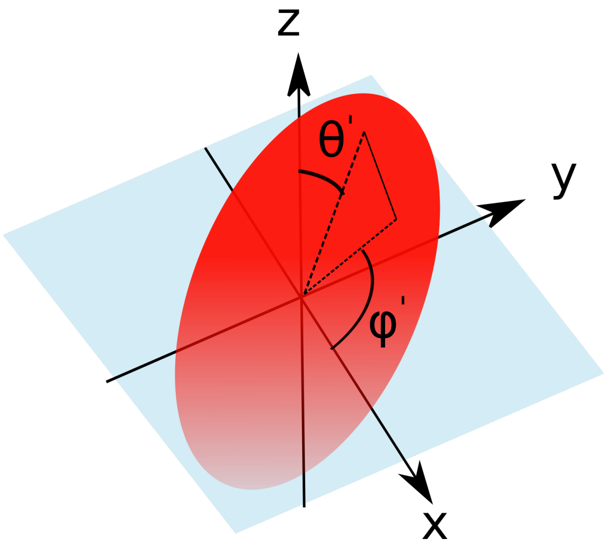

Fig. 6.1 Deformed uranium nucleus having prolate structure with $\beta > 0$. The nucleus is randomly oriented with respect to the laboratory frame with a polar tilt θ' and an azimuthal rotation ϕ'. The z axis represents the beam-axis in laboratory frame and (x,y) plane is the transverse plane. The figure is a modification from [106].

6.1.1 Geometry of the overlap region in deformed nuclei collisions:

In heavy-ion collision experiments, the deformed nuclei are injected through the beam pipe of the accelerator, where the colliding nuclei have random orientations in the laboratory frame. This is because the principal axes of the ellipsoids have random angles with the beam-axis. In particular, the principal axis has a polar tilt θ' and an azimuthal rotation ϕ' with respect to the beam-axis z in the laboratory frame, as shown in Fig. 6.1. As a result, at the time of the collision, the two deformed nuclei collide with two random orientations resulting in different shapes of the overlap area in each collision. This phenomenon has a great impact on the mean transverse momentum and harmonic flow. In this chapter, we consider uranium nuclei which have a positive β and hence have a prolate structure. Additionally, we restrict ourselves to central collisions where the overlap area of the two nuclei is maximum and the effect of the deformation is especially pronounced.

Let us consider central or ultracentral collisions of uranium nuclei with maximal overlap between the two nuclei. Let us also label the two nuclei as A and B with their orientations with respect to the collision axis in the lab frame, at the time of collision, defined by the sets of angles (θ'_A, ϕ'_A) and (θ'_B, ϕ'_B) respectively. There are two extreme cases of fully-overlapping scenario which are particularly interesting [104, 106]:

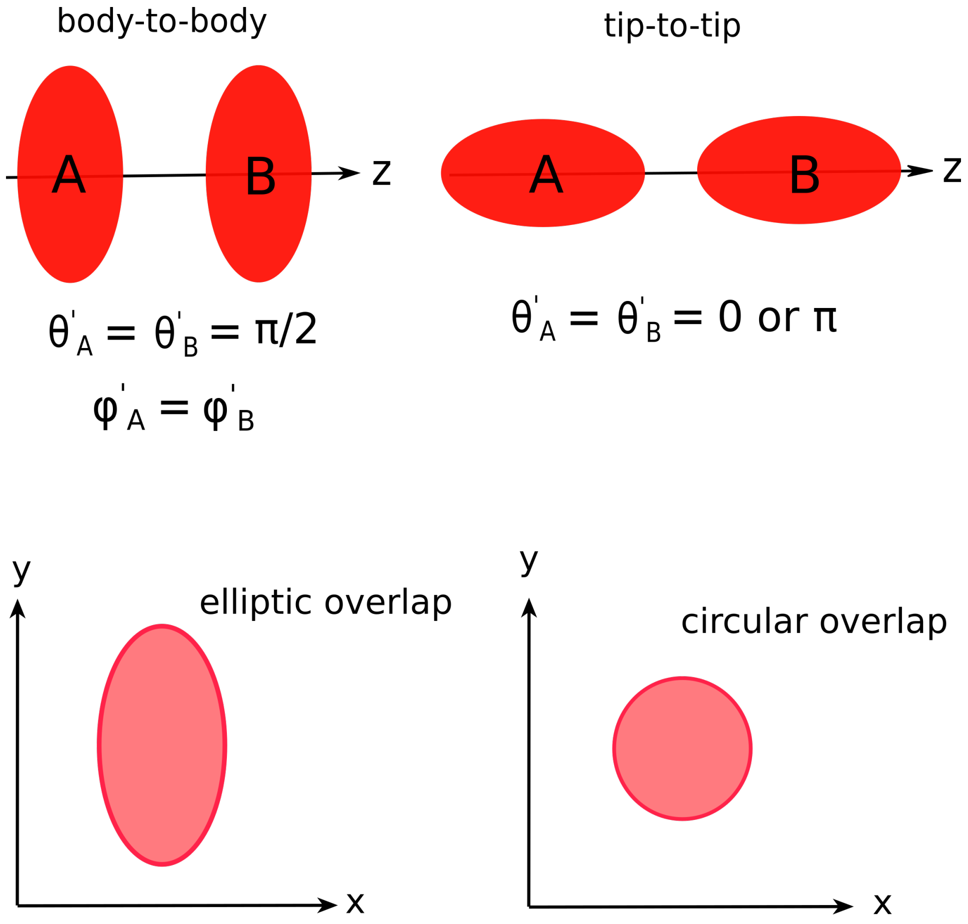

Fig. 6.2 Pictorial representation of the body-to-body and tip-to-tip collision of deformed uranium nuclei. For body-to-body collision (left) the polar angles of the nuclei with the collision axis assume $\theta'_A = \theta'_B = \pi/2$ and azimuthal angles $\phi'_A = \phi'_B$, resulting in an elliptic overlap area after collision. On the other hand a tip-to-tip collision (right) occurs when $\theta'_A = \theta'_B = 0$ or π, producing a circular overlap area after collision. The figure is motivated from [106].

- A *body-to-body* collision. In this case two nuclei are essentially perpendicular to the collision axis with $\theta'_A = \theta'_B = \pi/2$ and both nuclei are rotated by same azimuthal angle $\phi'_A = \phi'_B$ as shown in Fig. 6.2 (left). Then the overlap area on the transverse plane takes an elliptic shape, which originates from the shape of the colliding nuclei, enhancing the ellipticity of the initial state even in the *central collisions.*
- A *tip-to-tip* collision. In such configuration, the principal axis of each colliding nucleus coincides with the beam-axis (z) i.e. $\theta'_A = \theta'_B = 0$ or π. This results in a circular overlap

region on the transverse plane, as shown in Fig. 6.2 (right), having smaller transverse area than the body-to-body collisions.

The other configurations fall in between these two cases.

6.1.2 Deformation effect on the collective observables

In central collisions of deformed nuclei, the different configurations of the initial states directly influence the collective observables such as mean transverse momentum per particle $[p_T]$ and harmonic flow coefficients V_n in the final state.

Transverse momentum

Let us consider the above mentioned configurations for events with full overlap of the nuclei at fixed multiplicity i.e. fixed entropy in the initial state. In the case of a tip-to-tip collision, the transverse size of the overlap area (circular) or collision volume is smaller corresponding to a larger density at fixed multiplicity [104, 106]. According to relativistic thermodynamics, this results in larger temperature, hence larger pressure and larger energy per particle, which eventually give rise to larger transverse momentum per particle $[p_T]$. The opposite situation occurs when the collision is body-to-body, which leads to larger transverse size and hence a smaller $[p_T]$. Thus in central collisions of deformed nuclei, the deformation has a direct impact on $[p_T]$. Nuclear deformation contributes significantly to the event-by-event fluctuations of mean transverse momentum per particle. In general the average transverse momentum in heavy ion collision can be related to the temperature of QGP medium as [11],

$$\langle p_T \rangle \simeq 3T \ , \tag{6.4}$$

where T is the effective temperature of the medium. The dependence of $[p_T]$ on the transverse size of the overlap region R can be written as [106],

$$\frac{\delta p_T}{\langle p_T \rangle} \simeq -c_s^2 \frac{\delta R}{\langle R \rangle} \ , \tag{6.5}$$

where $\delta p_T = [p_T] - \langle p_T \rangle$, $\delta R = R - \langle R \rangle$, c_s is the speed of sound in the QGP and $\langle \ldots \rangle$ denote the event-averaged quantities. The negative sign denotes the anti-correlation between mean transverse momentum per particle and transverse size, as seen in Fig. 5.3.

Harmonic flow coefficients

The nuclear deformation largely affects the harmonic flow coefficients [106], specifically the elliptic flow, in central collisions. In a central collision of spherical nuclei, when two nuclei fully overlap, the harmonic flow is mostly driven by the event-by-event fluctuations. This is also the case for elliptic flow, unlike a non central collision where it is driven by the elliptic geometry of the initial state.

However, in case of deformed nuclei collision this is no longer true. Let us consider the two extreme cases of fully overlapping nuclei in central collision, as discussed earlier. In body-to-body collision, the overlap region takes the shape of an ellipse resulting in a significantly large ellipticity ϵ_2 even in central collision. This leads to an enhanced contribution to the elliptic flow v_2 in the final state which gets dominating contribution from geometry than fluctuations. On the other hand, in tip-to-tip collision, the overlap area is circular, which does not contribute to the geometrical component of v_2 but solely to the component arising from fluctuations. Thus deformation plays a significant role in enhancing the eccentricity and therefore the elliptic flow in central collision. This fascinating phenomena creates an unique opportunity to probe the deformation parameters by studying the correlations and fluctuations of flow and related observables.

The contribution of deformation to the initial eccentricity can be written as [109],

$$\epsilon_2\,\{2\}^2 = a_2' + b_2'\beta^2\ , \tag{6.6}$$

where, $\epsilon_2\,\{2\} = \sqrt{\langle \epsilon_2^2 \rangle}$ is the event averaged eccentricity (ellipticity) in analogy to $v_2\{2\}$. As discussed in Chapter-3, the elliptic flow can be related to the initial eccentricity as the hydrodynamic response of the initial state $v_2\{2\}^2 = k_2\,\epsilon_2\,\{2\}^2$, with k_2 being the hydro-response coefficient. Therefore, the elliptic flow can be related to the deformation parameter of the nucleus through similar parametric dependence,

$$v_2\{2\}^2 = a_2 + b_2\beta^2\ . \tag{6.7}$$

It should be noted that the coefficients a_2' and a_2 quantify the contributions to the participant eccentricity and elliptic flow, that do not arise from the deformation of the nucleus, while b_2' and b_2 pick up contributions to the eccentricity and elliptic flow driven by deformation of the colliding nuclei.

6.2 Fluctuations and correlations for deformed nuclei collision

Due to nuclear deformation, event-by-event fluctuations of harmonic flow which we studied in terms of the momentum dependent factorization-breaking coefficients, and the correlation coefficients or the cumulants between mean transverse momentum and harmonic flow get impacted, showing peculiar characteristics in central collisions of such deformed nuclei, which can be potentially used to put constraints on the deformation parameter β.

For the results presented in this section, we simulate U+U collisions at RHIC energy $\sqrt{s_{NN}} = 193$ GeV with TRENTO initial conditions and then relativistic hydrodynamic evolution through MUSIC. The Woods-Saxon and deformation parameters used for uranium-238 nucleus is presented in Table 6.1.

Nucleus	R_0 (fm)	a (fm)	β
^{238}U	6.86	0.42	0.265

Table 6.1 Woods-Saxon parameters for nuclear density distribution (Eq. 6.1) in deformed uranium nucleus [347, 134].

6.2.1 Factorization-breaking coefficients

Let us first discuss the factorization-breaking coefficients which measure the decorrelation between flow vectors in different transverse momentum bins as discussed in Chapter-3. Here we want to explore if nuclear deformation plays any role in modifying these factorization-breaking coefficients. For this, we consider three different scenarios: a) U+U collision with deformation ($\beta = 0.265$), which could be considered as the default case. b) Collision of deformed U+U but without any fluctuations in entropy deposition in the initial state. This is achieved by setting the fluctuation-parameter $k \gg 1$. and c) Collision of spherical U+U with $\beta = 0$ while keeping all other parameters same. This is not realized in reality but we consider this situation in order to show the impact of deformation more prominently by making a direct comparison with the deformed case.

Fig. 6.3 displays the factorization-breaking coefficients between flow vectors, where one of the flow harmonics is global or momentum averaged and the other one is momentum dependent as discussed in Chapter-3, for 0-5 % centrality in U+U collisions. The correlation coefficient gradually deviates from 1 with increasing transverse momentum (shown as $p \equiv p_T$), reflecting a significant decorrelation for both deformed (red curve) and spherical (orange curve) nuclei collisions. Spherical nuclei collisions show remarkably larger decorrelation with increasing transverse momentum as compared to the deformed nuclei collision. The particular difference emerges more profoundly when the fluctuations in the initial entropy deposition are switched off (blue curve), where the decorrelation is further reduced.

Let us explain the above results. The decorrelation of flow vectors in transverse momentum is governed by event-by-event fluctuations of flow, which means that the decorrelation would be larger where fluctuations dominate. In Fig. 6.3, as we consider 0-5 % centrality, for spherical nuclei collision the elliptic flow is mostly due to fluctuations and the overall magnitude is smaller. Therefore, it is easier to decorrelate and hence we observe a larger decorrelation between the flow vectors in transverse momentum. In case of deformed nuclei collisions, on the other hand, the presence of nuclear deformation increases the geometrical component in the total eccentricity.

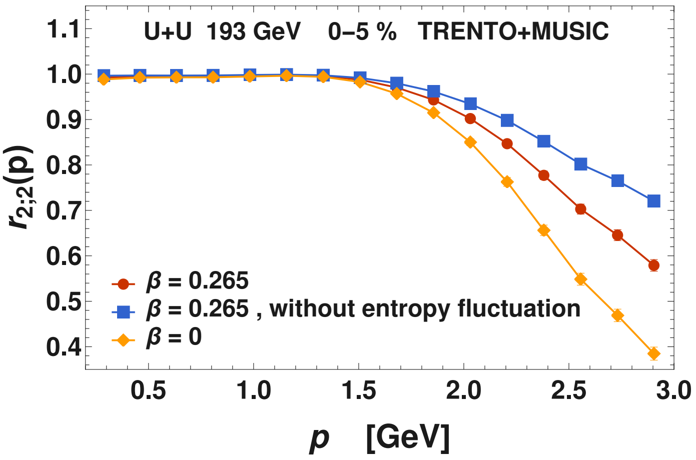

Fig. 6.3 Factorization-breaking coefficients of elliptic flow vector squared $r_{2;2}(p)$ between momentum averaged flow and momentum dependent flow for 0-5 % centrality in U+U collision at $\sqrt{s_{NN}} = 193$ GeV. The momentum dependent coefficients obtained from hydrodynamic simulation with TRENTO initial conditions for the spherical ($\beta = 0$) and deformed ($\beta = 0.265$) nuclei collisions, are denoted by orange diamonds and red circles respectively. The blue squares represent the simulation results obtained without fluctuations in the entropy deposition at the initial state, where the parameter k is set to $\gg 1$ while obtaining the initial conditions. The figure is from the original publication [130], coauthored by the author.

Therefore, even in central collisions there is significant influence of the elliptic geometry on the observed elliptic flow. The contribution of fluctuations to elliptic flow is partly washed out by the geometrical component resulting in a smaller decorrelation in transverse momentum as reflected in the results. This situation mimics the case of a semi-central collision of spherical nuclei (at a relatively large impact parameter) [355], where the overall magnitude of the flow is larger and the flow vectors in different transverse momentum bins are also more correlated with the overall orientation in the transverse plane, resulting in a smaller decorrelation in transverse momentum.

In the case of collision of deformed nuclei without fluctuations in the initial entropy deposition, event-by-event fluctuations of the elliptic flow are further reduced, resulting in an even smaller decorrelation as shown by the blue lines. This once again portrays the role of fluctuations in the flow decorrelation. The momentum dependent factorization breaking coefficients $r_{2;2}(p)$ puts useful constraints on β and could be verified in experiments.

Fig. 6.4 shows the flow magnitude factorization-breaking coefficients (left) and flow angle decorrelations (right) for the elliptic flow coefficients. Similar trends of the results are observed in both cases; the decorrelation is smaller for the deformed case. Both of these quantities can be measured experimentally and therefore would provide additional constraints on the deformation. Most notably, the relation proposed in Chapter-3, also holds true for the deformed nuclei collision,

$$[1 - r_{n;2}(p)] \simeq 2[1 - r_n^{v_n^2(p)}] \, . \tag{6.8}$$

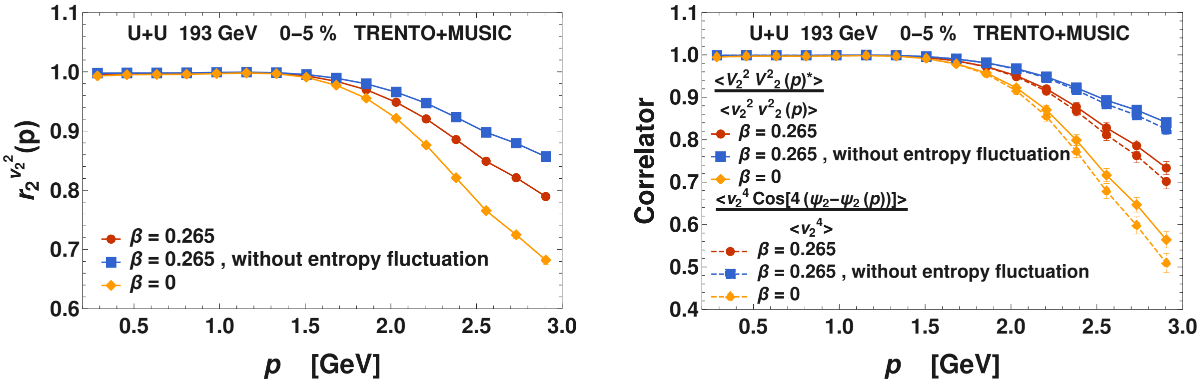

Fig. 6.4 Left: Flow magnitude squared factorization breaking coefficient for the elliptic flow $r_2^{v_2^2}(p)$ for 0-5 % centrality in U+U collision at 193 GeV. Right: Flow angle decorrelation between momentum averaged and momentum dependent elliptic flow coefficients. The symbols with different color have similar meaning as Fig. 6.3. The solid and the dashed lines on the right panel represent the results obtained with experimental estimation and the actual definition of flow angle decorrelation respectively. The figure is from the original publication [130], coauthored by the author.

Moreover, the experimental estimate of the angle decorrelation and true angle decorrelation coincide with each other also for deformed nuclei collisions, once again validating this approximation.

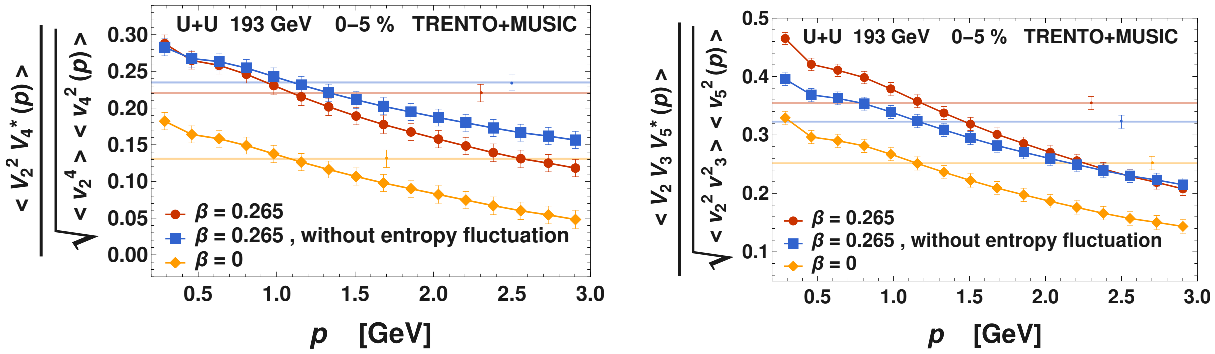

Fig. 6.5 :Momentum dependent mixed flow correlation between $V_2^2 - V_4(p)$ (left) and $V_2V_3 - V_5(p)$ (right) for 0-5 % centrality in U+U collision at 193 GeV. The results obtained for the spherical and deformed nuclei collisions are represented by orange and red lines respectively. The blue lines denote the results with no entropy fluctuations in the initial state. The horizontal lines with same colors represent the corresponding mixed flow correlations between the momentum averaged flow coefficients. The figure is from the original publication [130], coauthored by the author.

As the triangular flow is largely driven by the fluctuations, nuclear deformation has negligible to no effect on it, and is therefore irrelevant in the present context. To complete the picture, in Fig. 6.5 we present the results for the momentum dependent mixed-flow correlation between $V_2^2 - V_4(p)$ and $V_2V_3 - V_5(p)$. As expected, the correlation is larger for deformed nuclei collisions, also depicted by the corresponding baselines representing the respective correlation between momentum averaged flow. The transverse momentum dependence is similar for the deformed and spherical nuclei with however a slightly larger difference between the two curves at the low momentum. The study of such momentum dependent mixed flow correlations could give further constraints on the deformation and can be tested in experiments.

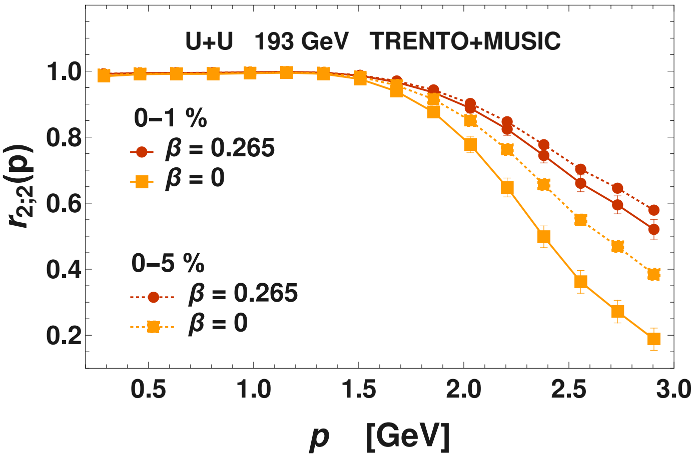

Fig. 6.6 Comparison of the deformation effect through flow vector factorization breaking coefficient for the elliptic flow in central $(0-5\%)$ and ultracentral $(0-1\%)$ U+U collisions at 193 GeV. The results obtained from hydrodynamic simulation for the spherical and deformed nuclei collisions are represented by the orange and red colors. The solid and the dashed lines represent the results corresponding to $0-1\%$ and $0-5\%$ centrality respectively. The figure is from the original publication [130], coauthored by the author.

In order to emphasize the fact that the deformation effect is more pronounced in central collisions or as the collisions are more central, in Fig. 6.6 we present results for the factorization-breaking coefficient $r_{2;2}(p)$ for two cases : 0-1 % centrality (solid lines) which represents the ultracentral collisions and usual 0-5 % centrality (dashed lines) which represents in general central collisions. It can be seen that the correlation is smaller as we move towards ultracentral collisions for both deformed and spherical nuclei. The difference between the two centralities is larger in spherical case, because of enhanced fluctuations and less prominent for the deformed case due to relatively smaller contributions of fluctuations, reflecting the fact that the eccentricity without deformation is smaller for 0-1% centrality. On the other hand, the relative difference between the spherical and the deformed case is substantially larger in $0-1\%$ centrality than $0-5\%$. Please note that when we say the effect of deformation, we particularly mean this relative difference.

6.2.2 Pearson correlation and symmetric cumulants

The nuclear deformation not only affects event-by-event fluctuations of the mean transverse momentum per particle and harmonic flow coefficients but also significantly impacts the correlation between them. In particular, we see that because of the deformed structure of uranium nuclei, there exist an anti-correlation between $[p_T]$ and v_2^2 in central collisions, which reduces the overall correlation between them [106] as discussed below.

Anti-correlation between $[p_T]$ and v_n^2

Let us consider the body-to-body case for fully overlapping nuclei in a central collision. We have seen that because of the larger transverse size or larger collision volume at fixed multiplicity, this leads to a smaller transverse momentum per particle. On the other hand, due to the elliptic shape of the overlap region the elliptic flow is enhanced. Therefore deformation of the nucleus has opposite effect on $[p_T]$ and v_2, resulting in a negative or anti-correlation between them, which drastically reduce the correlation and eventually makes it negative as one moves towards ultracentral collisions [106].

In this section we present the results for the Pearson correlation coefficient, normalized and symmetric cumulants as discussed in Chapter-5, for U+U collision at 193 GeV. Our simulation set-up remains same with three cases : deformed ($\beta = 0.265$), spherical ($\beta = 0$) and deformed without entropy fluctuations in the initial state ($\beta = 0.265, k \gg 1$).

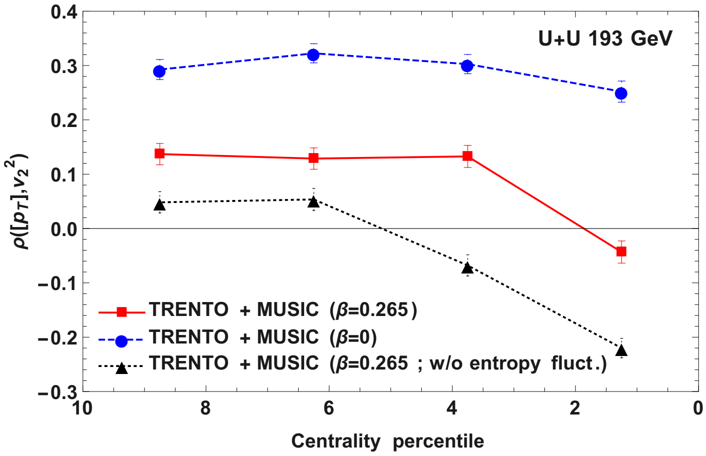

Fig. 6.7 The Pearson correlation coefficients between mean transverse momentum per particle and elliptic flow coefficient as a function of centrality in $0-10\%$ central collisions of U+U at 193 GeV. The red squares denote the results obtained from the hydrodynamic simulation with TRENTO initial condition for deformed nuclei ($\beta = 0.265$). The blue circles represent the corresponding results for the spherical nuclei ($\beta = 0$) collisions. The black triangles depict the results for the deformed nuclei collision without fluctuations in entropy deposition in the initial state. The figure is from the original publication [128], coauthored by the author.

Fig. 6.7 displays the results for the Pearson correlation coefficient [95] $\rho([p_T], v_2^2)$ for the three cases. As expected, the correlation is drastically smaller for deformed nuclei as compared to the spherical one. In the ultracentral region it even goes to negative, as discussed earlier. In the absence of entropy fluctuations in the initial state, the correlation get further reduced, as it should be because it suppress the fluctuations of both $[p_T]$ and v_2 and reduces correlation with multiplicity. In this case, the correlation coefficient is negative for centrality $< 5\%$. Please not that in this case we do not correct the correlation coefficient or the observables within it for multiplicity fluctuations. Because in central collisions, the covariances of the harmonic flow and mean transverse momentum with multiplicity are small. Furthermore, here we use

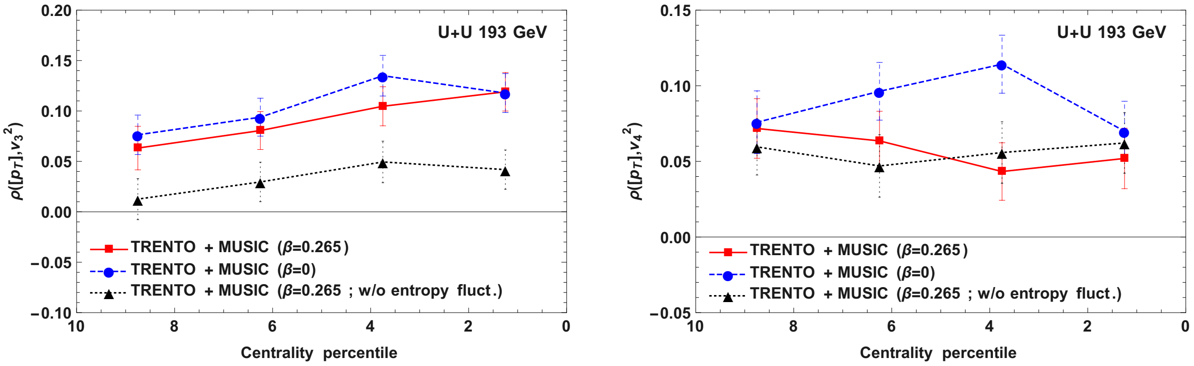

Fig. 6.8 Left: Pearson correlation coefficient between mean transverse momentum $[p_T]$ and triangular flow v_3^2, as a function of centrality in U+U collision. Right: The same for quadrangular flow v_4^2. The symbols carry same meaning as Fig. 6.7. The left panel of the figure is from the original publication [128], coauthored by the author.

(for the Pearson correlation) U+U collision with narrower centrality bins and we have checked that the corrections for multiplicity fluctuations to the correlation coefficients are small. The same holds true for the higher order symmetric cumulants[1]. Moreover, the correction for the multiplicity fluctuations is partially achieved in the third scenario where the fluctuations in entropy deposition in the initial state are switched off, resulting in significantly smaller multiplicity fluctuations. Therefore, in this section we only present results for the uncorrected Pearson correlation coefficients and symmetric cumulants for U+U collisions.

Fig. 6.8 shows the results for the correlation coefficients $\rho([p_T],v_3^2)$ (left) and $\rho([p_T],v_4^2)$ (right). As mentioned earlier, deformation has negligible effect on the triangular flow. Therefore for $\rho([p_T],v_3^2)$ the results are similar (consistent within errors) for the spherical and deformed nuclei collisions. However, the correlations encounter overall decrease in magnitude without initial entropy fluctuations. For the quadrangular flow, $\rho([p_T],v_4^2)$, on the other hand, shows a noticeable difference between the two cases around $2-6\%$ centrality, although not very large. This could be due to the non-linear mixing of v_2^2 with v_4 and the difference arises due to the effect of deformation on the elliptic flow.

Fig. 6.9 shows the third order normalized symmetric cumulant between $[p_T]$, v_2^2 and v_3^2 on the left and between $[p_T]$, v_3^2 and v_4^2 on the right. Both of the symmetric cumulants are very small in comparison to the Pearson correlation coefficients, because they pick genuine higher order correlations between the observables. For $NSC([p_T],v_2^2,v_3^2)$, the correlation is smaller (more negative) for deformed nuclei collisions than for the spherical case and removing the entropy fluctuations increases the correlation between them. However, the difference between the three cases is quite small. On the other hand, for $NSC([p_T],v_3^2,v_4^2)$, the cumulant is mostly negative for all the three cases and the deformed case has larger correlation (less negative) than the spherical nuclei collisions, highlighting the fact that v_3 is not influenced by the deformation, with little influence on v_4 due to non-linear mode.

---

[1] Although for the symmetric cumulants we use wider bins for accessing higher statistics

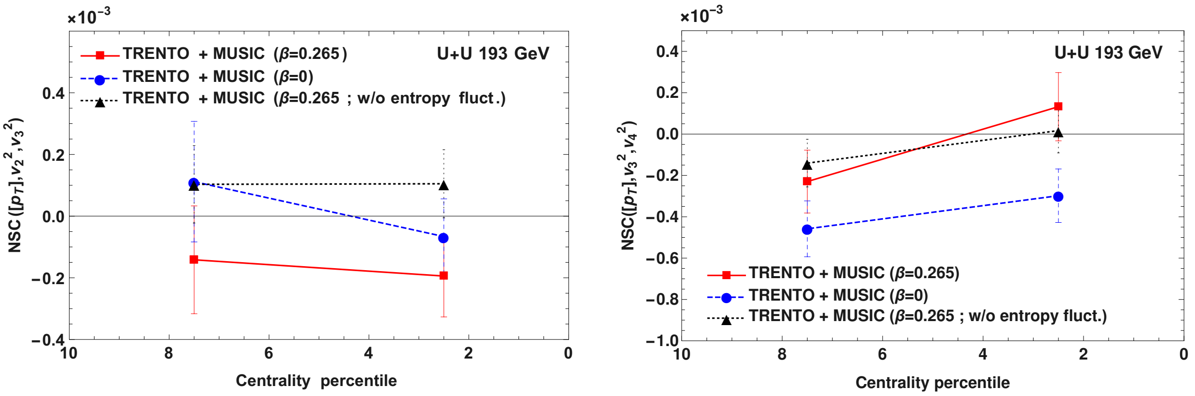

Fig. 6.9 Third order normalized symmetric cumulant between $[p_T]$, v_2^2 and v_3^2 (left) and $[p_T]$, v_3^2 and v_4^2 (right) as a function of centrality with two centrality bins in central collisions of U+U at 193 GeV. The symbols have similar meaning as Fig. 6.7. The left panel of the figure is from the original publication [128], coauthored by the author.

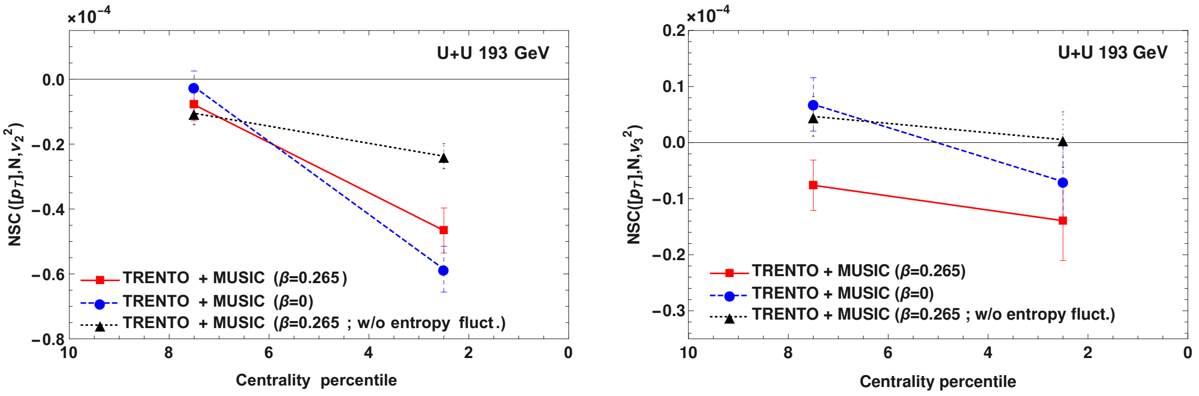

Fig. 6.10 Left: Third order normalized symmetric cumulant between mean transverse momentum, multiplicity and elliptic flow coefficient as a function of centrality in central collisions of U+U at 193 GeV (left). Right: Same but for the triangular flow coefficients. The symbols carry similar meaning as Fig. 6.9. The left panel of the figure is from the original publication [128], coauthored by the author.

Although the elliptic flow in central collision of deformed nuclei is dominated by the geometry arising from the nuclear deformation, the collective observables in such collisions are in general significantly impacted by the fluctuations in initial entropy and its azimuthal asymmetries, as seen before. Fluctuations of initial entropy dictate the fluctuations of final state multiplicities. Therefore, it would be interesting to study symmetric cumulants involving not only the mean transverse momentum and harmonic flow, but also the multiplicity in the event. Such observables have potential to pick up the effect of initial state entropy fluctuations more prominently. It is important to note that the results for the symmetric cumulants involving multiplicity as one of the observables could significantly depend on the definition of the centrality bin. In order to reduce such bias from centrality cuts, these observables could be measured experimentally using centrality bins defined on basis of other observables such as the total transverse energy deposited in the forward calorimeter (E_T) as discussed earlier.

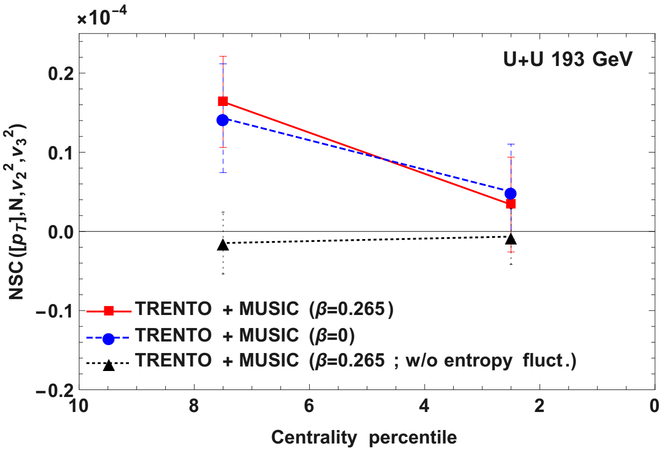

Fig. 6.11 Fourth order normalized symmetric cumulant between mean transverse momentum, multiplicity, elliptic and triangular flow coefficient as a function of centrality in U+U at 193 GeV. Symbols are similar as Fig. 6.10. The figure is from the original publication [128], coauthored by the author.

The third order normalized symmetric cumulants $NSC(p_T,N,v_2^2)$ and $NSC(p_T,N,v_3^2)$ are shown in Fig. 6.10. As expected, $NSC(p_T,N,v_2^2)$ shows a remarkable sensitivity to the fluctuations of entropy deposition from the participant nucleons as one moves towards more central collision. In particular, the fluctuations in entropy increase the magnitude (more negative) of $NSC(p_T,N,v_2^2)$. The deformation does not have a significant impact, both the spherical and deformed cases are consistent with each other in the centrality range considered. A similar effect is observed for $NSC(p_T,N,v_3^2)$ but with mild difference when fluctuations in entropy are turned off, the difference is significant for the centrality $5-10\%$. Such a reverse scenario is observed because v_3 is primarily dominated by fluctuations and switching them off affect both N and v_3. The fourth order cumulant $NSC(p_T,N,v_2^2,v_3^2)$, shown in Fig. 6.11, is positive for the cases involving entropy fluctuations in the initial states for both spherical and deformed nuclei

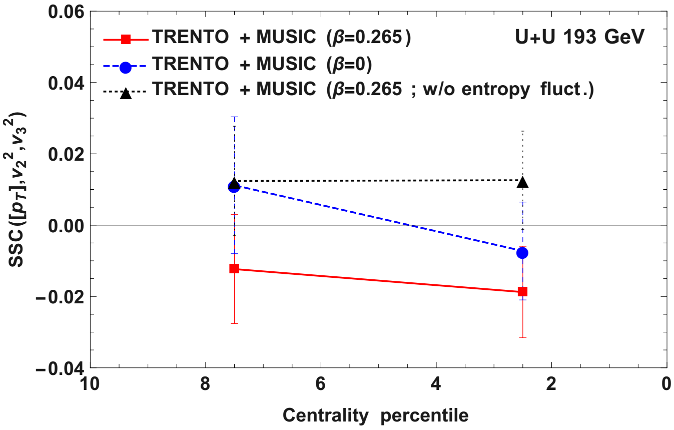

Fig. 6.12 Third order scaled symmetric cumulant between $[p_T]$, v_2^2 and v_3^2 in U+U collision at 193 GeV. Symbols carry similar meaning as in Fig. 6.9. The figure is from the original publication [128], coauthored by the author.

collisions. With entropy fluctuations switched off, the cumulant decreases[2] remarkably and is compatible with zero for the centrality range studied. Study of these cumulants showcases the importance of multiplicity fluctuation and its cross-correlation with other collective observables in the central collisions of deformed nuclei.

In order to complete the picture and maintain consistency with Chapter-5, in Fig. 6.12, we present the third order scaled symmetric cumulants for mean transverse momentum, elliptic and triangular flow in U+U collisions. The scaled symmetric cumulant $SSC([p_T],v_2^2,v_3^2)$ shows similar behavior as $NSC([p_T],v_2^2,v_3^2)$ and does not provide much new information apart from the fact that it has larger order of magnitude for the correlation, because of the changed normalization in the denominator. Moreover, its study does not require additional information on the average transverse momentum of the particles which is sometimes not known a priori.

---

[2] Please note that the absolute magnitudes of the cumulants involving multiplicity always decrease when there is no fluctuation in entropy deposition in the initial state.

Chapter 7

Summary and outlook

Finally, it brings us to the last chapter of this thesis, where we summarize the important findings and leave our concluding remarks for the research carried out. We also highlight further research possibilities on the similar topics, which lied beyond the current scope. We briefly discuss our future goals, prospective research directions and new potential problems that might be interesting to investigate in the coming years.

The main goal of this thesis is to study the properties and the collective dynamics of the QGP medium created at the collision of two heavy nuclei at ultrarelativistic energies. The most distinctive and exotic feature of the heavy-ion collision is the collective anisotropic flow of the final state particles, originating from the geometry of its initial state. One of the most exclusive features of this collective flow is its event-by-event fluctuations mainly stemming from the event-by-event fluctuations in the initial state. Our primary aim is to focus on the fluctuations and correlations of those collective observables such as mean transverse momentum per particle $[p_T]$, harmonic flow coefficients v_n etc. Relativistic hydrodynamics serves as an excellent theoretical tool to study the QGP medium, its initial state properties and unique collective signatures in the final state. This viscous hydrodynamic framework comprising a number of intermediate stages can be utilised in simulations or model, to study those collective observables and make robust predictions. Most interesting features of those observables originate from the initial state of the collision and their event-by-event fluctuations. Below we summarize the most important findings of our research and the conclusions coming out of them :

- The event-by-event fluctuations of the harmonic flow coefficients result in decorrelation between flow vectors in different transverse momentum bins. This decorrelation can be understood by studying the factorization-breaking coefficients between the flow vectors in two bins. In order to address experimental limitations due to low statistics in higher p_T-bins, we use one of the flow vectors as momentum averaged [87]. The flow vector decorrelation is partly due to flow magnitude and partly due to flow angle decorrelation, the experimental measurement of which requires the construction of the factorization-breaking coefficients between the squares of the flow [125]. Our model results for Pb+Pb collision at 5.02 TeV, qualitatively reproduce the ALICE data. The observed mismatch between our model results and the data arise from the potential presence of the non-flow correlations which can be substantially minimized by taking the transverse momentum bins separated by large pseudorapidity gap. We also present predictions for similar momentum dependent mixed-flow correlations which can be used to study non-linearity in the dynamics of the system and can provide useful constraints on the non-linear modes in the initial state, when confirmed in experiments. Factorization-breaking coefficients can serve as robust probes of the fluctuations of flow.

- Fluctuations of mean transverse momentum per particle in ultracentral Pb+Pb collisions display unique peculiar patterns, encoding important physical significance. The sudden steep decrease of $Var(p_T|N_{ch})$ in ATLAS data in the ultracentral region, can be explained by modelling the correlation between $[p_T]$ and N_{ch} at fixed impact parameter through a two dimensional correlated Gaussian distribution [126]. Our model results show that in the ultracentral limit, the contribution of the impact parameter fluctuations or the volume fluctuations gradually goes to zero causing the sharp decline. Our model fit to the data returns a strong correlation between $[p_T]$ and N_{ch} at fixed b, which appears to be a natural consequence of thermalization of the QGP system, a fundamental assumption in its hydrodynamic description. Additionally, we present robust predictions for the skewness and kutosis [127], characterizing the non-Gaussian features of $[p_T]$-fluctuation, based on a Gaussian-fluctuation model of impact parameter. The skewness and kurtosis show interesting patterns in the ultracentral regime around the knee of the multiplicity distribution, which arise mainly due to impact parameter fluctuations. As hinted by the measurements from the ALICE collaborations, our predictions can be verified by the upcoming measurement of the ATLAS collaboration in similar bins of centrality estimators. Our results unveil crucial physical aspects of the QGP medium, and highlight the importance of impact parameter and its fluctuations in heavy-ion collision.

- Correlation between $[p_T]$ and v_n^2 can serve as a fine tool to probe the correlation present in the initial state of the collision between eccentricities, transverse size, entropy etc. We present results for the Pearson correlation coefficient between $[p_T]$ and v_n^2 by comparing it with the data and the linear predictor from the initial state [128]. To measure higher order correlations, we propose normalized and scaled symmetric cumulants between mean transverse momentum, harmonic flow and multiplicity, measuring genuine correlations between these observables and putting additional layer of constraints on the initial state properties. Similar momentum dependent Pearson correlation coefficients can be defined, which do not depend on the specific p_T-cut dependence and show sensitivity to the granularity in the initial state [129]. We propose alternate constructions of such p_T-dependent correlation coefficients, which are experimentally favourable. Covariance between $[p_T]$ and p_T-dependent harmonic flow can be studied directly, providing a robust probe to the granularity. Such correlations and covariances between mean transverse momentum and harmonic flow coefficients capture the inter-correlation between the shape and the size of the QGP fireball, while putting additional constraints on the initial state properties.

- Although nuclear structure is primarily studied in low energy nuclear physics, high energy heavy-ion collision can provide an excellent platform to map the deformed nuclear structure through similar collective observables. In particular, we show that deformation has a direct impact on the transverse momentum and harmonic flow coefficients in central collision of uranium nuclei at 193 GeV at RHIC. We show that the factorization breaking coefficients for the elliptic flow [130] and the Pearson correlation coefficient between $[p_T]$ and v_2^2 can provide robust probes of the quadrupole deformation parameter β_2 of the uranium (^{238}U) nucleus. We also present momentum dependent mixed flow correlations and propose new different normalized symmetric cumulants constructed with $[p_T]$, v_n^2 and N_{ch}, which provide additional novel constraints on the deformation of ^{238}U [128]. Our results show that the collective flow and its fluctuations in central collisions provide a unique opportunity to investigate nuclear deformation through high energy nuclear collisions.

Future directions

The research carried out in this thesis paves a path for further development and novel research opportunities in future, in each sector. Moreover, the problems encountered in this work have motivated us to formulate new potentially interesting projects which we would like to explore in future. Below we discuss the scopes for further development in the related areas along with our future plans :

- We have studied the deformation of uranium nucleus through correlations and fluctuations-probing observables, which are relevant at RHIC energies. However, there exist other deformed nuclei such as ^{129}Xe, which are collided at the LHC at 5.44 TeV [120–123, 101, 102]. The xenon nucleus would be interesting to explore because, in addition to the quadrupole deformation (β or β_2), it also exhibits axial asymmetry in its structure, which is identified by triaxiality parameter (γ) [110, 111]. The particular triaxial structure appears when all the three axes of the nucleus are of different length ($0 < \gamma < 60°$) (Fig. (7.1)). Such structures affect the nuclear mass distribution [110],

$$\begin{aligned} \rho(r,\theta,\phi) &= \frac{\rho_0}{1+\exp[\frac{r-R(\theta,\phi)}{a}]} , \\ \text{with,} \quad R((\theta,\phi) &= R_0\{1+\beta[\cos\gamma Y_{2,0}(\theta,\phi)+\sin\gamma Y_{2,2}(\theta,\phi)]\} . \end{aligned} \tag{7.1}$$

Due to three possible different structures, the overlap area in central Xe+Xe collisions would assume three possible shapes, inducing the possibility of larger shape fluctuations at fixed multiplicities. Therefore it would be interesting to study similar observables such as factorization-breaking coefficients, Pearson correlation coefficients (already has been found to be sensitive to γ [110]), normalized and scaled symmetric cumulants between $[p_T]$, v_n^2 and N_{ch} etc. in Xe+Xe collision at 5.44 TeV, and can be compared to the results for Pb+Pb collisions, which are easily accessible at the LHC. Such quantitative and qualitative comparisons can shed light on the structure of Xe nuclei, providing sensitive constraints on its deformation parameter and triaxialiaty through high energy collisions.

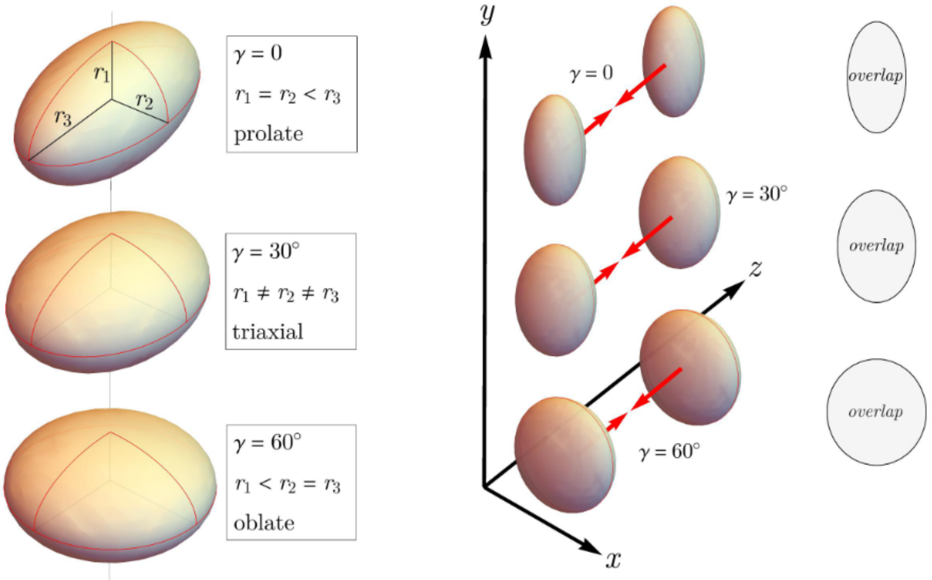

Fig. 7.1 Pictorial representation of the structure of xenon-129 nucleus with three possible configurations shown from top to bottom on the left: prolate, triaxial and oblete. Different configuration results in different shapes of the overlap region in central collisions. Figure taken from [110].

Moreover, recent studies suggest a significant hexadecapole deformation (β_4) for the uranium nuclei [118, 352] that can be constrained by the collective observabeles: flow cumulants, non-linear correlations etc. In future, we would be also interested to explore the hexadecapole deformation β_4 of ^{238}U, with the correlations, higher order cumulants and factorization breaking coefficients which contain huge potential to put robust constraints on β_4.

- In the present work, we have focused on the transverse momentum fluctuations in ultracentral Pb+Pb collision at the LHC. However, similar study for $[p_T]$-fluctuations can be performed in p+Pb collisions which also show significant collective phenomena at the LHC [356–361, 305, 362–364]. Being a much smaller system as compared to Pb+Pb, multiplicity fluctuations are expected to be significantly large in the ultracentral collisions (highest multiplicity). Therefore the fluctuations of $[p_T]$ at fixed multiplicity are also expected to be large, highlighting the importance of intrinsic or quantum fluctuations. Moreover the role of impact parameter would be interesting above the knee of the multiplicity distribution in p+Pb collision, which covers a large multiplicity range [365]. Therefore, investigation of $[p_T]$ fluctuations in ultracentral p+Pb collision and its direct comparison to Pb+Pb would be very interesting, which could unravel the dynamics of quantum fluctuations and its system-size dependence. A comparison to p+p collision would shed further lights on the issue and can be used as baselines for such studies.

Additionally, we would like to study collectivity in p+Pb collisions using new observables (e.g. factorization-breaking coefficients[1]) that have not been studied yet. In particular, the initial state properties and their correlations can be mapped to the final sate by constructing flow cumulants, correlations and symmetric cumulants between mean transverse momentum and harmonic flow coefficients.

- Furthermore, in future, we plan to study small collision systems such as O+O at both RHIC and LHC energies. The STAR collaboration has recently presented measurement on O+O collisions at RHIC energy (200 GeV) [366]. O+O collisions at the LHC (7 TeV) are planned for Run3 [367–369], with data expected soon. The study of O+O collisions is interesting because it can address several issues such as the structure of ^{16}O nucleus at the high energy scale, the limit of applicability of hydrodynamics for such small system, a direct comparison of the collective observables to Pb+Pb collision as O+O serves as a similar symmetric collision systems but with different centre of mass energy and much smaller size of the fireball etc. According to the low energy experiments, ^{16}O nucleus exhibit a tetrahedral structure with alpha-clusters at its edges [370, 221] shown in Fig. (7.2). As a result there exist surging theoretical interest to image the structure of ^{16}O nucleus and study its unique collective signatures in high-energy O+O collision [371, 370, 221, 372–375]. The measurements from the STAR collaboration highlight significant contributions from sub-nucleonic fluctuations and nucleon-nucleon correlation at the initial state of O+O collision. We plan to study O+O collision at both energies by using different approaches for obtaining the initial state density distributions such as fitting Woods-Saxon distribution to the nuclear density obtained from low energy *ab-initio* NLEFT, VMC, EQMD or PGCM calculations [370, 221, 373, 374], applying novel alpha-cluster+sub-nucleonic structure within initial condition model [221] (e.g. TRENTO), implementing non-zero octupole deformation (β_3) [373] to account for nuclear deformation etc. We would also like to identify the onset time for hydrodynamics in such small systems which is usually larger due to large inverse Reynold's number and Kundsen number [221]. Investigation of applicability of hydrodynamics in O+O collision would be interesting in general, which could be applicable for other small system collision. In O+O collision we would also

---

[1] Of course the statistics for such observable in small systems would be a big challenge.

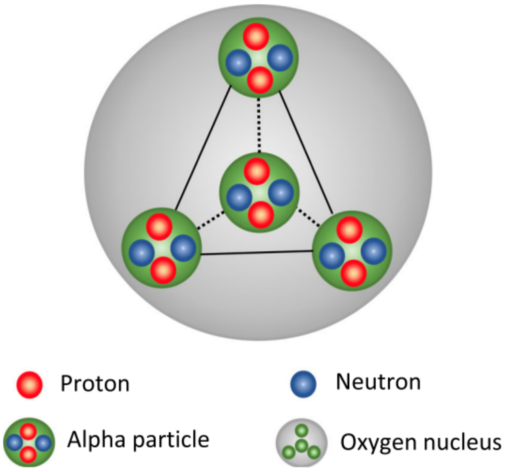

Fig. 7.2 Pictorial depiction of the α-clustered structure of oxygen-16 nucleus. Figure taken from [376]

like to map the final state observables to initial state properties through multi-particle correlations and cumulants.

In addition to the above mentioned prospective projects, we would also like to explore other small systems such as p+Au, d+Au and He+Au at RHIC energies. In particular, the study of factorization-breaking coefficients would be interesting in such systems probing the fluctuations of harmonic flow at a much smaller scale with comparable system-sizes. This could help us to have a clear insight on the origin of flow-decorrelation in different kinematic bins.

High energy heavy-ion collision has entered its third decade with the current Run3 program at the LHC. ultrarelativistic heavy ion collision has emerged as an established field of research by answering some of the most fundamental questions of physics over the past thirty years. From the first Au+Au collision at RHIC to the latest Run3 measurement of Pb+Pb at the LHC, the study of collectivity has helped us to understand many fundamental properties of the Quark-Gluon-Plasma with hydrodynamic description serving as its fundamental basis. However, in spite of the rapid progress in the field , availability of large data sets and abundance of collision systems, there remain some major fundamental issues which need to be addressed. Some of these include the limitation of hydrodynamic picture and its boundaries in small collision systems, origin of collective flow in small systems, nuclear structure and its accessibility in future collider e.g. at the Electron-Ion-Collider (EIC), Future Circular Collider (FCC) etc. The study of small system collisions at the current and future runs at the LHC (e.g. p+Pb, O+O, p+O, Ne+Ne, Ne+Pb etc.) would help us to remarkably push the limit of our understanding of the QGP medium and hence the quest is on …

References

[1] M.K. Gaillard, P.D. Grannis and F.J. Sciulli, *The Standard model of particle physics*, *Rev. Mod. Phys.* **71** (1999) S96 [`hep-ph/9812285`].

[2] M. Thomson, *Modern Particle Physics*, Cambridge University Press (2013).

[3] T. KOBAYASHI, *Experimental verification of the standard model of particle physics*, *Proceedings of the Japan Academy, Series B* **97** (2021) 211.

[4] U.W. Heinz, *Towards the Little Bang Standard Model*, *J. Phys. Conf. Ser.* **455** (2013) 012044 [`1304.3634`].

[5] S.A. Voloshin, A.M. Poskanzer and R. Snellings, *Collective phenomena in non-central nuclear collisions*, *Landolt-Bornstein* **23** (2010) 293 [`0809.2949`].

[6] W. Florkowski, *Phenomenology Of Ultra-relativistic Heavy-ion Collisions*, World Scientific Publishing Company (2010).

[7] U. Heinz and R. Snellings, *Collective flow and viscosity in relativistic heavy-ion collisions*, *Ann. Rev. Nucl. Part. Sci.* **63** (2013) 123 [`1301.2826`].

[8] W. Busza, K. Rajagopal and W. van der Schee, *Heavy Ion Collisions: The Big Picture, and the Big Questions*, *Ann. Rev. Nucl. Part. Sci.* **68** (2018) 339 [`1802.04801`].

[9] H. Fritzsch, M. Gell-Mann and H. Leutwyler, *Advantages of the Color Octet Gluon Picture*, *Phys. Lett. B* **47** (1973) 365.

[10] S. Weinberg, *Nonabelian Gauge Theories of the Strong Interactions*, *Phys. Rev. Lett.* **31** (1973) 494.

[11] F.G. Gardim, G. Giacalone, M. Luzum and J.-Y. Ollitrault, *Thermodynamics of hot strong-interaction matter from ultrarelativistic nuclear collisions*, *Nature Phys.* **16** (2020) 615 [`1908.09728`].

[12] J.E. Bernhard, J.S. Moreland and S.A. Bass, *Bayesian estimation of the specific shear and bulk viscosity of quark–gluon plasma*, *Nature Phys.* **15** (2019) 1113.

[13] M. Gyulassy and L. McLerran, *New forms of QCD matter discovered at RHIC*, *Nucl. Phys. A* **750** (2005) 30 [`nucl-th/0405013`].

[14] D.J. Gross and F. Wilczek, *Asymptotically Free Gauge Theories - I*, *Phys. Rev. D* **8** (1973) 3633.

[15] D.J. Gross and F. Wilczek, *ASYMPTOTICALLY FREE GAUGE THEORIES. 2.*, *Phys. Rev. D* **9** (1974) 980.

[16] B. Muller, J. Schukraft and B. Wyslouch, *First Results from Pb+Pb collisions at the LHC*, *Ann. Rev. Nucl. Part. Sci.* **62** (2012) 361 [`1202.3233`].

[17] P. Huovinen, *Hydrodynamical description of collective flow. Chapter 1.*, `nucl-th/0305064`.

[18] P.F. Kolb and U.W. Heinz, *Hydrodynamic description of ultrarelativistic heavy ion collisions*, `nucl-th/0305084`.

[19] P. Huovinen and P.V. Ruuskanen, *Hydrodynamic Models for Heavy Ion Collisions*, *Ann. Rev. Nucl. Part. Sci.* **56** (2006) 163 [`nucl-th/0605008`].

[20] J.-Y. Ollitrault, *Relativistic hydrodynamics for heavy-ion collisions*, *Eur. J. Phys.* **29** (2008) 275 [`0708.2433`].

[21] K. Dusling and D. Teaney, *Simulating elliptic flow with viscous hydrodynamics*, *Phys. Rev. C* **77** (2008) 034905 [`0710.5932`].

[22] T. Hirano, N. van der Kolk and A. Bilandzic, *Hydrodynamics and Flow*, *Lect. Notes Phys.* **785** (2010) 139 [`0808.2684`].

[23] M. Luzum and P. Romatschke, *Conformal Relativistic Viscous Hydrodynamics: Applications to RHIC results at s(NN)**(1/2) = 200-GeV*, *Phys. Rev. C* **78** (2008) 034915 [`0804.4015`].

[24] U.W. Heinz, *Early collective expansion: Relativistic hydrodynamics and the transport properties of QCD matter*, *Landolt-Bornstein* **23** (2010) 240 [`0901.4355`].

[25] A. Jaiswal and V. Roy, *Relativistic hydrodynamics in heavy-ion collisions: general aspects and recent developments*, *Adv. High Energy Phys.* **2016** (2016) 9623034 [`1605.08694`].

[26] P. Romatschke and U. Romatschke, *Relativistic Fluid Dynamics In and Out of Equilibrium*, Cambridge Monographs on Mathematical Physics, Cambridge University Press (5, 2019), 10.1017/9781108651998, [`1712.05815`].

[27] J.S. Moreland, J.E. Bernhard and S.A. Bass, *Bayesian calibration of a hybrid nuclear collision model using p-Pb and Pb-Pb data at energies available at the CERN Large Hadron Collider*, *Phys. Rev. C* **101** (2020) 024911 [`1808.02106`].

[28] JETSCAPE collaboration, *Multisystem Bayesian constraints on the transport coefficients of QCD matter*, *Phys. Rev. C* **103** (2021) 054904 [`2011.01430`].

[29] M.A. Stephanov, K. Rajagopal and E.V. Shuryak, *Signatures of the tricritical point in QCD*, *Phys. Rev. Lett.* **81** (1998) 4816 [`hep-ph/9806219`].

[30] Z. Fodor and S.D. Katz, *Critical point of QCD at finite T and mu, lattice results for physical quark masses*, *JHEP* **04** (2004) 050 [`hep-lat/0402006`].

[31] Y. Aoki, G. Endrodi, Z. Fodor, S.D. Katz and K.K. Szabo, *The Order of the quantum chromodynamics transition predicted by the standard model of particle physics*, *Nature* **443** (2006) 675 [`hep-lat/0611014`].

[32] M.A. Stephanov, *Non-Gaussian fluctuations near the QCD critical point*, *Phys. Rev. Lett.* **102** (2009) 032301 [`0809.3450`].

[33] A. Bazavov et al., *The chiral and deconfinement aspects of the QCD transition*, *Phys. Rev. D* **85** (2012) 054503 [`1111.1710`].

[34] S. Borsanyi, Z. Fodor, J.N. Guenther, R. Kara, S.D. Katz, P. Parotto et al., *QCD Crossover at Finite Chemical Potential from Lattice Simulations*, *Phys. Rev. Lett.* **125** (2020) 052001 [`2002.02821`].

[35] F. Gelis, *Some Aspects of the Theory of Heavy Ion Collisions*, *Rept. Prog. Phys.* **84** (2021) 056301 [`2102.07604`].

[36] B. Zhang, C.M. Ko, B.-A. Li and Z.-w. Lin, *A multiphase transport model for nuclear collisions at RHIC*, *Phys. Rev. C* **61** (2000) 067901 [`nucl-th/9907017`].

[37] Z.-W. Lin, C.M. Ko, B.-A. Li, B. Zhang and S. Pal, *A Multi-phase transport model for relativistic heavy ion collisions*, *Phys. Rev. C* **72** (2005) 064901 [`nucl-th/0411110`].

[38] Y. Mehtar-Tani, J.G. Milhano and K. Tywoniuk, *Jet physics in heavy-ion collisions*, *Int. J. Mod. Phys. A* **28** (2013) 1340013 [`1302.2579`].

[39] J.-P. Blaizot and Y. Mehtar-Tani, *Jet Structure in Heavy Ion Collisions*, *Int. J. Mod. Phys. E* **24** (2015) 1530012 [`1503.05958`].

[40] J.-Y. Ollitrault, *Anisotropy as a signature of transverse collective flow*, *Phys. Rev. D* **46** (1992) 229.

[41] S. Voloshin and Y. Zhang, *Flow study in relativistic nuclear collisions by Fourier expansion of Azimuthal particle distributions*, *Z. Phys. C* **70** (1996) 665 [`hep-ph/9407282`].

[42] H. Sorge, *Elliptical flow: A Signature for early pressure in ultrarelativistic nucleus-nucleus collisions*, *Phys. Rev. Lett.* **78** (1997) 2309 [`nucl-th/9610026`].

[43] A.M. Poskanzer and S.A. Voloshin, *Methods for analyzing anisotropic flow in relativistic nuclear collisions*, *Phys. Rev. C* **58** (1998) 1671 [`nucl-ex/9805001`].

[44] D. Teaney, J. Lauret and E.V. Shuryak, *Flow at the SPS and RHIC as a quark gluon plasma signature*, *Phys. Rev. Lett.* **86** (2001) 4783 [`nucl-th/0011058`].

[45] M. Bleicher and H. Stoecker, *Anisotropic flow in ultrarelativistic heavy ion collisions*, *Phys. Lett. B* **526** (2002) 309 [`hep-ph/0006147`].

[46] P. Huovinen, P.F. Kolb, U.W. Heinz, P.V. Ruuskanen and S.A. Voloshin, *Radial and elliptic flow at RHIC: Further predictions*, *Phys. Lett. B* **503** (2001) 58 [`hep-ph/0101136`].

[47] P. Bozek, *The Balance functions in azimuthal angle is a measure of the transverse flow*, *Phys. Lett. B* **609** (2005) 247 [`nucl-th/0412076`].

[48] B. Alver and G. Roland, *Collision geometry fluctuations and triangular flow in heavy-ion collisions*, *Phys. Rev. C* **81** (2010) 054905 [`1003.0194`].

[49] B. Schenke, S. Jeon and C. Gale, *Elliptic and triangular flow in event-by-event (3+1)D viscous hydrodynamics*, *Phys. Rev. Lett.* **106** (2011) 042301 [`1009.3244`].

[50] P. Bozek and I. Wyskiel, *Directed flow in ultrarelativistic heavy-ion collisions*, *Phys. Rev. C* **81** (2010) 054902 [`1002.4999`].

[51] M. Luzum, *Collective flow and long-range correlations in relativistic heavy ion collisions*, *Phys. Lett. B* **696** (2011) 499 [`1011.5773`].

[52] PHENIX collaboration, *Flow measurements via two particle azimuthal correlations in Au+Au collisions at s(NN)**(1/2) = 130-GeV*, *Phys. Rev. Lett.* **89** (2002) 212301 [`nucl-ex/0204005`].

[53] STAR collaboration, *Azimuthal anisotropy in Au+Au collisions at s(NN)**(1/2) = 200-GeV*, *Phys. Rev. C* **72** (2005) 014904 [`nucl-ex/0409033`].

[54] ALICE collaboration, *Elliptic flow of charged particles in Pb-Pb collisions at 2.76 TeV*, *Phys. Rev. Lett.* **105** (2010) 252302 [`1011.3914`].

[55] ATLAS collaboration, *Measurement of the azimuthal anisotropy for charged particle production in* $\sqrt{s_{NN}} = 2.76$ *TeV lead-lead collisions with the ATLAS detector*, *Phys. Rev. C* **86** (2012) 014907 [`1203.3087`].

[56] CMS collaboration, *Measurement of the Elliptic Anisotropy of Charged Particles Produced in PbPb Collisions at* $\sqrt{s_{NN}}$*=2.76 TeV*, *Phys. Rev. C* **87** (2013) 014902 [`1204.1409`].

[57] F.G. Gardim, F. Grassi, M. Luzum and J.-Y. Ollitrault, *Anisotropic flow in event-by-event ideal hydrodynamic simulations of* $\sqrt{s_{NN}} = 200$ *GeV Au+Au collisions*, *Phys. Rev. Lett.* **109** (2012) 202302 [`1203.2882`].

[58] J.-Y. Ollitrault, *Measures of azimuthal anisotropy in high-energy collisions*, *Eur. Phys. J. A* **59** (2023) 236 [`2308.11674`].

[59] ALICE collaboration, *Anisotropic flow of charged particles in Pb-Pb collisions at* $\sqrt{s_{\rm NN}} = 5.02$ *TeV*, *Phys. Rev. Lett.* **116** (2016) 132302 [`1602.01119`].

[60] ATLAS collaboration, *Measurement of the azimuthal anisotropy of charged particles produced in* $\sqrt{s_{_\text{NN}}}$ *= 5.02 TeV Pb+Pb collisions with the ATLAS detector*, *Eur. Phys. J. C* **78** (2018) 997 [`1808.03951`].

[61] B. Schenke, S. Jeon and C. Gale, *Higher flow harmonics from (3+1)D event-by-event viscous hydrodynamics*, *Phys. Rev. C* **85** (2012) 024901 [`1109.6289`].

[62] Z. Qiu, C. Shen and U. Heinz, *Hydrodynamic elliptic and triangular flow in Pb-Pb collisions at* $\sqrt{s} = 2.76 ATeV$, *Phys. Lett. B* **707** (2012) 151 [`1110.3033`].

[63] STAR collaboration, *Elliptic flow in Au + Au collisions at (S(NN))**(1/2) = 130 GeV*, *Phys. Rev. Lett.* **86** (2001) 402 [`nucl-ex/0009011`].

[64] PHENIX collaboration, *Elliptic flow of identified hadrons in Au+Au collisions at s(NN)**(1/2) = 200-GeV*, *Phys. Rev. Lett.* **91** (2003) 182301 [`nucl-ex/0305013`].

[65] CMS collaboration, *Centrality Dependence of Dihadron Correlations and Azimuthal anisotropy Harmonics in PbPb Collisions at* $\sqrt{s_{NN}} = 2.76$ *TeV*, *Eur. Phys. J. C* **72** (2012) 2012 [`1201.3158`].

[66] W. Broniowski and W. Florkowski, *Geometric relation between centrality and the impact parameter in relativistic heavy ion collisions*, *Phys. Rev. C* **65** (2002) 024905 [`nucl-th/0110020`].

[67] S.J. Das, G. Giacalone, P.-A. Monard and J.-Y. Ollitrault, *Relating centrality to impact parameter in nucleus-nucleus collisions*, *Phys. Rev. C* **97** (2018) 014905 [`1708.00081`].

[68] PHOBOS collaboration, *Charged particle multiplicity near mid-rapidity in central Au + Au collisions at* $S^{(1/2)}$ *= 56-A/GeV and 130-A/GeV*, *Phys. Rev. Lett.* **85** (2000) 3100 [`hep-ex/0007036`].

[69] STAR collaboration, *Multiplicity distribution and spectra of negatively charged hadrons in Au+Au collisions at s(NN)**(1/2) = 130-GeV*, *Phys. Rev. Lett.* **87** (2001) 112303 [`nucl-ex/0106004`].

[70] PHENIX collaboration, *Systematic studies of the centrality and s(NN)**(1/2) dependence of the d E(T) / d eta and d (N(ch) / d eta in heavy ion collisions at mid-rapidity*, *Phys. Rev. C* **71** (2005) 034908 [`nucl-ex/0409015`].

[71] ALICE collaboration, *Centrality determination of Pb-Pb collisions at* $\sqrt{s_{NN}}$ *= 2.76 TeV with ALICE*, *Phys. Rev. C* **88** (2013) 044909 [`1301.4361`].

[72] ATLAS collaboration, *Measurement of the pseudorapidity and transverse momentum dependence of the elliptic flow of charged particles in lead-lead collisions at* $\sqrt{s_{NN}} = 2.76$ *TeV with the ATLAS detector*, *Phys. Lett. B* **707** (2012) 330 [`1108.6018`].

[73] CMS collaboration, *Dependence on pseudorapidity and centrality of charged hadron production in PbPb collisions at a nucleon-nucleon centre-of-mass energy of 2.76 TeV*, *JHEP* **08** (2011) 141 [`1107.4800`].

[74] C.E. Aguiar, Y. Hama, T. Kodama and T. Osada, *Event-by-event fluctuations in hydrodynamical description of heavy ion collisions*, *Nucl. Phys. A* **698** (2002) 639 [`hep-ph/0106266`].

[75] J.-Y. Ollitrault, A.M. Poskanzer and S.A. Voloshin, *Effect of flow fluctuations and nonflow on elliptic flow methods*, *Phys. Rev. C* **80** (2009) 014904 [`0904.2315`].

[76] Z. Qiu and U.W. Heinz, *Event-by-event shape and flow fluctuations of relativistic heavy-ion collision fireballs*, *Phys. Rev. C* **84** (2011) 024911 [`1104.0650`].

[77] A. Bzdak and D. Teaney, *Longitudinal fluctuations of the fireball density in heavy-ion collisions*, *Phys. Rev. C* **87** (2013) 024906 [`1210.1965`].

[78] U. Heinz, Z. Qiu and C. Shen, *Fluctuating flow angles and anisotropic flow measurements*, *Phys. Rev. C* **87** (2013) 034913 [`1302.3535`].

[79] J. Jia and P. Huo, *A method for studying the rapidity fluctuation and decorrelation of harmonic flow in heavy-ion collisions*, *Phys. Rev. C* **90** (2014) 034905 [`1402.6680`].

[80] R.S. Bhalerao, J.-Y. Ollitrault, S. Pal and D. Teaney, *Principal component analysis of event-by-event fluctuations*, *Phys. Rev. Lett.* **114** (2015) 152301 [`1410.7739`].

[81] P. Bozek and W. Broniowski, *Longitudinal decorrelation measures of flow magnitude and event-plane angles in ultrarelativistic nuclear collisions*, *Phys. Rev. C* **97** (2018) 034913 [`1711.03325`].

[82] PHOBOS collaboration, *Non-flow correlations and elliptic flow fluctuations in gold-gold collisions at* $\sqrt{s_{NN}} = 200$ *GeV*, *Phys. Rev. C* **81** (2010) 034915 [`1002.0534`].

[83] CMS collaboration, *Evidence for transverse momentum and pseudorapidity dependent event plane fluctuations in PbPb and pPb collisions*, *Phys. Rev. C* **92** (2015) 034911 [`1503.01692`].

[84] ALICE collaboration, *Correlated event-by-event fluctuations of flow harmonics in Pb-Pb collisions at* $\sqrt{s_{\rm NN}} = 2.76$ *TeV*, *Phys. Rev. Lett.* **117** (2016) 182301 [`1604.07663`].

[85] ALICE collaboration, *Searches for transverse momentum dependent flow vector fluctuations in Pb-Pb and p-Pb collisions at the LHC*, *JHEP* **09** (2017) 032 [`1707.05690`].

[86] ATLAS collaboration, *Measurement of longitudinal flow decorrelations in Pb+Pb collisions at* $\sqrt{s_{NN}} = 2.76$ *and 5.02 TeV with the ATLAS detector*, *Eur. Phys. J. C* **78** (2018) 142 [`1709.02301`].

[87] ALICE collaboration, *Observation of flow angle and flow magnitude fluctuations in Pb-Pb collisions at sNN=5.02TeV at the CERN Large Hadron Collider*, *Phys. Rev. C* **107** (2023) L051901 [`2206.04574`].

[88] W. Broniowski, P. Bozek and M. Rybczynski, *Fluctuating initial conditions in heavy-ion collisions from the Glauber approach*, *Phys. Rev. C* **76** (2007) 054905 [`0706.4266`].

[89] G.-Y. Qin, H. Petersen, S.A. Bass and B. Muller, *Translation of collision geometry fluctuations into momentum anisotropies in relativistic heavy-ion collisions*, *Phys. Rev. C* **82** (2010) 064903 [`1009.1847`].

[90] D. Teaney and L. Yan, *Triangularity and Dipole Asymmetry in Heavy Ion Collisions*, *Phys. Rev. C* **83** (2011) 064904 [`1010.1876`].

[91] H. Holopainen, H. Niemi and K.J. Eskola, *Event-by-event hydrodynamics and elliptic flow from fluctuating initial state*, *Phys. Rev. C* **83** (2011) 034901 [`1007.0368`].

[92] F.G. Gardim, F. Grassi, M. Luzum and J.-Y. Ollitrault, *Mapping the hydrodynamic response to the initial geometry in heavy-ion collisions*, *Phys. Rev. C* **85** (2012) 024908 [`1111.6538`].

[93] R.S. Bhalerao, M. Luzum and J.-Y. Ollitrault, *Determining initial-state fluctuations from flow measurements in heavy-ion collisions*, *Phys. Rev. C* **84** (2011) 034910 [`1104.4740`].

[94] B. Schenke, P. Tribedy and R. Venugopalan, *Fluctuating Glasma initial conditions and flow in heavy ion collisions*, *Phys. Rev. Lett.* **108** (2012) 252301 [`1202.6646`].

[95] P. Bozek, *Transverse-momentum–flow correlations in relativistic heavy-ion collisions*, *Phys. Rev. C* **93** (2016) 044908 [`1601.04513`].

[96] B. Schenke, C. Shen and D. Teaney, *Transverse momentum fluctuations and their correlation with elliptic flow in nuclear collision*, *Phys. Rev. C* **102** (2020) 034905 [`2004.00690`].

[97] G. Giacalone, F.G. Gardim, J. Noronha-Hostler and J.-Y. Ollitrault, *Correlation between mean transverse momentum and anisotropic flow in heavy-ion collisions*, *Phys. Rev. C* **103** (2021) 024909 [`2004.01765`].

[98] G. Giacalone, B. Schenke and C. Shen, *Constraining the Nucleon Size with Relativistic Nuclear Collisions*, *Phys. Rev. Lett.* **128** (2022) 042301 [`2111.02908`].

[99] C. Mordasini, A. Bilandzic, D. Karakoç and S.F. Taghavi, *Higher order Symmetric Cumulants*, *Phys. Rev. C* **102** (2020) 024907 [`1901.06968`].

[100] ATLAS collaboration, *Measurement of flow harmonics correlations with mean transverse momentum in lead-lead and proton-lead collisions at* $\sqrt{s_{NN}} = 5.02$ *TeV with the ATLAS detector*, *Eur. Phys. J. C* **79** (2019) 985 [`1907.05176`].

[101] ALICE collaboration, *Characterizing the initial conditions of heavy-ion collisions at the LHC with mean transverse momentum and anisotropic flow correlations*, *Phys. Lett. B* **834** (2022) 137393 [`2111.06106`].

[102] ATLAS collaboration, *Correlations between flow and transverse momentum in Xe+Xe and Pb+Pb collisions at the LHC with the ATLAS detector: A probe of the heavy-ion initial state and nuclear deformation*, *Phys. Rev. C* **107** (2023) 054910 [`2205.00039`].

[103] P. Filip, R. Lednicky, H. Masui and N. Xu, *Initial eccentricity in deformed Au-197 + Au-197 and U-238 + U-238 collisions at sNN=200 GeV at the BNL Relativistic Heavy Ion Collider*, *Phys. Rev. C* **80** (2009) 054903.

[104] G. Giacalone, *Observing the deformation of nuclei with relativistic nuclear collisions*, *Phys. Rev. Lett.* **124** (2020) 202301 [`1910.04673`].

[105] H. Li, H.-j. Xu, Y. Zhou, X. Wang, J. Zhao, L.-W. Chen et al., *Probing the neutron skin with ultrarelativistic isobaric collisions*, *Phys. Rev. Lett.* **125** (2020) 222301 [`1910.06170`].

[106] G. Giacalone, *Constraining the quadrupole deformation of atomic nuclei with relativistic nuclear collisions*, *Phys. Rev. C* **102** (2020) 024901 [`2004.14463`].

[107] G. Giacalone, J. Jia and C. Zhang, *Impact of Nuclear Deformation on Relativistic Heavy-Ion Collisions: Assessing Consistency in Nuclear Physics across Energy Scales*, *Phys. Rev. Lett.* **127** (2021) 242301 [`2105.01638`].

[108] J. Jia, S. Huang and C. Zhang, *Probing nuclear quadrupole deformation from correlation of elliptic flow and transverse momentum in heavy ion collisions*, *Phys. Rev. C* **105** (2022) 014906 [`2105.05713`].

[109] J. Jia, *Shape of atomic nuclei in heavy ion collisions*, *Phys. Rev. C* **105** (2022) 014905 [`2106.08768`].

[110] B. Bally, M. Bender, G. Giacalone and V. Somà, *Evidence of the triaxial structure of* ^{129}*Xe at the Large Hadron Collider*, *Phys. Rev. Lett.* **128** (2022) 082301 [`2108.09578`].

[111] J. Jia, *Probing triaxial deformation of atomic nuclei in high-energy heavy ion collisions*, *Phys. Rev. C* **105** (2022) 044905 [`2109.00604`].

[112] H.-j. Xu, W. Zhao, H. Li, Y. Zhou, L.-W. Chen and F. Wang, *Probing nuclear structure with mean transverse momentum in relativistic isobar collisions*, *Phys. Rev. C* **108** (2023) L011902 [`2111.14812`].

[113] C. Zhang and J. Jia, *Evidence of Quadrupole and Octupole Deformations in Zr96+Zr96 and Ru96+Ru96 Collisions at Ultrarelativistic Energies*, *Phys. Rev. Lett.* **128** (2022) 022301 [`2109.01631`].

[114] J. Jia and C. Zhang, *Scaling approach to nuclear structure in high-energy heavy-ion collisions*, *Phys. Rev. C* **107** (2023) L021901 [`2111.15559`].

[115] J. Jia, G. Giacalone and C. Zhang, *Separating the Impact of Nuclear Skin and Nuclear Deformation in High-Energy Isobar Collisions*, *Phys. Rev. Lett.* **131** (2023) 022301 [2206.10449].

[116] J. Jia, G. Giacalone and C. Zhang, *Precision Tests of the Nonlinear Mode Coupling of Anisotropic Flow via High-Energy Collisions of Isobars*, *Chin. Phys. Lett.* **40** (2023) 042501 [2206.07184].

[117] B. Bally, G. Giacalone and M. Bender, *The shape of gold*, *Eur. Phys. J. A* **59** (2023) 58 [2301.02420].

[118] W. Ryssens, G. Giacalone, B. Schenke and C. Shen, *Evidence of Hexadecapole Deformation in Uranium-238 at the Relativistic Heavy Ion Collider*, *Phys. Rev. Lett.* **130** (2023) 212302 [2302.13617].

[119] STAR collaboration, *Azimuthal anisotropy in U+U and Au+Au collisions at RHIC*, *Phys. Rev. Lett.* **115** (2015) 222301 [1505.07812].

[120] ALICE collaboration, *Anisotropic flow in Xe-Xe collisions at* $\sqrt{\mathbf{s}_{\rm NN}} = \mathbf{5.44}$ *TeV*, *Phys. Lett. B* **784** (2018) 82 [1805.01832].

[121] CMS collaboration, *Charged-particle angular correlations in XeXe collisions at* $\sqrt{s_{\rm NN}} =$ *5.44 TeV*, *Phys. Rev. C* **100** (2019) 044902 [1901.07997].

[122] ATLAS collaboration, *Measurement of the azimuthal anisotropy of charged-particle production in* $Xe+Xe$ *collisions at* $\sqrt{s_{\rm NN}} = 5.44$ *TeV with the ATLAS detector*, *Phys. Rev. C* **101** (2020) 024906 [1911.04812].

[123] ATLAS collaboration, *Longitudinal Flow Decorrelations in Xe+Xe Collisions at* $\sqrt{s_{\rm NN}} = 5.44$ *TeV with the ATLAS Detector*, *Phys. Rev. Lett.* **126** (2021) 122301 [2001.04201].

[124] STAR collaboration, *Imaging Shapes of Atomic Nuclei in High-Energy Nuclear Collisions*, 2401.06625.

[125] P. Bozek and R. Samanta, *Factorization breaking for higher moments of harmonic flow*, *Phys. Rev. C* **105** (2022) 034904 [2109.07781].

[126] R. Samanta, S. Bhatta, J. Jia, M. Luzum and J.-Y. Ollitrault, *Thermalization at the femtoscale seen in high-energy Pb+Pb collisions*, *Phys. Rev. C* **109** (2024) L051902 [2303.15323].

[127] R. Samanta, J.a.P. Picchetti, M. Luzum and J.-Y. Ollitrault, *Non-Gaussian transverse momentum fluctuations from impact parameter fluctuations*, *Phys. Rev. C* **108** (2023) 024908 [2306.09294].

[128] P. Bozek and R. Samanta, *Higher order cumulants of transverse momentum and harmonic flow in relativistic heavy ion collisions*, *Phys. Rev. C* **104** (2021) 014905 [2103.15338].

[129] R. Samanta and P. Bozek, *Momentum-dependent measures of correlations between mean transverse momentum and harmonic flow in heavy-ion collisions*, *Phys. Rev. C* **109** (2024) 064910 [2308.11565].

[130] R. Samanta and P. Bożek, *Momentum-dependent flow correlations in deformed nuclei at collision energies available at the BNL Relativistic Heavy Ion Collider*, *Phys. Rev. C* **107** (2023) 054916 [`2301.10659`].

[131] G. Giacalone, *A matter of shape: seeing the deformation of atomic nuclei at high-energy colliders*, Ph.D. thesis, U. Paris-Saclay, 2020. `2101.00168`.

[132] K.S. Krane, *INTRODUCTORY NUCLEAR PHYSICS* (1987).

[133] B. Alver, M. Baker, C. Loizides and P. Steinberg, *The PHOBOS Glauber Monte Carlo*, `0805.4411`.

[134] C. Loizides, J. Nagle and P. Steinberg, *Improved version of the PHOBOS Glauber Monte Carlo*, *SoftwareX* **1-2** (2015) 13 [`1408.2549`].

[135] J.-Y. Ollitrault, *Determination of the reaction plane in ultrarelativistic nuclear collisions*, *Phys. Rev. D* **48** (1993) 1132 [`hep-ph/9303247`].

[136] A. Bialas, M. Bleszynski and W. Czyz, *Multiplicity Distributions in Nucleus-Nucleus Collisions at High-Energies*, *Nucl. Phys. B* **111** (1976) 461.

[137] D. Kharzeev and M. Nardi, *Hadron production in nuclear collisions at RHIC and high density QCD*, *Phys. Lett. B* **507** (2001) 121 [`nucl-th/0012025`].

[138] M.L. Miller, K. Reygers, S.J. Sanders and P. Steinberg, *Glauber modeling in high energy nuclear collisions*, *Ann. Rev. Nucl. Part. Sci.* **57** (2007) 205 [`nucl-ex/0701025`].

[139] R.J. Glauber, *Cross-sections in deuterium at high-energies*, *Phys. Rev.* **100** (1955) 242.

[140] R.J. Glauber, *Lectures in Theoretical Physics* , vol. 1, Interscience, New York (1959).

[141] A. Bialas, M. Bleszynski and W. Czyz, *Relation Between the Glauber Model and Classical Probability Calculus*, *Acta Phys. Polon. B* **8** (1977) 389.

[142] R.J. Glauber, *Quantum Optics and Heavy Ion Physics*, *Nucl. Phys. A* **774** (2006) 3 [`nucl-th/0604021`].

[143] X.-N. Wang and M. Gyulassy, *HIJING: A Monte Carlo model for multiple jet production in p p, p A and A A collisions*, *Phys. Rev. D* **44** (1991) 3501.

[144] W. Broniowski, M. Rybczynski and P. Bozek, *GLISSANDO: Glauber initial-state simulation and more..*, *Comput. Phys. Commun.* **180** (2009) 69 [`0710.5731`].

[145] J.J. Sakurai, *Modern quantum mechanics; rev. ed.*, Addison-Wesley, Reading, MA (1994).

[146] R.G. Newton, *Optical theorem and beyond*, *Am. J. Phys.* **44** (1976) 639.

[147] PARTICLE DATA GROUP collaboration, *Review of Particle Physics*, *J. Phys. G* **33** (2006) 1.

[148] PHENIX collaboration, *Transverse energy production and charged-particle multiplicity at midrapidity in various systems from* $\sqrt{s_{NN}} = 7.7$ *to 200 GeV*, *Phys. Rev. C* **93** (2016) 024901 [`1509.06727`].

[149] ATLAS collaboration, *Measurement of the centrality dependence of the charged particle pseudorapidity distribution in lead-lead collisions at $\sqrt{s_{NN}} = 2.76$ TeV with the ATLAS detector*, *Phys. Lett. B* **710** (2012) 363 [`1108.6027`].

[150] ALICE collaboration, *Pseudorapidity density of charged particles in p + Pb collisions at $\sqrt{s_{NN}} = 5.02$ TeV*, *Phys. Rev. Lett.* **110** (2013) 032301 [`1210.3615`].

[151] M. Rybczynski and W. Broniowski, *Wounded nucleon model with realistic nucleon-nucleon collision profile and observables in relativistic heavy-ion collisions*, *Phys. Rev. C* **84** (2011) 064913 [`1110.2609`].

[152] W. Israel, *Nonstationary irreversible thermodynamics: A Causal relativistic theory*, *Annals Phys.* **100** (1976) 310.

[153] W. Israel and J.M. Stewart, *Transient relativistic thermodynamics and kinetic theory*, *Annals Phys.* **118** (1979) 341.

[154] H. Grad, *On the kinetic theory of rarefied gases*, *Commun. Pure Appl. Math.* **2** (1949) 331.

[155] G.S. Denicol, T. Koide and D.H. Rischke, *Dissipative relativistic fluid dynamics: a new way to derive the equations of motion from kinetic theory*, *Phys. Rev. Lett.* **105** (2010) 162501 [`1004.5013`].

[156] A. Jaiswal, *Relativistic dissipative hydrodynamics from kinetic theory with relaxation time approximation*, *Phys. Rev. C* **87** (2013) 051901 [`1302.6311`].

[157] L. Landau and E. Lifshitz, *Fluid Mechanics, by L.D. Landau and E.M. Lifshitz*, Teoreticheskaia fizika, Pergamon Press (1959).

[158] C. Eckart, *The Thermodynamics of Irreversible Processes. 1. The Simple Fluid*, *Phys. Rev.* **58** (1940) 267.

[159] S. Pu, T. Koide and D.H. Rischke, *Does stability of relativistic dissipative fluid dynamics imply causality?*, *Phys. Rev. D* **81** (2010) 114039 [`0907.3906`].

[160] A. Jaiswal, R.S. Bhalerao and S. Pal, *Complete relativistic second-order dissipative hydrodynamics from the entropy principle*, *Phys. Rev. C* **87** (2013) 021901 [`1302.0666`].

[161] G.S. Denicol, T. Kodama, T. Koide and P. Mota, *Stability and Causality in relativistic dissipative hydrodynamics*, *J. Phys. G* **35** (2008) 115102 [`0807.3120`].

[162] G.S. Denicol, H. Niemi, E. Molnar and D.H. Rischke, *Derivation of transient relativistic fluid dynamics from the Boltzmann equation*, *Phys. Rev. D* **85** (2012) 114047 [`1202.4551`].

[163] B. Betz, G.S. Denicol, T. Koide, E. Molnar, H. Niemi and D.H. Rischke, *Second order dissipative fluid dynamics from kinetic theory*, *EPJ Web Conf.* **13** (2011) 07005 [`1012.5772`].

[164] R. Baier, P. Romatschke and U.A. Wiedemann, *Dissipative hydrodynamics and heavy ion collisions*, *Phys. Rev. C* **73** (2006) 064903 [`hep-ph/0602249`].

[165] W.A. Hiscock and L. Lindblom, *Stability and causality in dissipative relativistic fluids*, *Annals Phys.* **151** (1983) 466.

[166] W.A. Hiscock and L. Lindblom, *Generic instabilities in first-order dissipative relativistic fluid theories*, *Phys. Rev. D* **31** (1985) 725.

[167] B. Carter, *Convective variational approach to relativistic thermodynamics of dissipative fluids*, *Proceedings: Mathematical and Physical Sciences* **433** (1991) 45.

[168] M. Grmela and H.C. Ottinger, *Dynamics and thermodynamics of complex fluids. 1. Development of a general formalism*, *Phys. Rev. E* **56** (1997) 6620.

[169] A. Jaiswal, R.S. Bhalerao and S. Pal, *New relativistic dissipative fluid dynamics from kinetic theory*, *Phys. Lett. B* **720** (2013) 347 [`1204.3779`].

[170] C.-N. Yang and R.L. Mills, *Conservation of Isotopic Spin and Isotopic Gauge Invariance*, *Phys. Rev.* **96** (1954) 191.

[171] H.D. Politzer, *Asymptotic Freedom: An Approach to Strong Interactions*, *Phys. Rept.* **14** (1974) 129.

[172] PARTICLE DATA GROUP collaboration, *Review of particle physics*, *Phys. Rev. D* **86** (2012) 010001.

[173] F.G. Gardim, G. Giacalone and J.-Y. Ollitrault, *The mean transverse momentum of ultracentral heavy-ion collisions: A new probe of hydrodynamics*, *Phys. Lett. B* **809** (2020) 135749 [`1909.11609`].

[174] P. Huovinen and P. Petreczky, *QCD Equation of State and Hadron Resonance Gas*, *Nucl. Phys. A* **837** (2010) 26 [`0912.2541`].

[175] E. Braaten and A. Nieto, *On the convergence of perturbative QCD at high temperature*, *Phys. Rev. Lett.* **76** (1996) 1417 [`hep-ph/9508406`].

[176] J.P. Blaizot, E. Iancu and A. Rebhan, *On the apparent convergence of perturbative QCD at high temperature*, *Phys. Rev. D* **68** (2003) 025011 [`hep-ph/0303045`].

[177] O. Komoltsev and A. Kurkela, *How Perturbative QCD Constrains the Equation of State at Neutron-Star Densities*, *Phys. Rev. Lett.* **128** (2022) 202701 [`2111.05350`].

[178] S. Borsanyi, Z. Fodor, C. Hoelbling, S.D. Katz, S. Krieg and K.K. Szabo, *Full result for the QCD equation of state with 2+1 flavors*, *Phys. Lett. B* **730** (2014) 99 [`1309.5258`].

[179] S. Borsanyi, G. Endrodi, Z. Fodor, A. Jakovac, S.D. Katz, S. Krieg et al., *The QCD equation of state with dynamical quarks*, *JHEP* **11** (2010) 077 [`1007.2580`].

[180] HOTQCD collaboration, *Equation of state in (2+1)-flavor QCD*, *Phys. Rev. D* **90** (2014) 094503 [`1407.6387`].

[181] A. Bazavov et al., *The QCD Equation of State to $\mathcal{O}(\mu_B^6)$ from Lattice QCD*, *Phys. Rev. D* **95** (2017) 054504 [`1701.04325`].

[182] S. Borsanyi, Z. Fodor, J.N. Guenther, S.K. Katz, K.K. Szabo, A. Pasztor et al., *Higher order fluctuations and correlations of conserved charges from lattice QCD*, *JHEP* **10** (2018) 205 [`1805.04445`].

[183] R. Bellwied, S. Borsanyi, Z. Fodor, J.N. Guenther, J. Noronha-Hostler, P. Parotto et al., *Off-diagonal correlators of conserved charges from lattice QCD and how to relate them to experiment*, *Phys. Rev. D* **101** (2020) 034506 [`1910.14592`].

[184] A. Bazavov et al., *Skewness, kurtosis, and the fifth and sixth order cumulants of net baryon-number distributions from lattice QCD confront high-statistics STAR data*, *Phys. Rev. D* **101** (2020) 074502 [`2001.08530`].

[185] B. Müller, *Investigation of hot qcd matter: theoretical aspects*, *Physica Scripta* **2013** (2013) 014004.

[186] P. Bozek and H. Mehrabpour, *Correlation coefficient between harmonic flow and transverse momentum in heavy-ion collisions*, *Phys. Rev. C* **101** (2020) 064902 [`2002.08832`].

[187] H. Niemi, G.S. Denicol, H. Holopainen and P. Huovinen, *Event-by-event distributions of azimuthal asymmetries in ultrarelativistic heavy-ion collisions*, *Phys. Rev. C* **87** (2013) 054901 [`1212.1008`].

[188] T. Hirano and K. Tsuda, *Collective flow and two pion correlations from a relativistic hydrodynamic model with early chemical freezeout*, *Phys. Rev. C* **66** (2002) 054905 [`nucl-th/0205043`].

[189] P. Bozek, *Flow and interferometry in 3+1 dimensional viscous hydrodynamics*, *Phys. Rev. C* **85** (2012) 034901 [`1110.6742`].

[190] P. Bozek, *Splitting of proton-antiproton directed flow in relativistic heavy-ion collisions*, *Phys. Rev. C* **106** (2022) L061901 [`2207.04927`].

[191] J.D. Bjorken, *Highly Relativistic Nucleus-Nucleus Collisions: The Central Rapidity Region*, *Phys. Rev. D* **27** (1983) 140.

[192] D. Kharzeev, E. Levin and M. Nardi, *The Onset of classical QCD dynamics in relativistic heavy ion collisions*, *Phys. Rev. C* **71** (2005) 054903 [`hep-ph/0111315`].

[193] B. Schenke, P. Tribedy and R. Venugopalan, *Event-by-event gluon multiplicity, energy density, and eccentricities in ultrarelativistic heavy-ion collisions*, *Phys. Rev. C* **86** (2012) 034908 [`1206.6805`].

[194] J.S. Moreland, J.E. Bernhard and S.A. Bass, *Alternative ansatz to wounded nucleon and binary collision scaling in high-energy nuclear collisions*, *Phys. Rev. C* **92** (2015) 011901 [`1412.4708`].

[195] D. d'Enterria, G.K. Eyyubova, V.L. Korotkikh, I.P. Lokhtin, S.V. Petrushanko, L.I. Sarycheva et al., *Estimates of hadron azimuthal anisotropy from multiparton interactions in proton-proton collisions at $\sqrt{s} = 14$ TeV*, *Eur. Phys. J. C* **66** (2010) 173 [`0910.3029`].

[196] H. Song and U.W. Heinz, *Multiplicity scaling in ideal and viscous hydrodynamics*, *Phys. Rev. C* **78** (2008) 024902 [`0805.1756`].

[197] "trento 2.0." http://qcd.phy.duke.edu/trento/.

[198] L.D. McLerran and R. Venugopalan, *Gluon distribution functions for very large nuclei at small transverse momentum*, *Phys. Rev. D* **49** (1994) 3352 [`hep-ph/9311205`].

[199] L.D. McLerran and R. Venugopalan, *Computing quark and gluon distribution functions for very large nuclei*, *Phys. Rev. D* **49** (1994) 2233 [`hep-ph/9309289`].

[200] A. Krasnitz and R. Venugopalan, *The Initial gluon multiplicity in heavy ion collisions*, *Phys. Rev. Lett.* **86** (2001) 1717 [`hep-ph/0007108`].

[201] E. Iancu and R. Venugopalan, *The Color glass condensate and high-energy scattering in QCD*, in *Quark-gluon plasma 4*, R.C. Hwa and X.-N. Wang, eds., pp. 249–3363 (2003), DOI [`hep-ph/0303204`].

[202] T. Lappi, *Production of gluons in the classical field model for heavy ion collisions*, *Phys. Rev. C* **67** (2003) 054903 [`hep-ph/0303076`].

[203] C. Gale, S. Jeon, B. Schenke, P. Tribedy and R. Venugopalan, *Event-by-event anisotropic flow in heavy-ion collisions from combined Yang-Mills and viscous fluid dynamics*, *Phys. Rev. Lett.* **110** (2013) 012302 [`1209.6330`].

[204] S.A. Bass et al., *Microscopic models for ultrarelativistic heavy ion collisions*, *Prog. Part. Nucl. Phys.* **41** (1998) 255 [`nucl-th/9803035`].

[205] M. Bleicher et al., *Relativistic hadron hadron collisions in the ultrarelativistic quantum molecular dynamics model*, *J. Phys. G* **25** (1999) 1859 [`hep-ph/9909407`].

[206] J. Steinheimer, M. Bleicher, H. Petersen, S. Schramm, H. Stocker and D. Zschiesche, *(3+1)-dimensional hydrodynamic expansion with a critical point from realistic initial conditions*, *Phys. Rev. C* **77** (2008) 034901 [`0710.0332`].

[207] L. Pang, Q. Wang and X.-N. Wang, *Effects of initial flow velocity fluctuation in event-by-event (3+1)D hydrodynamics*, *Phys. Rev. C* **86** (2012) 024911 [`1205.5019`].

[208] R.S. Bhalerao, A. Jaiswal and S. Pal, *Collective flow in event-by-event partonic transport plus hydrodynamics hybrid approach*, *Phys. Rev. C* **92** (2015) 014903 [`1503.03862`].

[209] A. Kurkela, A. Mazeliauskas, J.-F. Paquet, S. Schlichting and D. Teaney, *Matching the Nonequilibrium Initial Stage of Heavy Ion Collisions to Hydrodynamics with QCD Kinetic Theory*, *Phys. Rev. Lett.* **122** (2019) 122302 [`1805.01604`].

[210] W. van der Schee, P. Romatschke and S. Pratt, *Fully Dynamical Simulation of Central Nuclear Collisions*, *Phys. Rev. Lett.* **111** (2013) 222302 [`1307.2539`].

[211] ALICE collaboration, *Centrality dependence of the pseudorapidity density distribution for charged particles in Pb-Pb collisions at $\sqrt{s_{\rm NN}} = 5.02$ TeV*, *Phys. Lett. B* **772** (2017) 567 [`1612.08966`].

[212] M.A. Stephanov, K. Rajagopal and E.V. Shuryak, *Event-by-event fluctuations in heavy ion collisions and the QCD critical point*, *Phys. Rev. D* **60** (1999) 114028 [`hep-ph/9903292`].

[213] HotQCD collaboration, *Chiral crossover in QCD at zero and non-zero chemical potentials*, *Phys. Lett. B* **795** (2019) 15 [`1812.08235`].

[214] A. Bzdak, S. Esumi, V. Koch, J. Liao, M. Stephanov and N. Xu, *Mapping the Phases of Quantum Chromodynamics with Beam Energy Scan*, *Phys. Rept.* **853** (2020) 1 [`1906.00936`].

[215] F. Cooper and G. Frye, *Comment on the Single Particle Distribution in the Hydrodynamic and Statistical Thermodynamic Models of Multiparticle Production*, *Phys. Rev. D* **10** (1974) 186.

[216] B. Schenke, S. Jeon and C. Gale, *(3+1)D hydrodynamic simulation of relativistic heavy-ion collisions*, *Phys. Rev. C* **82** (2010) 014903 [`1004.1408`].

[217] "iSS spectra sampler." https://github.com/chunshen1987/iSS.

[218] A. Monnai and T. Hirano, *Effects of Bulk Viscosity at Freezeout*, *Phys. Rev. C* **80** (2009) 054906 [`0903.4436`].

[219] P. Bozek, *Bulk and shear viscosities of matter created in relativistic heavy-ion collisions*, *Phys. Rev. C* **81** (2010) 034909 [`0911.2397`].

[220] "MUSIC-hydro manual." https://webhome.phy.duke.edu/~jp401/music_manual/.

[221] N. Summerfield, B.-N. Lu, C. Plumberg, D. Lee, J. Noronha-Hostler and A. Timmins, *^{16}O ^{16}O collisions at energies available at the BNL Relativistic Heavy Ion Collider and at the CERN Large Hadron Collider comparing α clustering versus substructure*, *Phys. Rev. C* **104** (2021) L041901 [`2103.03345`].

[222] SMASH collaboration, *Particle production and equilibrium properties within a new hadron transport approach for heavy-ion collisions*, *Phys. Rev. C* **94** (2016) 054905 [`1606.06642`].

[223] C. Shen, Z. Qiu, H. Song, J. Bernhard, S. Bass and U. Heinz, *The iEBE-VISHNU code package for relativistic heavy-ion collisions*, *Comput. Phys. Commun.* **199** (2016) 61 [`1409.8164`].

[224] S. Ryu, J.F. Paquet, C. Shen, G.S. Denicol, B. Schenke, S. Jeon et al., *Importance of the Bulk Viscosity of QCD in Ultrarelativistic Heavy-Ion Collisions*, *Phys. Rev. Lett.* **115** (2015) 132301 [`1502.01675`].

[225] G. Giacalone, B. Schenke and C. Shen, *Observable signatures of initial state momentum anisotropies in nuclear collisions*, *Phys. Rev. Lett.* **125** (2020) 192301 [`2006.15721`].

[226] H. Song and U.W. Heinz, *Causal viscous hydrodynamics in 2+1 dimensions for relativistic heavy-ion collisions*, *Phys. Rev. C* **77** (2008) 064901 [`0712.3715`].

[227] J. Noronha-Hostler, G.S. Denicol, J. Noronha, R.P.G. Andrade and F. Grassi, *Bulk Viscosity Effects in Event-by-Event Relativistic Hydrodynamics*, *Phys. Rev. C* **88** (2013) 044916 [`1305.1981`].

[228] "MUSIC-hydro code." https://github.com/MUSIC-fluid/MUSIC?tab=readme-ov-file.

[229] P. Bozek, *Components of the elliptic flow in Pb-Pb collisions at s**(1/2) = 2.76-TeV*, *Phys. Lett. B* **699** (2011) 283 [`1101.1791`].

[230] N. Borghini, P.M. Dinh and J.-Y. Ollitrault, *A New method for measuring azimuthal distributions in nucleus-nucleus collisions*, *Phys. Rev. C* **63** (2001) 054906 [`nucl-th/0007063`].

[231] N. Borghini, P.M. Dinh and J.-Y. Ollitrault, *Flow analysis from multiparticle azimuthal correlations*, *Phys. Rev. C* **64** (2001) 054901 [`nucl-th/0105040`].

[232] N. Borghini, P.M. Dinh and J.Y. Ollitrault, *Analysis of directed flow from elliptic flow*, *Phys. Rev. C* **66** (2002) 014905 [`nucl-th/0204017`].

[233] R.S. Bhalerao, N. Borghini and J.Y. Ollitrault, *Genuine collective flow from Lee-Yang zeroes*, *Phys. Lett. B* **580** (2004) 157 [`nucl-th/0307018`].

[234] A. Bilandzic, N. van der Kolk, J.-Y. Ollitrault and R. Snellings, *Event-plane flow analysis without non-flow effects*, *Phys. Rev. C* **83** (2011) 014909 [`0801.3915`].

[235] A. Bilandzic, R. Snellings and S. Voloshin, *Flow analysis with cumulants: Direct calculations*, *Phys. Rev. C* **83** (2011) 044913 [`1010.0233`].

[236] R.S. Bhalerao, J.-Y. Ollitrault and S. Pal, *Event-plane correlators*, *Phys. Rev. C* **88** (2013) 024909 [`1307.0980`].

[237] A. Bilandzic, C.H. Christensen, K. Gulbrandsen, A. Hansen and Y. Zhou, *Generic framework for anisotropic flow analyses with multiparticle azimuthal correlations*, *Phys. Rev. C* **89** (2014) 064904 [`1312.3572`].

[238] STAR collaboration, *Elliptic flow from two and four particle correlations in Au+Au collisions at s(NN)**(1/2) = 130-GeV*, *Phys. Rev. C* **66** (2002) 034904 [`nucl-ex/0206001`].

[239] ALICE collaboration, *Multiparticle azimuthal correlations in p -Pb and Pb-Pb collisions at the CERN Large Hadron Collider*, *Phys. Rev. C* **90** (2014) 054901 [`1406.2474`].

[240] F.G. Gardim, F. Grassi, M. Luzum and J.-Y. Ollitrault, *Breaking of factorization of two-particle correlations in hydrodynamics*, *Phys. Rev. C* **87** (2013) 031901 [`1211.0989`].

[241] T. Renk and H. Niemi, *Constraints from v_2 fluctuations for the initial-state geometry of heavy-ion collisions*, *Phys. Rev. C* **89** (2014) 064907 [`1401.2069`].

[242] L.-G. Pang, H. Petersen, G.-Y. Qin, V. Roy and X.-N. Wang, *Decorrelation of anisotropic flow along the longitudinal direction*, *Eur. Phys. J. A* **52** (2016) 97 [`1511.04131`].

[243] K. Xiao, L. Yi, F. Liu and F. Wang, *Factorization of event-plane correlations over transverse momentum in relativistic heavy ion collisions in a multiphase transport model*, *Phys. Rev. C* **94** (2016) 024905 [`1509.06070`].

[244] P. Bożek, *Angle and magnitude decorrelation in the factorization breaking of collective flow*, *Phys. Rev. C* **98** (2018) 064906 [`1808.04248`].

[245] E.G. Nielsen and Y. Zhou, *Transverse momentum decorrelation of the flow vector in Pb–Pb collisions at $\sqrt{s_{NN}}$ = 5.02 TeV*, *Eur. Phys. J. C* **83** (2023) 545 [`2211.13651`].

[246] P. Bozek and H. Mehrabpour, *Random model of flow decorrelation*, *Phys. Rev. C* **108** (2023) 024907 [`2304.12711`].

[247] J. Zhu, X.-Y. Wu and G.-Y. Qin, *Anisotropic flow, flow fluctuation and flow decorrelation in relativistic heavy-ion collisions: the roles of sub-nucleon structure and shear viscosity*, `2401.15536`.

[248] ALICE collaboration, *Harmonic decomposition of two-particle angular correlations in Pb-Pb collisions at $\sqrt{s_{NN}}$ = 2.76 TeV*, *Phys. Lett. B* **708** (2012) 249 [`1109.2501`].

[249] ATLAS collaboration, *Fluctuations of anisotropic flow in Pb+Pb collisions at $\sqrt{s_{\mathrm{NN}}}$ = 5.02 TeV with the ATLAS detector*, *JHEP* **01** (2020) 051 [`1904.04808`].

[250] ALICE collaboration, *Systematic study of flow vector decorrelation in* $\sqrt{s_{\mathrm{NN}}} = \mathbf{5.02}$ *TeV Pb-Pb collisions*, `2403.15213`.

[251] B.H. Alver, C. Gombeaud, M. Luzum and J.-Y. Ollitrault, *Triangular flow in hydrodynamics and transport theory*, *Phys. Rev. C* **82** (2010) 034913 [`1007.5469`].

[252] K. Werner, I. Karpenko, T. Pierog, M. Bleicher and K. Mikhailov, *Event-by-Event Simulation of the Three-Dimensional Hydrodynamic Evolution from Flux Tube Initial Conditions in Ultrarelativistic Heavy Ion Collisions*, *Phys. Rev. C* **82** (2010) 044904 [`1004.0805`].

[253] B. Müller and A. Schäfer, *Transverse Energy Density Fluctuations in Heavy-Ion Collisions in a Gaussian Model*, *Phys. Rev. D* **85** (2012) 114030 [`1111.3347`].

[254] U.W. Heinz, *The Strongly coupled quark-gluon plasma created at RHIC*, *J. Phys. A* **42** (2009) 214003 [`0810.5529`].

[255] H. Sorge, *Highly sensitive centrality dependence of elliptic flow: A novel signature of the phase transition in QCD*, *Phys. Rev. Lett.* **82** (1999) 2048 [`nucl-th/9812057`].

[256] M. Luzum and H. Petersen, *Initial State Fluctuations and Final State Correlations in Relativistic Heavy-Ion Collisions*, *J. Phys. G* **41** (2014) 063102 [`1312.5503`].

[257] ALICE collaboration, *Transverse momentum spectra and nuclear modification factors of charged particles in pp, p-Pb and Pb-Pb collisions at the LHC*, *JHEP* **11** (2018) 013 [`1802.09145`].

[258] ATLAS collaboration, *Charged-hadron production in pp, p+Pb, Pb+Pb, and Xe+Xe collisions at* $\sqrt{s_{NN}} = 5$ *TeV with the ATLAS detector at the LHC*, *JHEP* **07** (2023) 074 [`2211.15257`].

[259] ALICE collaboration, *Centrality dependence of* π*, K, p production in Pb-Pb collisions at* $\sqrt{s_{NN}} = 2.76$ *TeV*, *Phys. Rev. C* **88** (2013) 044910 [`1303.0737`].

[260] ALICE collaboration, *Production of charged pions, kaons, and (anti-)protons in Pb-Pb and inelastic pp collisions at* $\sqrt{s_{NN}} = 5.02$ *TeV*, *Phys. Rev. C* **101** (2020) 044907 [`1910.07678`].

[261] K.S. Lee, U.W. Heinz and E. Schnedermann, *Search for Collective Transverse Flow Using Particle Transverse Momentum Spectra in Relativistic Heavy Ion Collisions*, *Z. Phys. C* **48** (1990) 525.

[262] C.M. Hung and E.V. Shuryak, *Equation of state, radial flow and freezeout in high-energy heavy ion collisions*, *Phys. Rev. C* **57** (1998) 1891 [`hep-ph/9709264`].

[263] F.G. Gardim, F. Grassi, Y. Hama, M. Luzum and J.-Y. Ollitrault, *Directed flow at mid-rapidity in event-by-event hydrodynamics*, *Phys. Rev. C* **83** (2011) 064901 [`1103.4605`].

[264] STAR collaboration, *Azimuthal anisotropy at RHIC: The First and fourth harmonics*, *Phys. Rev. Lett.* **92** (2004) 062301 [`nucl-ex/0310029`].

[265] PHOBOS collaboration, *Energy dependence of directed flow over a wide range of pseudorapidity in Au + Au collisions at RHIC*, *Phys. Rev. Lett.* **97** (2006) 012301 [`nucl-ex/0511045`].

[266] STAR collaboration, *System-size independence of directed flow at the Relativistic Heavy-Ion Collider*, *Phys. Rev. Lett.* **101** (2008) 252301 [`0807.1518`].

[267] P. Bozek, W. Broniowski and J. Moreira, *Torqued fireballs in relativistic heavy-ion collisions*, *Phys. Rev. C* **83** (2011) 034911 [`1011.3354`].

[268] S. Chatterjee and P. Bożek, *Large directed flow of open charm mesons probes the three dimensional distribution of matter in heavy ion collisions*, *Phys. Rev. Lett.* **120** (2018) 192301 [`1712.01189`].

[269] T. Parida and S. Chatterjee, *Directed flow in a baryonic fireball*, `2211.15729`.

[270] M. Luzum and J.-Y. Ollitrault, *Directed flow at midrapidity in heavy-ion collisions*, *Phys. Rev. Lett.* **106** (2011) 102301 [`1011.6361`].

[271] P.M. Dinh, N. Borghini and J.-Y. Ollitrault, *Effects of HBT correlations on flow measurements*, *Phys. Lett. B* **477** (2000) 51 [`nucl-th/9912013`].

[272] N. Borghini, P.M. Dinh and J.-Y. Ollitrault, *Are flow measurements at SPS reliable?*, *Phys. Rev. C* **62** (2000) 034902 [`nucl-th/0004026`].

[273] Z. Moravcova, K. Gulbrandsen and Y. Zhou, *Generic algorithm for multiparticle cumulants of azimuthal correlations in high energy nucleus collisions*, *Phys. Rev. C* **103** (2021) 024913 [`2005.07974`].

[274] G. Giacalone, J. Noronha-Hostler and J.-Y. Ollitrault, *Relative flow fluctuations as a probe of initial state fluctuations*, *Phys. Rev. C* **95** (2017) 054910 [`1702.01730`].

[275] I. Kozlov, M. Luzum, G. Denicol, S. Jeon and C. Gale, *Transverse momentum structure of pair correlations as a signature of collective behavior in small collision systems*, `1405.3976`.

[276] F.G. Gardim, F. Grassi, P. Ishida, M. Luzum, P.S. Magalhães and J. Noronha-Hostler, *Sensitivity of observables to coarse-graining size in heavy-ion collisions*, *Phys. Rev. C* **97** (2018) 064919 [`1712.03912`].

[277] W. Zhao, H.-j. Xu and H. Song, *Collective flow in 2.76 A TeV and 5.02 A TeV Pb+Pb collisions*, *Eur. Phys. J. C* **77** (2017) 645 [`1703.10792`].

[278] CMS collaboration, *Studies of Azimuthal Dihadron Correlations in Ultra-Central PbPb Collisions at $\sqrt{s_{NN}}$ = 2.76 TeV*, *JHEP* **02** (2014) 088 [`1312.1845`].

[279] ALICE collaboration, *Searches for p_{T} dependent fluctuations of flow angle and magnitude in Pb-Pb and p-Pb collisions*, *Nucl. Phys. A* **931** (2014) 949 [`1407.7677`].

[280] P. Bożek, W. Broniowski, M. Rybczynski and G. Stefanek, *GLISSANDO 3: GLauber Initial-State Simulation AND mOre..., ver. 3*, *Comput. Phys. Commun.* **245** (2019) 106850 [`1901.04484`].

[281] J. Jia and P. Huo, *Forward-backward eccentricity and participant-plane angle fluctuations and their influences on longitudinal dynamics of collective flow*, *Phys. Rev. C* **90** (2014) 034915 [`1403.6077`].

[282] J. Jia, P. Huo, G. Ma and M. Nie, *Observables for longitudinal flow correlations in heavy-ion collisions*, *J. Phys. G* **44** (2017) 075106 [`1701.02183`].

[283] P. Bozek and R. Samanta, *Probing Flow Fluctuations Through Factorization Breaking of Harmonic Flows in Heavy-ion Collision*, *Acta Phys. Polon. Supp.* **16** (2023) 1 [`2208.01015`].

[284] ALICE collaboration, E. Nielsen. https://indico.cern.ch/event/854124/contributions/4134638/attachments/2169760/3663072/IS2021_slides_v8.pdf, 2021.

[285] D. Teaney and L. Yan, *Non linearities in the harmonic spectrum of heavy ion collisions with ideal and viscous hydrodynamics*, *Phys. Rev. C* **86** (2012) 044908 [`1206.1905`].

[286] J. Jia and D. Teaney, *Study on initial geometry fluctuations via participant plane correlations in heavy ion collisions: part II*, *Eur. Phys. J. C* **73** (2013) 2558 [`1205.3585`].

[287] Z. Qiu and U. Heinz, *Hydrodynamic event-plane correlations in Pb+Pb collisions at* $\sqrt{s} = 2.76 ATeV$, *Phys. Lett. B* **717** (2012) 261 [`1208.1200`].

[288] D. Teaney and L. Yan, *Event-plane correlations and hydrodynamic simulations of heavy ion collisions*, *Phys. Rev. C* **90** (2014) 024902 [`1312.3689`].

[289] J. Qian, U.W. Heinz and J. Liu, *Mode-coupling effects in anisotropic flow in heavy-ion collisions*, *Phys. Rev. C* **93** (2016) 064901 [`1602.02813`].

[290] G. Giacalone, L. Yan, J. Noronha-Hostler and J.-Y. Ollitrault, *Symmetric cumulants and event-plane correlations in Pb + Pb collisions*, *Phys. Rev. C* **94** (2016) 014906 [`1605.08303`].

[291] G. Giacalone, L. Yan and J.-Y. Ollitrault, *Nonlinear coupling of flow harmonics: Hexagonal flow and beyond*, *Phys. Rev. C* **97** (2018) 054905 [`1803.00253`].

[292] ATLAS collaboration, *Measurement of Event Plane Correlations in Pb-Pb Collisions at* $\sqrt{s_{\rm NN}}$*=2.76 TeV with the ATLAS Detector*, *Nucl. Phys. A* **910-911** (2013) 276 [`1208.1427`].

[293] ALICE collaboration, *Linear and non-linear flow modes in Pb-Pb collisions at* $\sqrt{s_{\rm NN}} =$ *2.76 TeV*, *Phys. Lett. B* **773** (2017) 68 [`1705.04377`].

[294] CMS collaboration, *Mixed higher-order anisotropic flow and nonlinear response coefficients of charged particles in* PbPb *collisions at* $\sqrt{s_{_{\rm NN}}} = 2.76$ *and* 5.02 *TeV*, *Eur. Phys. J. C* **80** (2020) 534 [`1910.08789`].

[295] ALICE collaboration, *Higher harmonic non-linear flow modes of charged hadrons in Pb-Pb collisions at* $\sqrt{s_{\rm NN}} = 5.02$ *TeV*, *JHEP* **05** (2020) 085 [`2002.00633`].

[296] J. Qian, U. Heinz, R. He and L. Huo, *Differential flow correlations in relativistic heavy-ion collisions*, *Phys. Rev. C* **95** (2017) 054908 [`1703.04077`].

[297] F. Liu, A. Tai, M. Gazdzicki and R. Stock, *On transverse momentum event by event fluctuations in string hadronic models*, *Eur. Phys. J. C* **8** (1999) 649 [`hep-ph/9809320`].

[298] S.A. Voloshin, V. Koch and H.G. Ritter, *Event-by-event fluctuations in collective quantities*, *Phys. Rev. C* **60** (1999) 024901 [`nucl-th/9903060`].

[299] R. Korus, S. Mrowczynski, M. Rybczynski and Z. Wlodarczyk, *Transverse momentum fluctuations due to temperature variation in high-energy nuclear collisions*, *Phys. Rev. C* **64** (2001) 054908 [`nucl-th/0106041`].

[300] E.G. Ferreiro, F. del Moral and C. Pajares, *Transverse momentum fluctuations and percolation of strings*, *Phys. Rev. C* **69** (2004) 034901 [`hep-ph/0303137`].

[301] S. Gavin, *Traces of thermalization from transverse momentum fluctuations in nuclear collisions*, *Phys. Rev. Lett.* **92** (2004) 162301 [`nucl-th/0308067`].

[302] W. Broniowski, B. Hiller, W. Florkowski and P. Bozek, *Event-by-event p(T) fluctuations and multiparticle clusters in relativistic heavy-ion collisions*, *Phys. Lett. B* **635** (2006) 290 [`nucl-th/0510033`].

[303] W. Broniowski, M. Chojnacki and L. Obara, *Size fluctuations of the initial source and the event-by-event transverse momentum fluctuations in relativistic heavy-ion collisions*, *Phys. Rev. C* **80** (2009) 051902 [`0907.3216`].

[304] P. Bozek and W. Broniowski, *Transverse-momentum fluctuations in relativistic heavy-ion collisions from event-by-event viscous hydrodynamics*, *Phys. Rev. C* **85** (2012) 044910 [`1203.1810`].

[305] P. Bożek and W. Broniowski, *Transverse momentum fluctuations in ultrarelativistic Pb + Pb and p + Pb collisions with "wounded" quarks*, *Phys. Rev. C* **96** (2017) 014904 [`1701.09105`].

[306] F.G. Gardim, G. Giacalone, M. Luzum and J.-Y. Ollitrault, *Effects of initial state fluctuations on the mean transverse momentum*, *Nucl. Phys. A* **1005** (2021) 121999 [`2002.07008`].

[307] G. Giacalone, F.G. Gardim, J. Noronha-Hostler and J.-Y. Ollitrault, *Skewness of mean transverse momentum fluctuations in heavy-ion collisions*, *Phys. Rev. C* **103** (2021) 024910 [`2004.09799`].

[308] S. Bhatta, C. Zhang and J. Jia, *Higher-order transverse momentum fluctuations in heavy-ion collisions*, *Phys. Rev. C* **105** (2022) 024904 [`2112.03397`].

[309] PHENIX collaboration, *Event-by-event fluctuations in mean p(T) and mean e(T) in s(NN)**(1/2) = 130-GeV Au+Au collisions*, *Phys. Rev. C* **66** (2002) 024901 [`nucl-ex/0203015`].

[310] PHENIX collaboration, *Measurement of nonrandom event by event fluctuations of average transverse momentum in s(NN)**(1/2) = 200-GeV Au+Au and p+p collisions*, *Phys. Rev. Lett.* **93** (2004) 092301 [`nucl-ex/0310005`].

[311] STAR collaboration, *Event by event < p(t) > fluctuations in Au - Au collisions at s(NN)**(1/2) = 130-GeV*, *Phys. Rev. C* **71** (2005) 064906 [`nucl-ex/0308033`].

[312] ALICE collaboration, *Event-by-event mean p_{T} fluctuations in pp and Pb-Pb collisions at the LHC*, *Eur. Phys. J. C* **74** (2014) 3077 [`1407.5530`].

[313] ALICE collaboration, *Event-by-event fluctuations of mean transverse momentum in Pb–Pb and Xe–Xe collisions with ALICE*, *J. Phys. Conf. Ser.* **2586** (2023) 012017 [`2211.14796`].

[314] ALICE collaboration, *Skewness and kurtosis of mean transverse momentum fluctuations at the LHC energies*, *Phys. Lett. B* **850** (2024) 138541 [`2308.16217`].

[315] S. Plumari, G.L. Guardo, F. Scardina and V. Greco, *Initial state fluctuations from mid-peripheral to ultra-central collisions in a event-by-event transport approach*, *Phys. Rev. C* **92** (2015) 054902 [`1507.05540`].

[316] C. Shen, Z. Qiu and U. Heinz, *Shape and flow fluctuations in ultracentral Pb + Pb collisions at the energies available at the CERN Large Hadron Collider*, *Phys. Rev. C* **92** (2015) 014901 [`1502.04636`].

[317] P. Carzon, S. Rao, M. Luzum, M. Sievert and J. Noronha-Hostler, *Possible octupole deformation of* ^{208}*Pb and the ultracentral* v_2 *to* v_3 *puzzle*, *Phys. Rev. C* **102** (2020) 054905 [`2007.00780`].

[318] L.-M. Liu, C.-J. Zhang, J. Zhou, J. Xu, J. Jia and G.-X. Peng, *Probing neutron-skin thickness with free spectator neutrons in ultracentral high-energy isobaric collisions*, *Phys. Lett. B* **834** (2022) 137441 [`2203.09924`].

[319] ExTrEMe collaboration, *Assessing the ultracentral flow puzzle in hydrodynamic modeling of heavy-ion collisions*, *Phys. Rev. C* **107** (2023) 044907 [`2203.17011`].

[320] K. Kuroki, A. Sakai, K. Murase and T. Hirano, *Hydrodynamic fluctuations and ultra-central flow puzzle in heavy-ion collisions*, *Phys. Lett. B* **842** (2023) 137958 [`2305.01977`].

[321] ATLAS collaboration, *Measurement of Transverse Momentum Fluctuations in Xe+Xe and Pb+Pb Collisions with ATLAS*, .

[322] M. Gyulassy and X.-N. Wang, *HIJING 1.0: A Monte Carlo program for parton and particle production in high-energy hadronic and nuclear collisions*, *Comput. Phys. Commun.* **83** (1994) 307 [`nucl-th/9502021`].

[323] F. Gelis, E. Iancu, J. Jalilian-Marian and R. Venugopalan, *The Color Glass Condensate*, *Ann. Rev. Nucl. Part. Sci.* **60** (2010) 463 [`1002.0333`].

[324] PHOBOS collaboration, *System size, energy, pseudorapidity, and centrality dependence of elliptic flow*, *Phys. Rev. Lett.* **98** (2007) 242302 [`nucl-ex/0610037`].

[325] K.V. Yousefnia, A. Kotibhaskar, R. Bhalerao and J.-Y. Ollitrault, *Bayesian approach to long-range correlations and multiplicity fluctuations in nucleus-nucleus collisions*, *Phys. Rev. C* **105** (2022) 014907 [`2108.03471`].

[326] M. Luzum and J.-Y. Ollitrault, *Extracting the shear viscosity of the quark-gluon plasma from flow in ultra-central heavy-ion collisions*, *Nucl. Phys. A* **904-905** (2013) 377c [`1210.6010`].

[327] ALICE collaboration, *Transverse momentum spectra and nuclear modification factors of charged particles in Xe-Xe collisions at* $\sqrt{s_{\rm NN}} = 5.44$ *TeV*, *Phys. Lett. B* **788** (2019) 166 [`1805.04399`].

[328] G. Nijs and W. van der Schee, *Predictions and postdictions for relativistic lead and oxygen collisions with the computational simulation code Trajectum*, *Phys. Rev. C* **106** (2022) 044903 [`2110.13153`].

[329] C.A. Bernardes, *Extracting the speed of sound in the strongly interacting matter created in relativistic nuclear collisions with the CMS experiment*, `2312.11758`.

[330] F.G. Gardim, F. Grassi, P. Ishida, M. Luzum and J.-Y. Ollitrault, *p_T-dependent particle number fluctuations from principal-component analyses in hydrodynamic simulations of heavy-ion collisions*, *Phys. Rev. C* **100** (2019) 054905 [`1906.03045`].

[331] M. Pepin, P. Christiansen, S. Munier and J.-Y. Ollitrault, *Multiplicity fluctuations and correlations in 5.02 TeV p+Pb collisions at zero impact parameter*, *Phys. Rev. C* **107** (2023) 024902 [`2208.12175`].

[332] ALICE collaboration, *Skewness of event-by-event $\langle p_{\mathrm{T}} \rangle$ distribution of charged particles at LHC energies with ALICE*, *PoS* **ICHEP2022** (2022) 1157.

[333] J.E. Bernhard, J.S. Moreland, S.A. Bass, J. Liu and U. Heinz, *Applying Bayesian parameter estimation to relativistic heavy-ion collisions: simultaneous characterization of the initial state and quark-gluon plasma medium*, *Phys. Rev. C* **94** (2016) 024907 [`1605.03954`].

[334] G. Nijs, W. van der Schee, U. Gürsoy and R. Snellings, *Bayesian analysis of heavy ion collisions with the heavy ion computational framework Trajectum*, *Phys. Rev. C* **103** (2021) 054909 [`2010.15134`].

[335] CMS collaboration, *Correlation Between Multiparticle Cumulants and Mean Transverse Momentum in Small Collision Systems with the CMS Detector*, *Acta Phys. Polon. Supp.* **16** (2023) 67.

[336] STAR collaboration, *Probing Initial- and Final-state Effects of Heavy-ion Collisions with STAR Experiment*, *Acta Phys. Polon. Supp.* **16** (2023) 1.

[337] C. Zhang, A. Behera, S. Bhatta and J. Jia, *Non-flow effects in correlation between harmonic flow and transverse momentum in nuclear collisions*, *Phys. Lett. B* **822** (2021) 136702 [`2102.05200`].

[338] S.H. Lim and J.L. Nagle, *Exploring origins for correlations between flow harmonics and transverse momentum in small collision systems*, *Phys. Rev. C* **103** (2021) 064906 [`2103.01348`].

[339] N. Magdy and R.A. Lacey, *Model investigations of the correlation between the mean transverse momentum and anisotropic flow in shape-engineered events*, *Phys. Lett. B* **821** (2021) 136625 [`2105.04879`].

[340] N. Magdy, P. Parfenov, A. Taranenko, I. Karpenko and R.A. Lacey, *Model study of the energy dependence of the correlation between anisotropic flow and the mean transverse momentum in Au+Au collisions*, *Phys. Rev. C* **105** (2022) 044901 [`2111.07406`].

[341] A. Olszewski and W. Broniowski, *Partial correlation analysis method in ultra-relativistic heavy-ion collisions*, *Phys. Rev. C* **96** (2017) 054903 [`1706.02862`].

[342] A. Mazeliauskas and D. Teaney, *Fluctuations of harmonic and radial flow in heavy ion collisions with principal components*, *Phys. Rev. C* **93** (2016) 024913 [`1509.07492`].

[343] T. Altinoluk, N. Armesto, A. Kovner, M. Lublinsky and V.V. Skokov, *Angular correlations in pA collisions from CGC: multiplicity and mean transverse momentum dependence of v_2*, *Eur. Phys. J. C* **81** (2021) 583 [`2012.01810`].

[344] STAR COLLABORATION collaboration, *Imaging the shape of atomic nuclei in high-energy collisions from STAR, talk given at the VII-th International Conference on Initial Stages of High Energy Nuclear Collisions, Copenhagen, Danemark, June 19-23* (2023) .

[345] D. Cline, *Nuclear shapes studied by coulomb excitation*, *Ann. Rev. Nucl. Part. Sci.* **36** (1986) 683.

[346] S. Raman, C.W.G. Nestor, Jr and P. Tikkanen, *Transition probability from the ground to the first-excited 2+ state of even-even nuclides*, *Atom. Data Nucl. Data Tabl.* **78** (2001) 1.

[347] Q.Y. Shou, Y.G. Ma, P. Sorensen, A.H. Tang, F. Videbæk and H. Wang, *Parameterization of Deformed Nuclei for Glauber Modeling in Relativistic Heavy Ion Collisions*, *Phys. Lett. B* **749** (2015) 215 [`1409.8375`].

[348] E.K. Warburton, J.A. Becker and B.A. Brown, *Mass systematics for A=29-44 nuclei: The deformed A ~ 32 region*, *Phys. Rev. C* **41** (1990) 1147.

[349] C. Force et al., *Prolate-Spherical Shape Coexistence at N=28 in* ^{44}S, *Phys. Rev. Lett.* **105** (2010) 102501 [`1007.4943`].

[350] P. Möller, A.J. Sierk, T. Ichikawa and H. Sagawa, *Nuclear ground-state masses and deformations: FRDM(2012)*, *Atom. Data Nucl. Data Tabl.* **109-110** (2016) 1 [`1508.06294`].

[351] Q. Yuan, J.G. Li and H.H. Li, *Ab initio calculations for well deformed nuclei: 40Mg and 42Si*, *Phys. Lett. B* **848** (2024) 138331.

[352] H.-j. Xu, J. Zhao and F. Wang, *Hexadecapole Deformation of U238 from Relativistic Heavy-Ion Collisions Using a Nonlinear Response Coefficient*, *Phys. Rev. Lett.* **132** (2024) 262301 [`2402.16550`].

[353] G. Giacalone et al., *The unexpected uses of a bowling pin: anisotropic flow in fixed-target* $^{208}Pb+^{20}Ne$ *collisions as a probe of quark-gluon plasma*, `2405.20210`.

[354] K. Kumar, *Intrinsic Quadrupole Moments and Shapes of Nuclear Ground States and Excited States*, *Phys. Rev. Lett.* **28** (1972) 249.

[355] G. Giacalone, J. Jia and V. Somà, *Accessing the shape of atomic nuclei with relativistic collisions of isobars*, *Phys. Rev. C* **104** (2021) L041903 [`2102.08158`].

[356] P. Bozek, *Collective flow in p-Pb and d-Pd collisions at TeV energies*, *Phys. Rev. C* **85** (2012) 014911 [`1112.0915`].

[357] P. Bozek and W. Broniowski, *Correlations from hydrodynamic flow in p-Pb collisions*, *Phys. Lett. B* **718** (2013) 1557 [`1211.0845`].

[358] P. Bozek and W. Broniowski, *Size of the emission source and collectivity in ultra-relativistic p-Pb collisions*, *Phys. Lett. B* **720** (2013) 250 [`1301.3314`].

[359] P. Bozek and W. Broniowski, *Collective dynamics in high-energy proton-nucleus collisions*, *Phys. Rev. C* **88** (2013) 014903 [`1304.3044`].

[360] K. Werner, M. Bleicher, B. Guiot, I. Karpenko and T. Pierog, *Evidence for Flow from Hydrodynamic Simulations of p-Pb Collisions at 5.02 TeV from* v_2 *Mass Splitting*, *Phys. Rev. Lett.* **112** (2014) 232301 [`1307.4379`].

[361] B. Schenke, S. Schlichting and R. Venugopalan, *Azimuthal anisotropies in p+Pb collisions from classical Yang–Mills dynamics*, *Phys. Lett. B* **747** (2015) 76 [`1502.01331`].

[362] ALICE collaboration, *Long-range angular correlations on the near and away side in p-Pb collisions at* $\sqrt{s_{NN}}$ = 5.02 *TeV*, *Phys. Lett. B* **719** (2013) 29 [`1212.2001`].

[363] CMS collaboration, *Observation of Long-Range Near-Side Angular Correlations in Proton-Lead Collisions at the LHC*, *Phys. Lett. B* **718** (2013) 795 [`1210.5482`].

[364] ATLAS collaboration, *Measurement with the ATLAS detector of multi-particle azimuthal correlations in p+Pb collisions at* $\sqrt{s_{NN}}$ *=5.02 TeV*, *Phys. Lett. B* **725** (2013) 60 [`1303.2084`].

[365] R. Samanta and J.-Y. Ollitrault, *Multiplicity fluctuations and rapidity correlations in ultracentral proton-nucleus collisions*, `2405.14671`.

[366] S. Huang, *Measurements of azimuthal anisotropies in* ^{16}O+^{16}O *and* γ*+Au collisions from STAR*, 12, 2023 [`2312.12167`].

[367] Z. Citron et al., *Report from Working Group 5: Future physics opportunities for high-density QCD at the LHC with heavy-ion and proton beams*, *CERN Yellow Rep. Monogr.* **7** (2019) 1159 [`1812.06772`].

[368] J. Brewer, A. Mazeliauskas and W. van der Schee, *Opportunities of OO and pO collisions at the LHC*, in *Opportunities of OO and pO collisions at the LHC*, 3, 2021 [`2103.01939`].

[369] ALICE collaboration, *The ALICE experiment – A journey through QCD*, `2211.04384`.

[370] M. Rybczyński and W. Broniowski, *Glauber Monte Carlo predictions for ultrarelativistic collisions with* ^{16}O, *Phys. Rev. C* **100** (2019) 064912 [`1910.09489`].

[371] M.D. Sievert and J. Noronha-Hostler, *CERN Large Hadron Collider system size scan predictions for PbPb, XeXe, ArAr, and OO with relativistic hydrodynamics*, *Phys. Rev. C* **100** (2019) 024904 [`1901.01319`].

[372] D. Behera, S. Deb, C.R. Singh and R. Sahoo, *Characterizing nuclear modification effects in high-energy O-O collisions at energies available at the CERN Large Hadron Collider: A transport model perspective*, *Phys. Rev. C* **109** (2024) 014902 [`2308.06078`].

[373] Y. Wang, S. Zhao, B. Cao, H.-j. Xu and H. Song, *Exploring the compactness of* α *clusters in O16 nuclei with relativistic O16+O16 collisions*, *Phys. Rev. C* **109** (2024) L051904 [`2401.15723`].

[374] C. Zhang, J. Chen, G. Giacalone, S. Huang, J. Jia and Y.-G. Ma, *Ab-initio nucleon-nucleon correlations and their impact on high energy* ^{16}O+^{16}O *collisions*, `2404.08385`.

[375] X.-L. Zhao, G.-L. Ma, Y. Zhou, Z.-W. Lin and C. Zhang, *Nuclear cluster structure effect in* ^{16}O+^{16}O *collisions at the top RHIC energy*, `2404.09780`.

[376] D. Behera, N. Mallick, S. Tripathy, S. Prasad, A.N. Mishra and R. Sahoo, *Predictions on global properties in O+O collisions at the Large Hadron Collider using a multi-phase transport model*, *Eur. Phys. J. A* **58** (2022) 175 [`2110.04016`].

[377] ALICE collaboration, *Centrality Dependence of the Charged-Particle Multiplicity Density at Midrapidity in Pb-Pb Collisions at $\sqrt{s_{\mathrm{NN}}}$ = 5.02 TeV*, *Phys. Rev. Lett.* **116** (2016) 222302 [`1512.06104`].

[378] E. Grossi, A. Soloviev, D. Teaney and F. Yan, *Soft pions and transport near the chiral critical point*, *Phys. Rev. D* **104** (2021) 034025 [`2101.10847`].

[379] A. Guillen and J.-Y. Ollitrault, *Fluid velocity from transverse momentum spectra*, *Phys. Rev. C* **103** (2021) 064911 [`2012.07898`].

Appendix A

Fluctuations of harmonic flow

A.1 Toy model for transverse momentum dependent flow decorrelation

The relation between flow vector, magnitude and angle decorrelation in Eq. (3.68) can be proved based on a simple toy model [246]. To account for the momentum dependent fluctuations, which are small, let us consider the transverse momentum dependent flow vector $V_n(p)$ as a small deviation from the integrated flow,

$$\vec{V}_n(p) = C(p)\vec{V}_n + \vec{\delta}(p), \tag{A.1}$$

where, $C(p)$ is a scalar and $\vec{\delta}(p)$ is a small vector deviation, both of which depend on the transverse momentum, denoted here by p. Then the event-by-event transverse momentum dependent fluctuations of $\vec{V}_n(p)$ is governed by both the scalar $C(p)$ and the vector $\vec{\delta}(p)$ where the latter is solely responsible for the flow angle fluctuations.

Next we take scalar product of Eq. (A.1) with $\vec{V}_n$ and then take average over events :

$$\langle \vec{V}_n \cdot \vec{V}_n(p)^\star \rangle = C(p)\langle \vec{V}_n \cdot \vec{V}_n^\star \rangle + \langle \vec{V}_n \cdot \vec{\delta}(p)^\star \rangle \ . \tag{A.2}$$

Now comes our main *model* assumption :

$$\langle \vec{V}_n \cdot \vec{\delta}(p)^\star \rangle = 0 \ , \tag{A.3}$$

which is based on the fact that transverse momentum dependent fluctuations are small and randomly oriented so that its correlation with the integrated flow can be taken to be zero. With this from Eq. (A.2), we have ,

$$C(p) = \frac{\langle \vec{V}_n \cdot \vec{V}_n(p)^\star \rangle}{\langle \vec{V}_n \cdot \vec{V}_n^\star \rangle} = \frac{\langle \vec{V}_n \cdot \vec{V}_n(p)^\star \rangle}{\langle v_n^2 \rangle} \ , \tag{A.4}$$

where $v_n^2 \equiv |\vec{V}_n|^2$.

A.1.1 Flow vector decorrelation in second order

The factorization-breaking coefficient between flow vector squared is given by Eq. (3.59),

$$r_{n;2}(p) = \frac{\langle \vec{V}_n^2 \cdot \vec{V}_n^*(p)^2 \rangle}{\sqrt{\langle v_n^4 \rangle \langle v_n^4(p) \rangle}} \; . \tag{A.5}$$

Using Eq. (A.1) the numerator becomes up to second order in $\delta(p)$,

$$\langle \vec{V}_n^2 \cdot \vec{V}_n^*(p)^2 \rangle = C(p)^2 \langle v_n^4 \rangle \; , \tag{A.6}$$

where we have used $\langle \vec{V}_n(p) \cdot \vec{\delta}(p)^\star \rangle = 0$ and $\langle \vec{V}_n(p)^2 \cdot \vec{\delta}^2(p)^\star \rangle = 0$. Similarly, in the denominator,

$$\langle v_n^4(p) \rangle = \vec{V}_n^2(p) \cdot \vec{V}_n^\star(p)^2 = C(p)^4 \langle v_n^4 \rangle + 4C(p)^2 \langle v_n^2 \delta(p)^2 \rangle \tag{A.7}$$

where $\delta(p)^2 = \vec{\delta}(p)\vec{\delta}(p)^\star$. With this Eq. (A.5) becomes,

$$r_{n;2}(p) = \frac{1}{\left(1 + 4\frac{\langle v_n^2 \delta(p)^2 \rangle}{C(p)^2 \langle v_n^4 \rangle}\right)^{1/2}} \simeq 1 - 2\Delta_n(p) \tag{A.8}$$

where,

$$\Delta_n(p) = \frac{\langle v_n^2 \delta(p)^2 \rangle}{C(p)^2 \langle v_n^4 \rangle} \tag{A.9}$$

is the decorrelation factor and it is small, quantifying the amount of decorrelation between transverse momentum dependent flow vector and momentum averaged flow vector.

A.1.2 Flow magnitude decorrelation

Factorization-breaking coefficient between flow magnitude squared is given by,

$$r^{v_n^2}(p) = \frac{\langle |\vec{V}_n|^2 |\vec{V}_n^*(p)|^2 \rangle}{\sqrt{\langle v_n^4 \rangle \langle v_n^4(p) \rangle}} \; . \tag{A.10}$$

The denominator remain same as before. The numerator can be expanded as,

$$\langle |\vec{V}_n|^2 |\vec{V}_n^*(p)|^2 \rangle = \langle v_n^4 C(p)^2 \rangle + \langle v_n^2 \delta(p)^2 \rangle = C(p)^2 \langle v_n^4 \rangle \Big(1 + \Delta_n(p) \Big). \tag{A.11}$$

Then Eq. (A.10) becomes,

$$r^{v_n^2}(p) \simeq (1+\Delta_n(p))(1-2\Delta_n(p)) \simeq 1-\Delta_n(p) \tag{A.12}$$

Thus Eqs. (A.8) and (A.12) satisfies the relation,

$$1 - r_{n;2}(p) = 2[1 - r^{v_n^2}(p)] \ , \tag{A.13}$$

as given in Eq. (3.61).

A.1.3 Flow angle decorrelation

The experimental estimate of the flow angle decorrelation is obtained by taking ratio of the flow vector and flow magnitude factorization-breaking coefficients and provides a measure of the actual angle decorrelation,

$$F_n(p) = \frac{\langle \vec{V}_n^2 \cdot \vec{V}_n^*(p)^2 \rangle}{\langle |\vec{V}_n|^2 |\vec{V}_n^*(p)|^2 \rangle} \simeq \frac{\langle v_n^4 \cos[2n(\Psi_n - \Psi_n(p))] \rangle}{\langle v_n^4 \rangle}. \tag{A.14}$$

Then using the previous equations one gets,

$$F_n(p) = \frac{1}{1+\Delta_n(p)} \simeq 1 - \Delta_n(p). \tag{A.15}$$

Thus from a simple toy model of transverse momentum dependent flow vectors with random small fluctuations, one can prove the relation presented in Eq. (3.68),

$$[1 - r_{n;2}(p)] \simeq [1 - r_n^{v_n^2(p)}] + [1 - F_n(p)] \tag{A.16}$$

which is also reflected in the results presented in Chapter-3.

Appendix B

Transverse momentum fluctuations

B.1 Simulations with hydrodynamics and HIJING

The setup of our hydrodynamic calculation in Chapter-4 is identical to that of Chapter-3. We use a boost-invariant version of the hydrodynamic code MUSIC [216] with the default freeze-out temperature $T_f = 135$ MeV. We assume a constant shear viscosity to entropy density ratio $\eta/s = 0.12$, and the bulk viscosity is set to zero. The initial entropy distributions are taken from the TRENTO model [194], where the parameters are fixed as follows. The most important parameter is the parameter p which defines the dependence of the density on the thickness functions of incoming nuclei, which is set to $p = 0$, corresponding to a geometric mean, which is the default choice. The parameter defining the strength of multiplicity fluctuations is set to $k = 2.5$ (the default being $k = 1$). With this choice, the relative multiplicity fluctuations is compatible (within statistical errors) with ATLAS data in Table 4.1. The nucleon-nucleon cross section is set to $\sigma_{NN} = 7.0$ fm^2 (instead of the default $\sigma_{NN} = 6.4$ fm^2).

The normalization of the entropy density from the TRENTO model is adjusted so as to reproduce the charged multiplicity measured by ALICE in Pb+Pb collisions at 5.02 TeV [377]. Despite this normalization, the average mulplicity is $\overline{N_{ch}} = 6660 \pm 30$, much larger than that seen by ATLAS (Table 4.1). The main reason is that some of the particles escape detection, even within the specified angular and p_T range, and the data are not corrected for the reconstruction efficiency. In addition, we expect deviations between the model and data for two reasons. First, hydrodynamic models typically underestimate the pion yield at low p_T [378, 379]. Since the calculation is adjusted to reproduce the total charged multiplicity, which is dominated by pions, this implies in turn that it should overestimate the yield for $p_T > 0.5$ GeV/c, which is the range where it is measured by ATLAS. Second, our hydrodynamic calculation assumes that the momentum distribution is independent of rapidity. In reality, it is maximum near mid-rapidity, in the region covered by the ALICE acceptance. This should also lead to slightly overestimating the multiplicity seen by ATLAS, whose inner detector covers a broader range in rapidity.

The width of p_T fluctuations from our hydrodynamic calculation is $\sigma_{p_T}(0) = 13 \pm 1$ MeV$/c$. Note that they are dynamical fluctuations only. The reason is that we do not sample particles according to a Monte Carlo algorithm, but simply calculate the expectation value of $[p_T]$ at freeze-out. Therefore, the width of $[p_T]$ fluctuations from the hydrodynamic calculation can in principle be compared directly with that measured experimentally. Our value is somewhat higher than the value $\sigma_{p_T}(0) = 9.357$ MeV$/c$ inferred from ATLAS data (see Fig. 4.1). The fact that hydrodynamics overestimates $[p_T]$ fluctuations is an old problem [304], which can be remedied by carefully tuning the fluctuations of the initial density profile [305, 12, 28]. It is the reason why we choose to fit the magnitude of $[p_T]$ fluctuations to data, rather than obtain it from a hydrodynamic calculation.

The Pearson correlation coefficient between N_{ch} and $[p_T]$ from our hydrodynamic calculation is $r_{N_{ch}} \sim 0.674$ which is in excellent agreement with the value $r_{N_{ch}} = 0.676$ returned by the fit to ATLAS data (Fig. 2 (c) of the paper). Simulations with HIJING shown in Fig. (4.2) of the paper follow the same setup as in Ref. [308]. The average multiplicity is $\overline{N_{ch}} = 5149$, somewhat lower than in the hydrodynamic calculation, and the average value of p_T, denoted by $\overline{p_T}$, is 941 MeV$/c$, also lower than in the hydrodynamic simulation ($\overline{p_T} = 1074$ MeV$/c$).

B.2 Fitting the variance of $[p_T]$ fluctuations

ATLAS provides us with two data sets for the centrality dependence of the variance, depending on whether centrality is determined with N_{ch} or E_T. We first carry out a standard χ^2 fit for each of these sets, where the error is the quadratic sum of the statistical and systematic errors on the data points. The three fit parameters are $\sigma_{p_T}(0)$ (the standard deviation of $[p_T]$ for $b = 0$), α (which defines the decrease of the variance as a function of impact parameter), and the Pearson correlation coefficient r between $[p_T]$ and the centrality estimator for fixed b. Consistency of our model requires that $\sigma_{p_T}(0)$ and α, whose definition does not involve the centrality estimator, are identical for N_{ch} and E_T based data for a given p_T selection. Values of $\sigma_{p_T}(0)$ are identical within less than 1%, but values of α differ by 6%, with E_T-based data favoring a larger α. We then fix the values of $\sigma_{p_T}(0)$ and α to the average values of N_{ch} and E_T-based results, and redo the fits by fitting solely the Pearson correlation coefficient r for each of the two data sets. Due to the small tension between the values of α, our fit slightly overestimates the variance for the lowest values of N_{ch}, and slightly underestimates it for the lowest values of E_T. This effect is of little relevance to our study which focuses on ultra-central collisions, and we have not investigated its origin.

The values of α are close to 1.2, which implies that the variation of dynamical fluctuations with impact parameter is faster than that of statistical fluctuations, for which $\alpha = 1$. The parameter $\sigma_{p_T}(0)$ is close to 10 MeV$/c$, while the average value of p_T is close to 1 GeV$/c$. This corresponds to a relative dynamical fluctuations of order 1% in central collisions. The values of the Pearson correlation coefficient end up being similar, between 0.6 and 0.7, for both data sets.

The results shown are obtained by assuming that the variance of the charged multiplicity is proportional to the mean, that is, $\mathrm{Var}(N_{ch}|c_b)/\overline{N_{ch}}(c_b)$ is constant. As explained in Sec. 4.1.3, we have also tested two alternative scenarios, assuming either that $\mathrm{Var}(N_{ch}|c_b)$ is constant or that the ratio $\mathrm{Var}(N_{ch}|c_b)/\overline{N_{ch}}(c_b)^2$ is constant. We have checked that the fit to the data is as good. The values of fit parameters vary only by 3% for α, and even less for $\sigma_{p_T}(0)$ and r.

B.3 Centrality dependence of multiplicity fluctuations

The probability distribution of the multiplicity at fixed impact parameter b is expected to be approximately Gaussian [67] and can be characterized by its mean $\overline{N_{ch}}(c_b)$ and standard deviation $\sigma_{N_{ch}}(c_b)$, which both depend on b. The mean can be reconstructed using the simple following rule. If a fraction c_b of events have a multiplicity larger than N, then $N \simeq \overline{N_{ch}}(c_b)$ [66]. This simple rule, which is applied to ATLAS data in Fig. B.1 (a), works well except for multiplicities around and above the knee. On the other hand, the centrality dependence of $\sigma_{N_{ch}}$ is not known, and we use state-of-the-art hydrodynamic calculations by the Duke group [27] and by the JETSCAPE collaboration [28] to evaluate it. However, we want to avoid running massive hydrodynamic calculations, and we therefore estimate the multiplicity fluctuations from the initial conditions of these calculations. We assume that for every collision event, the multiplicity is proportional to the initial energy. Both Duke and JETSCAPE analyses employ

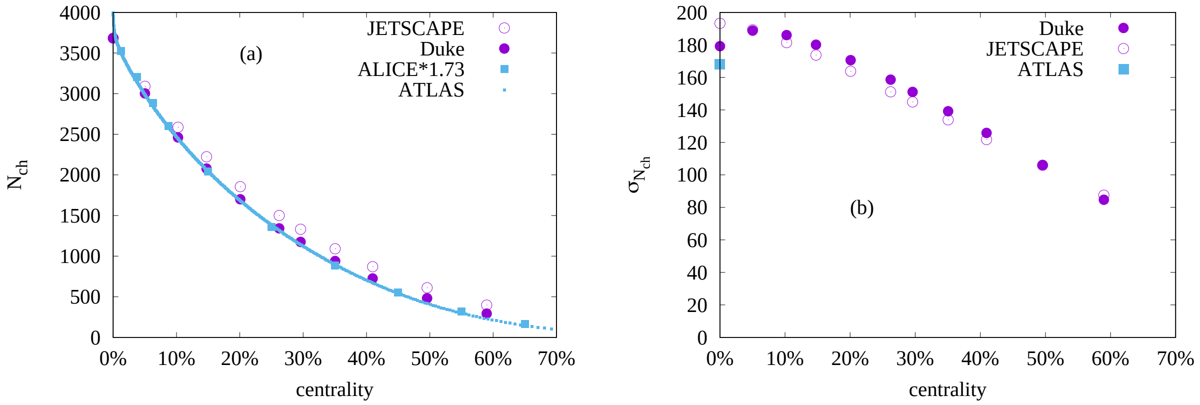

Fig. B.1 Left: Variation of charged multiplicity N_{ch} with centrality in Pb+Pb collisions at $\sqrt{s_{NN}} = 5.02$ TeV measured by ATLAS [102] and ALICE [377]. For ATLAS, the centrality is defined from the cumulative distribution of N_{ch} and then divided by a calibration factor 1.153 [60], which corrects for the fact that for the largest centrality fractions, some of the recorded events are fake. The ALICE results have been re-scaled by a factor 1.73 to correct for the different acceptance and efficiency of the detector. The circles display the centrality dependence of the mean initial energy for the T$_\mathrm{R}$ENTo parametrizations used by the Duke [27] and JETSCAPE analyses [28]. The centrality is defined as $\pi b^2/\sigma_{\mathrm{Pb}}$, where $\sigma_{\mathrm{Pb}} = 767$ fm^2 is the total inelastic cross section. Right: Variation of the standard deviation of N_{ch} with centrality.

the TRENTo parametrization [194] for the initial energy density, but with slightly different values of the parameters. We run these TRENTo initial conditions for several fixed values of b (specifically, $b = 0$, 3.5, 5, 6, 7, 8, 8.5, 9.25, 10, 11, 12 fm). For each b, we generate 10^5 events with both Duke and JETSCAPE parameters, and we compute the initial energy of each event. We rescale this energy by a constant factor so that it matches the ATLAS result for the charged multiplicity at $b = 0$ [126]. The variation of the mean N_{ch} with centrality is displayed in Fig. B.1 (a). Experimental data are also shown. One sees that ALICE and ATLAS data are in excellent agreement once properly rescaled. The calculation using the Duke parametrization agrees very well with experiment. Agreement is not quite as good, but still reasonable, for the JETSCAPE parametrization.

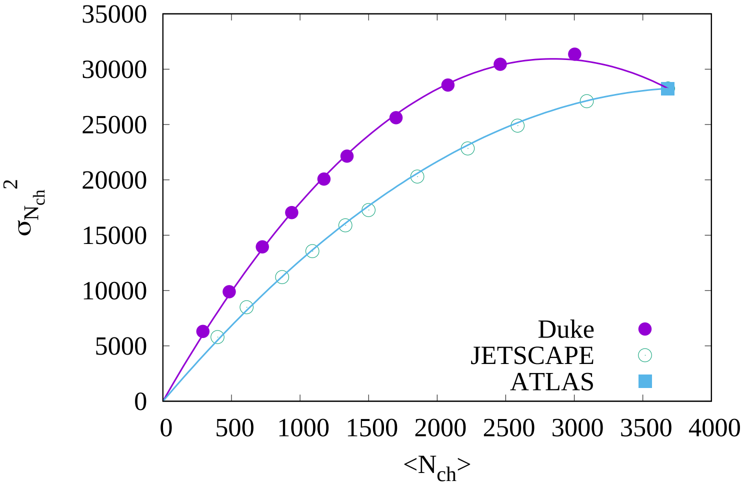

Fig. B.2 Parametric plot of the mean and variance of N_{ch} as a function of b. Both models have been calibrated in such a way that they match data at $b = 0$. Solid lines are fits using $y = \gamma x + (1-\gamma)x^2$, where $y \equiv \sigma^2_{N_{ch}}(b)/\sigma^2_{N_{ch}}(0)$ and $x \equiv \overline{N_{ch}}(c_b)/\overline{N_{ch}}(0)$, with $\gamma = 2.83$ (Duke) and $\gamma = 1.90$ (JETSCAPE). The calculation in Sec. 4.1 was done with $\gamma = 1$ (variance proportional to mean).

We then calculate the standard deviation of N_{ch}, $\sigma_{N_{ch}}$, for each value of b. Results are displayed in Fig. B.1 (b). The standard deviation can only be measured at $b = 0$ [325] from the tail of the distribution of N_{ch}, therefore, there is only one data point on this plot. One sees that both model calculations are in reasonable agreement with this data point, but slightly overestimate it. We use model calculations only to predict the b-dependence of $\sigma_{N_{ch}}$, not the value at $b = 0$ which is measured precisely. We therefore rescale $\sigma_{N_{ch}}$ from the model calculation by a constant factor so that it matches the experimental value at $b = 0$. The resulting predictions for $b > 0$ are displayed in Fig. B.2. We plot the variance $\sigma^2_{N_{ch}}$ as a function of the mean. If N_{ch} is the sum of k identical, uncorrelated distributions, where k depends on b, both the mean and the variance are proportional to k, therefore, they are proportional to one another. This behavior is only observed for large values of b. Both model calculations predict that the variance increases more slowly as b decreases. The Duke calculation even predicts that it decreases for the smallest value of b. The two solid lines, which are polynomial fits to our calculations, are used as two limiting cases which define the error bands in Fig. 4.8 and Fig. 4.9.